AD/A-005 357

NONDESTRUCTIVE DETECTION OF STRUCTURAL DAMAGE UNIQUELY ASSOCIATED WITH FATIGUE

J. F. Moore, et al

Rockwell International Corporation

Prepared for:

Air Force Materials Laboratory
Advanced Research Projects Agency
Arizona University

July 1974

NOTICE

When Government drawings, specifications, or other data are used for any purpose other than in connection with a definitely related Government procurement operation, the United States Government thereby incurs no responsibility nor any obligation whatsoever; and the fact that the Government may have formulated, furnished, or in any way supplied the said drawings, specifications, or other data, is not to be regarded by implication or otherwise as in any manner licensing the holder or any other person or corporation, or conveying any rights or permission to manufacture, use, or sell any patented invention that may in any way be related thereto.

This technical report has been reviewed and is approved for publication

JOHN E. ALLISON
Project Engineer

FOR THE COMMANDER

D. M. FORNEY, JR., CHIEF
NONDESTRUCTIVE EVALUATION BRANCH
METALS AND CERAMICS DIVISION

Copies of this report should not be returned unless return is required by security considerations, contractual obligations, or notice on a specific document.

AFML-TR-74-131

NONDESTRUCTIVE DETECTION OF STRUCTURAL DAMAGE UNIQUELY ASSOCIATED WITH FATIGUE

JOHN F. MOORE
SCHILLINGS TSANG
DONALD O. THOMPSON
ROCKWELL INTERNATIONAL CORPORATION

STUART A. HOENIG
UNIVERSITY OF ARIZONA

LOS ANGELES AIRCRAFT DIVISION
ROCKWELL INTERNATIONAL CORPORATION
INTERNATIONAL AIRPORT
LOS ANGELES, CALIFORNIA 90009

Technical Report AFML-TR-74-131

JULY 1974

AIR FORCE MATERIALS LABORATORY
AIR FORCE SYSTEMS COMMAND
WRIGHT–PATTERSON AFB, OHIO 45433

ib

This page is intentionally left blank.

Unclassified

SECURITY CLASSIFICATION OF THIS PAGE (When Data Entered)

REPORT DOCUMENTATION PAGE		READ INSTRUCTIONS BEFORE COMPLETING FORM
1. REPORT NUMBER	2. GOVT ACCESSION NO.	3. RECIPIENT'S CATALOG NUMBER AD/A005357
4. TITLE (and Subtitle) Nondestructive Detection of Structural Damage Uniquely Associated With Fatigue		5. TYPE OF REPORT & PERIOD COVERED Final Technical Report 1 June 1972 - 31 May 1974
		6. PERFORMING ORG. REPORT NUMBER NA-74-342
7. AUTHOR(s) J. F. Moore, S. Tsang, D. O. Thompson, and S. A. Hoenig (University of Arizona)		8. CONTRACT OR GRANT NUMBER(s) F33615-72-C-1733
9. PERFORMING ORGANIZATION NAME AND ADDRESS Rockwell International Corporation International Airport Los Angeles, California 90009		10. PROGRAM ELEMENT, PROJECT, TASK AREA & WORK UNIT NUMBERS Project No. 7351 ARPA Order No. 1244 Code 1D10 Amendment No. 6
11. CONTROLLING OFFICE NAME AND ADDRESS Nondestructive Testing and Mechanics Branch (LLN) Metals and Ceramics Division, Air Force Materials Laboratory, Wright-Patterson Air Force Base, Ohio		12. REPORT DATE July 1974
		13. NUMBER OF PAGES xii + 200
14. MONITORING AGENCY NAME & ADDRESS (if different from Controlling Office)		15. SECURITY CLASS. (of this report) Unclassified
		15a. DECLASSIFICATION/DOWNGRADING SCHEDULE

16. DISTRIBUTION STATEMENT (of this Report)

Approved for public release; distribution is unlimited.

17. DISTRIBUTION STATEMENT (of the abstract entered in Block 20, if different from Report)

18. SUPPLEMENTARY NOTES

19. KEY WORDS (Continue on reverse side if necessary and identify by block number)

Fatigue, Fatigue Damage, Exoelectron Emission, Surface Potential Difference, Ellipsometry, Acoustic Emission, Photoemission, Ultrasonic Wave, Surface Oxide, Nondestructive Test Method, Auger Spectrum, Aerospace Structure, Mechanical Scanner.

20. ABSTRACT (Continue on reverse side if necessary and identify by block number)

This is the final technical report for a program directed at the development of reliable nondestructive testing and inspection methods to locate and assess fatigue damage in Air Force aircraft structures. The primary nondestructive test approach is the application of exoelectron emission to the detection of fatigue damage. The program initially conducted a series of controlled fatigue tests in an ultrahigh vacuum chamber equipped with devices to

DD FORM 1 JAN 73 1473 EDITION OF 1 NOV 65 IS OBSOLETE

Unclassified

SECURITY CLASSIFICATION OF THIS PAGE (When Data Entered)

20. Abstract - Continued

measure the photo-stimulated exoelectron current and to fully characterize the surface state of the specimen prior to, during, and after fatigue measurement. The stimulated exoelectron current was found to increase with increase in applied strain amplitude and decrease with surface oxide thickness. A new exoelectron emission mechanism based upon the roughness-enhanced, optical-photoyield coupling phenomena was developed. Next, the program was directed to perform a series of fatigue tests in air on specimens of different shapes with and without discontinuities under various loading and environmental conditions, in order to develop a practical technique for applying exoelectron emission and surface potential difference measurements to assess fatigue damage as well as to predict final failure sites. Based upon the nondestructive measurements, a quantitative-statistical method was developed to facilitate the analysis and comparison of exoelectron emission data gathered during fatigue test for the prediction of the failure site. Another method of analyzing both exoelectron emission and surface potential difference data obtained during several interruptions of the fatigue cycling was also developed. Finally, a porotype system design for the automatic scanning and exoelectron emission testing of aircraft-type structures was developed.

FOREWORD

This is the final technical report on a study for the nondestructive detection of structural damage uniquely associated with fatigue performed by the Los Angeles Aircraft Division (LAAD) of Rockwell International. This research was supported by the Air Force Materials Laboratory (LLN) of the Air Force Systems Command, USAF, Project 7351, contract F33615-72-C-1733, and Advanced Research Projects Agency of the Department of Defense, under ARPA order 1244, amendment 6, program code 1D10. The contract was monitored by the AFML, LLN, with Lieutenant John Allison as the project engineer. This report complies with the contractual requirement delivery item 0002, sequence A003, and covers the period from June 1, 1972 to May 31, 1974.

This program was conducted by Materials and Producibility of LAAD, Mr. N. Klimmek, manager, under the direction of Mr. J. F. Moore, program manager. Personnel responsible for the effort described in this report include J. F. Moore, Dr. S. Tsang, and Mr. F. M. Coate of LAAD; Dr. D. O. Thompson, Dr. T. Smith, Dr. G. Alers, and Dr. L. Graham of the Science Center of Rockwell International; and Professor S. A. Hoenig of the University of Arizona.

This page is intentionally left blank.

TABLE OF CONTENTS

TABLE OF CONTENTS (CONT)

TABLE OF CONTENTS (CONT)

LIST OF ILLUSTRATIONS

LIST OF TABLES

Section I

SUMMARY

This program was directed toward the development of reliable nondestructive testing (NDT) and inspection methods to locate and assess fatigue damage in Air Force aircraft structures. The primary NDT approach has been the application of exoelectron emission for the detection of fatigue damage. This report describes the development of a more fundamental understanding of the nature of the exoelectron emission phenomenon, a practical technique for applying exoelectron emission and surface potential difference measurements to assess fatigue damage as well as to predict final failure site, and the development of a prototype exoelectron emission measuring system.

Other NDT methods evaluated on a limited basis included ultrasonic attenuation, acoustic emission, and penetrant, which showed limited applicability for particular fatigue conditions.

A significant achievement of the program was the development of a more fundamental understanding of the nature of exoelectron emission phenomenon. This development effort was conducted in an ultrahigh vacuum (10^{-10} torr) chamber where exoelectron emission currents were made on aluminum specimens fatigued under low-stress, high-cycle fatigue conditions. The vacuum chamber was equipped with an ellipsometer, a surface potential difference measuring device, an argon ion bombardment gun, and an Auger electron spectrometer. Thus, it was possible to characterize fully the surface state of the specimen prior to, during, and after the fatigue measurements. It is shown that the photo-simulated exoelectron current increases with strain (or stress) amplitude during fatigue. During fatigue, the emission current stops at the point at which the fatigue-generated crack has grown to the point that failure occurs. The initial current level is somewhat variable from specimen to specimen, even though they were similarly prepared; however, the trend of the initial current is definitely increasing with decreasing oxide thickness. The incremental difference between the final and initial values of the current increases very significantly with decreasing oxide thickness, and the difference between the stationary and vibrating current values also increases with diminishing oxide thickness. The result of the exoelectron emission as a function of the oxide thickness experiments indicates that the principal role of the oxide is that of an attenuator of emission, not, as has been suggested, as a source of the emission. Analysis of the data further shows that a single measured current value under these

conditions would be ambiguious in defining the fatigue state of the material. An auxiliary measure or method of either fatigue or current data analysis must be found which can be used reliably in conjunction with the photo-stimulated exoelectron emission to remove the ambiguity.

A new mechanism relating the stimulated exoelectron emission to roughness-enhanced photoemission is suggested. Surface roughness serves to couple light from vacuum (air) into the surface plasmon modes of a nearly free-electron-like metal. The optical frequency at which the maximum roughness-enhanced photoemission takes place can be expected to move toward smaller optical energies as the wave length of the roughness increases. The nonuniformity of fatigue deformation manifests itself with some degree of regularity in the slip patterns produced. These patterns can contribute significantly to a fatigue-generated surface roughness condition many orders of magnitude greater than the rms roughness required to produce optical coupling into the plasmon modes.

Exoelectron emission and surface potential difference measurements were made under ambient laboratory conditions to nondestructively evaluate the effects of fatigue damage on 2024 and 7075 aluminum alloys, annealed Ti-6Al-4V, and SRH-1050 condition PH14-8Mo steel under various loading conditions and environmental conditions. The loading conditions included low-cycle, high-cycle, spectrum (low-high, high-low, and low-high-low stress range), and elastic loading. The environmental conditions evaluated included general plastic deformation, atmospheric humidity, and corrosion. All the tensile fatigue (zero to maximum load) tests were conducted in air at a rate between 1 and 20 Hz. Exoelectron emission from the specimen was measured without interrupting the fatigue test. The effect of the various fatigue loading and environmental conditions on the exoelectron emission measurements was evaluated and, in general, did not adversely affect ability of the measurement to detect the fatigue damage and the eventual failure site. The exoelectron emission measurement was shown to be capable of monitoring the fatigue process, to observe the buildup of damage at a known defect and to predict by the change in exoelectron current at the location of eventual failure site in specimens containing holes (open or covered), slots or changes in cross section, and simulated bolted joints. A quantitative-statistical method was developed to facilitate analysis and comparison of the exoelectron current data. This method is based on a 10-point data sampling along each side of the straight (constant width) test zone of the specimen. These data are compared at selected cycling increments during the fatigue test and plotted to show when and where a significant change in emission occurs. The failure site could be predicted with a good probability

by noting this emission change, occurring usually at the specimen side from which the fatigue crack first emerges. The failure site can also be approximately located by either comparing the exoelectrom emission and surface potential difference data or by analyzing the data from one of the two measurement methods obtained during several interruptions of the fatigue cycling.

A prototype exoelectron emission system and an automatic scanning subsystem were developed. The scanner permits in situ measurement of exoelectron emission on the coupon-type specimens without interrupting the fatigue cycling action. The electron emission readout may be continuous or may be selected as a function of number fatigue cycles and automatically recorded. This system provides for unattended monitoring of high-cycle fatigue experiments and forms a basis for evaluating the scanning inspection requirements for air vehicle applications. A prototype transducer system was also developed for measuring exoelectron emission inside holes approximately 12mm in diameter.

Recommendations for future investigations for the nondestructive determination of fatigue damage include the further development of the exoelectron emission method, which has proven to be highly promising. This development should include a more complete definition and characterization of the exoelectron emission phenomenon in terms of origin and energy levels, as presently being investigated at the Rockwell International Science Center under an AFOSR contract. Since this program showed that a single exoelectron emission measurement would be ambiguous in determining the degree of fatigue damage, another supplementary measurement is needed to predict fatigue life. The selection of such a measurement is premature at this time and will be significantly facilitated when further information regarding the definition of exoelectron emission characteristics, i.e., energy levels, frequency spectrum, etc., and definition of the mechanical-metallurgical characteristics of the fatigued material. Examples of supplementary measurement methods that appear potentially promising include optical description of the fatigue surface using ellipsometric methods and selected exoelectron emission excitation methods using thermal or ultrasonic methods. Finally, the exoelectron emission method should be evaluated on actual aircraft structures to establish the true capabilities and restrictions of the measurement method.

Section II

INTRODUCTION

Previous work by Rockwell International [1] screened eight techniques for fatigue damage detection and selected exoelectron emission and surface wave attenuation and velocity change as the most promising. This is confirmed by the work performed in the University of Arizona, [2] showing that exoelectron emission had considerable potential for developing a new nondestructive test (NDT) technique to detect and assess fatigue damage in aerospace structures.

The overall objective of this program is to increase the safety, reliability, and integrity of Air Force aircraft structures that are subjected to repeated loading and/or extensive vibration by developing reliable nondestructive testing and inspection (NDT/NDI) methods to locate and assess fatigue damage. It is expected that the successful completion of this objective should lead to the location of fatigue damage and anaysis of damage severity in maintenance or overhaul, and could be used to predict remaining safe-life and schedule replacement of selected aircraft hardware on a cost-effective basis. Additional careful monitoring of areas indicating intermediate advanced fatigue damage with crack detection technique could preclude catastrophic failures leading to extensive damage or losses of aircraft and crews.

The specific program development areas include:

1. Screening experiments to determine the types of fatigue damage and cracking that potential techniques may be reasonably expected to detect and measure

2. Study of material history, material surface, and environment influence upon the abilities of exoelectron emission and surface potential difference to assess fatigue damage in aluminum, steel, and titanium alloys and simulated aircraft structure hardware

3. Design and evaluation of a prototype equipment justified on the basis of preceding experiments

---

[1] Moore, et al, 1971

[2] Hoenig, 1971

Section III

LITERATURE REVIEW

This literature review is directed at determining and assessing the state of knowledge relating to the nondestructive measurement of fatigue damage in aerospace structures to provide an increased understanding of the fatigue process in terms of the measurement parameters and expected magnitudes. Therefore, a careful review of recent literature on these subjects was continued, following the previous program plan, [1] with most of the work reported herein gathered from the literature since 1970. Some information, however, is also derived from the publications in the late 1960's to cover the work previously overlooked.

FATIGUE PROCESS

FATIGUE AT ULTRASONIC FREQUENCIES

The initial series of experiments directed at establishing a model for the exoelectron emission phenomena was planned using a specimen cyclic loading rate in the 100 to 1,000 cycles-per-second range. The reason for the relatively high cyclic rates was based on the need to complete high cycle fatigue life conditions in reasonable time periods consistent with the planned number of observations using vacuum environment conditions.

Tests for metal fatigue are usually conducted at frequencies below about 0.17 kHz. The microstructural change, fatigue properties, and fatigue mechanism do not change significantly within this frequency range. When the frequency is raised to the ultrasonic range (about 17 kHz), the microstructural changes during fatigue become apparent. Furthermore, at high cycling rates, the heat evolved during the test cannot be dissipated fast enough to keep the specimen at the ambient temperature. Although the temperature increase is not high (for example, amounting to 4.6 to 5.1 K per 1,024 cycles in testing a zinc specimen at 19 kHz and a maximum displacement amplitude of 16.2 μm), (3) the measured temperature can be used to estimate the distribution of stress and plastic strain along the test specimen. At low displacement amplitudes and with the fatigue life of the zinc specimen greater than 10^8 cycles, the rate of temperature increase decreases continuously as a consequence of decreasing plastic deformation due

---

[3] Wielke, et al, 1973

to the increased work hardening. Similar behavior is observed in the early stage of a test where the specimens is subjected to a high displacement amplitude. However, after a number of cycles, depending on the maximum displacement amplitude, this temperature increment rises again as cycling proceeds. This reversion, which occurs approximately one or two orders of magnitude before final fracture takes place, is associated with the presence of crack in the specimen. Therefore, crack detection and possible life estimation in ultrasonic fatigue test may be accomplished by monitoring the temperature rise during test.

The fatigue of metals of various crystal structures in the ultrasonic frequency range is described in the following paragraphs.

Face-Centered Metal

At normal test frequency and small strain amplitudes (10^{-4} to 10^{-3}), the slip in alpha brass (an fcc alloy) spreads densely over a grain, with no slip-band cracking after 10^7 to 10^8 cycles. At ultrasonic frequency and the same strain amplitudes, the slip concentrates in single isolated bands in only occasional grains and reduces these to microcracks. [4] With further cycling, slip begins to spread from the slip-zone microcrack. Finally, some microcracks deepen into macrocracks which advance by producing at their heads a concentration of dense slip in which further slips and microcracking originate. It thus appears that the apparently safe strain amplitude for alpha brass observed in test at normal fatigue frequency may be quite unsafe if the test is carried out at ultrasonic frequency. On the other hand, fatigue cracks cannot be generated in copper at such high frequency and low strain amplitudes at room temperature. This is attributed to its high internal friction.

The fatigue life of some age-hardened aluminum alloys containing copper, magnesium, and zinc, may be lengthened by more than one order of magnitude at ultrasonic frequency range. [5] The crack at the initiation region is mainly straight and transcrystalline, oriented normal to the stress axis at the surface. Away from this region, the crack appears to follow an intercrystalline route.

Body-Centered Metal

The S/N curve of a bcc metal at normal test frequency usually exhibits a safe fatigue limit defined by stress or strain amplitude. This safe strain amplitude for iron is 13×10^{-4}. When the same iron is tested at ultrasonic

[4] Mason and Wood, 1968
[5] Hockenhull, 1967

frequency, fatigue cracks develop at a strain amplitude of 4×10^{-4}, about one-third the value which is regarded safe at normal frequency. [6] Moreover, whereas small amplitudes at normal frequency spread abnormal deformation primarily in grain boundaries, those at ultrasonic frequency concentrate it in a relatively few isolated slip bands. Hence, like alpha brass, iron behaves differently in fatigue at these two frequency ranges.

Hexagonal Close-Packed Metal

Titanium has limited slip systems, but at low frequencies it exhibits a safe limit of strain amplitude (about 3×10^{-3}) below which it has infinite life. Tests conducted on ultrasonic frequencies indicate a safe limit also of the order of 3×10^{-3} strain. [7] The microstructural changes, however, are different. In the normal frequency tests at higher strain amplitude than the safe limit, occasional grains develop slip, but this slip does not produce cracks. The microscopic damage that leads to fatigue takes the form of long transgranular shear cracks through grains showing no sign of slip. The ultrasonic frequency, on the other hand, develops highly isolated slip, as in the fcc and bcc metals. The fatigue begins with the cracking of the grains containing the isolated slip.

SLIPLESS FATIGUE

The studies of slipless fatigue are characterized by their use of low strain amplitude, high frequency, and resonant oscillation of the specimen. [8] Typically, the failure mode involves the production of a few isolated slip zones which are limited to single crystals. These slip zones are the sites where cracks are initiated; these cracks then progress by link-up from grain to grain and lead to catastrophic failure.

It has been suggested that significant strain builds up in individual crystals before any slip occurs. Eventual release of this stored energy produces almost immediate crack initiation in that particular crystal. The fact that significant strain energy is released by crack formation may allow the crack to move quite rapidly through the specimen from grain to grain until failure occurs. Slipless fatigue would then be characterized by the buildup of strain in otherwise elastic grains. Precrack phenomena might involve the formation of lines or depressions at the location where a crack will ultimately develop. When a crack does form, there is significant shear displacement across the crack itself. This displacement releases the strain energy that had been stored in the crystal.

---

[6] Wood and Mason, 1969
[7] MacDonald and Wood, 1971-A
[8] Wood, 1970

The observable slip that occurs in a few plastic grains, before cracks initiate in the elastic grains, is considered to be harmless. The fact that cracks appear in the elastic grains, rather than the grains which show evidence of slip, is considered to be the best indicator of slipless fatigue. [9]

The elastic cracking associated with slipless fatigue is detected at various stages of the fatigue process by means of scanning electron microscopy. It has been observed in titanium; [8][9][10] however, it is not certain whether this type of cracking also exists in face-centered or body-centered metals such as aluminum and iron.

SPECTRUM LOADING

The studies of spectrum loading in fatigue process are not new; many articles dealing with this subject and the similar type of loading - random loading - have been written. The literature is not reviewed here. However, the recent finding of the variation of fatigue life with the pattern of spectrum loading should be reported.

In one series of tests, three patterns of spectrum loading were applied to 2024-T3 aluminum clad sheets: [11] random program loading with short periods (40 cycles) and program loading with long periods (4×10^4 cycles). Two sequences (negative-positive cycles and positive-negative cycles) were tried in random loading; while in both program loadings, three sequences (low-high, high-low, and low-high-low amplitudes) were considered. The maximum and minimum loads in all the fatigue tests were the same. However, the test results indicate a strong dependence of fatigue life of notched and precracked specimens on the load sequence. The life for the random loading with the positive-negative cycles was slightly higher than the life with the negative-positive cycles, which was the lowest in all the tests. This result was opposite other observation. [12] Apparently, the damage accumulation by random loading is a complex problem not yet solved.

In the program loading for the same load sequence, [11] the life of a specimen exposed to the long period (4×10^4 cycles) is higher than the specimen exposed to the short period (40 cycles). When the three sequences in the long period were compared, the life of the specimen subjected to the low-high amplitude was the shortest and the high-low amplitude led to the longest life, which was also the longest in all the tests. The development of residual stresses in the crack tip area was thought to influence the fatigue life under these various load sequences.

---

[9] MacDonald and Wood, 1971-B
[10] MacDonald and Wood, 1971-C
[11] Schijve, 1972
[12] McMillan and Hertzberg, 1968

FATIGUE CRACK

Generally, it is thought that fatigue crack growth in metal proceeds in two stages. In the first stage, cracks result from dislocation motion along a slip plane in a maximum shear direction. The crack is, therefore, necessarily crystallographic from this definition. The crack propagates until the specimen fails or until it turns into a tensile direction for the second-stage growth. The stage II crack direction is thus governed by the direction of maximum tensile stress. There appears in the literature, however, some confusion about fatigue crack growth. It is found that cracks started by slip do not necessarily follow the stage I shear rule. The final macroscopic fracture can be in a transverse shear direction, rather than in a tensile direction as predicted by the two-stage model. Furthermore, the stage II crack can be crystallographic or noncrystallographic. Wood and his associates [13] found that a crack developed in torsional fatigue of annealed brass tube extended by a defacto propagation process of linking together existing crystallographic fissures of both the stage I slip band and misfit type (fissues at subgrain boundaries or grain boundaries). Thus, on a microscopic basis, the crack is made of stage I slip band and misfit fissures, but on a macroscopic basis, the crack would be a stage II tensile crack. It is not clear how this crack is classified by the two-stage model.

Wood and his associates found that dividing metals into two major classes of plastic and elastic clarified the analysis of fatigue cracking. In plastic metals, dislocation motion is easy and fatigue is the result of such motion. The crack starts from slip bands, subgrain boundaries, grain boundaries, or cell boundaries. The slip band fissures tend to be in a shear direction, but fissures at subgrain, grain, or cell boundaries may be in the shear direction or other directions. The crystallographic fissures then link together in a defacto propagation process which proceeds in either a shear or tensile direction. In elastic metals, dislocation motion is difficult because of the presence in the matrix of obstacles such as misfitting boundaries, precipitates, and solid-solution alloy atoms. Noncrystallographic shear crack is started by local inhomogeneous strains and internal stress and may have little to do with slip. In titanium, the "slipless" shear cracks propagate without the linking stage that is observed in plastic metals. The cracks then change to a tensile direction in the final stage of propagation. If an elastic metal is fatigued at strain amplitudes where dislocation motion is produced, the mechanisms of plastic and elastic fatigue will be in competition to produce the fatigue cracking.

---

[13] Gilmore, et al, 1972

Therefore, Wood and his associates suggest a division of metals into two major classes called plastic and elastic to clarify the analysis of fatigue cracking which occurs still in several stages: initiation, linking, and propagation. The type of material being tested will determine which stage will be present and what character each stage will have.

FATIGUE LIFE

Estimation of Fatigue Life

Fatigue life, N_f, can be defined as the sum of times required for crack initiation, N_o, its growth from microscopic size to macroscopic size, N_t, and propagation of the macroscopic crack to final failure, N_c. The ratio between the length of the periods varies widely with the size and geometry of the specimen or part. In recent years, considerable effort has been expended on N_c, the last term of the fatigue life. Analytical solutions have stemmed from several distinct disciplines of engineering science. After reviewing a number of concepts, Walton and Ellison [14] divided the various approaches for estimating N_c into three groups: models developed from dislocation theories, models formed on fracture mechanics and dimensional considerations, and semi-empirical models founded on cyclic material behavior. Most of the models can be expressed mathematically by the following expression:

$$\frac{da}{dN} = c\,\sigma^{m}\,a^{n} \tag{1}$$

where

a = semicrack length

N = number of cycles

σ = applied tensile stress

c, m, and n = constants

However, large deviations occurred in applying Equation 1 over a great variety of crack propagation rates. The approach by fracture mechanics leading to the equation

$$\frac{da}{dN} = M\,(\Delta K)^{\alpha} \tag{2}$$

[14] Walton and Ellison, 1972

where ΔK is the range of stress-intensity factor and both M and α are constants appears more satisfactory. After integration, Equation 2 becomes

$$N = \text{constant} \cdot \left[(\Delta k_c / \Delta k_i)^{\alpha - 2} - 1 \right] \tag{3}$$

where the subscripts c and i denote, respectively, the initial state (N = 0) and the terminal state ($N = N_c = N_f$). The usefulness of Equation 3 depends on the reliability of the knowledge of a_i, k_c, and α. It also depends on the validity of three other assumptions implied in Equation 1; namely, that (1) the crack growth rate depends on stress-range alone, being nearly enough independent of mean stress; (2) the relation is valid within the range between Δk_i and Δk_c; and (3) under nominally identical experimental or operational conditions, the relation is reproducible within a tolerable scatter range.

Freudenthal[15] presents detailed discussions of the uncertainties associated with the three assumptions. He suggests that the uncertainty and risk associated with the use of Equation 3 is too high to rely on in the prediction of the design life. The conditions under which the fracture-mechanics model approaches reality are exactly the conditions that should be avoided. It appears, therefore, the principal value of the fracture-mechanics approach to fatigue design is its use in the identification and avoidance of these conditions.

Fatigue Life of Some Aluminum Alloys

It is often rather uncertain to use the information in the literature concerning the three periods of time (N_o, N_t, and N_c) of a material for one's own investigation. The difficulties lie partly in a definition of terms and partly in the resolution of the observational techniques. In order to make one's test results useful to others, one must not only give definitions of the three stages, but also must state the crack nucleation site and the growth rate in a known geometrical configuration. A brief literature search of the fatigue crack initiation and propagation in some aluminum alloys follows. This information, which yields a better understanding of the fatigue damage, is essential to the present program toward the development of an NDT device for detecting and assessing fatigue damage in aircraft structures.

---

[15] Freudenthal, 1972

Fatigue cracks in 1100 aluminum nucleate at the surface in slip bands.[16] The formation of an intrusion-extrusion surface topography within these slip bands is well established. Dislocation activity unique to a surface layer approximately 10 μm deep results in the early formation of a dense cluster of dislocation dipoles on the most active glide planes. The formation of the intrusion-extrusion surface topography is a natural byproduct of this dislocation activity. It is commonly stated that the intrusion is the starting point for slip band fissures which are observed by electron microscopy at a magnification of 8,000 as early as 0.5 percent of life of a notched specimen under axial tension-compression loading at a stress of 4,160 psi. These fissure cracks grow in depth at the average rate of 2×10^{-2} angstroms per cycle, and link into a dominant crack across the surface (3.2 mm or 1/8 inch long) at 65 to 70 percent of fatigue life. If the nucleation time is defined as the time to nucleate any one microcrack, the time is less than 1 percent of life. If the transition stage occupies the time taken to develop a dominant crack across the notch surface, nearly 70 percent of total life is then necessary. Using the terminalogies N_f, N_t, and N_c, it can be said that, for the notched 1100 aluminum specimen under axial fatigue at 4,160 psi, N_o = 0.01 x life, N_t = 0.69 x life, and N_c = 0.3 x life.

Fine slip lines are also observed by electron microscopy on the notch surface of 2024-T4 alloy before the appearance of cracks.[17] These slip lines occur despite the fact that the concentrated stress at the root is only approximately one-half the yield strength of the alloy. Once formed, this fine slip is not observed to develop further with increased fatigue cycling. The length of these slip lines is limited by interaction of the helical dislocation loops with the large elongated constituent particles. All primary failure cracks are nucleated at surface constituent particle inclusions.[16] No concentrated slip can be seen in association with the early cracks. Nucleation of these cracks at a stress of 13.6 ksi requires about 5 percent of life. The cracks nucleate in pairs on opposite sides of the inclusion. A single crack-pair grows completely across the notch surface in approximately 90 percent of life. At higher stress of 18 ksi, many crack-pairs nucleate on the notch surface and link together to form a dominant crack across the notch at approximately 50 percent of life. Hence, for 2024-T4 alloy, N_o = 0.05 x life, N_t = 0.45 to 0.85 x life, and N_c = 0.1 to 0.5 x life.

Fatigue cracks in notched 7075-T6 alloy are nucleated in pairs at surface inclusions as a result of localized plastic deformation produced by stress concentration around the inclusion.[18] At least 65 percent of life is expended before a crack greater than 20 μm is observable in the notch. About 80 percent of life is spent to traverse the notch surface at a stress of 13.4 ksi.

---

[16] Grosskreutz and Shaw, 1965
[17] Grosskreutz and Shaw, 1968
[18] Grosskreutz and Shaw, 1966

The fractions of total life for the three stages are then, respectively, 0.65, 0.15, and 0.2. Transmission electron micrograph shows a high density of dislocations at the crack tip. This indicates that crack extension is accomplished by highly localized plastic deformation. There is also evidence of overaging at the crack tip, as shown by the increase in the average size of the Guinier-Preston zone within the plastic zone. Crack growth through this softer material might be slower because of the increase energy loss to plastic deformation. Such overaging, however, is not observed in 2024-T6 alloy.

EFFECT OF ATMOSPHERIC HUMIDITY ON FATIGUE LIFE

One of the environmental parameters to be investigated in the present program is evaporation, which is defined by the change in humidity of the air. It has been evident for some years that atmospheric conditions that could not normally be considered corrosive can have a marked effect on the fatigue strength of metals. The atmospheric constituent responsible for the reduction in fatigue life, as compared with the results of tests in vacuum for some age-hardened aluminum alloys, is water vapor. Flexural fatigue tests on cladded 2024-T3 aluminum alloy (19) under conditions of high, intermediate, and low atmospheric humidity conditions showed that a decrease in relative humidity from 90 to 12 percent caused an increase in the mean life at a given stress level by a factor of about two. The change in life appeared to be progressive with the change in humidity at all stress levels.

The water content of the atmosphere can be defined in either absolute or relative terms. For a particular value of absolute humidity in number of grains of water per pound of air, the relative humidity in percentage may vary widely, depending on the temperature and, within normal atmospheric limits, slightly on the pressure. Bare 2024-T3 aluminum alloy was tested in an environmental chamber in which the relative and absolute humidity could be varied independently, in order to find whether absolute or relative humidity had the controlling influence on the atmospheric humidity.(19) At a given stress level, the fatigue life decreased with increase in either humidity value. In the absence of a hypothesis for the mechanism by which fatigue strength is affected by atmospheric humidity, the only criterion upon which it is possible to determine which of the humidity parameters has the dominant influence is that of goodness of fit of the data to some plausible curve. In deciding on a plausible curve, it can only be suggested that it is most probable that the quantities involved would vary monotonically. The test data obtained by varying the absolute humidity were found to closely fit this criterion. Accordingly, absolute humidity is probably a more significant parameter than is

[19] Dunsby and Wieke, 1969

relative humdity in reducing fatigue life of metals. It is possible to mitigate some of the effect of humidity by the simple expedient of coating the specimen with lubricating oil.

ACTUAL CASE OF FATIGUE DAMAGE IN AIRCRAFT

The fatigue damage of an aircraft is often referred to as the severity of fatigue cracks which are detected in the maintenance work during its service life. Since the aircraft is literally made of many differently shaped pieces put together by various joining methods, fatigue damage cannot be completely assessed unless it is subject to a thorough destructive structural teardown inspection. This has actually been performed on some B-52 bombers. (20) The inspection results, including damage by fatigue, stress corrosion, and corrosion, of one airplane are described in the following paragraphs.

Prior to cutting and disassembling, the aircraft was subject to nonmagnified visual, eddy-current, and 10-X magnification examination. Specimen clusters removed from critical areas, such as joints and splice, were stripped of all finishes and sealant. Aluminum alloy stripped parts were etched and either given a fluorescent dye-penetrant inspection or 10-X visual inspection. Steel parts were magnetic-particle inspected. Cracks and areas of significant corrosion, wear, and fretting located by the inspection underwent further metallurgical examination, using optical and two-stage plastic-carbon replica electron fractography and standard metallographic techniques.

A number of areas of the wing suffered damage by fatigue, stress corrosion, and corrosion; whereas, damage by fatigue and corrosion was found in some areas of the fuselage. Empennage appeared to suffer much less severe damage; only minor fatigue cracks were detected on the empennage of the horizontal stabilizer lower surface skins.

As to the location of fatigue cracks relating to the geometry of the damaged area, most cracks occurred at holes intended for inserting fasteners, rivets, hinges, or bearing pins. There was high incidence of cracking at fastener holes. Some fastener holes might give no indication of damage at either end, but cracks were found at the hole bore surface. Fillet radius marking the change of cross section was also where crack was often found. Other places where fatigue cracking might occur included corner radius and area adjacent to the weldment.

---

[20] Boeing Report, 1971

Cracks caused by stress corrosion were not as numerous as cracks caused by fatigue. Stress corrosion cracking occurred mostly at fillet radius, shear pinhole, and the web of stiffener. Three types of corrosion were found by inspection: exfoliation, intergranular corrosion, and pitting corrosion.

In sum, fatigue cracking in an aircraft took place mostly at a stress raiser, such as a hole or a fillet radius. The hole used for inserting a fastener is more likely than other holes to develop cracks. Moreover, cracking occurs often at the bore surface, rather than at either end. In routine maintenance check, more attention should, therefore, be paid on inspecting fasteners and their holes for fatigue damage.

NONDESTRUCTIVE DETECTION OF FATIGUE DAMAGE

Since the publication of last review on the subject, [1] a report on the early detection of fatigue damage issued by Australian Defense Scientific Service [21] became available. The methods for detection of fatigue cracking described in the report are electron microscopy, use of cholesteric materials, infrared, eddy current, and ultrasonics. It is concluded that although the sensitivities of existing methods are probably adequate (for detecting crack size of a few hundred microns), more knowledge of the fatigue process is needed before positive identification of early fatigue cracking becomes possible.

The search of improved or new techniques for detecting fatigue damage by nondestructive means appearing in the literature since the previous review was continued in the present program. The results are presented in the following paragraphs.

OPTICAL CORRELATION METHOD

A U.S. patent has been granted on the detection of fatigue with the optical correlation process (U.S. patent 3631713, 1972). The approach of this process is to detect small changes in surface microstructures in the fatigue-stressed area by means of optical cross correlation using coherent light. The loss of correlation between the surface containing fatigue damage and the same surface in its initial state gives an early warning of impending fatigue failure.

---

[21] Scot, 1969

Maron and Mueller [22] found that the correlation intensity versus fatigue cycles curve generally undergoes three stages of change: (1) the initial stage involving an intensity decrease by no more than 50 percent and lasting a few thousand cycles, (2) the intermediate stage of more or less constant intensity, and (3) the last stage of continuous decrease. A 50-percent decrease in correlation intensity from its value at the beginning of the last stage would indicate the occurrence of a crack on the order of 1 mm in length, regardless of the stress level or surface finish, in aluminum alloys.

The success of this process depends upon the ability of detecting the small changes in surface microstructure. However, surface microstructure can be altered by other means than fatigue stressing, such as oxidation, corrosion, scratching, rubbing, etc. Therefore, when this process is used to assess the damage of a structural component after part of its fatigue life has been spent, the decrease in the correlation intensity in the last stage can be attributed to fatigue damage, as well as the other extraneous sources.

Bond and his associates [23] tried to relate the complete correlation process to surface effects by the use of metallurgical techniques, such as optical and electron microscopy, Nomarski interference microscopy, and Michelson interferometry. They showed that, as a silicon iron specimen was fatigued in flexure, the curve depicting the change in relative correlation intensity with flexure cycles was similar to the one for aluminum alloy.[22] Several times during the fatigue cycling period, the specimen was removed and examined using optical and electron replica microscopy in an attempt to establish the metallurgical micromechanism responsible for the changing correlation. Slip lines were observed to form after approximately 200 cycles, but no additional visible effects were detected in the test zone throughout the balance of the specimen life. Electron replica microscopy revealed that, within those matrix regions bounded by strong slip bands, extensive fine slip occurred in the form of long, straight, small amplitude slip lines, which generally formed at planes ranging from 45 to 90 degrees with respect to the stress axis. As the deformation proceeded, development of these closely spaced strain centers apparently produced the spatial frequency diffracting centers, which accounted for the decrease in correlation intensity with continued fatigue cycling.

Grain boundary distortion as revealed by Nomarski interference microscopy did not occur until 500,000 cycles. The final catastrophic loss of correlation corresponded to the nucleation and propagation of an edge crack. The degree of gross distortion caused by the crack formation was studied by the interferogram made with a Michelson interferometer. The corelation technique

---

[22] Marom and Mueller, 1971
[23] Bond, et al, 1971

was then able to detect the fatigue crack forming at a point remotely located from the segment of the specimen under study.

This optical correlation technique was also applied to assess fatigue damage of solder joints of printed circuit boards. [24] Strains developed during thermal fluctuation were the prime cause of fatigue cracking failure. This was caused by differences in the coefficients of thermal expansion between the component leads, the printed circuit boards, and the plastic material making up the solder joint system. Correlation intensity was found to decrease in the course of thermal cycling of the solder joint. The greatest drop in the intensity is a measure of the elastic plus plastic deformation. As the joint cools, the elastic strain is removed, but the joint will not return to its original state because it has been strained beyond its elastic limit. The difference between the correlation intensity before heating and after the joint has cooled to room temperature is a measure of the plastic deformation. If the drop in correlation intensity after each thermal cycle is plotted versus the number of thermal cycles, a curve characteristic of the plastic strain occurring in the solder joint is obtained. This curve displays a continuous downward trend, indicating increase of plastic strain with fatigue cycles. Consequently, the solder joint whose correlation intensity drops fastest and has thus the steepest slope of the curve would be undergoing the greatest permanent deformation and, therefore, would be likely to fail before the others. These predictions were found to agree with laboratory test results.

EDDY CURRENT

One of the limitations of this method is that the probe is quite sensitive to the proximity. A new probe consisting of a U-shaped core with a winding of copper wire at the center has been reported to overcome this shortcoming. [25] The system consists of a probe, oscillator, bridge circuit, detector, various filters, compensation circuitry, and readout device. The probe is positioned such that the part to be tested forms the flux path of the legs of the "U," and the flux passes through the test material. Crack signals were observed as early as 10 percent of fatigue life of notched 6061-T6 aluminum alloy specimens. It is claimed that the probe is not only insensitive to probe proximity, but also to generalized surface damage, which, however, is not categorized.

Commercially available eddy current instrument, however, has been used to predict the location and geometry (length and depth) of fatigue cracks in fastener holes. [26] The tests used probes manufactured by the Ideal Specialty

---

[24] Jenkins and McIlwain, 1971
[25] Moross, 1971
[26] Padilla and Parks, 1969

Company of Tulsa and the Magnaflux Magnatest ED-520 eddy current instrument. Fatigue cracks can be easily distinguished from scratches and other forms of surface roughness by the shape of the curves recorded from eddy current responses. Cracks as small as 0.1 mm (0.004 inch) deep are found in fastener holes ranging from 6.3 to 12.7 mm (1/4 to 1/2 inch) in diameter.

MAGNETIC PERTURBATION

The use of magnetic perturbation for the detection of fatigue cracks was described in the last review. (1) Since then, a prototype equipment has been developed to automatically inspect helicopter transmission gears. (27) On the basis of the limited evaluations conducted in the laboratory, it has been established that the equipment is capable of completing an automatic inspection of a gear in about 90 minutes. The crack length that can be detected is estimated to be in the 0.25 to 0.5 mm (0.01 to 0.02 inch) range.

MICROWAVE METHOD

Fatigue damage can be in the form of surface cracks. The life of a part can be lengthened if all cracks are removed. The amount of material to be removed is usually determined by repeated machining and dye-penetrant or magnetic particle inspection until no crack indications on the machined surface are evident. The method is too time-consuming. Ultrasonic methods can be used to determine the crack depth and, hence, the amount of material to be removed. However, they are generally inaccurate if the cracks are very thin and have large depth-to-width aspect ratio.

The depth of very thin surface cracks can be measured by microwave. (28) Microwave power in higher order modes is generated in a circular waveguide and directed against a sample surface which lies within the Fresnel zone of the coupling aperture. A crack on the surface causes the power in the higher order mode to degenerate to the fundamental mode, which is then measured. The TM_{01} and TE_{01} modes are, respectively, suitable for magnetic materials and nonmagnetic, low-resistivity materials because of their greater sensitivity.

One uncertainty in using the method is the lack of a good calibration curve to correlate the depth of machined thin slots with the microwave measurement. Ultrasonic and X-ray methods are useless for calibration because they provide only qualitative measurement. Microscope is used, but the calibration is good only for slot depth less than 500 μm. For slot depths from 500 to

---

[27] Kusenberger and Barton, 1969
[28] Hruby and Feinstein, 1970

5,000 μm, use of shim stock depth gages yields a crude, inaccurate calibration. Therefore, more work on good calibration is needed for this microwave system.

ULTRASONIC METHODS

Ultrasonic methods have been used extensively in industries to detect fatigue crack and monitor its growth. Little work on the detection of crack initiation by ultrasonic waves, however, appears in the literature. Probably the scarcity is due to the uncertainty of the definition of crack initiation. Norris and his coworkers [29] reported using surface wave to detect crack initiation in notched specimens (stress concentration factor = 1.5, 2, and 4) in low low-cycle fatigue. Four surface wave transducers were positioned on each specimen at 90-degree intervals so that the entire surface could be monitored individually by pulse-echo technique for some given time. This time depended on the speed of a time base relay that was used to switch from transducer to transducer. Crack initiation was defined by the detection of a crack approximately 0.13 mm (0.005 inch) deep, determined after sectioning a few specimens at the point of detection. A single longitudinal wave transducer was used to monitor further crack growth. The crack initiation stage was found to occupy a greater portion of the fatigue life as the applied stress was raised.

Another ultrasonic technique to detect fatigue damage is to measure the attenuation during fatigue test. [30] The attenuation of longitudinal wave pulse propagation through aluminum or steel specimens initially remains constant, increases slowly, and then increases catastrophically just prior to fracture. Hence, the history of attenuation during fatigue of the specimen can provide an index to the onset of failure. In a typical test on aluminum, the attenuation began to rise at about 2.8×10^6 cycles in 26 hours and proceeded catastropically to failure at about 3.5×10^6 cycles after 33 hours, giving a 7-hour warning. On the other hand, conventional ultrasonic monitoring by pulse-echo technique was unable to detect any additional echoes due to energy reflected from the crack until about 2 hours prior to fracture. Hence, the warning of eminent fracture given by attenuation measurement was 5 hours earlier than detection by conventional techniques. In this attenuation measurement, surface wave is found to be inferior to bulk wave.

ACOUSTIC EMISSION METHOD

Although appreciable amount of data in acoustic emission are available in the literature, only a few investigators have monitored acoustic emission in fatigue tests. The reason is probably the difficulty in separating the

---

[29] Norris, et al, 1969
[30] Green and Pond, 1973

acoustic emission signal from the background noise. Since a recent review on acoustic emission during fatigue test can be found elsewhere, [30] this subject will not be further discussed here, to avoid duplication.

FATIGUE LIFE GAGE

Fatigue life gages are small strain sensors physically similar to strain gages. They will incur a permanent resistance change or "zero shift" when subjected to a fatigue environment. This resistance change is attributed to strain hardening of the grid material. Since the amount of strain hardening depends on the magnitude of strain and the number of cycles at this strain, the fatigue gage in essence records the strain history of the material on which it is mounted. A correlation can then be established between resistance change of the gage and the amount of fatigue damage suffered by the material.

These gages are intended for determination of fatigue crack initiation in the low-cycle region, and appreciable life may exist after the gage ceases to function. Annealed 304 stainless steel specimen and the gage under test, conducted by Harbert and Stephens, [31] formed one arm of the Wheatstone bridge which, along with an amplifier and recording system, allowed continuous monitoring of gage resistance. A 10-percent decrease in vibration amplitude of the specimen, tested at resonance frequency between 10 and 14 Hz, was considered fatigue failure. A log-log plot of gage resistance change versus number of cycles indicated a slope change ranging from 0.45 to 0.9 time of the total life in the particular tests at fully reversed strain amplitudes of 0.0015 to 0.0045. Examination of the specimen at a magnification of 36X did not reveal cracks until after the slope change occurred. After the slope change, however, the resistance increased rapidly and the gages became erratic.

ELLIPSOMETRIC METHOD

A powerful technique[1] for characterizing the condition of a metal surface covered with an oxide layer is to reflect polarized light from the surface and measure the amplitude and the state of polarization of the reflected light. The measurable quantities at a given wavelength and angle of incidence can be reduced to the parameters

Δ = the phase shift caused by reflection

and

ψ = arc tangent of the ratio of the normal to the parallel polarization components of the reflected light.

[31] Harbert and Stephens, 1969

These parameters can be related to the complex refractive index of the transparent surface film

$$\hat{n}_f = n_f (1+ik_f)$$

and of the underlying metal substrate

$$\hat{n}_s = n_s (1+ik_s)$$

Since there are more unknowns (n_f, k_f, n_s, k_s, and film thickness, t) than there are measurables (Δ and ψ), anticipated values for the unknowns must be inserted into a computer program and values for the measurables deduced for comparison with the actual data. Although this procedure could lead to ambiguous interpretations, an a priori knowledge of what the mechanisms for changes in the film should be, coupled with a knowledge of how n and k modify, has proven sufficient to arrive at meaningful results.

In the case of fatigue damage, it is anticipated that the primary effect will be caused by surface roughening. If the roughness is on a scale larger than the optical wavelength, then the only effect will be on the absolute value of the scattered light intensity, because the distorted regions simply scatter light away from the analyzer and are not measured. For roughness on a scale small compared to the wavelength, drastic changes in Δ and ψ can be expected, and a model for the geometry of the surface and its film must be incorporated.

The ellipsometric parameters Δ and ψ of the surface of fatigued 7075-T6 aluminum alloy and annealed D6AC steel were measured.[1] Variation of the parameters with fatigue life was noted, but no correlation could be obtained from the limited amount of data reported.

SURFACE POTENTIAL METHOD

The surface potential difference between two metals is the difference in work function between them. Thus,

$$\phi = \phi_c - \phi_r$$

where

ϕ = surface potential difference

ϕ_c = work function of specimen

ϕ_r = work function of reference electrode

There are two methods for measuring ϕ. One involves measuring the very small current (10^{-14} amp) which the potential difference ϕ drives through a circuit, consisting of a high-impedance electrometer whose input resistance r is in series with the resistance R of the air gap which separates the specimen from the reference electrode. Under these conditions, the surface potential difference current is

$$I_s = \frac{\phi}{R + r}$$

The air gap resistance R is lowered to the point that $R << r$ by subjecting the air gap to ionizing radiation from a small radioactive source such as Am^{241}. In this case, $I_s = \phi/r$ and, since r is known from the specification of the electrometer, a measurement of I_s yields ϕ directly.

The other method of measuring ϕ is to form a parallel plate capacitor out of the specimen and reference electrode. This capacitor may reside in a vacuum and will have a potential difference between its plates of ϕ. Thus, it will have a charge on the plates given by

$$Q = C\phi$$

where C is the capacity of the capacitor. If the capacitance C is changed (for example, by changing the spacing between the electrodes), then the charge Q will change to keep ϕ fixed, and this change can be used to measure ϕ. When a specimen is vibrated at a frequency ω in the vacuum, ϕ is determined by measuring the current (dQ/dt) flowing through an external circuit at a frequency ω.

The surface potential of a few fatigued 7075-T6 aluminum alloy specimens had been measured, with respect to a reference electrode. (1) The electrode was scanned along the specimen test section which had varying cross-sectional area. In one specimen, the surface potential difference was found to change with the severity of damage, which was highest at the middle of the test section having the smallest cross-sectional area. However, these results could not be repeated on other similarly fatigued specimens.

Since the difference in potential between two metals depends upon the difference between their work functions, and since the work function of a metal is influenced by plastic deformation, (32)(33)(34) and by chemisorption of water or oxygen, (35) the surface potential difference could be related to fatigue stressing under different surface conditions. Hence, a nondestructive

---

[32] Andreev and Palige', 1962
[33] Andreev and Palige', 1964
[34] Mints, et al, 1973
[35] Huber and Kirk, 1966

test technique might be developed using this physical phenomenon. More experimental work is needed to explore the capabilities of this method.

EXOELECTRON EMISSION METHOD

The review of literature on the exoelectron emission by plastic deformation was resumed after the publication of the previous work. [1] The articles reviewed are presented in Appendix A. Most of the emission experiments were still performed in vacuum, but measurements in air were reported by three sources. [1][2] [36] Stimulation by ultraviolet light was necessary to enhance the emission current so that it could become measurable. Additional thermal stimulation, although not essential, was helpful to further enhance the emission. Stimulation by ultrasonics on aluminum and other metals under abrasion was tried, [37][38] but the measurements of the emission current were made using the Geiger-Müller-type counter. Emission excited by electron bombardment, using an electron gun on tungsten, [39] germanium, [40] $CaSO_4/Mn$, and some metal oxides, [41] and by the X-rays on some metals, metal oxides, as well as metal sulfides [42] and on germanium, [43] had been attempted. However, all the test specimens were not subject to plastic deformation; the electron emission was excited only by either electron bombardment or the X-rays. Furthermore, the emission was enhanced by heat and measured by a Geiger-Müller counter or by secondary electron multiplier in vacuum. The emission in vacuum from metals under the action of laser beam and the stimulation of heat had also been reported. [44] Therefore, in addition to ultraviolet light, the other four stimulation sources previously described could also be considered when the exoelectron emission from plastically deformed metals is measured in air.

---

[36] Gel'man and Fainshtein, 1973
[37] Langenecker and Ray, 1964
[38] Williams, 1966
[39] Seeger, 1955
[40] Seeger, 1957
[41] Vogel, 1960
[42] Hieslmair and Muller, 1956
[43] Seidl, 1959
[44] Kovtov, et al, 1971

Section IV

MATERIAL SELECTION AND SPECIMEN DESIGN

The material requirements for this program were based primarily on the selection of representative aerospace materials to insure suitable qualification and applicability of the developed nondestructive test (NDT) techniques. In general, the materials and alloys were selected based on the B-1 air vehicle design, since these materials are currently used in other Air Force aircraft structures and were readily available. The selected materials and their mechanical properties are:

Material	Yield Strength, ksi	Ultimate Tensile Strength, ksi	Percentage of Elongation (in 2 inches)
2024-T3 aluminum alloy	–	–	–
2024-T81 aluminum alloy	68	73	7
Annealed Ti-6Al-4V	138	149	11
Heat treated (SRH 1050) PH 14-8 Mo steel	208	216	5

Also included were 1100-0, 2219-T851, and 7075-T6 aluminum alloy materials used in prior experiments.

The materials were purchased in sheets which were covered with paper to keep the sheet surface free of grease, water, or dirt and to protect them from scratches and mechanical damage by handling. The aluminum alloy was obtained in the T3 condition. The T81 condition was later achieved by heat treatment. Both the titanium alloy and the steel were purchased in the annealed condition. The steel was heat-treated to the required SRH-1050 condition after the specimens were prepared.

Two types of specimens were used: a specially designed, triangular specimen and the standard dogbone-type specimen.

The triangular specimen was so designed that it would fit in an available ultrahigh vacuum chamber and have an area subject to constant surface strain amplitude in flexural fatigue. The surface area was sufficiently large to accommodate the instruments necessary for the NDT measurements to be made during fatigue in vacuum. Details of the specimen design are given in Appendix B. The specimens were electropolished before each test, and their surfaces were nearly mirror-like in brightness of finish. It was observed that fatigue damage to the bright surfaces could be easily observed with the unaided eye early in the fatigue test by noting that the shiny surface of the specimen became cloudy. This cloudiness extended quickly over the triangular section, indicating a uniformity in fatigue damage.

The standard dogbone-type specimens were used in the nondestructive evaluation after the fatigue test. The specimen shape included a straight 50.8-mm (2-inch) test section 12.7 mm (0.5 inch) wide. A 76.2-mm (3-inch) radius connected the test section with the 25.4-mm-wide (1 inch) specimen ends. The overall specimen length was 203 mm (8 inches). This standard specimen was modified by the introduction of discontinuities such as holes and slots in the straight test section to localize fatigue damage. A series of complex-shaped specimens were also tested. These included bolted joints, weld joints, and specimens with curved shapes to accentuate the change in cross section. Details of these special specimens are given with the description of the specific experiment.

After machining, the specimens which were to be used in the as-received condition (2024-T3, 7075-T6, and annealed Ti-6Al-4V alloys) were cleaned before fatigue testing. Composition of the chem-milling solution for the aluminum alloy on a 1-gallon basis is 20 ounces sodium hydroxide, 2 percent by weight sodium gluconate, and 2 percent by weight sodium sulfide. The temperature of the solution was kept at about 160° F. The pickling solution for the titanium alloy contains 33.2 percent nitric acid and 1.6 percent hydrofluoric acid by weight and operating at a temperature of 75° to 140° F. The 2024-T81 specimens were similarly chem-milled after the heat treatment. The PH14-8Mo steel specimens were heat-treated to the SRH-1050 condition and cleaned in a solution containing 8 percent nitric acid and 7 percent Turco 414 (manufactured by Turco Products, Wilmington, California) by volume at room temperature. The resulting specimen thickness after the surface preparation for the aluminum alloys, titanium alloy, and steel was approximately 2, 1.5, and 1.3 mm (0.08, 0.06, and 0.05 inch), respectively. After measurement of the dimensions, the test section of each specimen was wrapped with tissue paper to preserve the specimen surface in the as-prepared condition.

Section V

SCREENING EXPERIMENTS

INTRODUCTION

The research described in this section was directed at further clarifying the mechanism of exoelectron emission as related to fatigue damage in a metal. Experiments were designed to (1) relate exoelectron emission with other physical phenomena which are influenced by fatigue damage, and (2) determine the role of surface films on exoelectron emission and other fatigue-related properties. All of the fatigue tests and measurements were performed under ultrahigh vacuum conditions so that both the environment around the specimen and the surface condition could be closely controlled.

The following discussion describes the experimental test system, specimen design, and procedures used to prepare them for measurement, and experimental results. Discussion of the results is divided into three parts:

1. A discussion of the data obtained for the emission as a function of strain amplitude at constant oxide thicknesses

2. A description of the data obtained for the emission as a function of oxide thickness at constant strain amplitude

3. A brief description of other experiments, including the surface potential difference tests, optical constant work, measurements on the exoelectron emission decay with time, and an experiment on electron spin resonance.

The discussion of results is directed at identifying various models for emission which do not seem to be applicable, a discussion concerning the differences observed between the vibrating and quiescent-state emission curves, and a definition of what is the best working hypothesis to explain exoelectron emission.

EXPERIMENTAL SYSTEM

A high-vacuum fatigue cycling system was developed to relate the surface condition of fatigued materials to fatigue damage and the nondestructive test (NDT) measurements. A fatigue-testing machine was installed inside an ultrahigh vacuum chamber, and a specimen was designed to permit the surface conditions to be monitored by various NDT techniques during the fatigue-vacuum conditions.

ELECTROMAGNETIC DRIVE SYSTEM

It was decided to locate the fatigue system inside the vacuum chamber to avoid the problems associated with bellows and mechanical linkage systems typical of external loading systems. However, special consideration was required in selection of the drive materials used inside the chamber due to the problem of outgassing. The final drive system design used an electromagnetic excitation system enclosed in a stainless steel enclosure within the vacuum chamber.

The apex end of the triangular specimen was clamped, and the base end was driven electromagnetically by a fixed coil interacting with an attached soft iron armature. The driving force arises from an alternating magnetic field attracting and repelling the iron armature symmetrically placed between two magnets, shown schematically in Figure 1. The magnetic cores are rectangular in shape, with a section cut out at the top to accommodate the armature. These two magnets are driven in quadrature so that when the force from one magnet is at a maximum, the other is at zero. In order to minimize eddy current heating of the magnets, the cores were made of 0.1-mm-thick (0.004 inch) laminated sheets of Selectron (a trade name for a silicon iron magnetic material with high-saturation magnetization). The cores were insulated by a thin, insulating lacquer material and then insulated with Formvar. Approximately 120 turns of size 28 copper wire were wrapped around the core to form the coil. Since the insulating material in the cores and on the wire would not be suitable for exposure to an ultrahigh vacuum, the coils were placed inside a stainless steel container which was fitted in the bottom of the vacuum chamber. A small slot was built into the top of the container to fit into the gap in the cores and to provide a channel in which the armature on the specimen could move freely. Cooling of the electromagnetic driver was provided by passing cooling air through the enclosure using metallic tubing extending outside of the vacuum chamber.

A block diagram of the electrical system used to drive the specimen in the ultrahigh vacuum chamber is shown in Figure 2. Since the coils on the left and right of the armature must apply a force to the armature in the correct phase, two separate drive channels must be used. A single audio oscillator (Frequency Devices, Inc, model 434) was connected to a system of capacitors which generates two outputs having a relative phase difference of 90 degrees. Each of these outputs goes through an audio power amplifier (McIntosh model 2100) and drives each of the coils separately. The current and voltage meters shown in the illustration are required to measure the drive power. Any difference in the force balance between the two coils could also be detected by an off-center reading from the optical system used for measuring the cycling amplitude at the end of the specimen.

The specimen was supported by a firm clamp suspended from the top of the chamber. This clamp was attached to a flange at the top of the chamber,

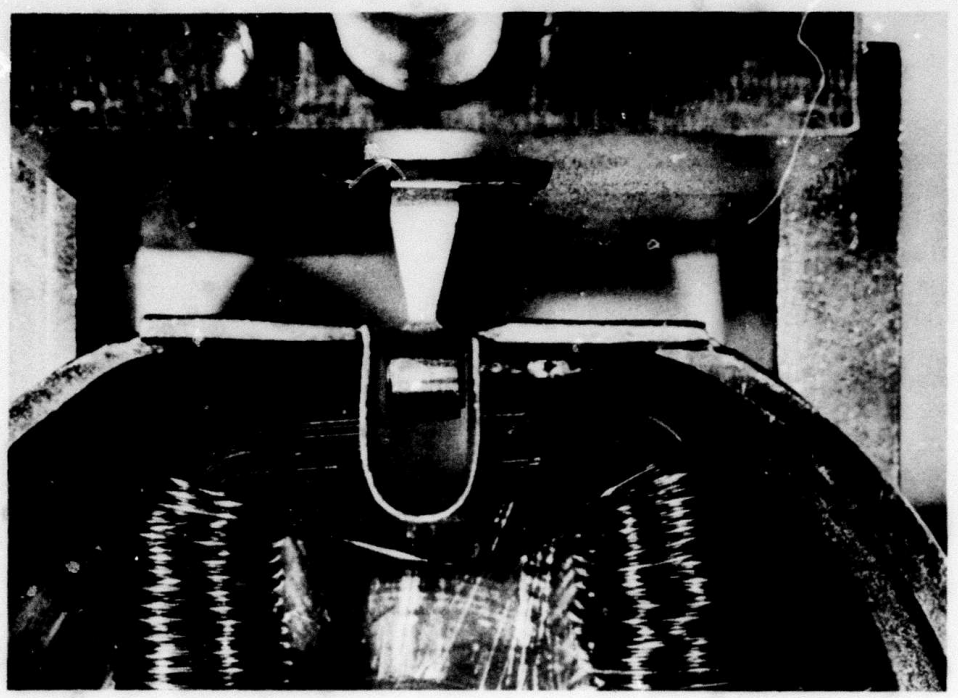

S - specimen
A - armature
C - magnet core
D - coil (38.1 dia x 50.8 mm)

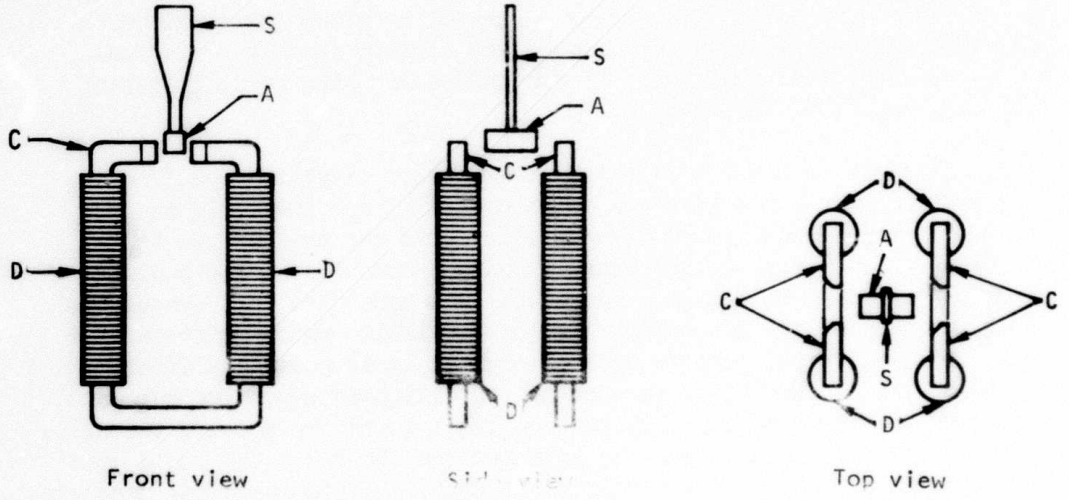

Figure 1. Electromagnetic drive system and schematic.

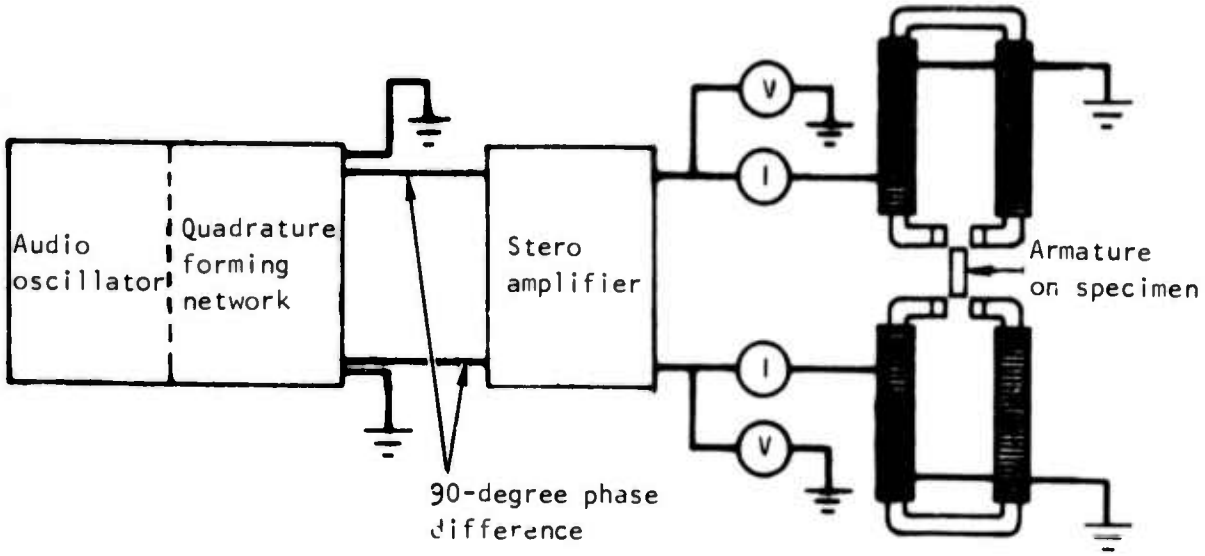

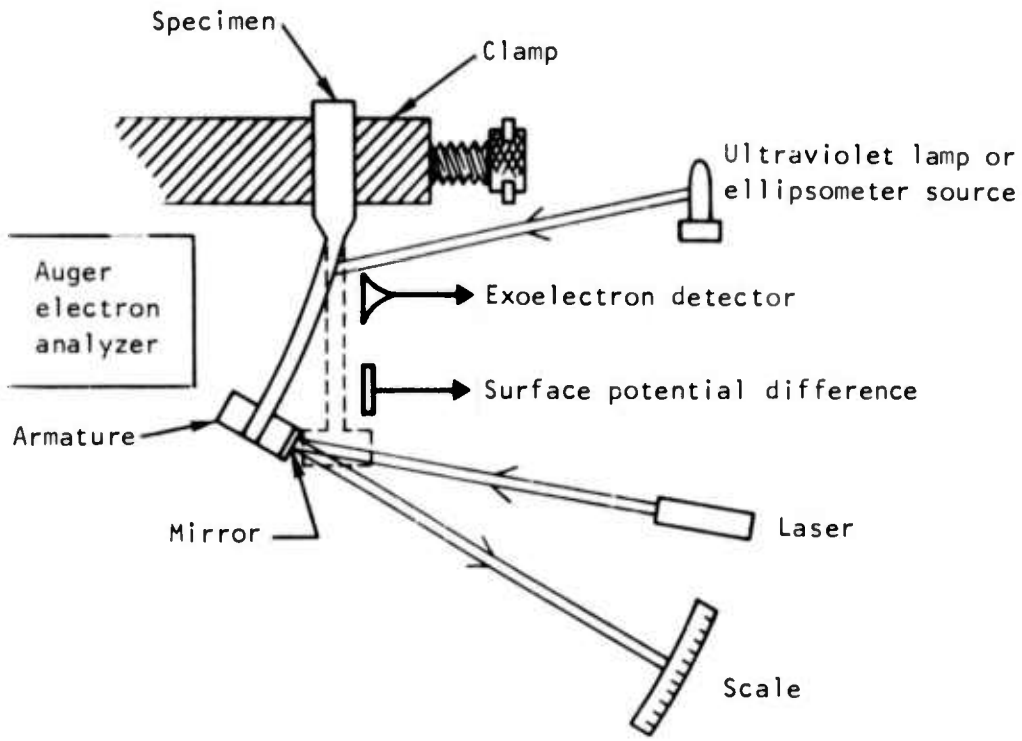

Figure 2. Diagrams of specimen excitation system and measurement systems.

which could be moved in many directions so that the specimen can be raised and lowered relative to the driver. The specimen could also be rotated and moved in the X and Y planes. The NDT measurement systems were positioned with respect to the specimen within the chamber, as also shown in Figure 2. The Auger electron spectrometer was positioned on the rear side of the specimen, and the following systems were located in front of the specimen:

- Ellipsometer system data obtained from light reflected from the top of the specimen
- Exoelectron current system data measured by a Channeltron electron multiplier located at the center of the specimen
- Surface potential difference system data measured by an electrode at the bottom of the specimen
- The deflection of the end of the specimen, determined by measuring the angular deflection of a laser beam reflected from a mirror mounted on the armature at the free end of the specimen

SPECIMENS

A number of NDT measurements were planned within the vacuum chamber, and it was desired that the measurement transducers remain fixed with respect to the specimen. Therefore, since the specimens were to be flexurally loaded in bending, a specimen design was developed to provide a relatively constant surface strain by tapering the width of the specimen.

Several different specimen design shapes were investigated, as shown in Figure 3. Specimen A was an early design in which the iron armature was a small cylinder forced into a hole transverse to the specimen plane. Note that this specimen failed at the narrowest part of the specimen, indicating a concentration of fatigue damage at this point and, hence, a lack of uniform strain over the triangular area. Specimen B was of similar shape to A and used the armature attachment method shown on specimen, and also failed at the narrowest point. Specimen C used the results of the mathematical analysis (given in Appendix B) to modify the sides of the triangular shape so that the point of intersection of the sides, when extended, lay beyond the armature center of mass. In this case, the failure occurred in the triangular section, indicating that this specimen shape successfully distributed the fatigue damage over the triangular area.

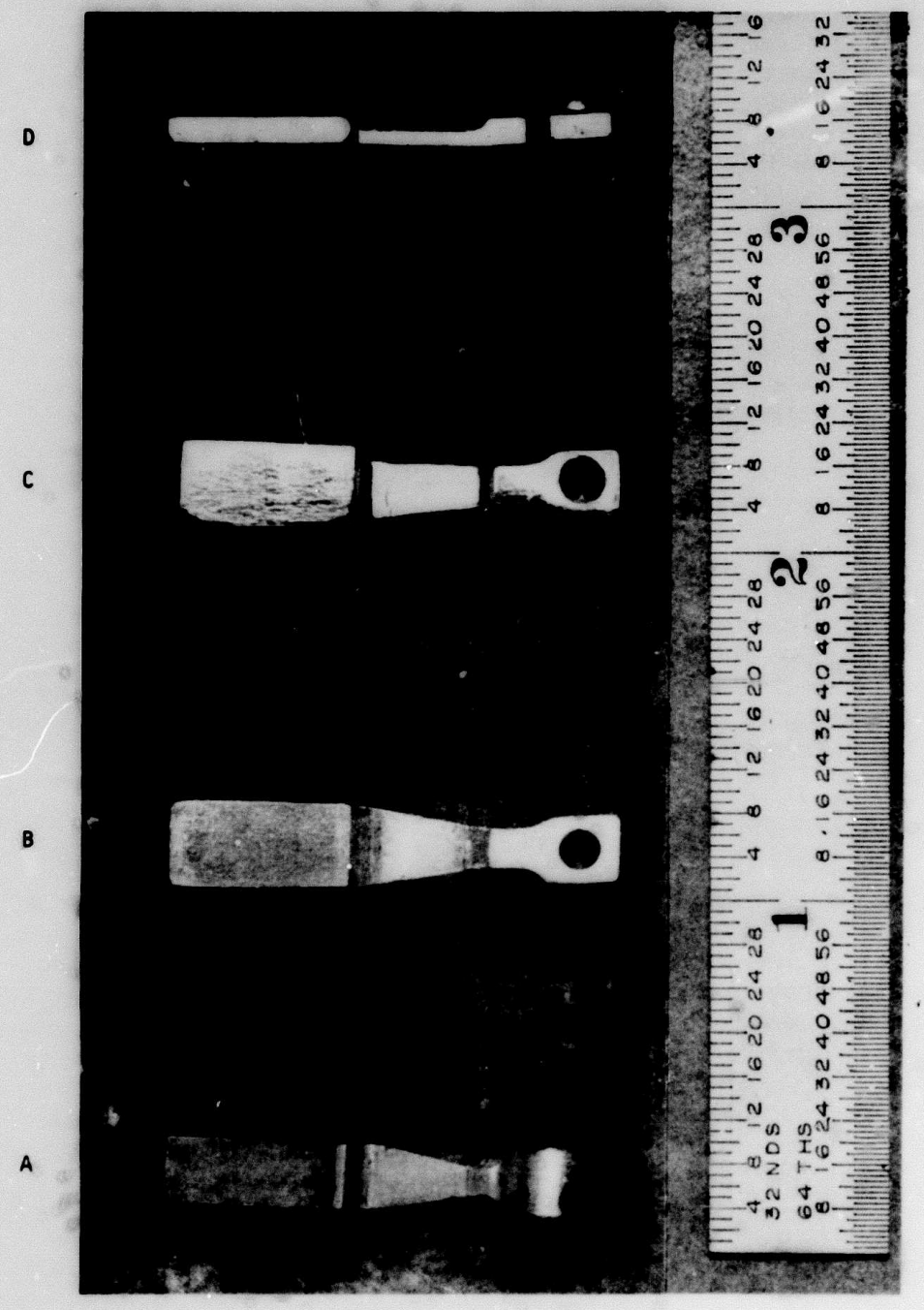

Figure 3. Various design shapes evaluated for triangular specimens.

PRELIMINARY SYSTEM EVALUATION

A number of preliminary experiments confirmed design of the triangular specimen and drive system. During these tests, the fatigue cycling was interrupted, and measurements were made of the exoelectron emission current, surface potential difference, resonant frequency of the specimen, and ellipsometry data. It was confirmed that the exoelectron emission current and surface potential difference could be measured under both static and dynamic conditions. The resonant frequency of the specimen and quality (Q) factor were determined, as shown in Figure 4. Note that the Q-factor decreases during the early part of the test and remains relatively constant between 10^3 and 10^5 cycles. Near the end of the test, Q increases again and then drops abruptly at the fatigue limit of 10^6 cycles. For this particular experiment, the resonant frequency of the specimen was 410 Hz and varied little during the course of the fatigue test. The resonant frequency of other specimens evaluated during these experiments ranged from approximately 150 to 300 Hz.

During performance of these tests, a nonlinear behavior of the specimen and the drive current was observed at high excitation levels. This nonlinear behavior was traced to the fact that the drive current was sufficient to saturate the magnetic core material in the drive system. This saturation gave to changes in the effective inductance of the drive coil, which introduced distortions in the electrical drive signals. This distortion introduced higher harmonics into the drive field, which tended to excite the specimen in different vibrational modes. To compensate for the saturation effects, the specimen was thinned to approximately 0.5-mm (0.02-inch) thickness, permitting the use of drive currents below the saturation level.

MATERIALS AND TEST PROCEDURES

The specimen materials used in this work were aluminum alloys 2024-T3 and 1100-0 or chemically pure material. The specimens were prepared to vibrate in bending. The specimens were annealed and surface-etched. In the case of the 2024-T3 aluminum alloy, one specimen was quenched and measured immediately, and the other specimen was quenched and subsequently aged at room temperature. No essential difference in the results for the emission was obtained. All of the specimens were measured prior to fatigue by ellipsometric and Auger techniques. These techniques served to establish the thickness of the oxide coat on the specimens, and to identify the chemical composition of the oxide layer. In some cases, the specimens were bombarded with argon inside the vacuum-fatigue apparatus (Figure 5) to produce a minimal oxide thickness. In addition to the external ellipsometric measurements, in situ measurements were also made of this parameter as a function of fatigue.

All of the stimulated exoelectron measurements were made using an ultraviolet lamp, with the principal component of light being at about

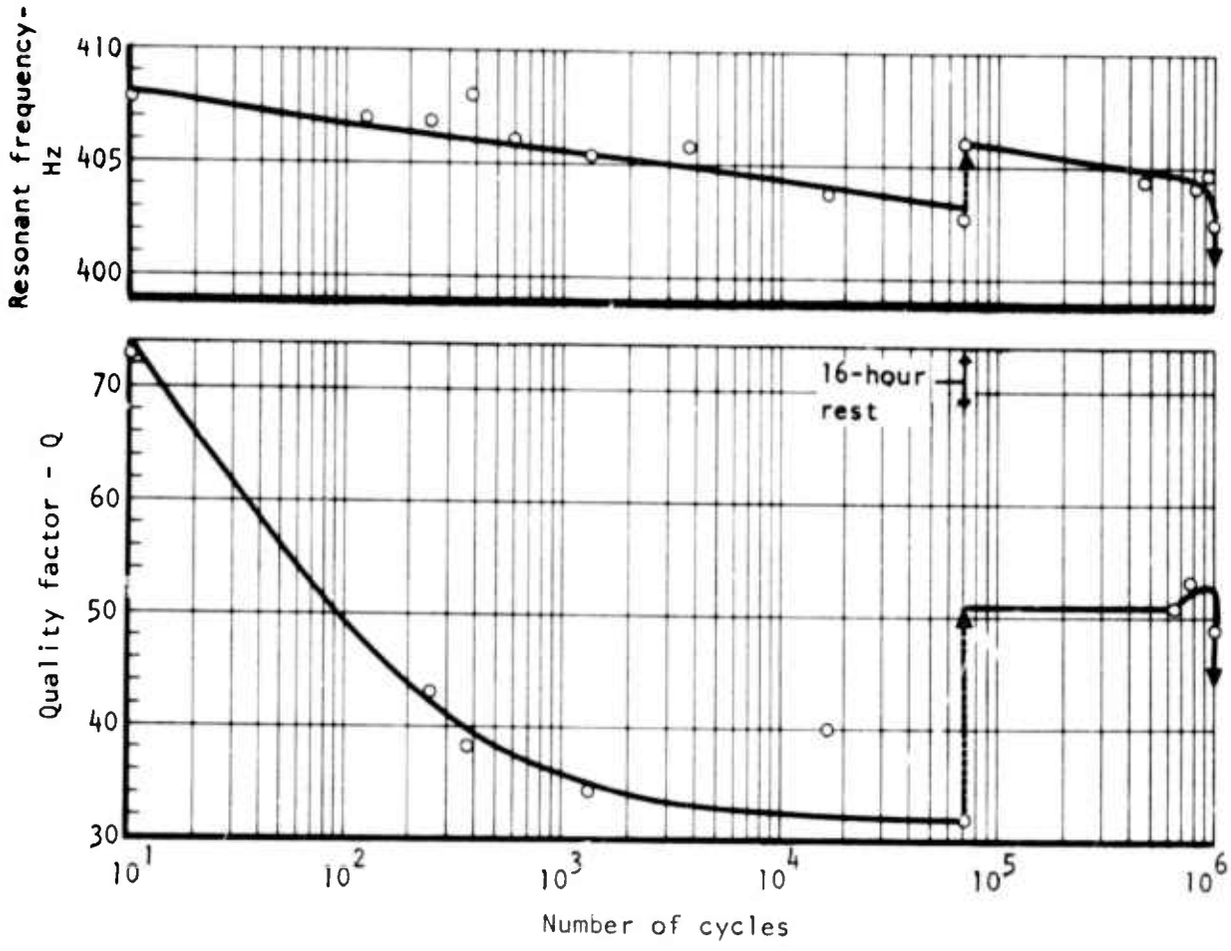

Figure 4. Variation of quality factor Q and resonant frequency of a triangular 1100 aluminum specimen tested in air.

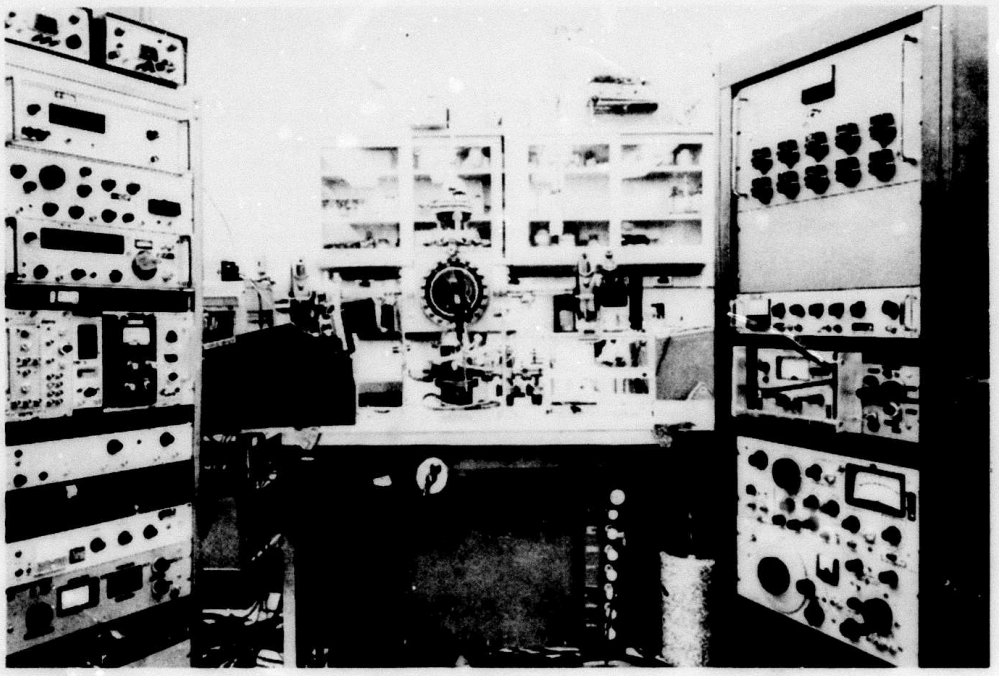

Figure 5. High-vacuum fatigue test system including vacuum chamber, ellipsometer, and Auger spectrometer.

2,500 angstroms. This light was flashed on only long enough during the fatigue test to permit measurement of the current.

EXPERIMENTAL RESULTS

EMISSION AS A FUNCTION OF STRAIN AMPLITUDE AT CONSTANT OXIDE THICKNESS

A series of specimens was fatigued, and the emission was measured as a function of strain amplitude at a constant oxide thickness of about 60 angstroms. Figure 6 shows one of these curves measured at a strain amplitude of 2.16×10^{-3}. In this illustration, the ordinate is the exoelectron current given in terms of 10^{-8} ampere; the abscissa is time to failure in minutes. At the top of the scale, the same scale is given in cycles; noting that the frequency of vibration was about 200 Hz, the two scales (top and bottom) are consequently related. The interesting feature to note in this curve is that it rises very rapidly from the origin as fatigue begins, and tends to saturate out as failure approaches. Failure in this case, as in all the cases to be described here, was taken to be the point at which a sufficient sized crack developed in the materials so that vibration of the specimen in the resonant mode was no longer possible. Figure 7 shows another specimen in the same set, but taken at a strain amplitude of 2.64×10^{-3}. The top curve was obtained by momentarily stopping the specimen, flashing the ultraviolet light to stimulate the emission, and recording it. The lower curve was obtained by letting the specimen continue to vibrate, flashing the light, and recording the current. As will be discussed later, there was a continuing difference between the two measurements. Note that the axes in this figure are the same as those given in Figure 6, with the exception of the actual time to failure. Figure 8 shows another specimen tested in the same series, but at a higher strain amplitude of 2.88×10^{-3}. Again, the same qualitative features of the data were evaluated and it is observed that the current increases more rapidly at the start and continues to a higher value. Details of the specimen failure were similar for all tests. Specimen vibration ceased as the crack became large enough to destroy the resonance condition.

Figure 9 summarizes the data from the first three specimens. In this case, the exoelectron current normalized and the current change from its initial value was plotted as a function of time to failure. When the data are plotted with a family parameter of strain amplitude, it is seen that, very systematically, the current increases at a given time as the strain amplitude is increased. With increasing strain amplitude, of course, the number of cycles to failure is diminished. Figure 10 shows a plot of the exoelectron current as a function of the family parameter (strain amplitude), shown in Figure 9, at the time of failure. Thus, taking a crosscut of the data in Figure 9 at the failure point, it is shown that the exoelectron current is a linear function of the strain amplitude. No particular significance should

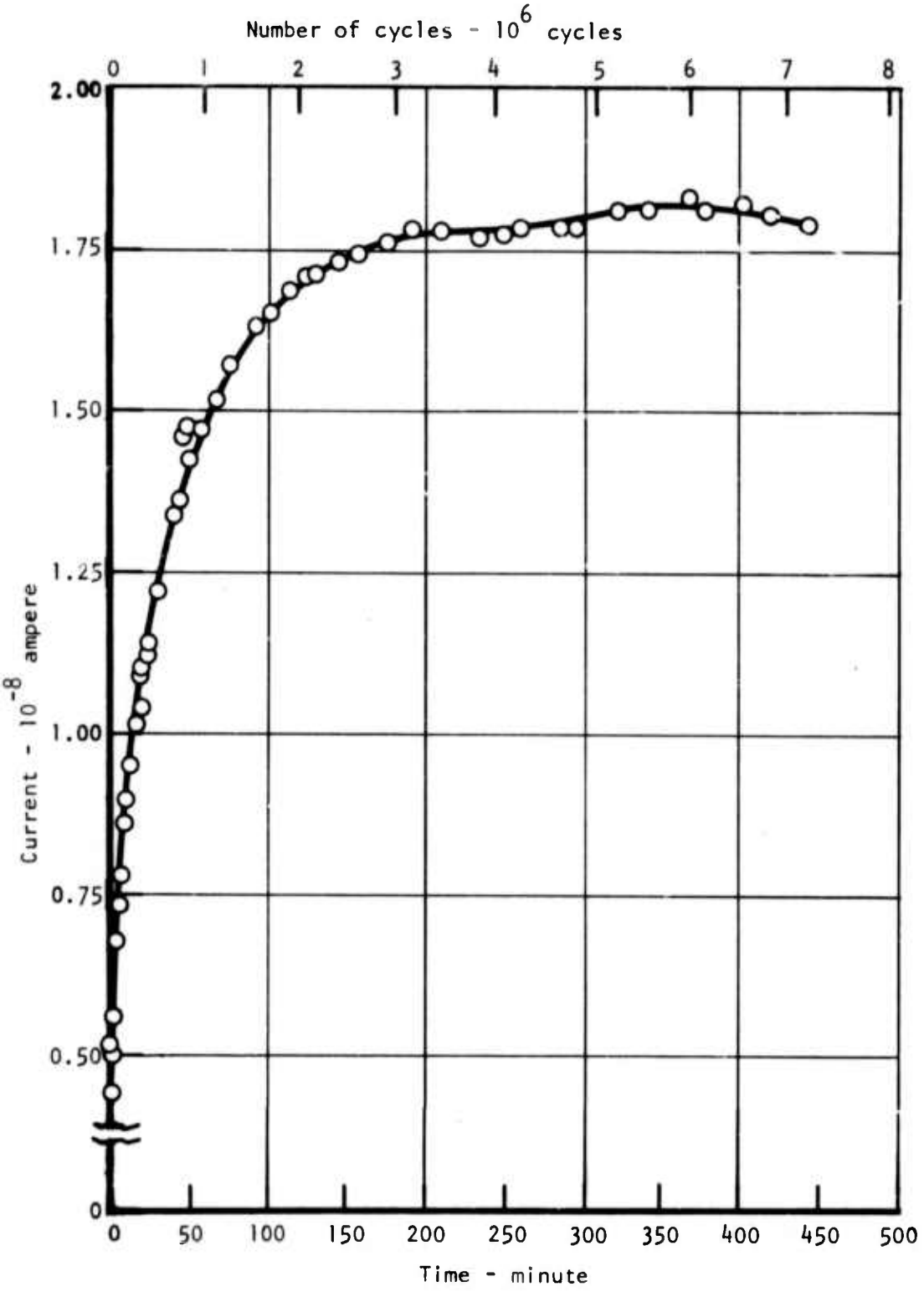

Figure 6. Exoelectron emission curve for 1100 aluminum in fatigue at a strain amplitude of 2.16×10^{-3} in vacuum.

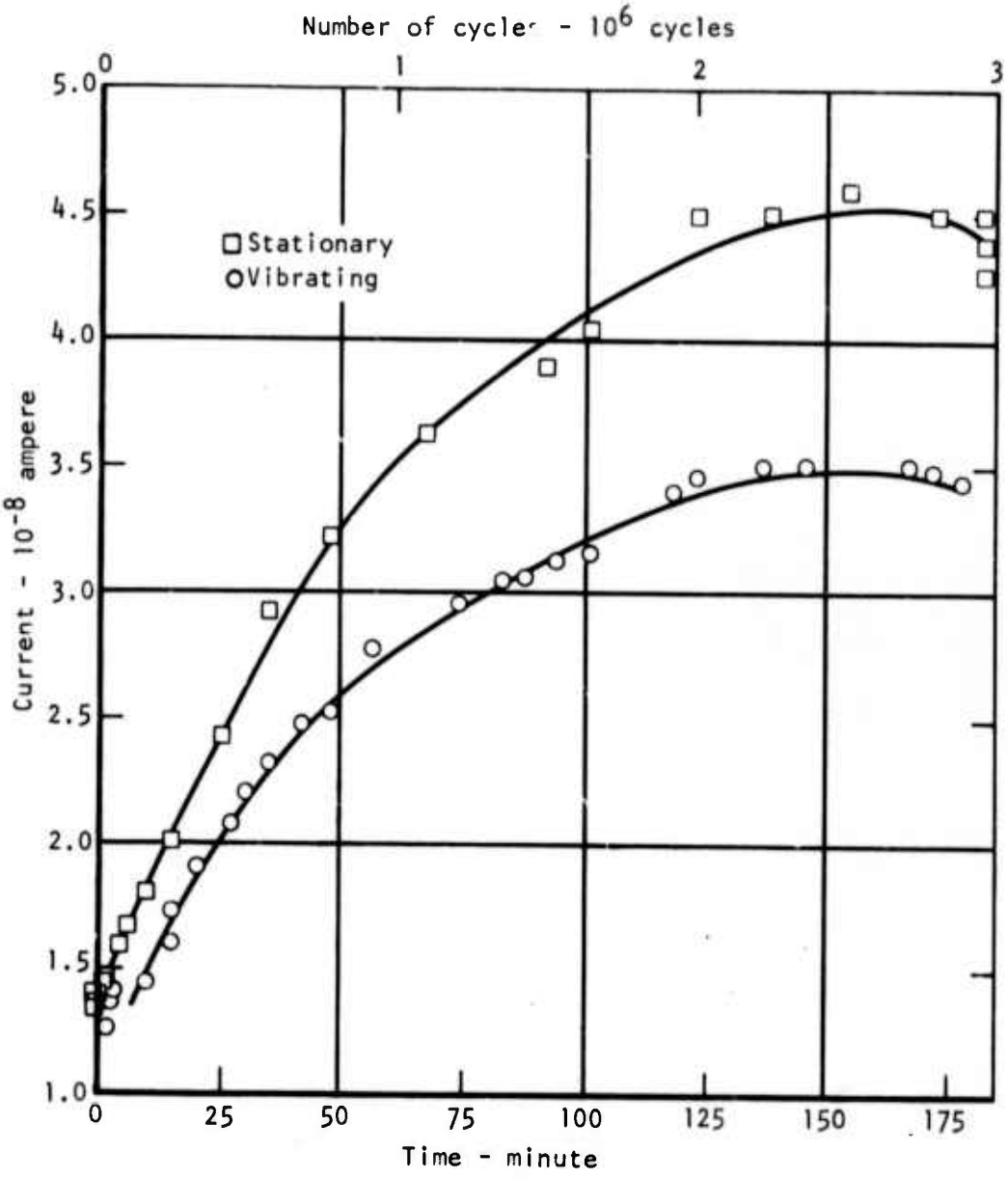

Figure 7. Exoelectron emission curves for 1100 aluminum in fatigue at a strain amplitude of 2.64×10^{-3} in vacuum.

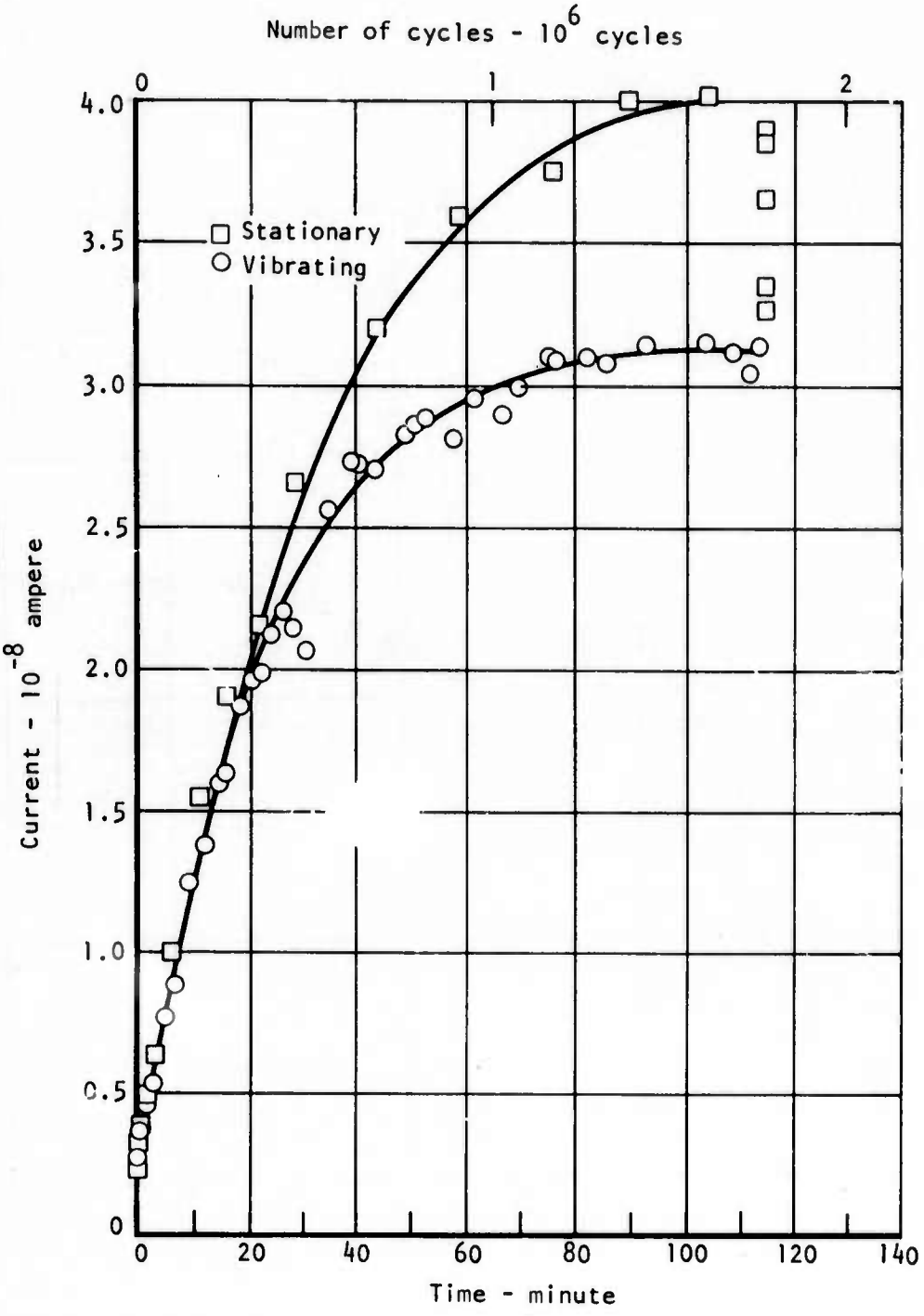

Figure 8. Exoelectron emission curves for 1100 aluminum in fatigue at a strain amplitude of 2.88×10^{-3} in vacuum.

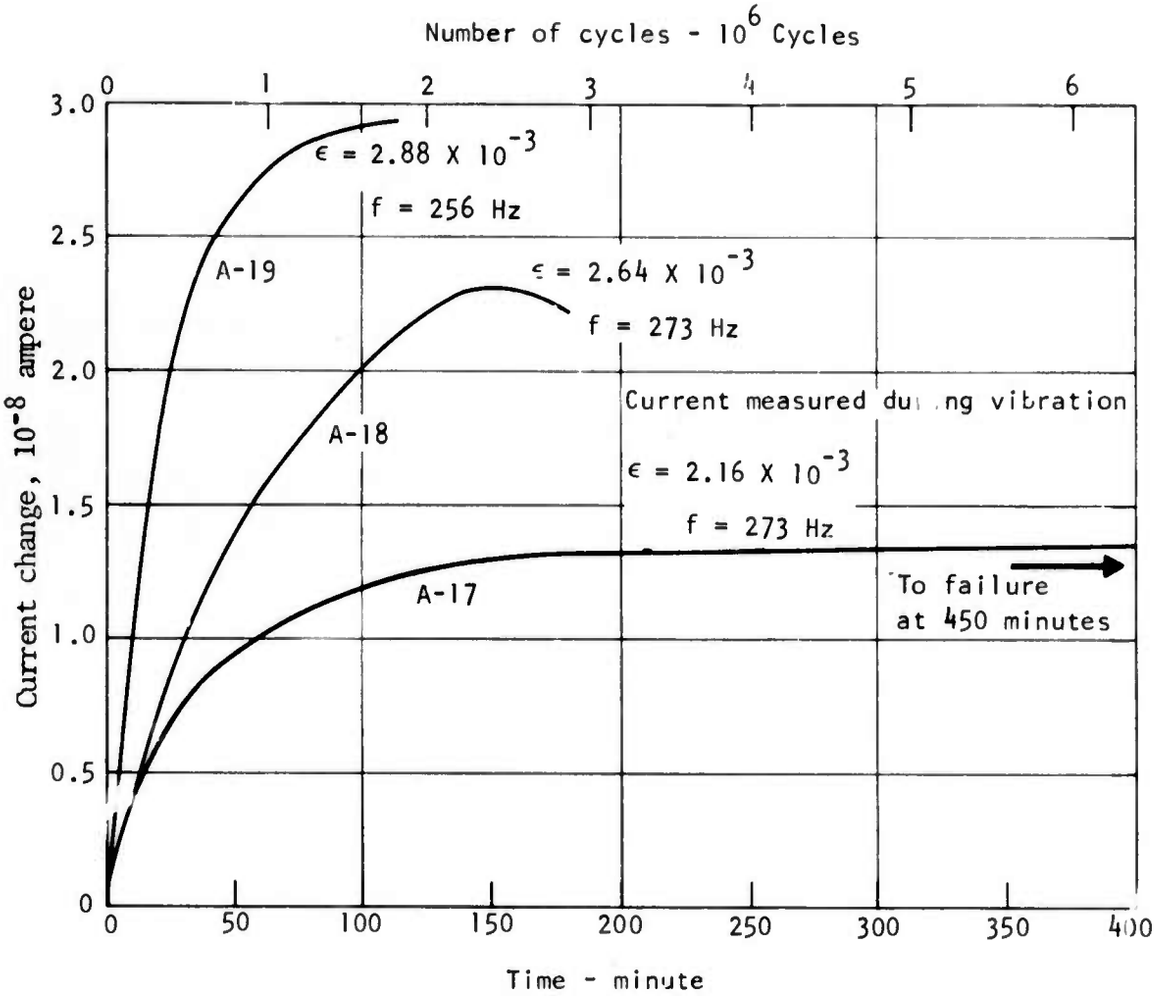

Figure 9. Exoelectron emission curves for 1100 aluminum in fatigue at various strain amplitudes in vacuum.

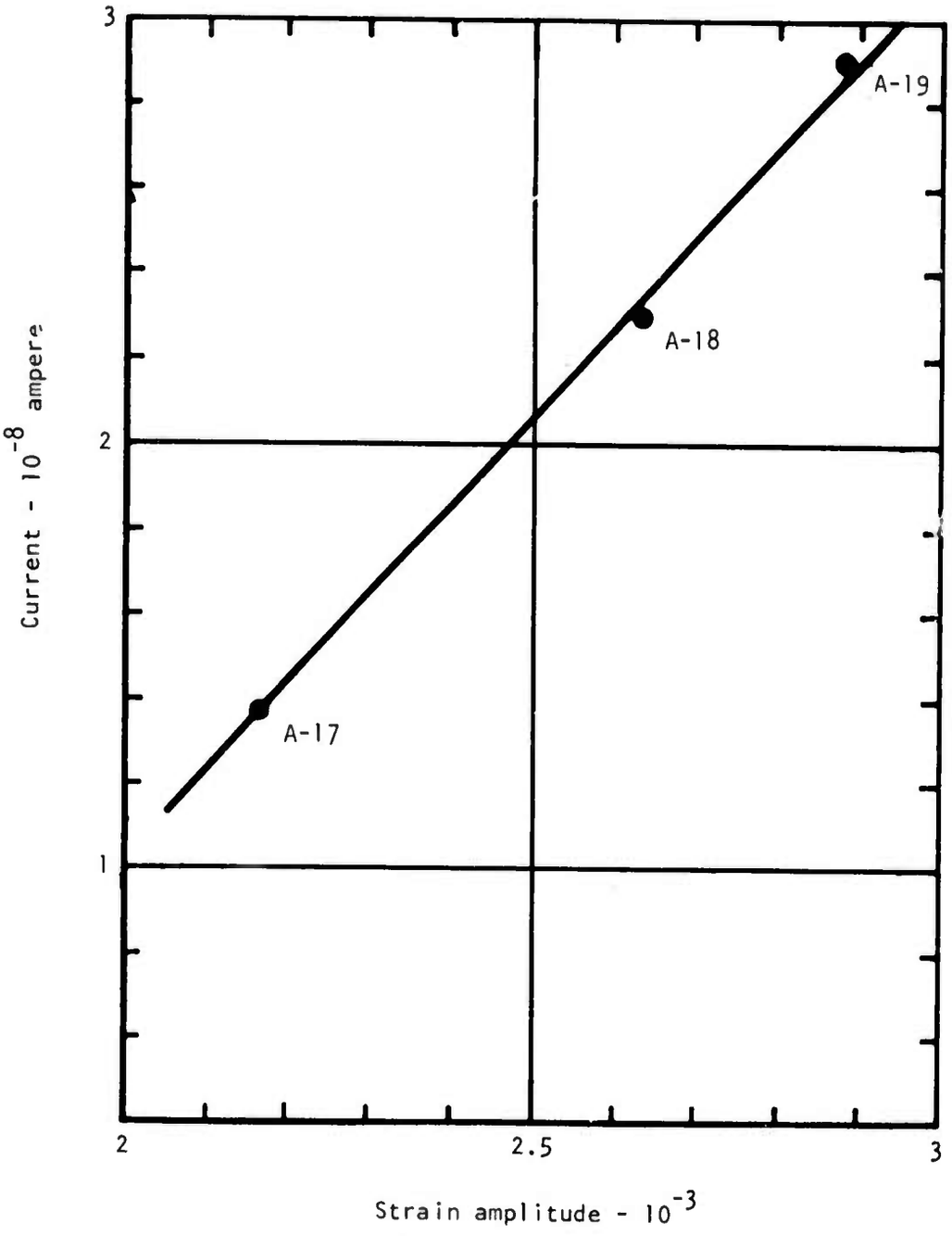

Figure 10. Relation of exoelectron current at fatigue failure of 1100 aluminum in vacuum with strain amplitude.

be made at this time of the fact that this curve appears to be linear. However, it is significant that the current increases as the strain amplitude (or equivalently, the stress amplitude) of the fatigue cycle is increased. This, of course, is an extremely important point as far as the applicability of exoelectron emission to the detection of the fatigue damage is concerned.

A similar plot for a specimen of 2024 alloy, which was annealed and quenched before the test, fatigued at a strain amplitude of 6.65×10^{-3} is shown in Figure 11. Because this aluminum alloy has a considerably higher yield strength than the 1100 alloy, these data were obtained at a larger strain amplitude. There are several significant features to note in this figure. There is some evidence that there is a slight incubation period at the start of this curve, in contrast to that noted in the 1100 alloy test series. A more important point to note is the fact that the magnitude of the emission current is smaller than in the 1100 alloy test series. Greater study will be needed in order to elucidate the differences. It is, however, significant to note that qualitatively the features are the same in this material as in the 1100 alloy series. Another 2024 alloy specimen was quenched and aged at room temperature for several days before the fatigue test. During the course of the test, the strain amplitude increased at the points indicated on the curve in Figure 12. The interesting feature to note is that, as the amplitude was increased toward the end of the run, the exoelectron current increased. This result is consistent with that noted on the 1100 alloy test series, in which case a constant amplitude was maintained throughout the test. It is shown that the magnitude of emission current increases with the strain or stress amplitude applied during the fatigue cycle for both 1100-0 and 2024-T3 aluminum materials.

EMISSION AS A FUNCTION OF OXIDE THICKNESS AT CONSTANT STRAIN AMPLITUDE

This paragraph contains the results of experiments made to determine the effect of aluminum oxide thickness on the exoelectron emission. An Auger spectral analysis was made on each specimen prior to the ellipsometric measurements to determine the chemical composition and determine how it varied as a function of the oxide thickness. Figure 13 shows an Auger spectrum of an 1100-0 specimen before fatigue, with an oxide thickness of approximately 60 angstroms. The ordinate is measured in arbitrary units, and the scale for the abscissa is 2 volts per millimeter. The voltage represents the measure of the Auger electrons emitted in the analysis. The aluminum oxide peaked at approximately 55 volts. The oxygen peak is shown at 515 volts. It should be noted that the arbitrary scale on the ordinate is multiplied by 10 for aluminum; i.e., the aluminum magnitude is diminished by a factor of 10 relative to the oxygen peak in this particular plot. After fatigue, a similar Auger spectrum plot is shown in Figure 14. It is seen that no essential differences occur in the Auger spectrum before or after fatigue. Figure 15 shows an Auger spectrum

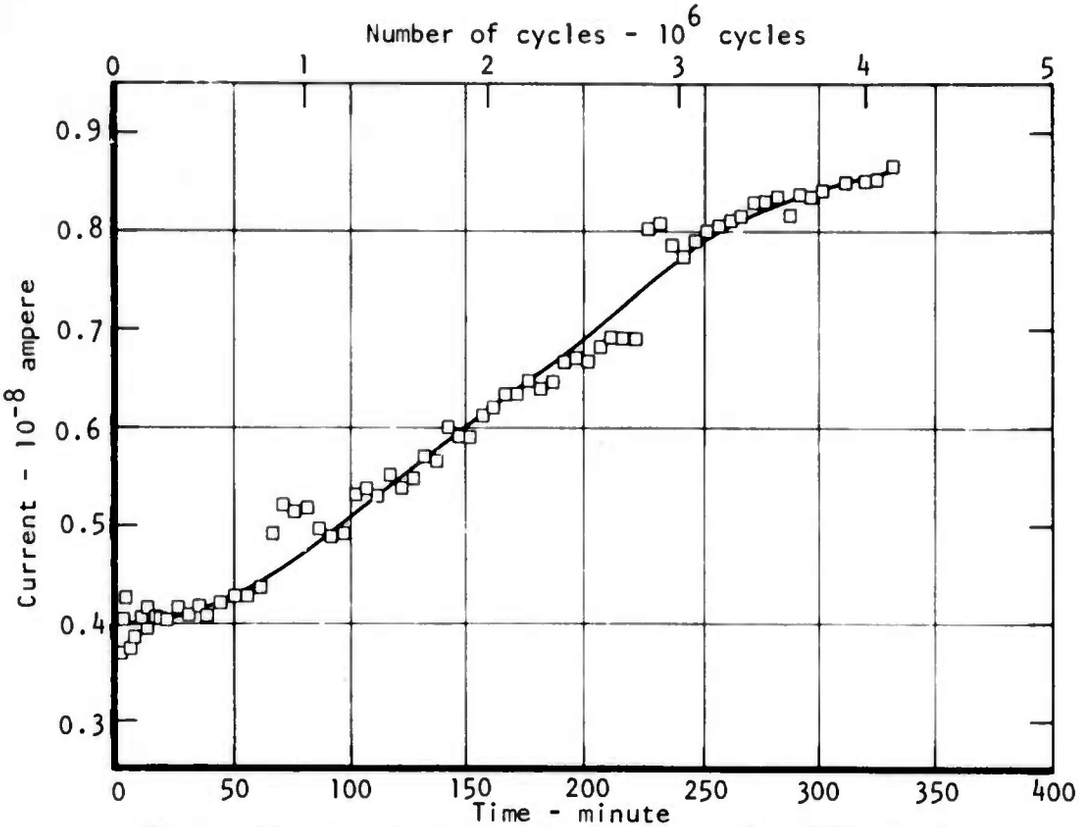

Figure 11. Exoelectron emission curve for 2024-T3 aluminum alloy in fatigue at strain amplitude 6.65×10^{-3} in vacuum.

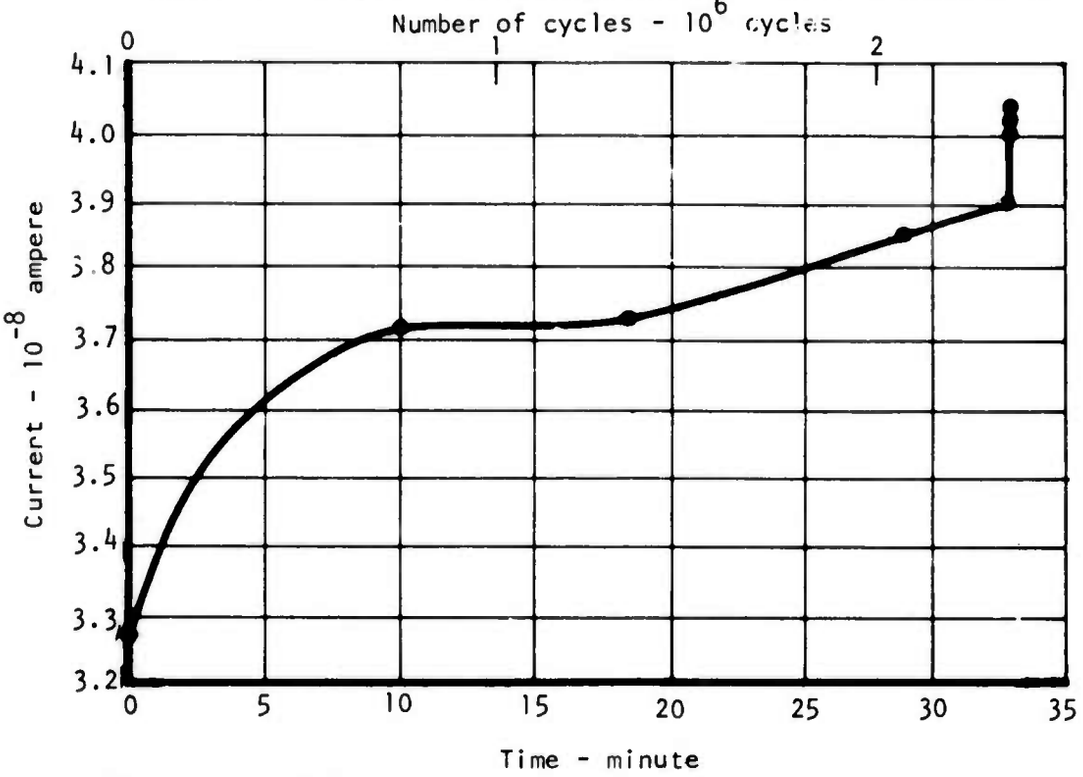

Figure 12. Effect of strain amplitude on exoelectron emission of 2024-T3 aluminum alloy in fatigue in vacuum.

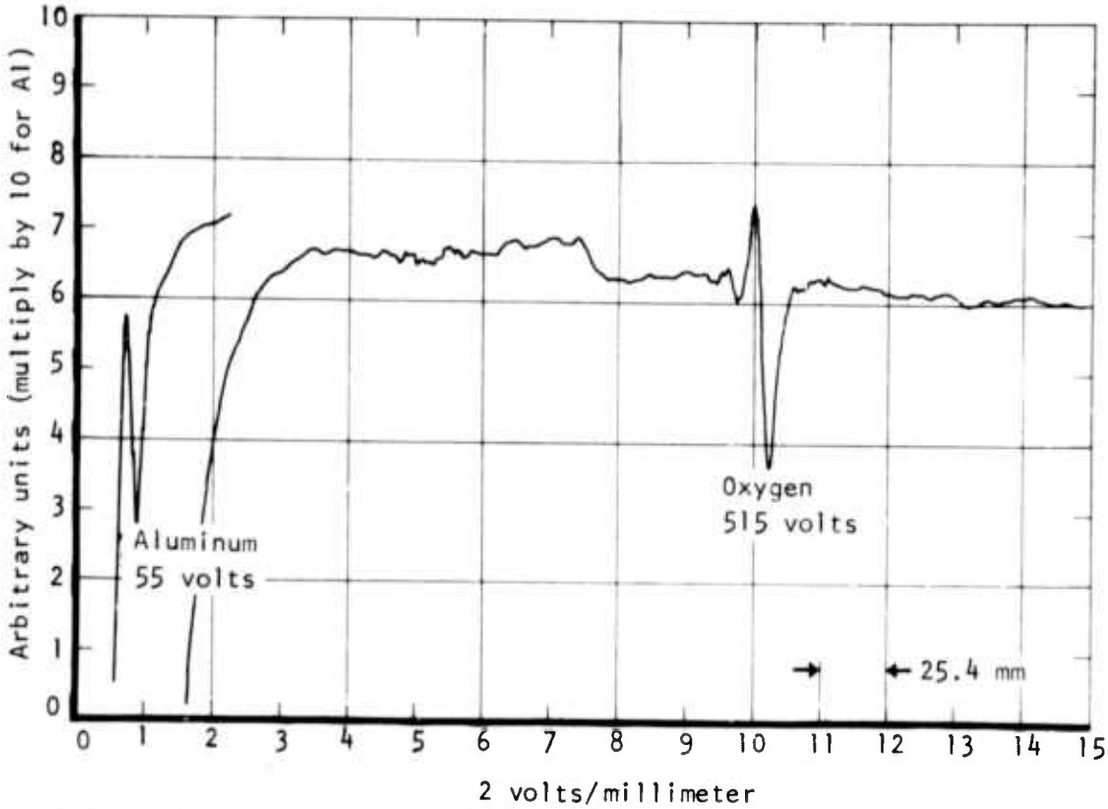

Figure 13. Auger spectrum before fatigue in vacuum of 1100 aluminum with 60 angstroms surface oxide.

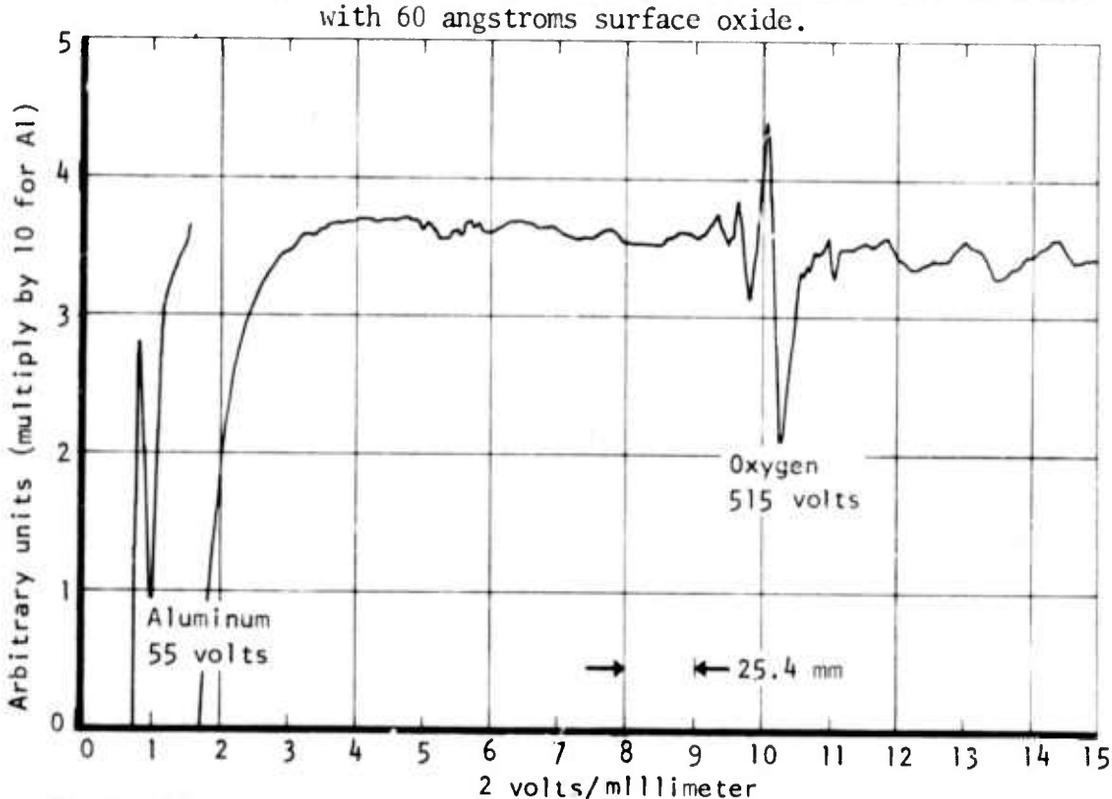

Figure 14. Auger spectrum after fatigue in vacuum of 1100 aluminum with 60 angstroms surface oxide.

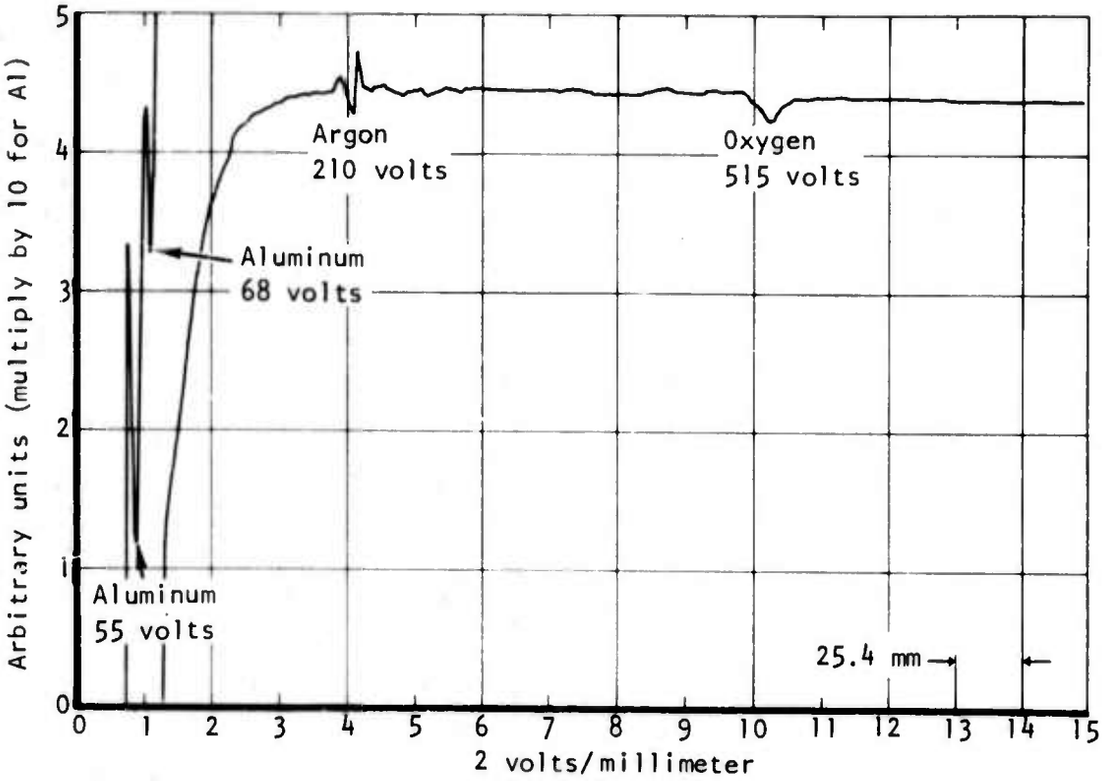

Figure 15. Auger spectrum after argon bombardment of 1100 aluminum to reduce the surface oxide thickness from 60 to 35 angstroms.

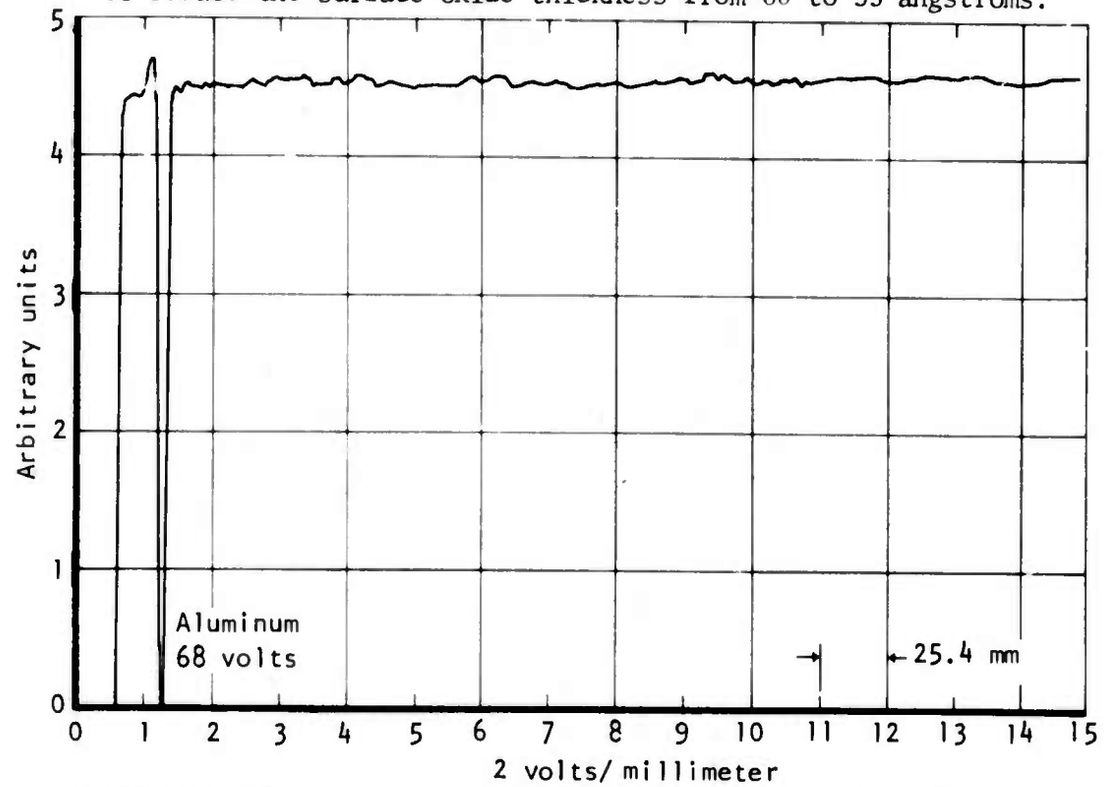

Figure 16. Auger spectrum after argon bombardment of 1100 aluminum to remove surface oxide.

for an 1100 aluminum specimen after an argon bombardment in which the oxide was reduced to a thickness of approximately 35 angstroms. The aluminum peak splits into two peaks, one at 55 volts and one at 68 volts. Additionally, there is evidence that argon has stuck to the surfaces of the specimen and, on a relative basis, the oxygen magnitude is diminished. The split of the aluminum peak seems to be characteristic of the results obtained as the oxide thickness becomes smaller and the aluminum peak shifts toward a higher value. The results are indicative of the fact that there are two conditions, one peak for the aluminum in aluminum oxide and one peak (the higher voltage aluminum peak) characteristic of the pure aluminum surface. Figure 16 shows a plot of the Auger spectrum for another 1100 aluminum specimen after argon bombardment which reduced the oxide thickness to essentially zero, as measured by ellipsometry. The significant feature is that there is only one major peak at 68 volts for aluminum which is of very large magnitude and essentially no oxygen. The peak attributed to argon is also absent. Evaporation might be the cause of the disappearance of this peak. As the oxide thickness has been reduced to zero, it is apparent that the aluminum peak shifted from 55 to 68 volts, which is characteristic now of the pure aluminum surface.

The exoelectron emission from an 1100 aluminum specimen with oxide thickness about 35 angstroms subject to fatigue at a strain amplitude of 2.6×10^{-3} is shown in Figure 17. The upper curve is from the stationary specimen, and the lower curve gives the value of the exoelectron emission while the specimen is in vibration. Qualitatively, it is noticed that the magnitude of the current is greater than the current measured on the specimen with oxide layer 60 angstroms thick fatigued at the same strain amplitude shown in Figure 7. Separation between the two current curves in Figure 17 is also wider. Figure 18 shows the exoelectron emission measured on a specimen with nearly zero surface oxide thickness fatigued at approximately the same strain amplitude as before. The data show the largest exoelectron currents that were measured in the course of these experiments, and also the greatest separation between the vibrating and stationary specimen cases. There seems to be some effect upon the time to failure of the specimen. The significant feature is the increase in the exoelectron emission as the oxide is reduced in thickness. The following table summarizes the results obtained at various oxide thicknesses and at constant strain amplitude for all the 1100-0 specimens measured in this series. The table gives the specimen number, the value of the oxide thickness obtained by the ellipsometric measurement, the initial stationary value of the current prior to fatigue test, the current just prior to failure in the stationary condition, and the incremental value between the initial and final values for the current.

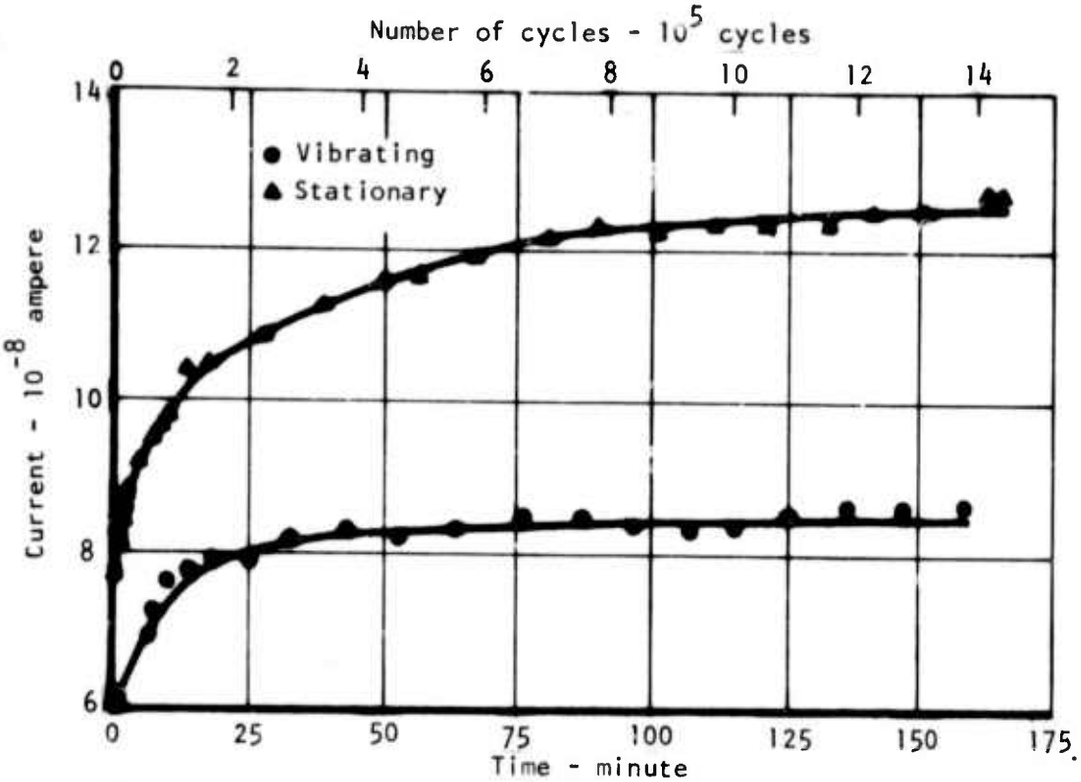

Figure 17. Exoelectron emission curves for 1100 aluminum with 35 angstroms surface oxide in fatigue at strain amplitude 2.6×10^{-3} in vacuum.

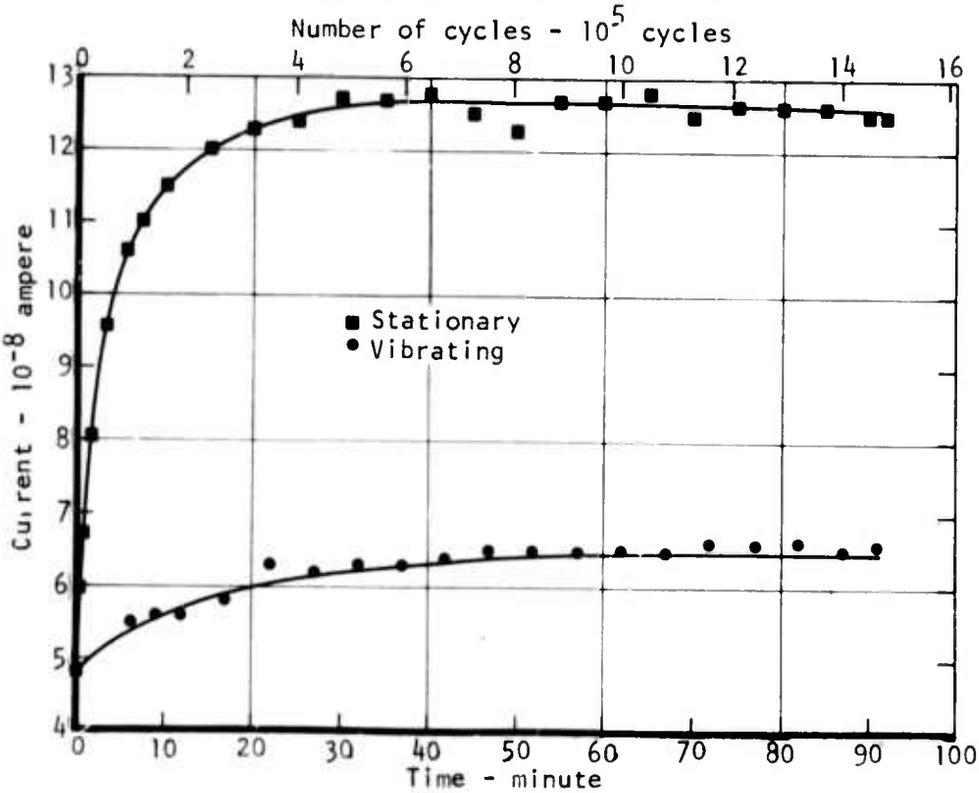

Figure 18. Exoelectron emission curves for 1100 aluminum without surface oxide in fatigue at strain amplitude 2.7×10^{-3} in vacuum.

VARIATION IN EXOELECTRON CURRENT AT FATIGUE FAILURE WITH SURFACE OXIDE THICKNESS ON 1100 ALUMINUM

Specimen No.	Oxide Thickness (angstrom)	Exoelectron Current (10^{-8} ampere)		
		Initial	Final	Increment
A-27	300	0.2	1.6	1.4
A-18	60	1.25	4.6	3.3
A-20	55	1.5	4.3	2.8
A-21	35	6.0	12.5	6.5
A-26	0	4.8	12.8	8.0

The incremental current value is plotted in Figure 19 as a function of the surface oxide thickness. It is apparent that, as the oxide thickness is reduced to zero, the current approaches the maximum value. Although not plotted in this illustration, it is significant to note that the differences between the stationary and vibrating specimen values also increase as the oxide is removed. It may be concluded that the oxide does not affect the emission in any significant way except to apparently act as an attenuator. Also, it should be remembered that these measurements were made in a high-vacuum condition with oxygen partial pressure at about 2×10^{-10} torr. These results are considered significant in the elucidation of the mechanism of the exoelectron emission.

SURFACE POTENTIAL DIFFERENCE MEASUREMENTS

The surface potential difference between an 1100 aluminum specimen and a reference electrode was measured during fatigue in air. The qualitative features of the resulting curve shown in Figure 20 are similar to the exo-electron emission curves in Figures 6 through 8. This may not be an unexpected result, since it would appear that the surface potential difference may be related to the difference between the stationary and vibrating specimen curves. The effect might be associated with charge storage in the oxide layer which builds up a surface potential difference and provides a rectification effect on the exoelectron current.

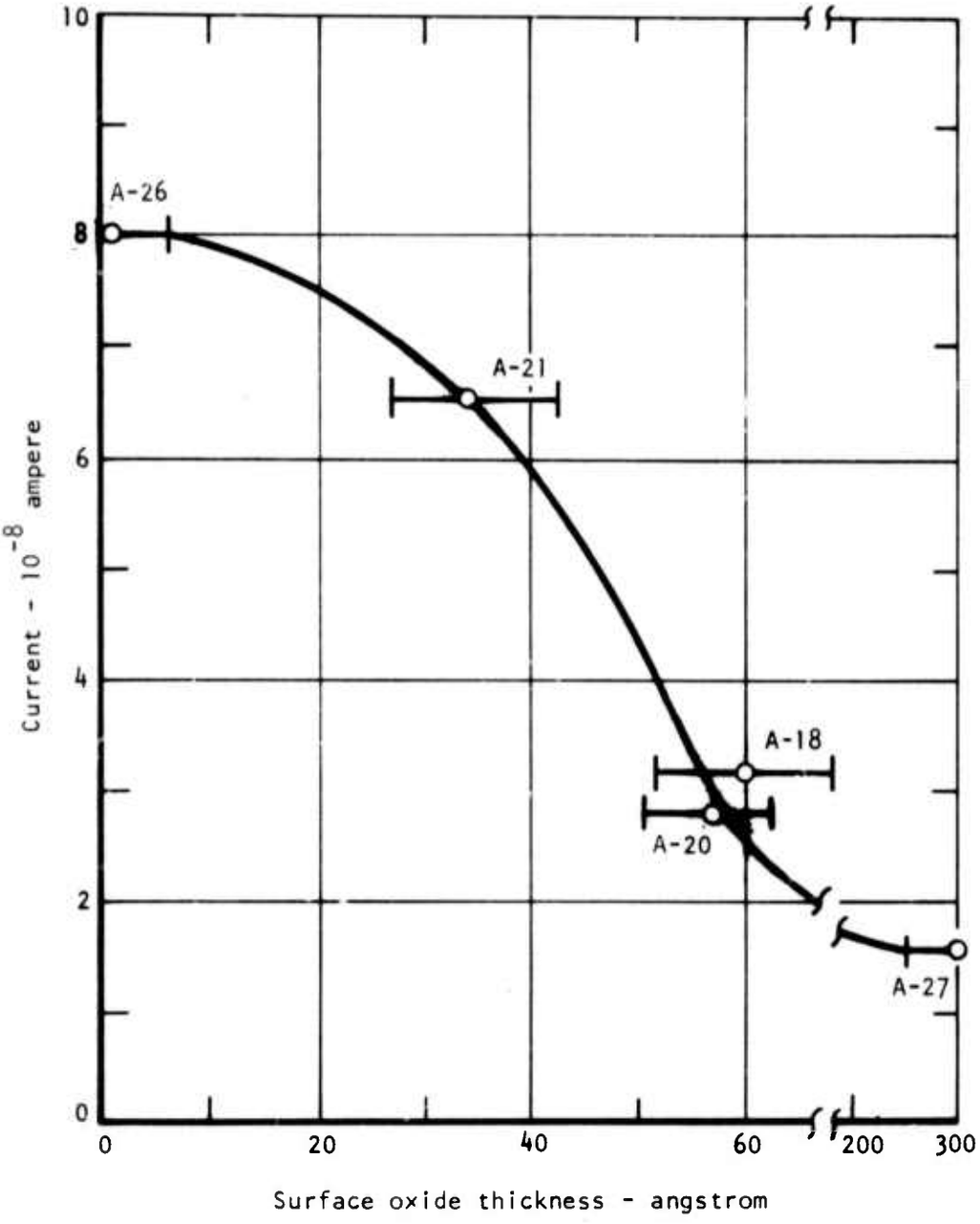

Figure 19. Effect of surface oxide thickness on exoelectron current at fatigue failure of 1100 aluminum in vacuum.

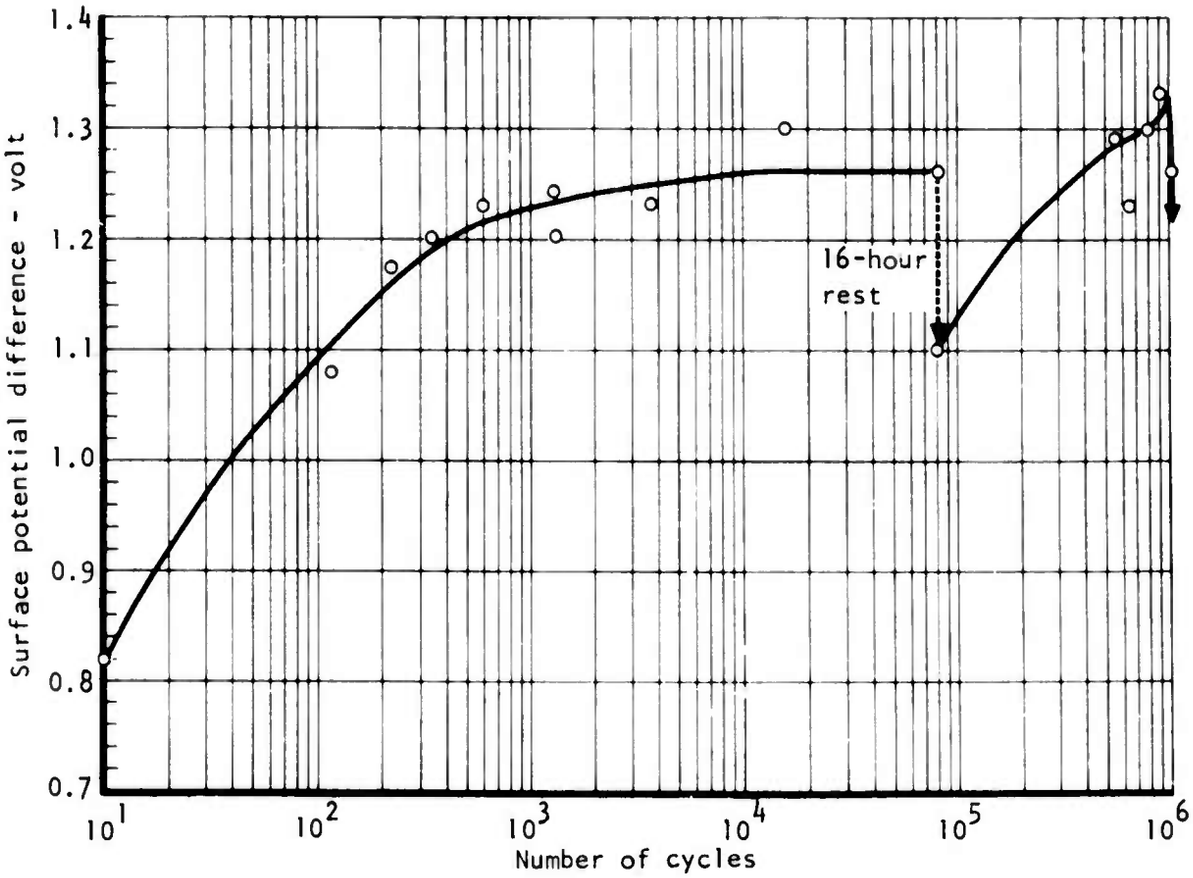

Figure 20. Variation of surface potential difference with fatigue life for a triangular 1100 aluminum specimen tested in air.

OPTICAL CONSTANT MEASUREMENTS

Two ellipsometric parameters, the phase shift caused by reflection and the arc tangent of the ratio of the normal to the parallel polarization components of the reflected light, were measured on four 1100 aluminum specimens during fatigue at strain amplitudes from 2.61×10^{-3} to 2.88×10^{-3}. The surface optical properties, the refractive index and the absorption coefficient, of the aluminum substrate were calculated and plotted versus the percentage of fatigue life in Figure 21. Changes in the optical properties in fatigue appear to be somewhat unaffected by strain amplitudes. It is also noted that appreciable changes occur only at early fatigue life (10 to 15 percent).

Although changes in the ellipsometric parameters in fatigue may be due to lattice distortion of either the oxide or the metal, they seem too large for this mechanism. Surface roughening on a submicroscopic scale (less than wavelength), however, may account for such changes. Roughening after fatigue was detected by profilometer trace of the specimen surface shown in Figure 22.

Similar measurements on 2024 aluminum alloy specimens were also attempted, but the surface roughening results were not observed. The difference between the 1100 and 2024 aluminum may be associated with the deformation modes and the amount of accompanying surface roughening. The areas around a crack and away from a crack of both the 1100 and 2024 aluminum alloy specimens after fatigue test were examined by scanning electron microscopy. The photomicrographs to be described later reveal a marked difference in the surface appearance: the surface of 1100 material after fatigue is much rougher than the surface of 2024 material. It is speculated that the 2024 material does not roughen in a way that contributes at the wavelength of light used to make the ellipsometric measurements.

The surface property curves in Figure 21 do not resemble the exoelectron emission curves in Figures 6 through 8. However, all of the curves display a significant change in the early stage (10 to 15 percent of total life) of the fatigue process. Additional work should be done as a function of optical frequency on other materials to extend the correlation between surface optical properties and exoelectron emission in fatigue.

EXOELECTRON EMISSION DECAY

Exoelectron current measurements were made as a function of time after the fatigue failure of a 2024-T3 aluminum alloy specimen under ultrahigh vacuum conditions, while oxygen was admitted to the chamber to create various oxidation conditions. The resulting emission decay curve is given in Figure 23. The portion of negative time of the abscissa indicates the state of the specimen after failure, but prior to the first admission of oxygen, which is represented

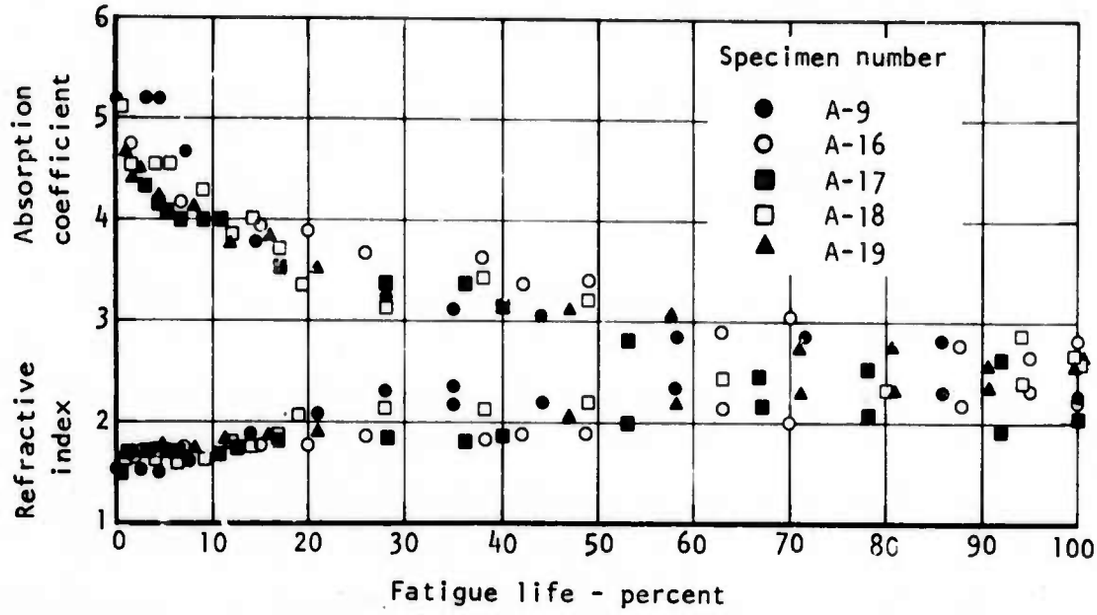

Figure 21. Variation in surface optical properties with percentage of fatigue life in vacuum for 1100 aluminum.

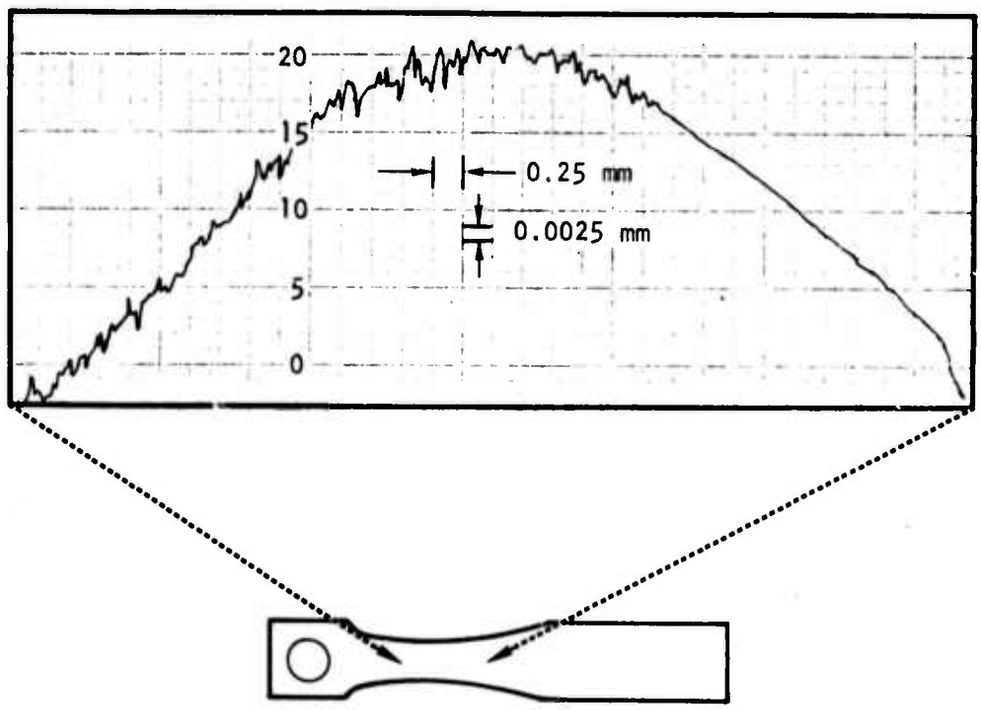

Figure 22. Profilometer trace for 1100 aluminum specimen surface after fatigue in vacuum.

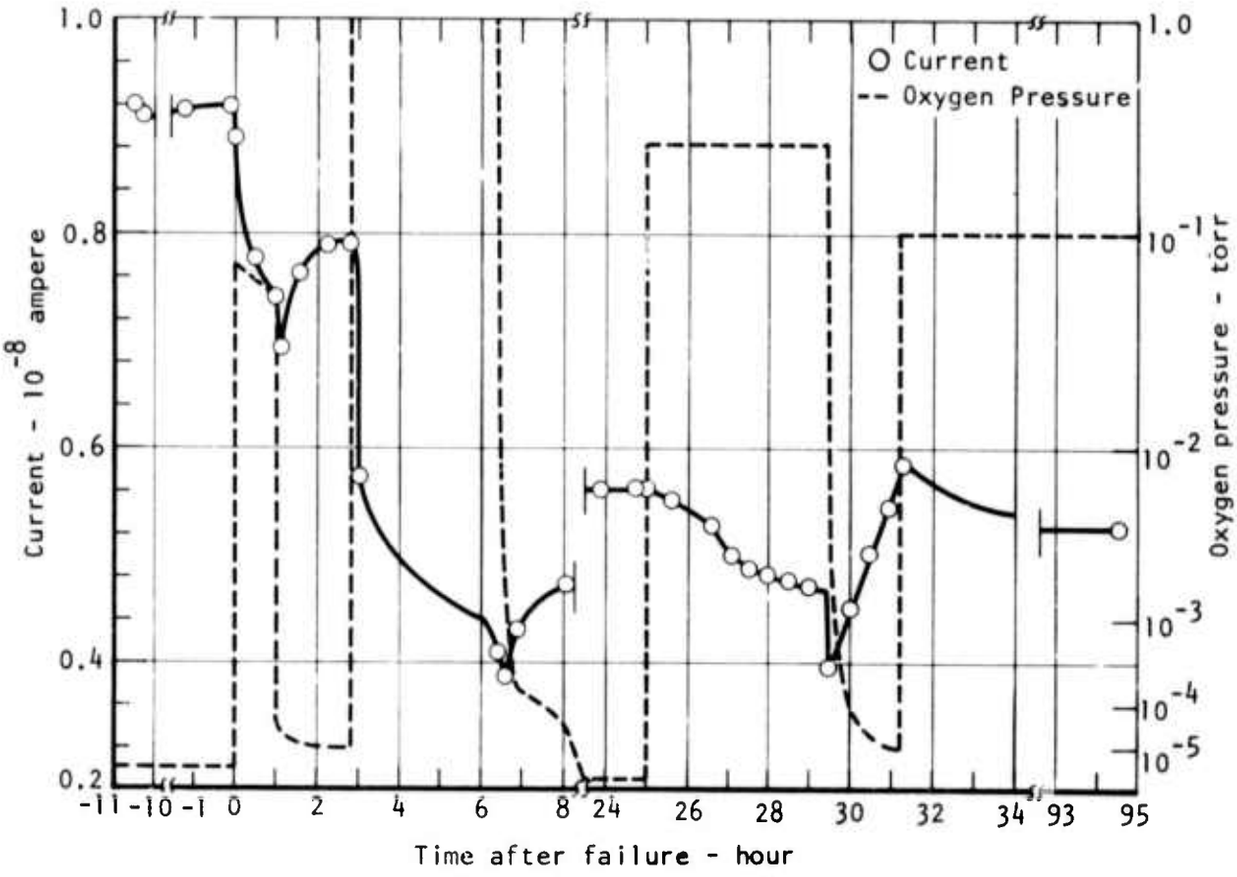

Figure 23. Exoelectron emission decay curve after fatigue failure of 2024-T3 aluminum alloy under various partial pressures of oxygen.

by zero time. The solid curve depicts the change in exoelectron current, while the dashed line and curve represent the variation in partial pressure of oxygen in the chamber. It is noted that, for several hours after the failure had occurred and before oxygen was first admitted, the exoelectron current stayed relatively constant. As oxygen was admitted, the current started to diminish. Upon pumping out the oxygen, the current decreased further and followed generally the same pattern as the first cycle of removal and readmission, through the course of the experiment. After the specimen was fully oxidized, the current leveled off to approximately 0.6×10^{-8} ampere. It then remained unchanged indefinitely thereafter.* It may be concluded that the oxygen effects are not such as to diminish the value of the current, other than to provide an oxide layer through which the emission must take place and in which attenuation effects play a role. They do not suggest, however, that oxidation plays an intrinsic role in the emission decay process observed here.

ELECTRON SPIN RESONANCE

One of the thoughts relating to exoelectron emission phenomena is that the emission associated with vacancy creates transport in the outside layer with some kind of a charge change and charge storage in the oxide. An electron spin resonance measurement was conducted on both unfatigued and fatigued 1101 aluminum specimens. No difference was obtained between the two cases. The negative result tends to indicate that vacancy transport is not a source of the emission itself. It should be noted, however, that the measurement was made on an extremely small volume of oxide, and presumably was at the margins of sensitivity of the electron spin resonance effort used in this investigation (10^{12} spins).

SCANNING ELECTRON MICROSCOPY

A detailed scanning electron microscopic evaluation was made in an attempt to determine the characteristics of the fatigue effects in both the 1100 and 2024-T3 aluminum alloy specimens. This evaluation was directed specifically at determining the presence of slip, persistent slip, void coalescence, and microcracking in and near the fatigue-damaged zone of the specimens as well as crack characteristics at the fracture zone. The photomicrographs in Figure 24 show the general surface appearance of both 1100 and 2024-T3 alloys before and after fatigue test. Both materials before fatigue test have a relatively smooth surface except that the 2024-T3 surface contains some constituent particle inclusions.** After fatigue, the surface of 1100-0 appears to be rougher than the surface of 2024-T3. The lesser amounts of surface roughness of 2024-T3 might be the reason that no meaningful ellipsometric measurements

*An earlier experiment has shown that 2024-T3 alloy fully oxidizes in about 2.5 hours after similar processing under vacuum conditions.

**The minor indication on the 1100 alloy photomicrograph before fatigue test are etch pits.

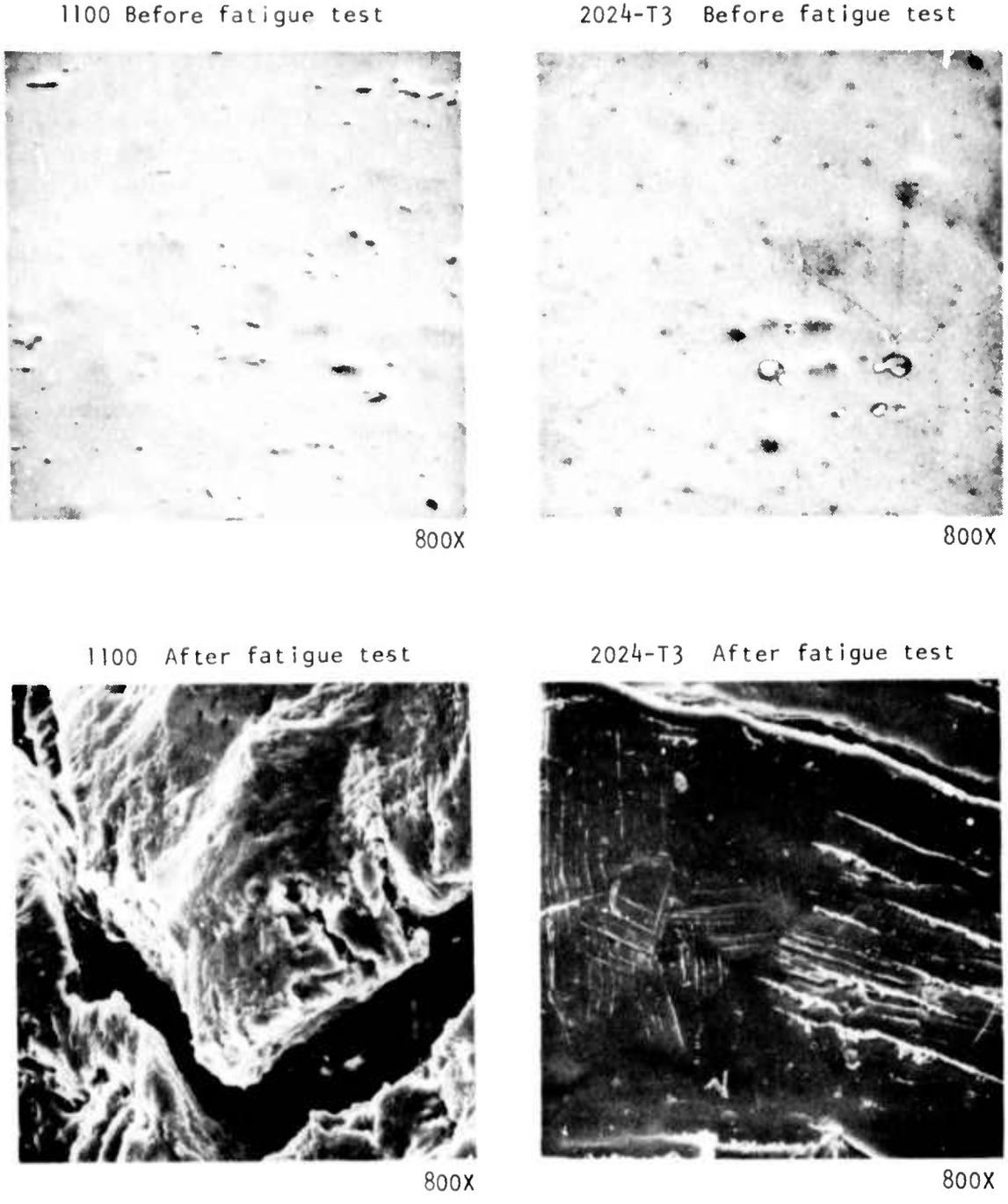

Figure 24. Scanning electron micrographs showing general surface appearance of 1100 and 2024-T3 aluminum alloys before and after fatigue test.

could be made on that material. Because of the unusual surface appearance of 2024-T3, it was subject to further examination by scanning electron microscopy. Slip lines and cracks are shown in three magnifications in Figure 25. The fatigue fracture initiation site of 2024-T3 was also located. The photomicrograph in Figure 25 shows the butte-like features characteristic of the fracture of 2024-T3 material.

DISCUSSION

It is apparent that stimulated exoelectron emission provides an extremely viable approach for the development of a fatigue detector. There are, however, two key features in the data presented herein which point out salient needs that must be fulfilled so that the detector can be used with the full confidence required of an NDT device. Figures 6 through 9 show that the stimulated exoelectron current is related to the fatigue strain amplitude. This feature is a necessary requirement in order that the stimulated current be a reliable measure of the fatigue state of a material. However, due to the ambiguity of the current data, it is obviously not sufficient. According to the data, a single measured current value under these conditions would not be sufficient to uniquely define in the fatigue state of the material. An auxiliary measure or method of either fatigue or current data analysis must, therefore, be found which can be used reliably in conjunction with the stimulated exoelectron emission to remove the ambiguity. Additionally, the actual fatigue state of an air vehicle structure would represent spectrum loading rather than the constant loading conditions of these experiments, which would further substantiate the need for a second method or measurement parameter.

The difference between the stationary and vibrating current levels was analyzed. A part of these differences were considered to be involved with the way in which the data to date were obtained; i.e., with a dc electrometer. Further work demonstrated that there is an ac component in the exoelectron emission current with a frequency the same as the applied stress frequency. In fact, the size of the ac signal is such that it may be easier to detect in the field than the dc component. However, it must be realized that, in an imagined NDT device application, the ac and dc components are complementary. If one is talking about real-time surveillance of fatigue damage, the ac component may be much more desirable, for it can be synchronized with real-time fatigue stress spectral loads; on the other hand, after-the-fact inspection of aircraft for fatigue damage is better done with the dc inspection. It is currently believed that the differences between the stationary and vibrating data are due to rectification effects which may arise in the dc apparatus, or perhaps, with rectification effects due to charge storage effects in the oxide layers.

The results obtained for the emission as a function of oxide thickness on aluminum are extremely interesting. They appear to be inconsistent with the predictions of one of the most widely accepted models for the origin of the

100X

800X

2,000X

800X

Figure 25. Scanning electron micrographs showing slip lines, cracks, and fracture initiation site of 2024-T3 aluminum alloy after fatigue test.

emission. This model in its simplest form suggests that the emission results from chemical reactions when a fresh metallic surface is oxidized. The fresh, metallic surface will be generated in a fatigue experiment as slip bands penetrate the surface, or microcracks are formed in the material. Under the conditions of the present experiment, it would be expected, according to this model, that the stimulated emission would be reduced at the small oxide thickness end of Figure 19, rather than increased as it is observed. As was noted earlier, these experiments were performed in vacuum conditions in which the oxygen partial pressures were about 2×10^{-10} torr; it is considered unlikely that increased oxidation rates would be sustained in this thin atmosphere. The results suggest, rather, that the oxide's principal role is that of an attenuator of the emission, which is certainly to be expected in this range of electron energies.

Other mechanisms have also been suggested as the source of the emission. One of these is vacancy transport to the surface with a form of charge interchange. The vacancies are undoubtedly created in the fatigue process. There is difficulty with this model in interpreting the aforementioned results. Vacancy transport in aluminum is known to proceed with an activation energy for diffusion of about 0.6 electron volt. At room temperature, there should have been a noticeable incubation period between the start of fatigue cycling and the appearance of changes in the emission current due to diffusion times: Figures 6 through 8 show that this is not the case; on the contrary, the emission is found to change with fatigue in the very first few cycles. The 2024 aluminum alloy data show a slight incubation period. It is not known at this time why a difference exists. Undoubtedly, there are contributions to an emission from thermally stimulated and associated phenomena, but it is apparent that they are not the large contributors to what is called stimulated exoelectron emission in this work. Other suggestions have been made that the stimulated emission results from dislocations as they protrude through a surface as a result of the deformation associated with fatigue; whereas it is not possible to rule this suggestion out, it does not seem as plausible as an alternative mechanism.

On the basis of present knowledge, it is believed that the approach most likely to lead to an understanding of stimulated exoelectron emission associated with fatigue can be identified with the enhanced photoemission that occurs from a material under conditions of increased surface roughening. It is further believed that the similarities which exist between the so-called stimulated exoelectron emission and the roughness-enhanced photoemission have largely gone unnoticed because the subjects have been pursued largely by groups of people who do not share common interests.

Endriz and Spicer [45] [46] have recently discussed the roughness enhanced photoemission in some detail. Here, surface roughness serves to couple light from a vacuum (air) into the surface plasmon modes of a nearly free-electron-like metal. Under conditions of an atomically smooth surface, this is not

[45] Endriz and Spicer, 1972-A

[46] Endriz and Spicer, 1972-B

possible because of the difference in the velocity of light in the two media and the impossibility of conserving momentum under these conditions. However, it has been shown that surface roughening removes this impossibility. This turns out to be the case, since the roughness introduces a condition of periodicity into the solution of Maxwell's equations in the surface, which allows momentum to be conserved. Thus, the optical frequency at which the maximum in the roughness-enhanced photoemission takes place can be expected to move toward smaller optical energies as the wavelength of the roughness increases. This shift is apparently very sensitive to the surface roughness. Endriz and Spicer have shown that, in changing the rms surface roughness of deposited aluminum films from 16 to 28 angstroms, the maximum in the photoyield curves moves downward in energy from about 10 to 9 volts (the plasmon edge for aluminum is about 10.5 volts). Coupled with the changes in the photoyield (or photoemission) are changes in the optical reflectivity. Drops in reflectance are measurable at positions in photon energy which correspond to maxima in the photoyield curves; this coupled information was a key point in establishing that the roughness-enhanced photoyield was a consequence of optical coupling to the plasmon modes.

It is important to discuss the way in which the roughness-enhanced effects are expected to be generated by fatigue damage. Surface roughness generated by fatigue damage results from several mechanisms. Plastic deformation of metal and other crystalline (as opposed to amorphous) solids proceeds predominately by the formation and motion of dislocations. This permits slip and lateral displacements along preferred crystallographic planes, which produces macroscopic changes of sample dimensions. Slip does not occur uniformly on an atomic scale, but is concentrated in regions generally called slip lamella and slip bands. These surface irregularities may show a high degree of periodicity and may very well be associated with different stages of fatigue. Depending upon the material and deformation modes peculiar to the material, slip steps may be of the order of a micron in height with spacings of the order of 5 to 10 times the height. Thus, the nonuniformity of fatigue deformation manifests itself with some degree of regularity in the slip patterns produced. These patterns are expected to contribute significantly to a fatigue-generated surface roughness condition many orders of magnitude greater than the rms roughness required to produce optical coupling into the plasmon modes. In fact, it would be expected that in some materials, at least, the roughness induced by fatigue would serve more like a diffration grating than an rms roughness. A grating effect might be expected to further enhance the optical-photoyield coupling phenomenon.

It is worthwhile to point out the way in which the data presented earlier from the stimulated exoelectron experiment are consistent with the pattern of results to be expected from the roughness-enhanced photoyield work. For aluminum, the plasmon edge occurs at approximately 10.5 volts, which is equivalent to a photon excitation wavelength of about 1,000 angstroms. An

ultraviolet excitation with predominant wavelength at about 2,500 angstroms was used in the present experiment. It is straightforward to reason that the stimulated exoelectron curves shown in Figures 6 through 8 result from the passage of the photoyield maximum through the "window" at 2,500 angstroms as the surface roughening proceeds due to fatigue in the specimen. In a few cases, it was observed (including the middle curve of Figure 9) that the emission decreased just prior to fatigue failure. Such a behaviour is consistent with the model proposed and, in this context, corresponds to the maximum in the photoyield current having moved through the window at 2,500 angstroms to longer wavelengths with continued surface roughening. Another feature of the results which can be accommodated by this working hypothesis is the variation in the initial values of the exoelectron currents. Slight variations in the surface roughness would easily account for it. A third feature which can be accommodated within the surface plasmon model is that of the effect of surface oxides through the oxide dielectric constant. The dielectric serves to alter the dispersion curves of the surface plasmon modes of the host material and thus change the optical cutoff frequencies; however, a detailed analysis is quite complicated and has not as yet been performed. An additional effect that has been reported in the exoelectron literature which is also consistent with this hypothesis is the enhancement of the emitting current by acoustic surface waves in the presence of acoustic excitation of the specimen. Whereas it is difficult to couple this with either of the models for exoelectron emission discussed earlier (oxidation and vacancy transport), it is straightforward to see that it can be accommodated within the surface roughness context. Acoustic waves produce surface modulations, on a periodic basis, which would be expected to couple the incident light to the surface plasmons. Thus, it appears that the roughness-enhanced photoemission is an approach to generate a fundamental understanding of the stimulated exoelectron emission phenomenon.

In summary, this discussion has sought to identify the phenomenon of exoelectron emission with fatigue by various mechanisms. Several mechanisms have been advanced, and, in terms of this program, are evaluated as follows:

1. Vacancy transport - If the exoelectron emission is associated only with vacancy transport (the vacancies being generated by fatigue), the emission should be consistent with a diffusion time governed by about a 0.6 ev activation energy for Al. This was not observed.

2. Vacancy transport and electron tunneling through the metal oxide interface - Only limited information was obtained from this program. However, the electron spin resonance experiment casts doubts on this as being a potential mechanism.

3. Oxide formation on fresh metal surface - This program has shown that oxidation is not necessary in order to observe "exoelectron emission." Hence, one must conclude that the stimulated emission we have observed is unrelated to oxidation of fresh metal surfaces.

4. Surface roughing - It is believed that all of the program results are consistent with this mechanism. Work is continuing under an AFOSR contract in order to verify this mechanism as the proper explanation of the exoelectron emission/fatigue phenomenon.

Section VI

FATIGUE TEST CONDITIONS

AXIAL TENSION FATIGUE

All specimens were subjected to axial tensile fatigue testing (zero to maximum load) at a rate between 1 and 20 Hz. The tests at 1 Hz were conducted in a modified Detroit Testing Machine Company unit at the University of Arizona; tests between 6 to 10 Hz were conducted in a specially developed hydraulically operated fatigue machine [1]. Since an excessively lengthly time period would be required to complete high-cycle tests at these low rates, high-cycle fatigue tests were performed at 20 Hz in a Baldwin-Hamilton-Lima IVY-12 fatigue machine. The cyclic rates used were well below the ultrasonic range, and it was not expected that the fatigue behavior of the material would be affected. To insure that the test rate did not affect the evaluation, a 2024-T81 specimen was scanned in fatigue test at various cyclic rates and at three-stress levels (26, 28, and 30 ksi). At each stress level, a test was performed for preselected numbers of cycles at 8, 4, 1, and back to 8 Hz. The current at any one location decreased a little (less than 10 percent) as the test rate changed, but the overall shape of all the current curves recorded at one given stress level was almost identical. It can thus be said that the test rate between 1 and 20 Hz has only slight effect on the exoelectron emission behavior of 2024-T81 material in fatigue.

TEST PROCEDURES

ESTABLISHMENT OF BASELINE DATA

Baseline data experiments were designed to provide a set of reference data to evaluate the effect of fatigue damage in specimens containing discontinuities, complex shapes, prior deformation or whose surfaces were altered by exposure to different environmental conditions. Standard type specimens were tested under normal ambient conditions.

Four types of fatigue tests formed the baseline group:

- Low-cycle (10^4 - 10^5 cycles) fatigue
- High-cycle (10^6 - 10^7 cycles) fatigue
- Spectrum loading
- Elastic loading

Low-cycle and high-cycle fatigue specimens were tested to approximately 25, 50, or 75 percent of the fatigue life to allow progressive nondestructive evaluation of the accumulated damage. The applied stress levels and number of fatigue cycles for the 2024-T81 and Ti-6Al-4V alloy specimen are given in Tables 1 and 2 and Appendix C.

The spectrum loading sequences used for the 2024-T81 and Ti-6Al-4V materials included low-high, high-low, and low-high-low conditions. A stress range between 22 and 38 ksi with a 4 ksi increment was used to test the 2024-T81 specimens. The number of cycles at each stress level was increased with the decrease in stress level. The stress levels and the corresponding number of cycles were the same in low-high and high-low sequences. In the low-high-low sequence, both the stress increment and the stress range remained unchanged except at 38 ksi, when the number of cycles was reduced in half since the sequence was repeated at that stress level for subsequent sequences. The total number of cycles in each load sequence was 5×10^5. Details of the stress levels and the number of actual fatigue cycles are shown in Table 1.

The procedure for spectrum loading the annealed Ti-6Al-4V material was similar to the aluminum except that the stress range was from 40 to 88 ksi with a stress increment of 12 ksi. Table 2 gives the stress levels and the number of fatigue cycles at each stress level in the three loading sequences.

Elastic fatigue loading was only performed on the 2024-T81 alloy. The tensile test on this material yielded a proportional limit of about 55 ksi. Since the stress for high-cyclic fatigue was 22 ksi, an even lower stress of 11 ksi was applied in elastic loading to insure that the specimen would not fail in the high-cycle fatigue range of 10^6 to 10^7 cycles (Table 1).

Except for the elastic loaded specimen, the fatigue tests were repeated once or twice so that the progress of the fatigue damage could be evaluated by NDT methods.

SPECIAL TESTS

Fatigue Location

One of the primary objectives of this program for assessing fatigue damage is the evaluation of the capabilities of the NDT methods to predict the final failure site. The test specimens used for this evaluation were either the standard type, the standard type containing discontinuities, or complex configurations such as a bolted joint, weld joint or curved shape. The test materials included 2024-T81, 2024-T3, 2219-T851, and 7075-T6 aluminum alloy

TABLE 1. TEST CONDITIONS AND NUMBER OF SPECIMENS FOR 2024-T81 ALUMINUM ALLOY

Fatigue Test Condition	Number of Specimens
Baseline data	
Low cycle, % life of 10^4 - 10^5 cycles	
25	3
50	3
75	5
High cycle, % life of 10^6 - 10^7 cycles	
25	3
50	3
75	3
Spectrum loading*	
1	3
2	5
3	4
Elastic loading	
2.5×10^6 cycles	2
1×10^7 cycles	1
Fatigue location**	
Standard	49
1, 3, 4, or 7 holes	20
1 or 3 slots	11
Bolted joint	2
Curved shape	3
Weld with no flaws	2
Weld with pores	6
Environment condition	
General plastic deformation, % life of 10^4 - 10^5 cycles***	
25	2
50	2
Corrosion (soak for 24 hours in salt solution)	1

TABLE 1. TEST CONDITIONS AND NUMBER OF SPECIMENS FOR 2024-T81 ALUMINUM ALLOY (CONCL)

Fatigue Test Condition	Number of Specimens
Evaporation, % relative humidity	
30	1
45	1
60-65	1
65-70	2
65-100	3
Total	141

*Spectrum loading sequence

1 = low-high (22, 26, 30, 34 and 38 ksi for 36×10^4, 10×10^4, 3×10^4, 8×10^3 and 2×10^3 cycles, respectively)

2 = high-low (38, 34, 30, 26 and 22 ksi for 2×10^3, 8×10^3, 3×10^4, 10×10^4 and 36×10^4 cycles, respectively)

3 = low-high-low (22, 26, 30, 34, 38, 34, 30, 26 and 22 ksi for 18×10^4, 5×10^4, 1.5×10^4, 4×10^3, 2×10^3, 4×10^3, 1.5×10^4, 5×10^4 and 18×10^4 cycles, respectively)

**Three of the 20 specimens containing holes, three of the 11 specimens containing slots, and the three curve-shaped specimens are 7075-T6 alloy. Eight weld specimens are 2219-T851 alloy.

***Two of the four specimens are 2024-T3 alloy.

TABLE 2. FATIGUE TEST CONDITIONS AND NUMBER OF SPECIMENS FOR ANNEALED Ti-6AL-4V ALLOY

Fatigue Test Condition	Number of Specimens
Baseline Data	
Low cycle, % life of 10^4 - 10^5 cycles	
25	3
50	3
75	3
High cycle, % life of 10^6 - 10^7 cycles	
25	3
50	3
75	3
Spectrum loading*	
1	3
2	3
3	3
Fatigue location	
Standard	1
Three slots	3
Total	31

*Spectrum loading sequence

1 = low-high (40, 52, 64, 76 and 88 ks: for 36 x 10^4, 10 x 10^4, 5 x 10^4, 8 x 10^3 and 2 x 10^3 cycles, respectively)

2 = high-low (88, 76, 64, 52 and 40 ksi for 2 x 10^3, 8 x 10^3, 3 x 10^4, 10 x 10^4 and 36 x 10^4 cycles, respectively)

3 = low-high-low (40, 52, 64, 76, 88, 76, 64, 52 and 40 ksi for 18 x 10^4 5 x 10^4, 1.5 x 10^4, 4 x 10^3, 2 x 10^3, 4 x 10^3, 1.5 x 10^4, 5 x 10^4 and 18 x 10^4 cycles, respectively)

specimens (Table 1). The approximate stress levels for testing these various types of specimens, were determined by the baseline data. Similar tests were also conducted on a limited number Ti-6Al-4V alloy specimens.

Environmental Effects

The surface condition of a material undergoing fatigue is influenced by the environment. The parameters of environment investigated were general plastic deformation, evaporation, and corrosion. These parameters were evaluated to determine the effect on the fatigue properties of the material and the ability of an NDT method to detect and assess the fatigue damage.

The effect of general plastic deformation was investigated using 2024-T81 and 2024-T3 specimens which had previously been subjected to a tensile strain of about 27×10^{-3} to initiate bulk plastic flow in the test zone as indicated by the deviation of the linear load-deflection plot. The detail history of the fatigue tests on these specimens is given in Appendix C.

The environment conditions for fatigue testing 2024-T81 aluminum alloy and PH14-8Mo steel in SRH-1050 condition under the influence of evaporation were created by varying the relative humidity of the air surrounding the specimen. The humidity was produced within a plastic cover placed over the specimen grips and enclosing the specimen and the exoelectron emission transducer by bubbling compressed air through a water bath into the plastic cover. The level of humidity was determined while fatigue test was in progress by drawing out a sample of the air and passing it through a Cambridge Systems Corporation model 880 dewpointer. The relative humidity was controlled within a range of 30 to 74 percent during tests. Increasing the relative humidity above 74 percent resulted in moisture condensation on the test machine and caused a momentary shorting in the electrical circuit of the exoelectron emission transducer. An environment condition of 100-percent relative humidity was created by storing the specimen between fatigue tests in wet paper towels for 2 to 5 day periods. Afterward, the specimen was tested to failure in the normal laboratory ambient condition. The specific relative humidity levels used in the fatigue tests were 30, 45, 60 to 65, 65 to 70, and 65 to 100 percent. The stress levels for the 2024-T81 material were selected through use of the baseline data. The stress levels for the steel specimens were between 44 and 69 ksi. The relative humidity level and fatigue test data of the specimens are shown in Appendix C.

The effect of general corrosion on the surface of the test specimen was evaluated. A 2024-T81 alloy specimen was first soaked in a 0.05M salt solution for 24 hours. It was then fatigue tested at a maximum load of 1,000 pounds (approximately 23 ksi) to failure.

RESULTS AND DISCUSSION

BASELINE DATA

An evalutaion of the high cycle fatigue data shows that, of the nine 2024-T81 specimens tested at 22 ksi, only three (A10, C14, and D3) failed between 10^6 and 10^7 cycles. After two tests to a total life greater than 5×10^6 cycles without failure, each of the remaining six specimens failed at a higher stress of 38 ksi. The decision to significantly increase the loading stress was made primarily to conserve test time since the only available fatigue system operated at only 8 Hz requiring approximately 35 hours to reach 10^6 cycles. Test time was also jeopardized by frequent malfunctioning of the servo control system which was totally redesigned and replaced. The fatigue cycling at the higher stress obviously resulted in low-cycle type fatigue loading condition. The average life of these six specimens at 38 ksi is 7.2×10^4 cycles, which is of the same order of magnitude of the average life of 6.1×10^4 cycles for the nine specimens subjected to high-cycle fatigue at 38 ksi. This indicates that damage incurred earlier at the low stress level of 22 ksi was negligible in terms of influencing the later fatigue life at the higher stress of 38 ksi.

This phenomenon was also apparent in testing the annealed Ti-6Al-4V alloy where the chosen stress levels of 40 and 88 ksi were too low to produce failure in the life range between 10^4 and 10^7 cycles. A higher stress of 110 ksi was finally applied to produce specimen fracture. Since the average life at 110 ksi for the six high-cycle specimens (F14, F15, F20, F45, F61, and F62) lies around 10^5 cycles, which is also the average life of the four low-cycle specimens (F3, F12, F23, and F47, neglecting F22 and F40, which had relatively longer life), the damage suffered by the specimen under test at 40 or 88 ksi can be considered minimal. Nevertheless, it is of considerable interest to know whether the potential failure site can be located earlier in the fatigue life as a result of the prior low-stress fatigue loading.

The test procedure used for the spectrum loading was to repeat a loading sequence before finally testing the specimen to failure at the highest stress level in the sequence. It was assumed that the severity of fatigue damage by spectrum loading would differ with loading sequence and that the specimen with the severest damage in a loading sequence would have the shortest life. All three 2024-T81 specimens (A3, A26, and B24) subject to low-high sequence survived two spectrum loads; only one (B28) of five specimens under high-low sequence went through two spectrum loadings. The remaining four specimens (C4, C12, E18, and F8) did not complete the first spectrum loading. In the low-high-low sequence, none of the four specimens tested survived two spectrum loadings. Only one specimen (D7) was unbroken after first loading. Since the stress increment, stress range, and number of cycles at each stress level were identical for each loading sequence, the low-high-low

sequence appears more severe than low-high or high-low sequence in the spectrum loading of 2024-T81 aluminum alloy. The final fatigue life at 38 ksi of specimens (A3, A26, and B28) having undergone low-high or high-low loading is of the same magnitude; however, judging by the fact that three out of four specimens failed to complete the first high-low test, whereas all three specimens survived the low-high test twice, it can be said that high-low loading is apparently more severe than low-high loading. This finding is not in agreement with the results obtained by Schijve,[11] who found that, in axial tension-compression spectrum loading of notched and precracked 2024-T3 Alclad specimens, the loading sequence in increasing order of severity were high-low, low-high-low, and low-high. The reason for this discrepancy was attributed to the major differences between the loading conditions and specimen configurations between the experiments.

The spectrum loading of the annealed Ti-6Al-4V alloy at the stress levels of 40 and 88 ksi showed negligible effect with all six specimens (F2, F6, F13, F21, F49, and F55) surviving two loading sequences. A higher stress level of 110 ksi was then applied for the third test. The extent of fatigue damage incurred as a result of the various spectrum loading conditions could not be ascertained since the fatigue life at 110 ksi is about 10^5 cycles if the relatively longer life of specimen F55 is ignored, regardless of the loading sequence.

At the completion of NDT evaluation after elastic fatigue loading, the 2024-T81 specimens E3 and E4 were each tested to failure at a higher stress of 38 ksi. The life at 38 ksi of 4.3×10^4 cycles is of the same order of magnitude as the fatigue life in low-cycle fatigue (6.1×10^4 cycles). Hence, preelastic loading apparently has negligible effect on a specimen subsequently fatigue tested at a high stress level.

SPECIAL TESTS

The specimens used to evaluate the NDT methods for predicting the fatigue location were planned to be tested at only one stress level to failure. However, if the stress was too low to cause fracture in the 10^6 to 10^7 cycles range, a higher stress was applied in the second test. Sometimes, three or even four tests at increasing stress levels were necessary to complete the evaluation of one specimen. The detail test conditions and test results for each specimen in this category are presented in Appendix C.

The specimens listed in Tables 1 and 2 under the heading of fatigue location were tested for the purpose of nondestructive evaluation. The fatigue test results of these specimens will be discussed later in connection with nondestructive tests.

Fatigue tests of the two 2024-T81 specimens (B7 and E20) which had experienced prior plastic deformation indicate an average life of 3.7×10^4 cycles. This life span is of the same order of magnitude as that of the specimens in low-cycle fatigue at the same stress level. It was concluded that plastic deformation induced by tension loading to a strain of 27×10^{-3} had negligible effect on the fatigue life of 2024-T81 alloy under subsequent fatigue conditions.

Eight 2024-T81 alloy specimens were tested for the effect of humidity in air on fatigue properties, and the test results are in agreement with the data available in the literature [19]. A trend is indicated that the fatigue life aluminum alloy decreases with the increase of relative humidity. At high relative humidity, however, the corrosion effect also plays an important role in reducing fatigue life since corrosion pits were observed on the specimen surface. Failure could initiate in one of the pits, especially where they were located close to the end of the straight test zone where change in cross-sectional area occurs.

The one 2024-T81 alloy specimen which has been soaked for 24 hours in a 0.05M salt solution before testing at a stress level of 23 ksi had a fatigue life of about 4×10^4 cycles. A comparison of this data with the data from specimens tested at varying levels of relative humidity shows that corrosion can significantly reduce the fatigue life. This was quite evident after a visual examination of the specimen surface. A number of pits were observed on the surface and failure had initiated at one of the pits.

Six PH14-8Mo steel specimens in SRH-1050 condition were also tested in 64 to 74 percent relative humidity at a maximum stress between 44 and 69 ksi. Because of lack of test data on other humidity levels, it was not possible to evaluate the overall effect of humidity on the fatigue life. The reason for testing in this humidity range was to study the ability of the exoelectron emission test method to predict the failure site at various stress levels in a highly humid environment.

Section VII

NONDESTRUCTIVE TEST METHOD EVALUATION

INTRODUCTION

Exoelectron emission and surface potential difference were the primary nondestructive test methods utilized to evaluate fatigue damage in the prepared specimens. Exoelectron emission was measured either continuously, during, or after the fatigue test, while the surface potential difference was measured after the fatigue test. All of the measurements were made in air at room temperature. These NDT methods were evaluated in terms of their ability to detect areas of fatigue damage and predict the location of the fracture site. The predicted location was checked with the actual location, which was determined after the final test to failure.

Acoustic emission and ultrasonic test methods were also evaluated on a limited number of specimens.

MEASURING EQUIPMENT AND PROCEDURE

SURFACE POTENTIAL DIFFERENCE

The surface potential difference between a fatigued specimen and a reference electrode was measured using a high-impedance electrometer in a circuit similar to the one described by Moore and his associates[1]. The present measuring system illustrated in Figure 26 consists of a radioactive source used to ionize the air between the test specimen and a reference electrode, a Keithly model 602 multirange electrometer and a scanner to traverse the radioactive source along the specimen surface. This source consists of an Americium 241 radioactive element, 0.01 millicurie, sealed in a glass envelope and positioned behind a 1.8-mm-thick (0.07 inch) nickel foil window. The sealed element measures approximately 6.4 mm-thick (0.25 inch) (1/4 inch) in diameter and is mounted in an approximately 38.1-mm-diameter (1.5 inch) diameter radiation shield. The radioactive source is commercially available from International Chemical and Nuclear Corporation, Irvine, California, under catalog No. 7400, modified to include the nickel window.

The source transducer was supported on a scanning lathe bed capable of precise X-Y positioning. The specimen was electrically grounded and positioned beneath the source with a spacing of 3.2 mm (1/8 inch). The spacing was not critical, and minor changes of ±1.6 mm (1/16 inch) did not significantly affect the measurements. The specimen was scanned lengthwise, and an X-Y recorder was used to plot the surface potential difference as a function of transducer position. Two scans were made at each specimen edge, and one scan was made along the specimen centerline on each side of the specimen.

The surface of the specimens frequently had grease, tape, or other handling marks as a result of the prior fatigue testing and handling. A test to determine the effect of cleaning the surface with acetone applied lightly with a cotton swab showed effectively no change in the measured voltage polarity or magnitude. Consequently, all specimens were uniformly cleaned prior to measuring. The effect of scan rate was evaluated and, after adjusting the electrometer for fast response measurement, the maximum scan rate was limited by the pen response of the X-Y recorder. Repeated scans over the same test specimen area showed good data reproducibility.

EXOELECTRON EMISSION

Two exoelectron emission measuring systems were used. They are quite similar, the main differences being the transducer design and the mechanism used to move the transducer for scanning. In one system, schematically illustrated in Figure 27, the electron detector (the transducer), which is composed of the collector and the short-wave ultraviolet light in a shielded housing, was driven along the specimen at a rate of 12.7 mm per minute (1/2 inch per minute) by a linear motor triggered by a cycle timer. Lateral movement of the transducer was controlled by two hand-adjusted machine screws, and an automatic scanning mode was also available. In the automatic mode, the transducer scans along the specimen to the end of the travel and then returns quickly to the starting point to repeat the scan. A microscope was mounted on the scanning fixture for observing the specimen during cycling and it provided a reticule for the measurement of crack growth. Later in the present work, another transducer was added to the monitoring system, so that each side of the specimen could be scanned for exoelectron emission during fatigue test. This system was developed for fatigue tests conducted in the modified Detroit Testing Machine Company unit at a rate of 1 Hz.

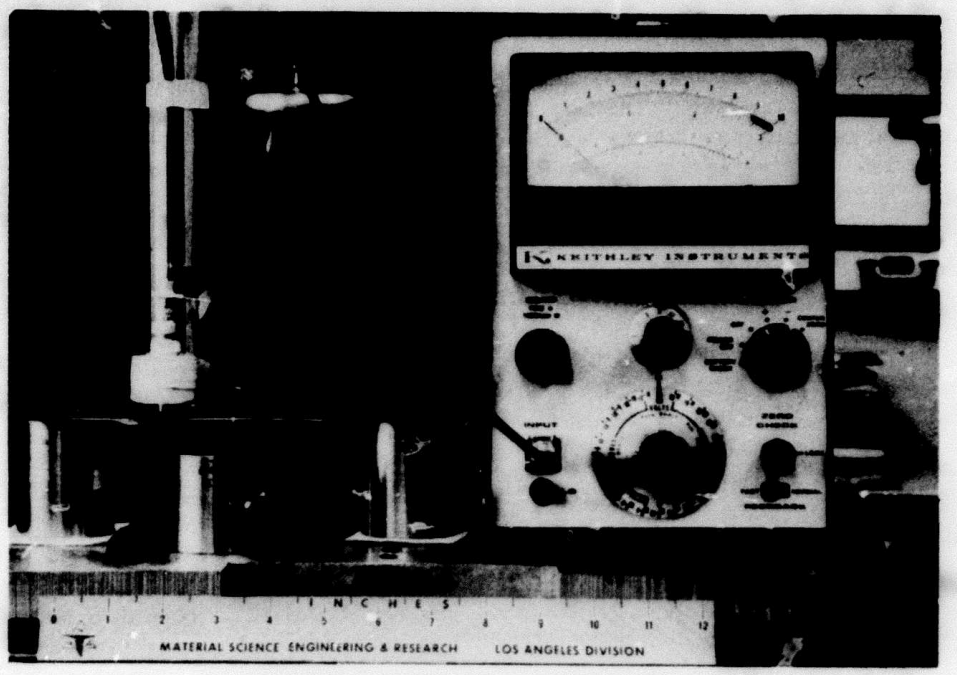

Figure 26. Surface potential difference scanning system.

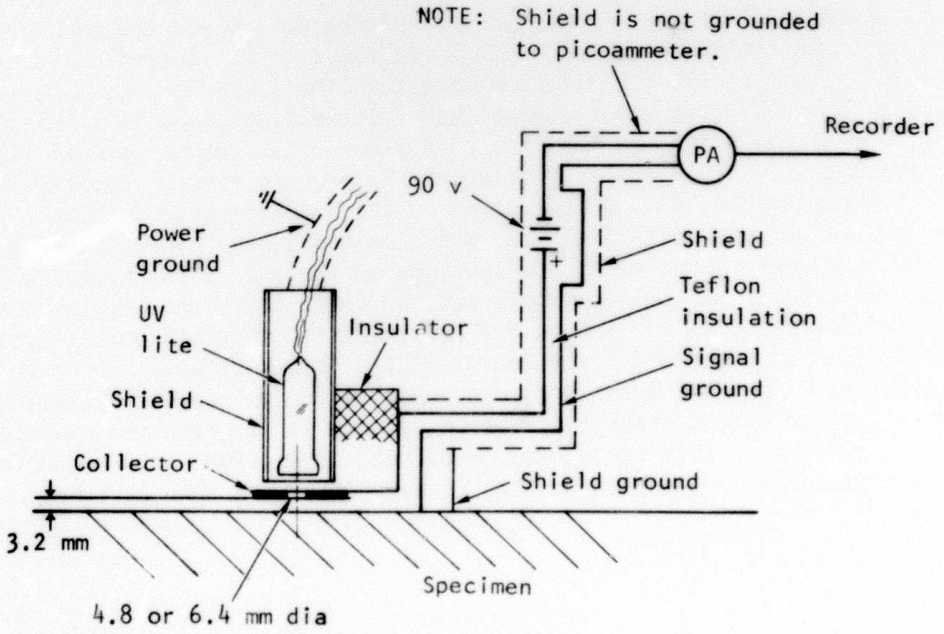

Figure 27. Schematic diagram for exoelectron emission system.

The other monitoring system was used to measure exoelectron emission during fatigue tests carried out in the cyclic range between 6 and 20 Hz, using either the specially developed hydraulically operated fatigue machine or the Baldwin-Hamilton-Lima IVY-12 machine. This system, shown in Figure 28, is fully described in the section on proto-type system development.

Either system could be operated either continuously or intermittently, during the fatigue test. In either case, the transducer was moved along the length of the specimen to obtain a continuous record of emission current along the straight portion of the specimen. Since the opening of the transducer is large enough to allow ultraviolet illumination upon the full width of the specimen, no lateral movement of the transducer was needed in the measurement.

QUANTITATIVE ANALYSIS METHOD FOR LOCATING FATIGUE DAMAGE

A qualitative method of analyzing the exoelectron emission curves by noting the change in the slope of the successive curves, although easy to apply, is not reliable because of uncertainties where there is no slope change or there are changes at several locations along the specimen length. It is thought that the change in exoelectron current rather than its measured quantity at a location is a better indicator of fatigue damage. However, use of this preliminary analysis method sometimes yielded obscure results when all the exoelectron emission curves were very similar.

Therefore, a systematic, quantitative analysis method was developed for locating the failure site. In using this method, the emission curve for each scan was divided into 10 equal parts. Both the exoelectron current and the number of cycles at each point were measured and recorded. The emission current data obtained from the first scan were taken as the reference, and the change in current at the same location on the subsequent curves was computed with respect to the reference current. The failure site could be situated at one of the locations where the exoelectron current exhibited a significant change.

It was observed in a review of early test data that the change in emission can increase, decrease, or both increase and decrease during a fatigue test. This change in emission may be attributed to the manner of

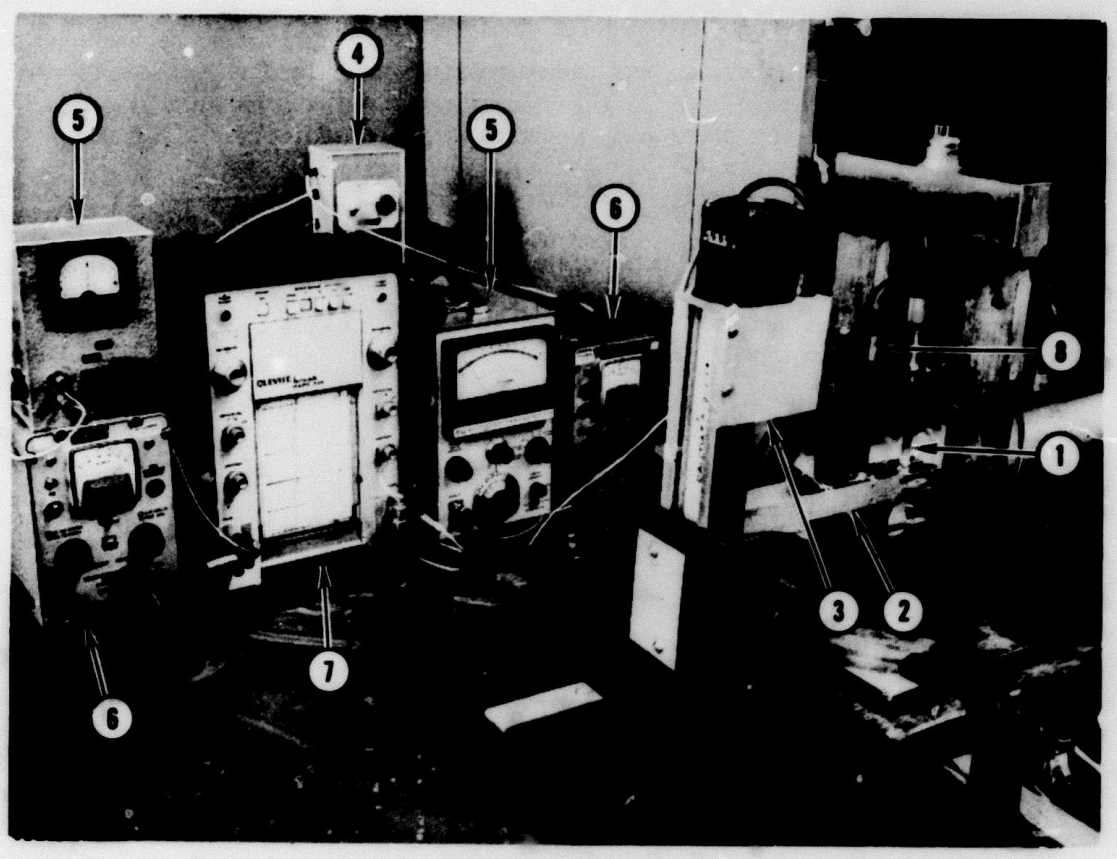

1. Fatigue specimen
2. Support arm for electron transducers
3. Transducer scanner
4. Scanner controller
5. Current meters
6. Accelerating voltage power supply
7. Dual-channel recorder
8. Acoustic emission transducer

Figure 28. Dual-channel exoelectron emission measuring system.

the fatigue damage development, crack initiation, and crack propagation relative to the position and movement of the transducer. During the initial portion of the program, the exoelectron emission current was measured at only one side of the specimen, and significant changes in current may have been unobserved on the opposite side of the specimen. The exoelectron emission measuring system was modified to allow both sides of the fatigue specimens to be scanned simultaneously during the fatigue test.

RESULTS AND DISCUSSION

EVALUATION FOR FATIGUE LOCATION

The fatigue failure site of a specimen was located by two methods. The first method, the ten-point quantitative analysis, was used to analyze the series of exoelectron emission curves obtained in a test. The second method was to correlate and evaluate both the exoelectron emission and surface potential difference curves as determined after each fatigue test increment.

Representative exoelectron emission curves used in the first method are reproduced in Figure 29, and were selected from measurement data obtained from the series of curves of the specimen side on which the fatigue crack first emerged. The 2024-T81 specimens H98 and H71 were tested to failure at a stress of 23 and 28 ksi, respectively. Specimen H62, however, was tested at three stress levels of 28, 30 and 34 ksi because it survived after more than one million cycles each at the first two stress levels. Finally it failed at the higher stress of 34 ksi in approximately 1.16×10^5 cycles. Hence only the exoelectron emission curves at the stress of 34 ksi together with the initial curve prior to the test at 28 ksi are shown in Figure 29. Analysis of the data shows that, in a successful detection case, the curve depicting the current change at the failure site is generally located at the upper or lower bounds of the scatter band encompassing similar curves for the other test locations. However, if the curve for the measurement data at the failure site falls within the scatter band, it is impossible to predict the failure site because the current change therein is not markedly different from the changes at other measurement locations. Results of the analysis for the three specimens described in Figure 29 are presented in Figure 30.

It is seen in Figure 30 that the change in exoelectron current can increase as well as decrease but also appears to vary with test condition. Figure 31 shows the current change at the failure site of two 2024-T81 specimens in low-cycle and high-cycle fatigue. The larger and more rapid change in exoelectron current in low-cycle fatigue test could be attributed to heavier damage and faster rate of damage accumulation. The relation of the current change with material having a comparable fatigue life but at different stress levels is illustrated in Figure 32. Though the steel specimen underwent larger change than the aluminum alloy specimen, it should not be construed

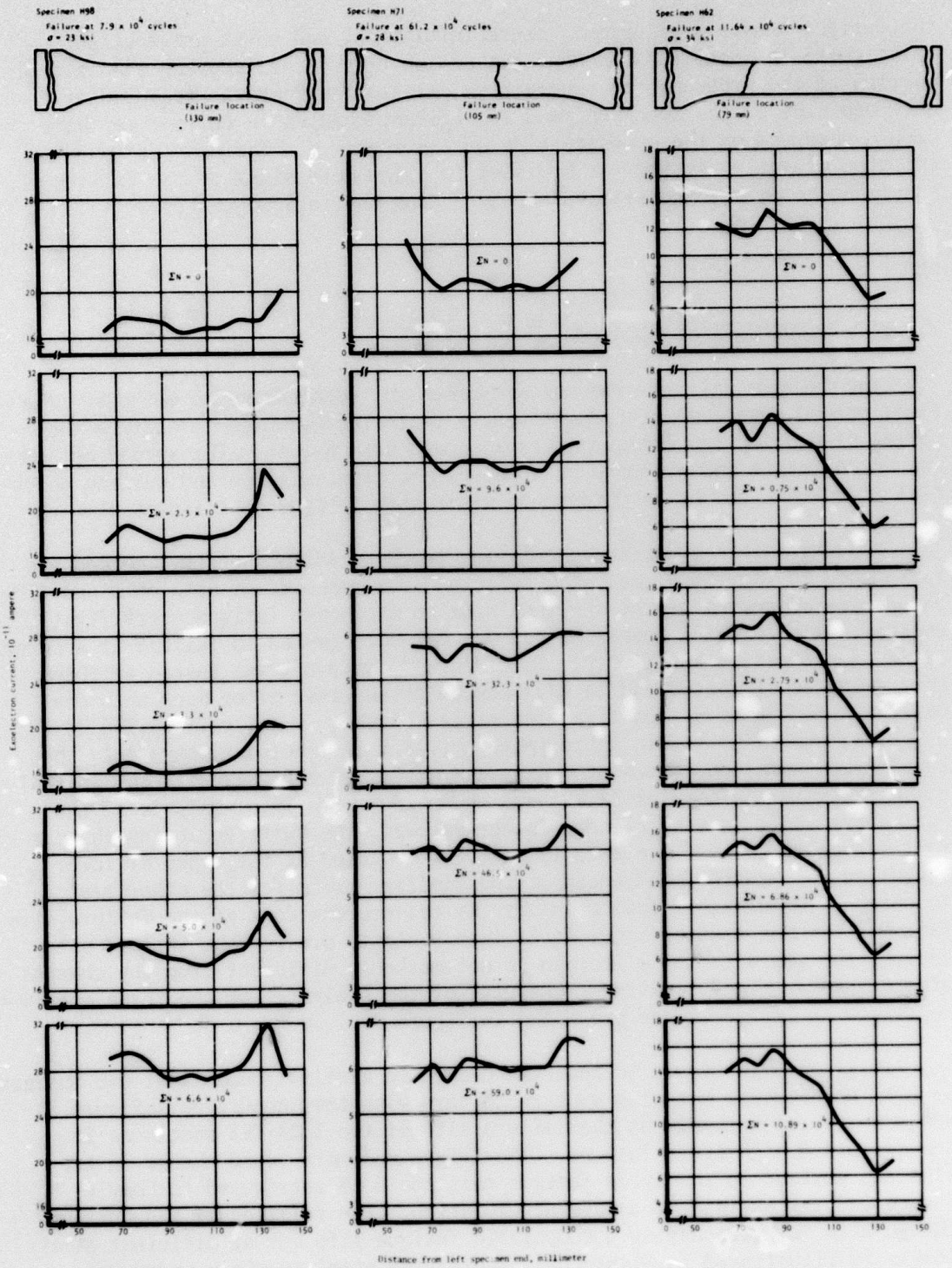

Figure 29. Exoelectron emission curves of 2024-T81 aluminum alloy during fatigue test.

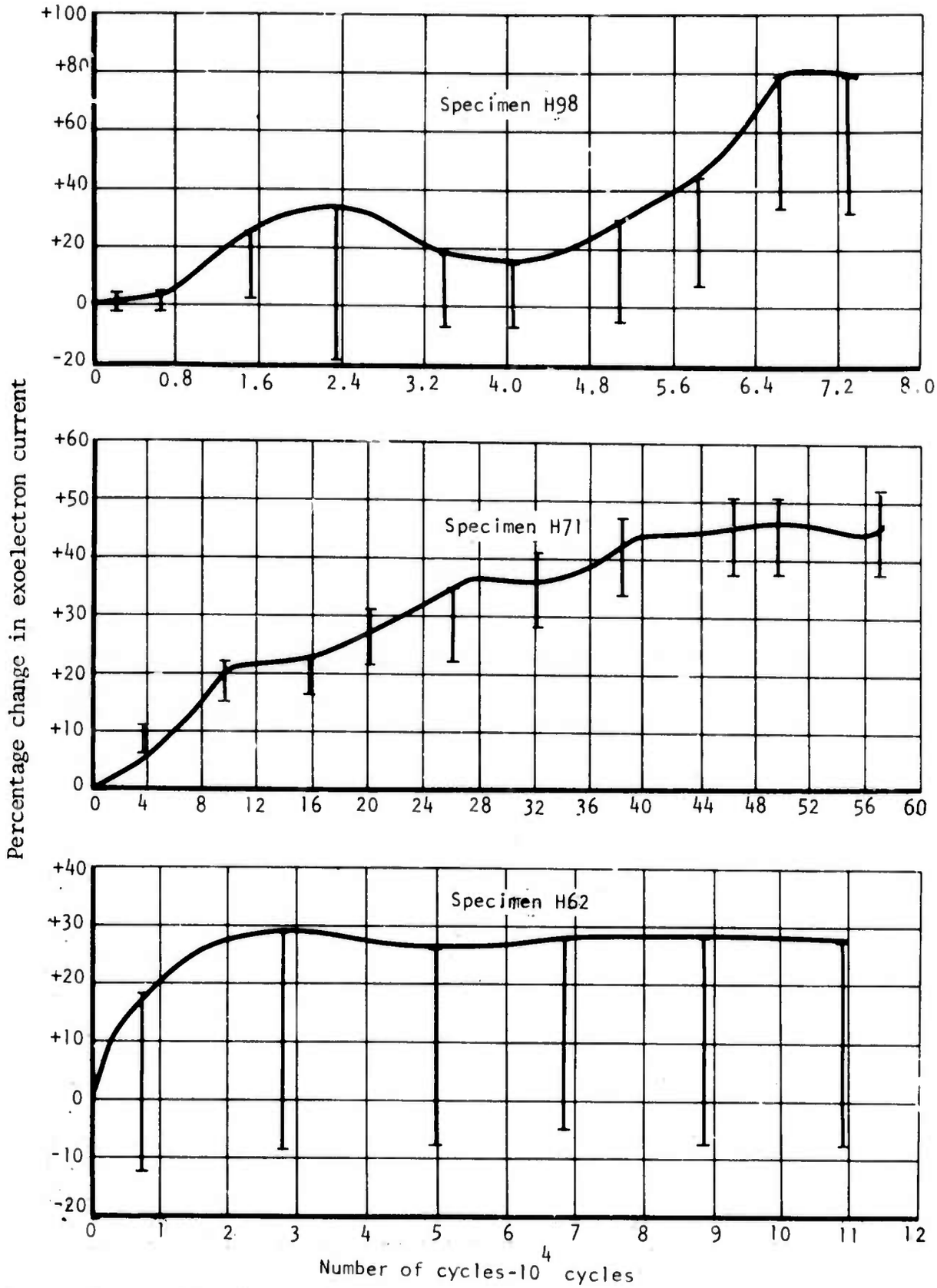

Figure 30. Change in exoelectron current at failure site of 2024-T81 aluminum alloy during fatigue test.

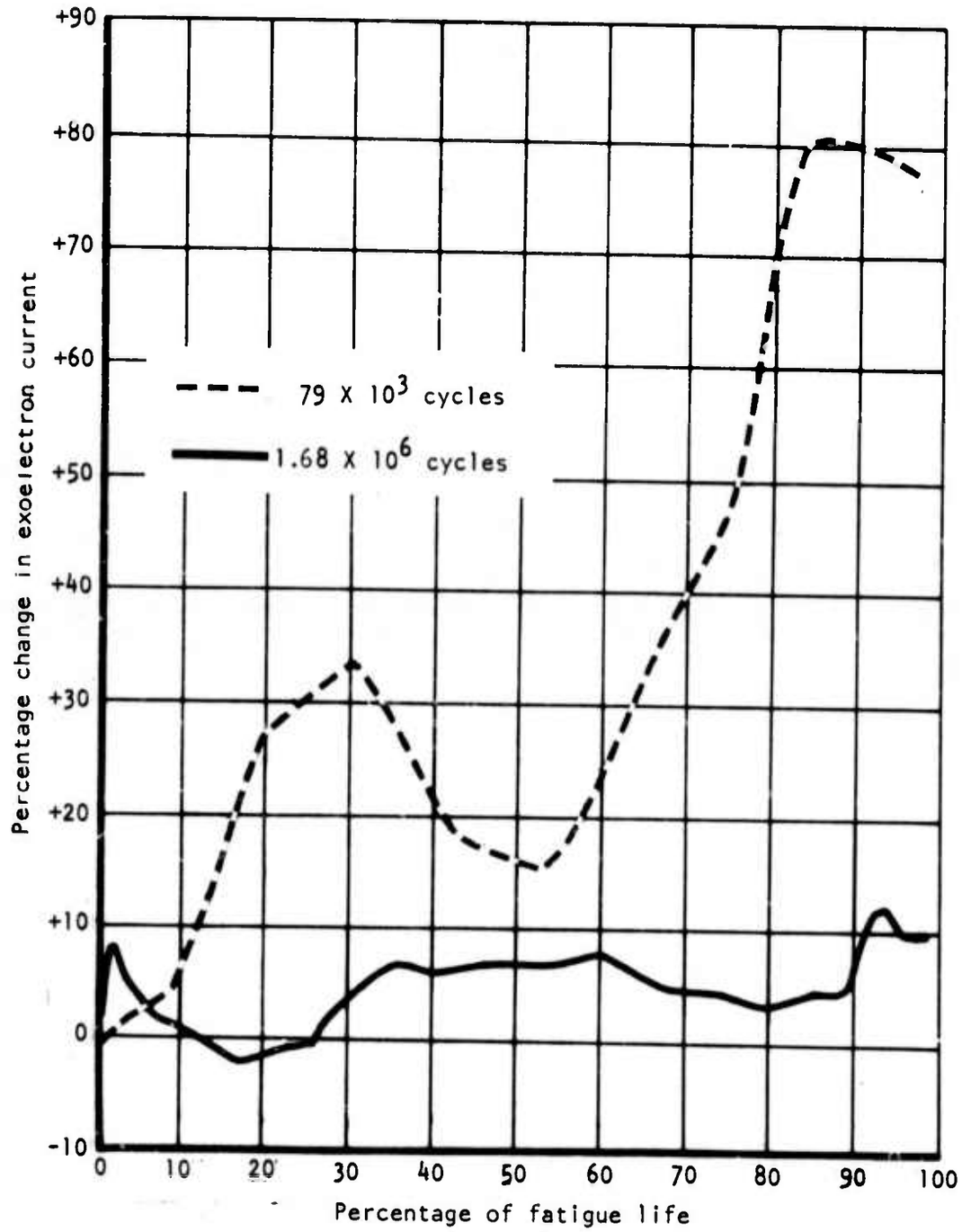

Figure 31. Change in exoelectron current at failure site of 2024-T81 aluminum alloy during low-cycle and high-cycle fatigue tests.

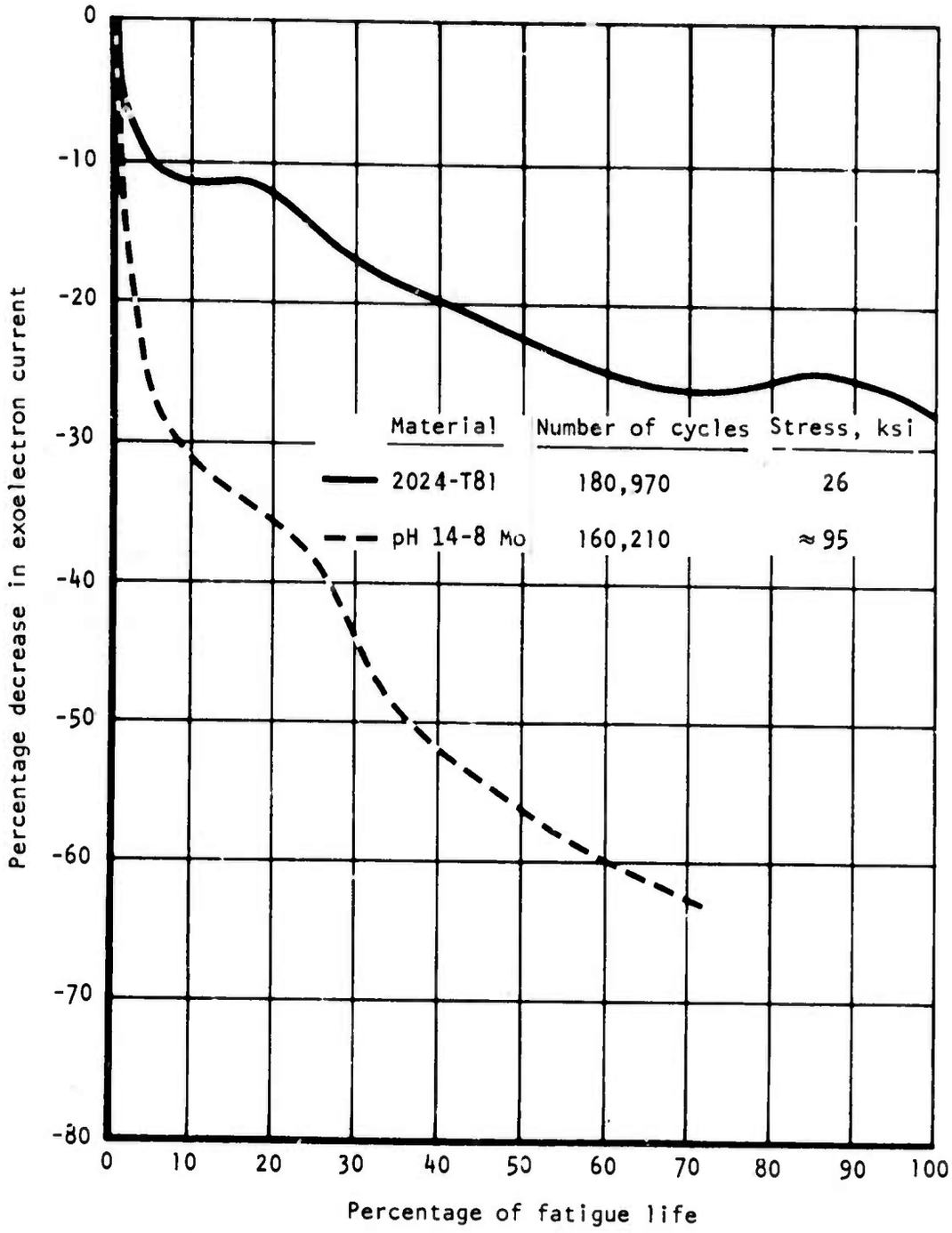

Figure 32. Change in exoelectron current at failure site of 2024-T81 aluminum alloy and SRH-1050 condition PH 14-8 Mo steel during fatigue tests.

that this difference is general. In addition to material, test condition, specimen geometry and surface condition may also influence the exoelectron emission phenomenon of a specimen under fatigue.

The second method was mostly applied to evaluate the specimens belonging to the baseline group. As shown in Table 1, the test conditions for the baseline specimens included low-cycle fatigue, high-cycle fatigue, spectrum loading, and elastic loading conditions. After the completion of each fatigue test increment, the specimen was removed from the machine and nondestructively tested using exoelectron emission and surface potential difference measurement methods. Each side of the specimen was measured at least twice for exoelectron emission and three times for the surface potential difference. The time interval between the end of the fatigue test and the beginning of the nondestructive measurement varied from several hours to several days. This interval appeared to have no effect on the shape of the recorded emission or potential difference curves so long as the specimen surface was protected from mechanical damage or contamination during storage.

Typically, the NDT data recordings display a number of maxima and minima. In most cases, the overall shape of the curve for one side of the specimen was quite similar to that of the other side although the position of some maxima and minima sometimes could not be matched, indicating that the fatigue damage in a given location on one specimen surface might differ from the damage in the same location on the other surface. The general shape of the data curves recorded after additional fatigue cycling remained essentially the same for many specimens, but changed significantly for a limited number of specimens. However, the same method was used to evaluate the accuracy of the measurements in locating the potential failure site on the specimens.

It is shown in Figures 6, 7 and 8 that the exoelectron current increases with cycling and levels off or even decreases toward the end of the fatigue test. The fatigue damage appears then to increase with emission and the emission peak near the end of the test could be an indicator of imminent failure. It has also been shown[1] that in a fatigue test, after an early increase (less than 1 percent of total life), the exoelectron emission from a specimen can decrease steadily and subsequently increase rapidly near the end of the test. This reversal of the slope of an emission curve indicates that fatigue damage has occurred and that this change can be taken as a precursor of impending fracture. The particular location on the specimen where the emission curve shows a maximum or a minimum is, therefore, considered a potential failure site.

It was shown in Figure 20 that the surface potential difference measured on a specimen increases during the fatigue test and decreases rapidly near the end of the test. It has also been shown[1] that for the same increment of fatigue life, the surface potential difference between a fatigued aluminum alloy specimen and a reference electrode decreases with an increase of applied

that this difference is general. In addition to material, test condition, specimen geometry and surface condition may also influence the exoelectron emission phenomenon of a specimen under fatigue.

The second method was mostly applied to evaluate the specimens belonging to the baseline group. As shown in Table 1, the test conditions for the baseline specimens included low-cycle fatigue, high-cycle fatigue, spectrum loading, and elastic loading conditions. After the completion of each fatigue test increment, the specimen was removed from the machine and nondestructively tested using exoelectron emission and surface potential difference measurement methods. Each side of the specimen was measured at least twice for exoelectron emission and three times for the surface potential difference. The time interval between the end of the fatigue test and the beginning of the nondestructive measurement varied from several hours to several days. This interval appeared to have no effect on the shape of the recorded emission or potential difference curves so long as the specimen surface was protected from mechanical damage or contamination during storage.

Typically, the NDT data recordings display a number of maxima and minima. In most cases, the overall shape of the curve for one side of the specimen was quite similar to that of the other side although the position of some maxima and minima sometimes could not be matched, indicating that the fatigue damage in a given location on one specimen surface might differ from the damage in the same location on the other surface. The general shape of the data curves recorded after additional fatigue cycling remained essentially the same for many specimens, but changed significantly for a limited number of specimens. However, the same method was used to evaluate the accuracy of the measurements in locating the potential failure site on the specimens.

It is shown in Figures 6, 7 and 8 that the exoelectron current increases with cycling and levels off or even decreases toward the end of the fatigue test. The fatigue damage appears then to increase with emission and the emission peak near the end of the test could be an indicator of imminent failure. It has also been shown[1] that in a fatigue test, after an early increase (less than 1 percent of total life), the exoelectron emission from a specimen can decrease steadily and subsequently increase rapidly near the end of the test. This reversal of the slope of an emission curve indicates that fatigue damage has occurred and that this change can be taken as a precursor of impending fracture. The particular location on the specimen where the emission curve shows a maximum or a minimum is, therefore, considered a potential failure site.

It was shown in Figure 20 that the surface potential difference measured on a specimen increases during the fatigue test and decreases rapidly near the end of the test. It has also been shown[1] that for the same increment of fatigue life, the surface potential difference between a fatigued aluminum alloy specimen and a reference electrode decreases with an increase of applied

stress. Since fatigue damage should be more severe at the higher applied stress, the decrease in surface potential difference can be associated with an increase in fatigue damage. Therefore, it is predicted that the maxima or minima of a surface potential difference curve recorded after the fatigue test represents a potential failure site.

This method of noting the changes in nondestructive test measurement data curves was employed to evaluate the capability of the NDT methods to detect fatigue damage and to locate potential failure sites on the baseline specimens. Representative exoelectron emission curves for three specimens tested in high-cycle, low-cycle and spectrum loading conditions after two or three interrupted tests are illustrated in Figure 33. The curves depict the change in emission from the side of the specimen where the fatigue crack originated. The corresponding surface potential curves are given in Figure 34. The potential failure sites as indicated by the two nondestructive test methods are marked by dashed lines on the curves. Position of the failure sites is defined as the distance measured from one end of the specimen.

If maxima and minima points of the exoelectron emission curve occur close together, the potential failure site is not denoted by a point on the curve but rather by the interval between these maxima and minima as shown in Figure 33. The surface potential difference measurements were made along the centerline and along the edges of each specimen. The location of the minima at these locations were within ±5 mm. Only the centerline data were reproduced in Figure 34. The potential failure site is again located within an interval even though it was marked as single point in Figure 34. The selected potential failure sites for all of the specimens in the baseline group are listed in Tables 3 and 4 for 2024-T81 alloy and annealed Ti-6Al-4V alloy, respectively.

At the completion of the nondestructive measurements the specimen was fatigued to failure. The location of the failure site was based upon the measurements from the specimen end which had been referenced in the exoelectron emission and surface potential difference measurements. The actual failure sites are also listed in Figures 33 and 34 as well as in Tables 3 and 4.

During the data analysis, any marked change appearing in the curves for the same specimen was considered as a potential failure site. As indicated in Tables 3 and 4, there can be a number of potential failure sites. Since there were two or more potential sites located by both the exoelectron emission and surface potential difference measurements, the probability of predicting the final failure site by either method can at most be only 50 percent. In the early stage, several potential failure sites may be identified without any becoming the actual site. New potential sites can develop later, and the damage at one of the new sites may grow faster than the rest, to become the final failure site. This shift of fatigue damage and failure site is evidenced

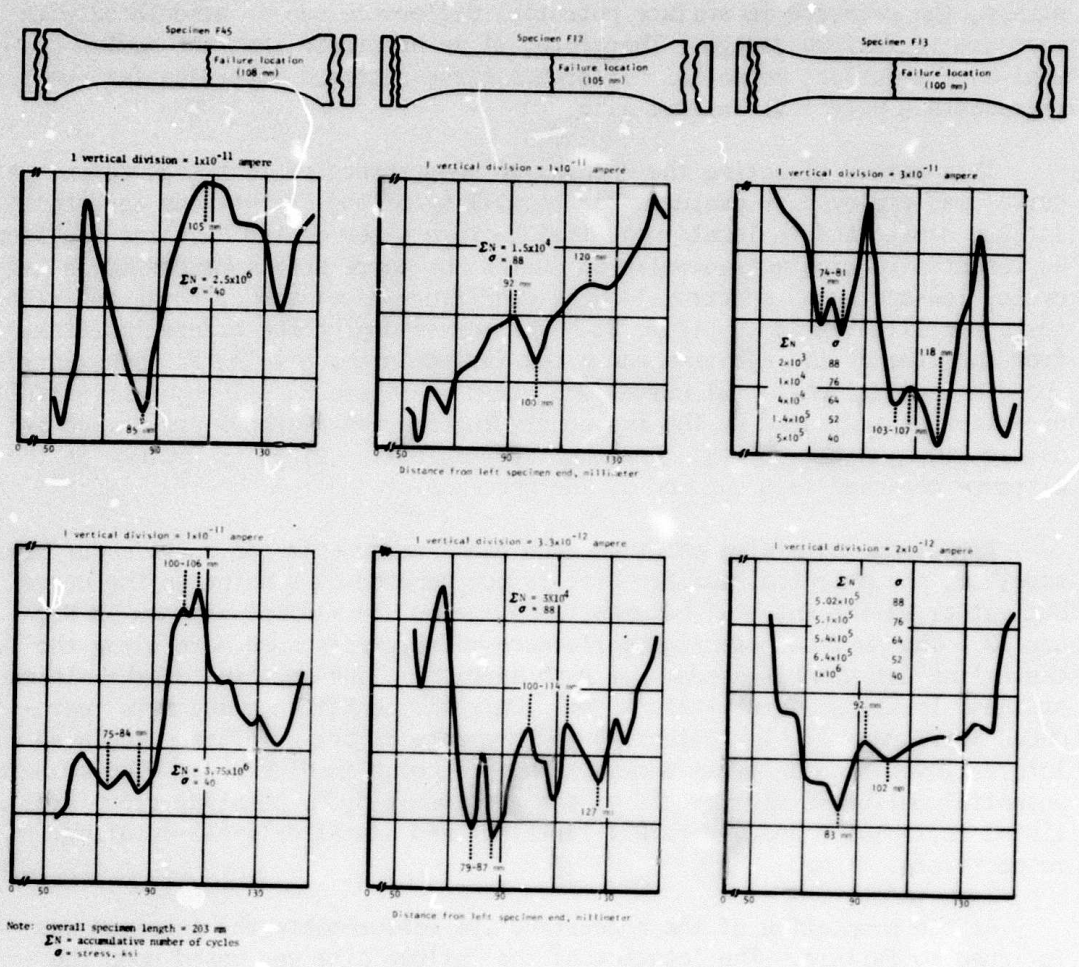

Figure 33. Exoelectron emission curves of annealed Ti-6Al-4V specimens after two or three fatigue tests.

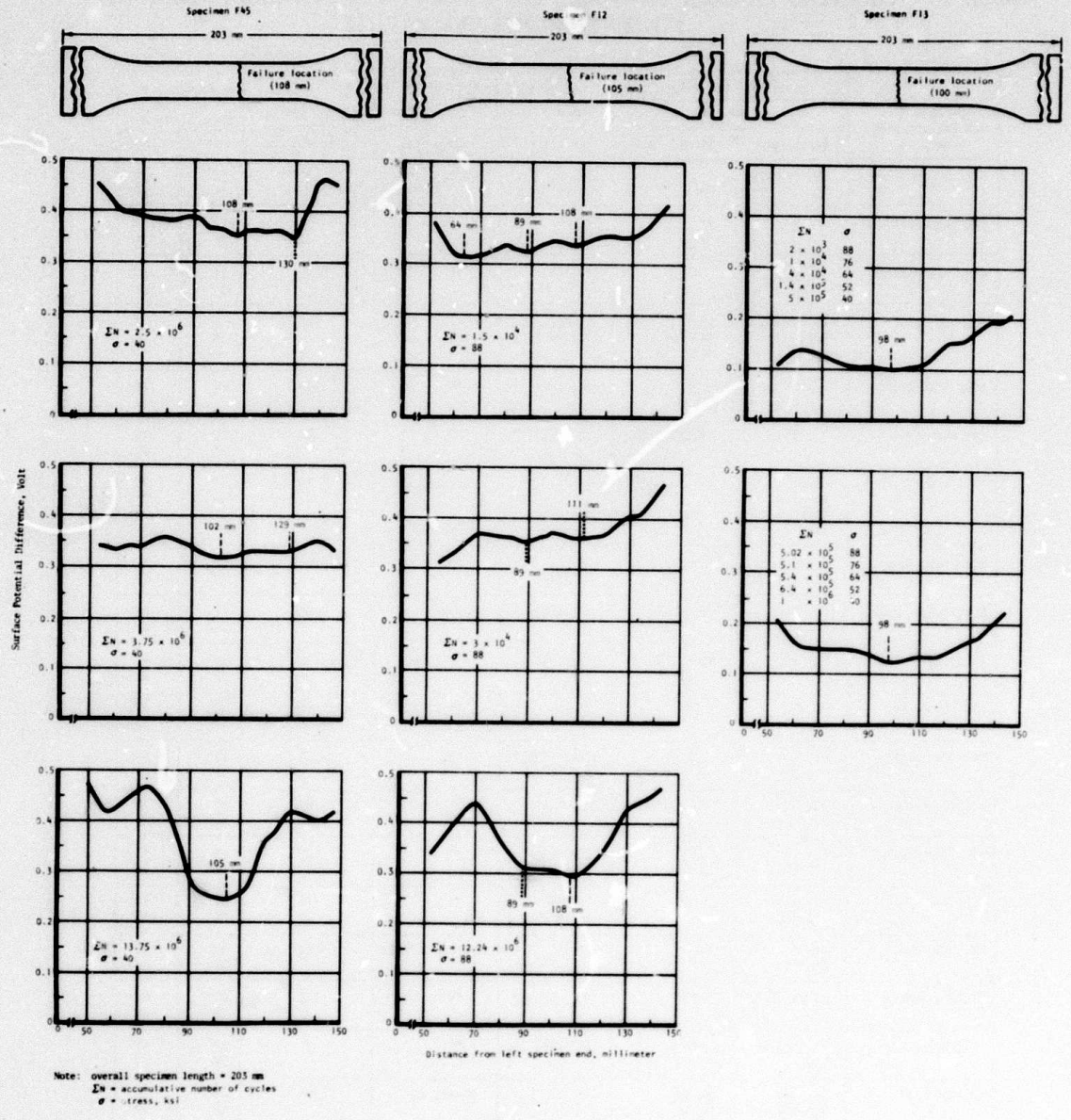

Note: overall specimen length = 203 mm
ΣN = accumulative number of cycles
σ = stress, ksi

Figure 34. Surface potential difference curves of annealed Ti-6Al-4V specimens after two or three fatigue tests.

TABLE 3. LOCATING FATIGUE FAILURE SITE IN 2024-T81 ALUMINUM ALLOY BY NONDESTRUCTIVE EVALUATION

Specimen No. and Fatigue Test Condition	Potential Failure Site, mm From Specimen (203 mm Length) End				Actual Failure Site, mm from Specimen End	Prediction Accuracy (True or False)	
	Exoelectron Emission		Surface Potential Difference				
	First Test	Second Test	First Test	Second Test		EEE*	SPD*
A27; high-cycle	75, 90, 120	74, 86, 98-104	64-66, 90-95	94-96	72	1T 4F	0T 2F
D1; high-cycle	**	83, 113	94	86	76	0T 2F	0T 2F
C14, high-cycle	68-70, 119-123	**	80,104	**	70	1T 1F	0T 2F
B6; high-cycle	78, 90-94, 120	84-90, 112-116, 122, 133	60-65, 93-104	65-75, 93-104	132	1T 5F	0T 3F
A10; high-cycle	**	**	80, 110	**	133	**	0T 2F
C6; high-cycle	**	78, 97, 128	89, 99, 117	95	130	1T 2F	0T 4F
D21; high-cycle	73-77, 80-83, 110-115, 128	75, 100-108	111	106, 116	72	1T 4F	0T 3F
D3; high-cycle	74-79, 93-95, 103	**	77-85, 97-102	**	92	1T 2F	1T 1F
C-10; high-cycle	**	77, 83-90	101-106, 131	85, 91	76	1T 1F	0T 4F
A22; low-cycle	71, 83, 124	86-89, 122	79-81, 98, 123	71, 95-100	108	0T 4F	0T 5F
A7; low-cycle	80	**	77	**	68	0T 1F	0T 1F
A5; low-cycle	91, 124	**	100, 120-122	**	128	1T 1F	0T 2F
B3; low-cycle	78, 92, 121	78, 86, 125	64, 106	96-101	66	0T 5F	1T 2F
A29; low-cycle	84, 106, 112-118	**	104-106, 124-130	**	120	1T 2F	1T 1F
B10; low-cycle	81, 95-98, 105, 127	**	104-107, 127-130	**	130	1T 3F	1T 1F
C18; low-cycle	74-78, 91-103	82, 97, 109-113	90-95	90-95, 130	83	1T 3F	0T 2F
D11; low-cycle	82-86, 122, 129	**	93, 118-123	**	130	1T 2F	0T 2F
D17; low-cycle	78-83, 96, 112	**	103-106, 126	**	81	1T 2F	0T 2F
A3; low-high	76, 84, 100-108, 120-124	84-96, 92-95, 114-117	73, 89	80-83, 90	130	0T 6F	0T 2F
A26; low-high	94-100, 110-114, 122	78-83, 101-108	63, 83, 105	60, 83-95, 130	79	1T 4F	1T 3F
B-24; low-high	74-77, 105, 120	**	86	**	73	1T 2F	0T 1F

TABLE 3. LOCATING FATIGUE FAILURE SITE IN 2024-T81 ALUMINUM ALLOY BY NONDESTRUCTIVE EVALUATION (CONCL)

Specimen No. and Fatigue Test Condition	Potential Failure Site, mm From Specimen (203 mm Length) End				Actual Failure Site, mm from Specimen End	Prediction Accuracy (True or False)	
	Exoelectron Emission		Surface Potential Difference				
	First Test	Second Test	First Test	Second Test		EEE*	SPD*
B28; high-low	80-84, 97-102	90-94, 100-104, 129-132	73-76, 122-130	84, 130-137	133	1T 3F	1T 2F
D7; low-high-low	80-83, 99-103 118-124	**	71-79, 85-101	**	67	0T 3F	1T 1F
E3; elastic	78, 104, 120-124	73-80, 90-96, 108-110	65, 79-95	79-95, 116	76	1T 4F	1T 2F
E4; elastic	72-78, 86, 96-103	78-80, 88-90 100-110	76, 92	69, 95-105	73	1T 4F	1T 2F
B7; plastic deformation	89, 100-108, 118-122	73-76, 105-111, 122-128	64-67, 89-98	59-67, 90-102, 133-137	132	1T 4F	1T 3F
E20; plastic deformation	86-94, 98-114, 120	**	83-95, 114-121	**	122	1T 2F	1T 1F
A4;*** plastic deformation	79, 91, 96-110, 124	80-90, 102-105, 124	73-79, 95-98, 121-127	75-79, 98-105	70	0T 3F	1T 3F
B12,*** plastic deformation	98, 126	71-75, 96-98, 124-127	67, 108-121	102 .	117	0T 2F	1T 2F

*EEE = Exoelectron emission
SPD = Surface potential difference
**No test was conducted due to unavailability of nondestructive test equipment.
***The specimen is 2024-T3 alloy.

TABLE 4. LOCATING FATIGUE FAILURE SITE IN ANNEALED Ti-6Al-4V ALLOY BY NONDESTRUCTIVE EVALUATION

Specimen No. and Fatigue Test Condition	Potential Failure Site, mm From Specimen (203 mm Length) End					Actual Failure Site, mm From Specimen End	Prediction Accuracy (True or False)	
	Exoelectron Emission		Surface Potential Difference					
	First Test	Second Test	First Test	Second Test	Third Test		EEE[a]	SPD[a]
F14; high-cycle	80-85, 110, 127	76, 98-104, 120-124	70-79 98-102	81-89, 108-114	**	78	1T 4F	1T 2F
F-15; high-cycle	90, 97-102 110-115	92, 102-108, 126	67, 95-108	62, 105-111	86, 92, 108-114	114	0T 4F	1T 4F
F-20; high-cycle	80-86, 95, 115-119	82-86, 96-100, 110-114, 122	64, 79-89, 124-127	81-86, 105	83-89, 95-106	114	1T 4F	0T 4F
F45; high-cycle	85, 105	75-84, 100-106	95-108, 121-130	70, 98-102, 114, 129	92-95, 105-111	108	1T 2F	1T 5F
F61; high-cycle	74-80, 106-110	84-89, 104-108, 120	73-86, 105	76-84, 121	67-70, 86-89, 114-117	73	1T 3F	1T 4F
F62; high-cycle	80-86, 103, 110-133	76-79, 93-97	60-76, 111-124	64-67, 83-95 105-121	62, 83-92, 102	79	1T 3F	1T 4F
F3; low-cycle	93-97, 110-115	82-89, 92-95, 112-118	90, 121	95, 127	62, 67, 98-102	71	0T 3F	1T 6F
F12; low-cycle	92, 100, 120	79-87, 86-89, 100-124, 127	64-67, 83-89, 108-114	89, 111-117	86-89, 108-116	105	1T 4F	1T 2F
F22; low-cycle	80-84, 90-95, 107	90-96, 108	62, 79-83, 108-121	86, 95-102, 120	**	105	1T 2F	1T 4F
F23; low-cycle	90, 100-105, 126-130	88, 101-106, 122	64, 83-86, 95-98	70, 76-79, 102-108	**	129	1T 4F	0T 6F
F40; low-cycle	90-93, 105, 120-127	70-73, 94-98, 101-105	90, 111-114	114-121	**	94	1T 2F	1T 2F
F47; low-cycle	80-84, 120	75-80, 90-95, 101-103, 124-127	89-95, 114	98-105	**	124	1T 4F	0T 3F
F2; low-high	94, 104	105-111	64-70, 95-102	64-73, 89-95, 108	**	71	0T 3F	1T 3F

TABLE 4. LOCATING FATIGUE FAILURE SITE IN ANNEALED Ti-6Al-4V ALLOY BY NONDESTRUCTIVE EVALUATION (CONCL)

Specimen No. and Fatigue Test Condition	Potential Failure Site, mm From Specimen (203 mm Length) End					Actual Failure Site, mm From Specimen End	Prediction Accuracy (True or False)	
	Exoelectron Emission		Surface Potential Difference				EEE*	SPD*
	First Test	Second Test	First Test	Second Test	Third Test			
F6; low-high	72-84, 92	80, 96-100, 110-116	73-76, 98	76-81, 95-98	**	89	1T 3F	0T 3F
F13; high-low	74-81, 92, 103-107, 118	83, 92, 102	98-105	98-105	**	100	1T 3F	1T 0F
F21; high-low	88-92, 105, 124-127	85-88, 105-108	92-105	64, 95-105	**	127	1T 3F	0T 2F
F49; low-high-low	80-86, 90-98, 107-112	73-79, 84-88, 108-111	63, 95-98, 111	67-75 114-121	**	86	1T 3F	0T 5F
F55; low-high-low	84-86, 105-108, 116-119	102-105, 116-120	70, 95-102	70-76, 98-102	**	76	0T 3F	1T 2F

*EEE = Exoelectron emission
SPD = Surface potential difference
**No third test was conducted because the specimen failed in fatigue test.

in the test data obtained after the first fatigue test and has also been reported in the literature.[47]

The capability of NDT methods to accurately predict the final failure site was analyzed. An accurate prediction is judged to have occurred when the predicted and actual failure sites occur within ±5 mm. This range was chosen to allow for the errors introduced in matching the emission and potential difference curves with the test section of the specimen. The prediction results are summarized in the last column in Tables 3 and 4. It is shown that of the 25 aluminum alloy specimens belonging to the baseline group in Table 3, the exoelectron emission and surface potential difference measurements accurately predicted 18 and 9 failure sites, respectively. It is noted that the two specimens E3 and E4 were first subjected to elastic loading at 11 ksi for 2.5×10^6 cycles before they were tested at a higher stress of 38 ksi. Elastic loading is not expected to cause significant damage. However, according to the adopted rating system, the failure site of specimen E3 was located after the first test. Since the failure site is close to the end of the straight test section where change of the cross section takes place, undercutting in machining the specimen could have caused stress concentrating and, hence, leave deformation in that area. The fatigue damage incurred there by elastic loading might be severe enough to be detected. Similarly, this could also have happened in specimens C6, C10, and D1, which survived fatigue tests after 4×10^7 cycles at a stress of 22 ksi. Although they eventually failed at a higher stress of 38 ksi, the failure sites were located by either one of the two NDT methods before this additional test.

The tabulation of the indications listed in Table 4 shows 14 and 12 true indications by exoelectron emission and surface potential difference measurements, respectively, on the 18 annealed Ti-6Al-6V specimens. A statistical analysis of the data for the baseline group specimens showed that at a 95 percent confidence level, the probability of accurately predicting the fracture site in the 2024-T81 aluminum alloy specimens by exoelectron emission and surface potential difference measurements is from 0.52 to 0.91 and 0.17 to 0.57, respectively. A statistical analysis of the test data for the annealed Ti-6Al-4V specimens at a 95 percent confidence level gives a probability factor of from 0.52 to 0.94 for exoelectron emission measurement and from 0.40 to 0.87 for the surface potential difference measurement. Hence, neither the exoelectron emission nor surface potential method alone appears to be sufficient; rather, both should be applied, with one complementing the other. Also, measurements should be made several times in the fatigue process because the location of the final failure site can shift as the severity of fatigue damage accumulates at a number of locations on the specimen. These two methods show a good potential developing into a new technique for detecting fatigue damage as well as predicting the location at which fatigue failures eventually take place.

---

47 Baxter, 1972

FATIGUE LOCATION IN SIMULATED STRUCTURES

Specimens Containing Discontinuities

Discontinuities in the form of slots and holes were introduced in the specimens to act as stress raisers to localize fatigue damage. A 7075-T6 aluminum alloy specimen was tested with a slot 0.71 mm (0.028 inch) wide and 0.3 mm (0.012 inch) deep cut across the specimen width. The specimen was scanned for exoelectron emission and fatigue tested at a net maximum stress of 12.5 ksi. The scanning was continuous during cycling until specimen failure. The results are graphically illustrated in Figure 35. The lowest trace represents the exoelectron current before the test. Some electron emission from the slot is evident. As the cycling began, the current level increased slightly and the area of high emission broadened as fatigue damage increased near the slot. This process continued until specimen failure with a burst of exoelectron just prior to failure.

The data suggest that the exoelectron emission can be used to observe the buildup of damage at a discontinuity (slot) during fatigue loading. The fact that this particular specimen had several other surface defects and a deposit of salt from an earlier cleaning process did not preclude the use of exoelectron emission for the detection of fatigue damage. It was noted that the other surface defects and the salt deposit area produced an appreciable amount of exoelectron emission before the test. This emission may obscure the normal rise in emission that occurs along the specimen length during the early fatigue process; however, it should not interfere with detection of the emission from the slot or the presence of an increase of fatigue damage near the slot.

A clean, slotted 7075-T6 specimen was tested at a lower maximum net stress of 6.28 ksi. The emission current at the slot again increased continuously in the test, but the gradual broadening of this emission current was not observed. The current along the specimen length was approximately of the same magnitude as before and was below the current level at the slot. The variation of the current level at the slot and along the specimen length again increased as the fatigue cycling progressed as shown in Figure 36.

Specimens of different materials containing three slots 0.76 mm (0.03 inch) wide and 0.3 mm (0.012 inch) deep with 15.9 mm (5/8 inch) center-to-center distance were also scanned with the exoelectron emission system during fatigue. The exoelectron current of a 2024-T81 specimen remained practically constant until the transducer was directly opposite the slot and then increased rapidly. The peak current at each slot differed, but the slot which displayed the largest increase in current proved to be the final failure site. Figure 37 presents the emission data for a slotted 2024-T81 specimen which failed at 37,045 cycles at a maximum load of 250 pounds.

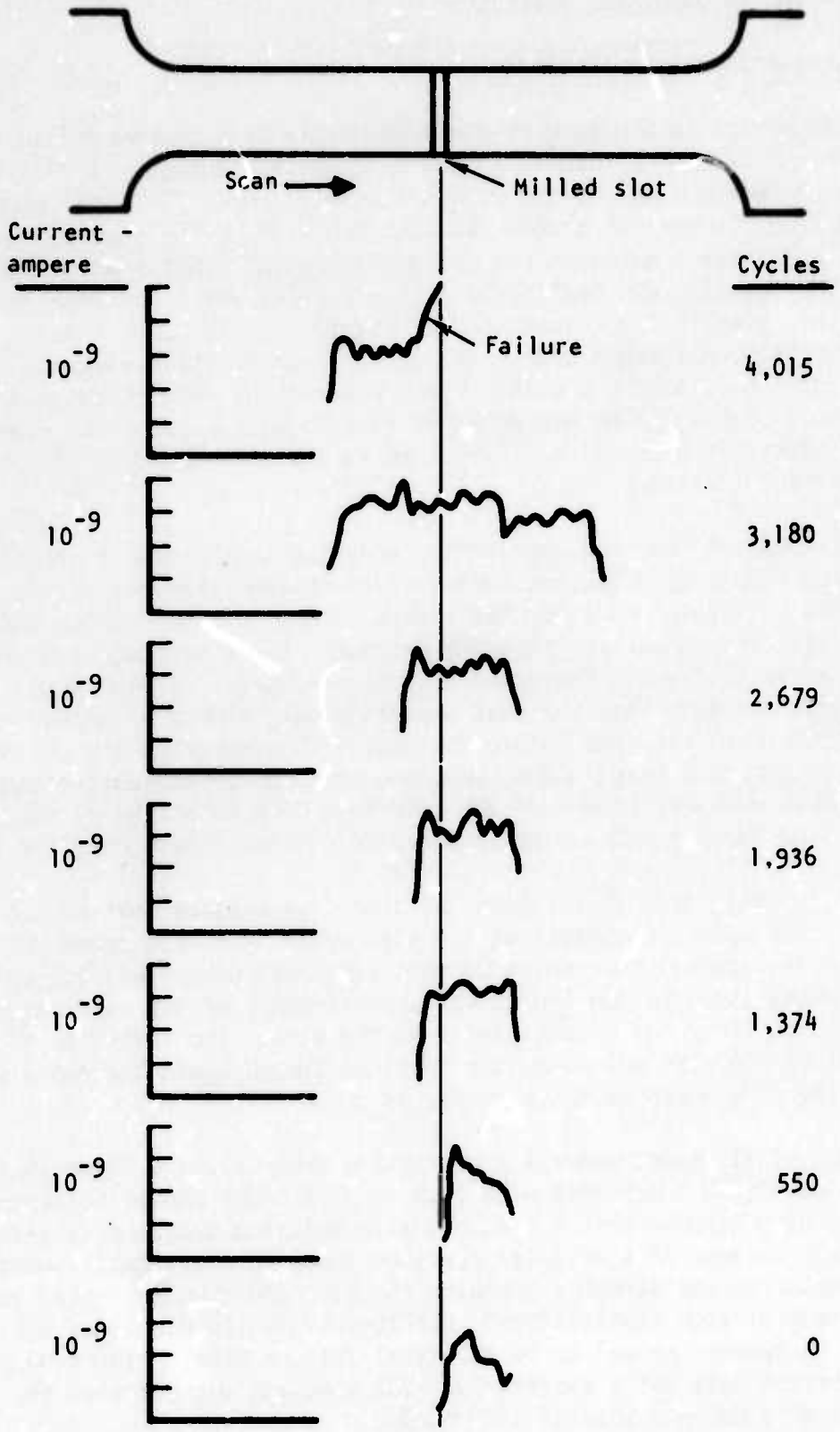

Figure 35. Changes in exoelectron emission current along length of a slotted 7075-T6 aluminum alloy specimen during fatigue.

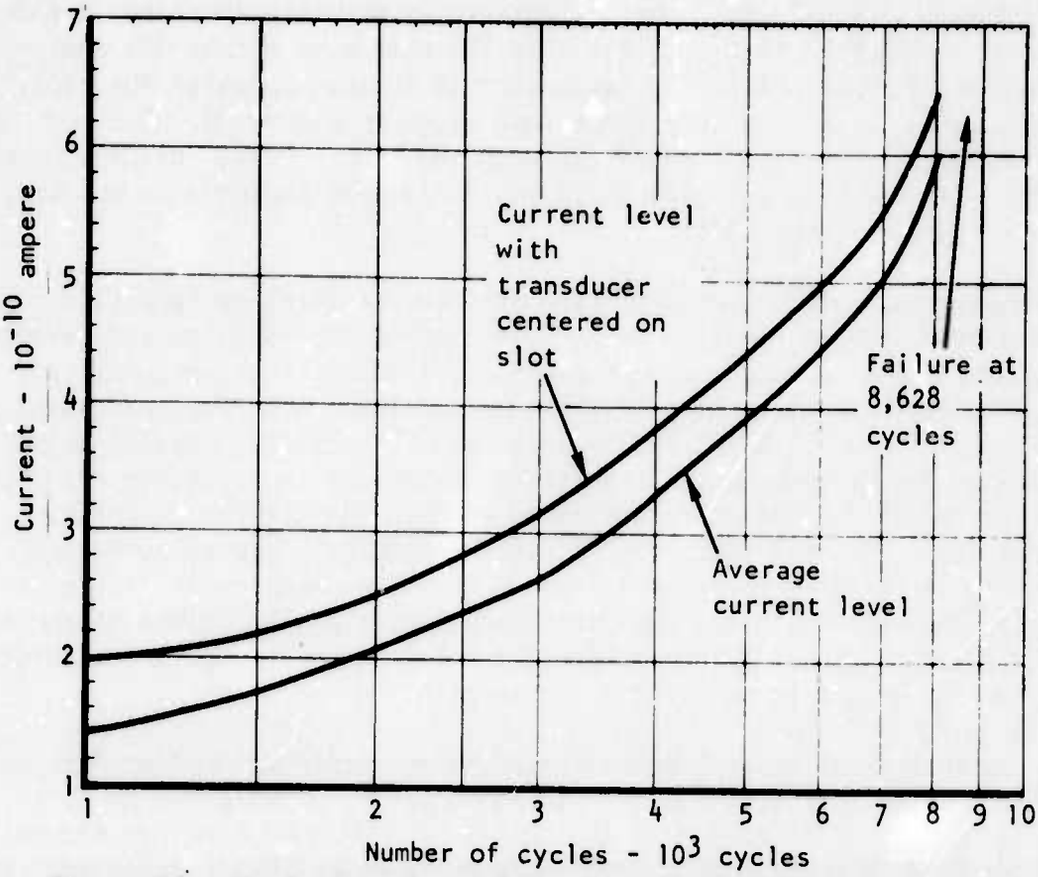

Figure 36. Variation of exoelectron emission current for a clean slotted 7075-T6 aluminum alloy specimen with fatigue.

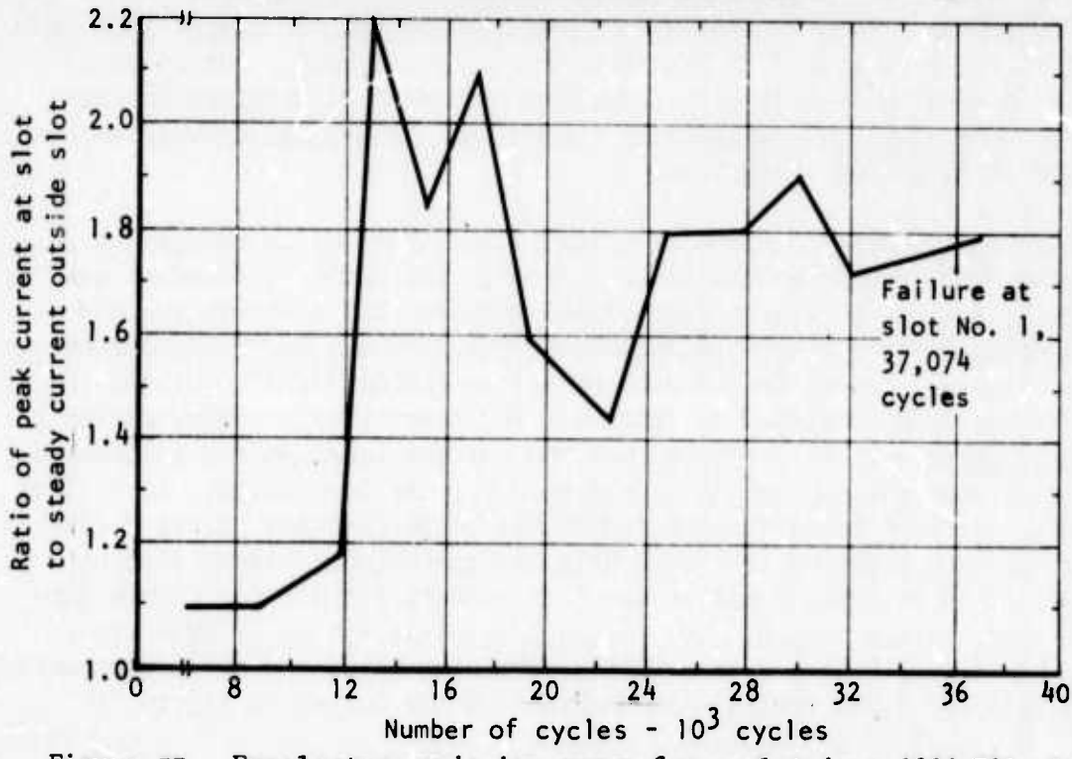

Figure 37. Exoelectron emission curve for a slot in a 2024-T81 aluminum alloy specimen under fatigue in air at 250 pounds.

The change in exoelectron current pattern in scanning annealed Ti-6Al-4V specimens is similar to that from the 2024-T81 specimens except for changes in the background current before the transducer is located opposite the slot. The typical emission curves for three slots are given in Figure 38. The peak current at each slot rises first and falls with the time. Final failure, however, still occurs at the slot at which there is the largest increase in current, such as slot No. 3 in Figure 38.

An experiment was conducted to find whether the final failure site could be located after partial fatigue using both exoelectron emission and surface potential difference measurements on eight slotted 2024-T81 specimens (B23, C9, D28, E2, X11, S12, X13, and X14). These specimens were fatigue cycled for either 1.25×10^6 or 2.5×10^6 cycles at 8 ksi. A technique similar to the one developed for evaluating the standard specimens of the baseline group was employed to locate failure site, which was checked against the actual site determined after a second test at 13 ksi. The results, however, were poor. Since the nondestructive measurements were made after high-cycle fatigue at a low stress level of 8 ksi, and despite stress concentrating effect of the slot, the fatigue damage at the three slots might not be great enough to be detected. Further work is needed to verify this assumption.

The capability of exoelectron emission measurements to measure fatigue damage in specimens containing holes was evaluated. A single 7.8 mm (5/16 inch) diameter hole was drilled at the center of a 7075-T6 specimen and was tested at a load of 1,000 pounds. The hole was scanned continuously for exoelectron emission during the test and was monitored with a microscope at a magnification of 50X. A network of cracks inside the hole was observed at the elapse of 20 cycles. Simultaneously, a surge of exoelectron current followed by a rapid decrease was noted on the recording graph. Similar surges and decreases were observed repeatedly as cycling proceeded to specimen failure (Figure 39). The surges of exoelectron current are thus qualitatively related to the crack formation and extension.

In order to see how the emission around a number of holes changes, a 2024-T81 specimen containing four holes 3.2 mm (0.125 inch) in diameter was scanned during fatigue test at a load of 800 pounds. The test was stopped without specimen failure after 3,000 cycles. The specimen was taken out of the test machine and stored in the ambient air condition for 10 days and the fatigue test was then continued to failure. Representative emission curves are shown in Figure 40. It is shown that the current level at the initiation of the fatigue test was approximately the same for the four holes. As cycling proceeded the emission level for the individual holes changed. After 2,000 cycles the emission level at the No. 3 hole was appreciably higher than at other holes. This relative emission level characteristic did not change during the ten-day storage period. The emission level at the No. 3 hole continued to be significantly higher than at the remaining holes and failure occurred there at a total of 8,980 cycles. An analysis of the curves in Figure 40

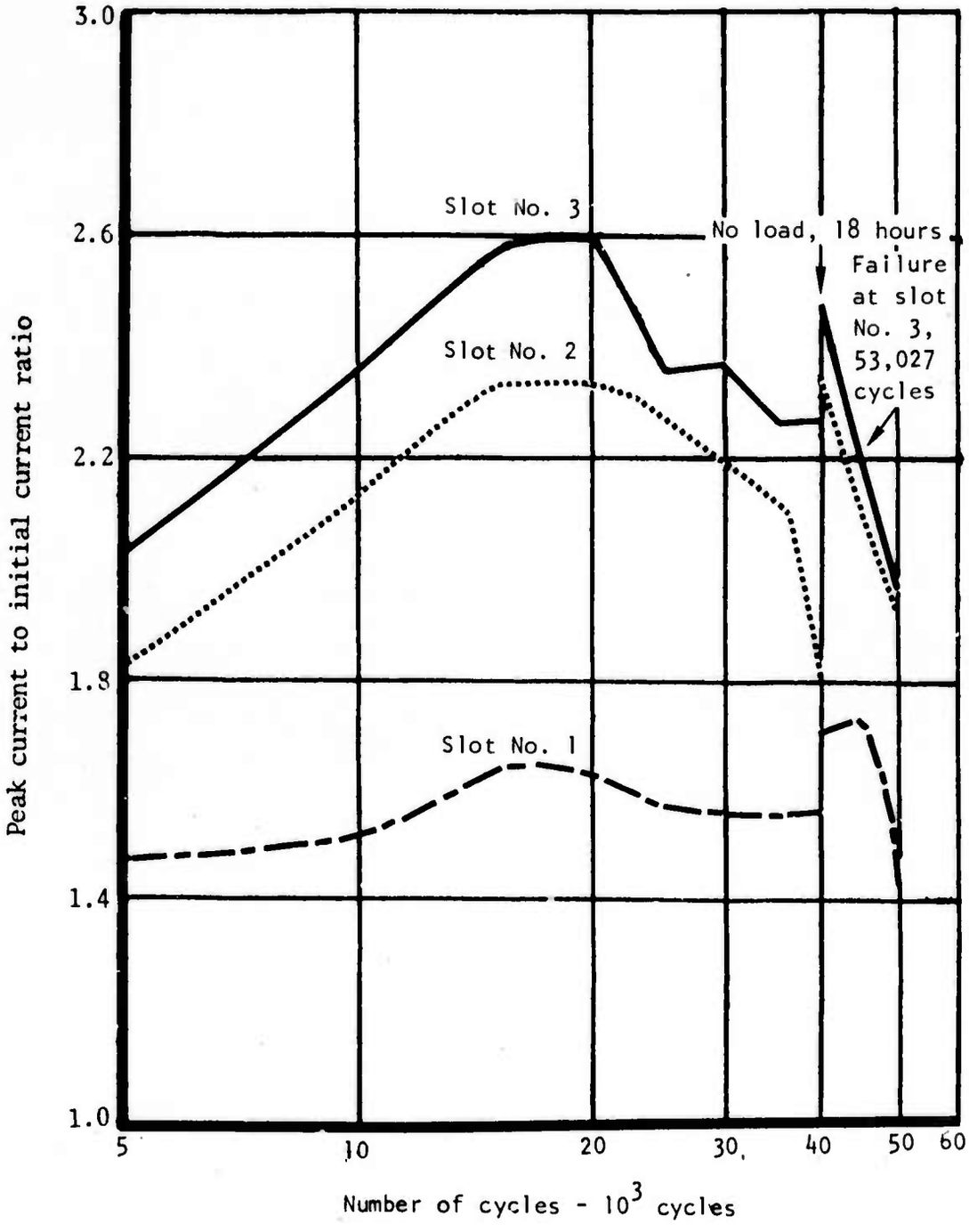

Figure 38. Exoelectron emission curves for three slots in a Ti-6Al-4V specimen under fatigue at 350 pounds.

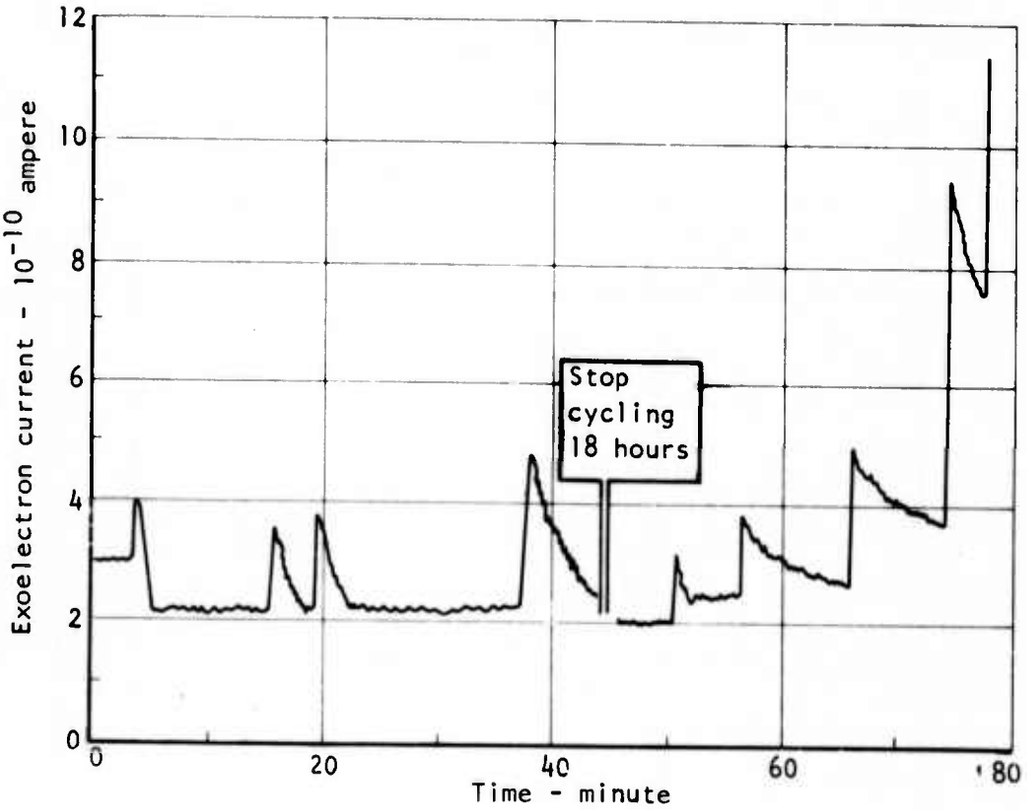

Figure 39. Change in exoelectron current during fatigue of a 7075-T6 aluminum alloy specimen containing one hole.

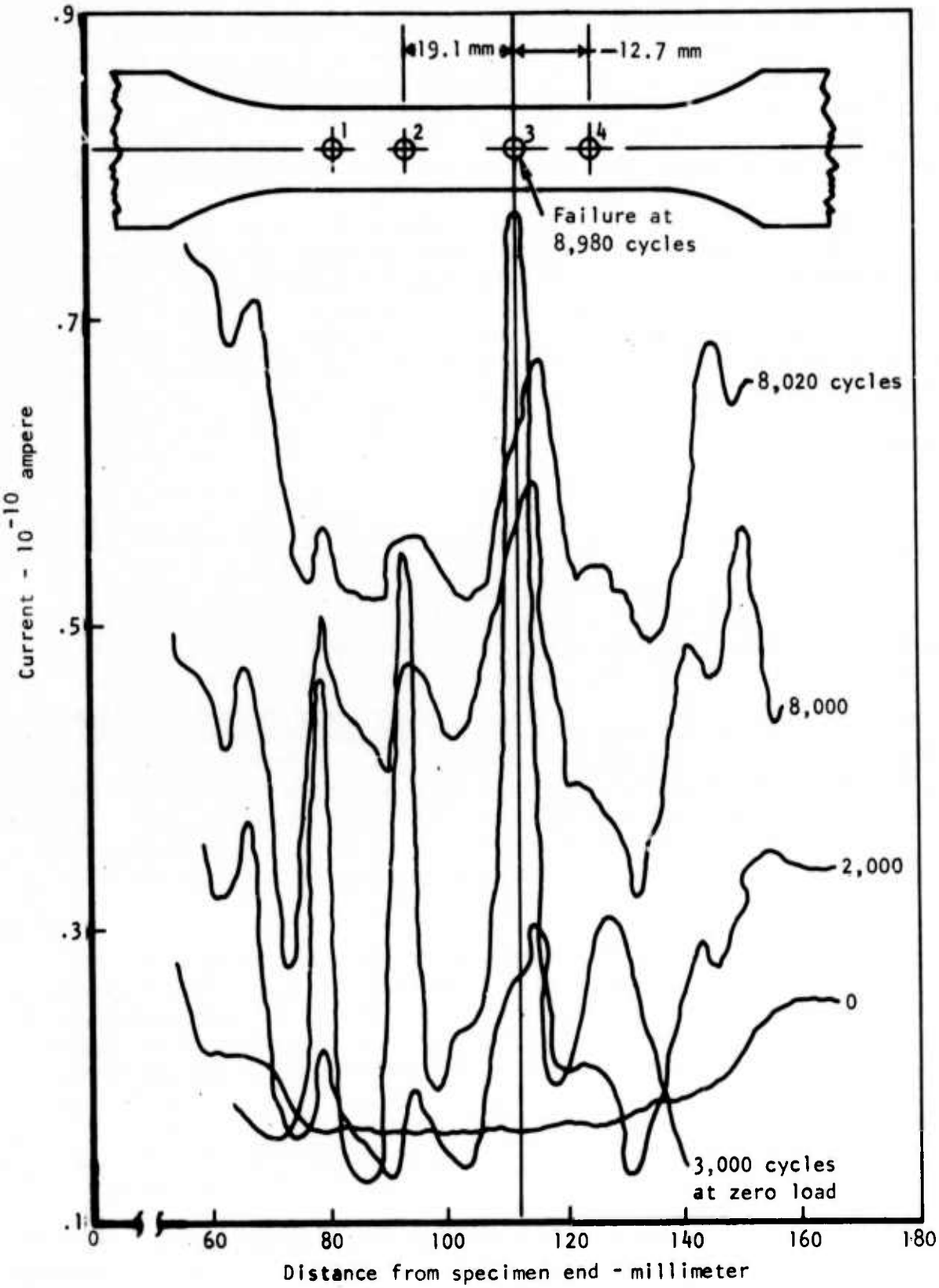

Figure 40. Exoelectron emission curves during fatigue test of a 2024-T81 aluminum alloy specimen containing four holes.

shows that the largest change in exoelectron current occurred at the No. 3 hole in the first test and shifted to the No. 2 hole in the second test, when the current change was based on the emission curve at 3,000 cycles under zero load. Thus it appears that the initial fatigue damage was highest at the No. 3 hole. As fatigue cycling continues, the fatigue damage at the No. 2 hole also increases but is apparently not as great as that at the No. 3 hole.

Another test on a 7075-T6 specimen containing four holes exhibited similar results. The initial emission level shown in Figure 41 was uniform. Before reaching 50 percent of the fatigue life the emission level at the No. 3 and No. 4 holes began to increase. This is illustrated in the next curve where the emission level at the No. 3 hole exhibited the greatest increase. The current on the subsequent record exceeded the range of the measuring meter. Failure subsequently occurred at No. 3 hole. Figure 41 shows that both the No. 3 and No. 4 holes exhibited relatively high emission levels as well as large changes in exoelectron emission levels as compared with the emission levels from the No. 1 and No. 2 holes.

A series of 2219-T851 aluminum specimens containing 12.7 mm (1/2 inch) diameter holes were evaluated to determine the ability of several NDT methods to detect fatigue damage and cracking inside the holes. The test specimen had a 12.7 by 50.8 mm (1/2 by 2 inch) constant section approximately 22.8 cm (9 inches) long and 48.2 cm (19 inches) overall length. A 12.7 mm (1/2 inch) diameter hole was located in the center of the specimen with two 2.54 mm (0.1 inch) diameter side notches to provide a stress concentration site for fatigue evaluation (Figure 42). The fatigue tests were performed at constant amplitude with a stress factor of 0.05 at 3 Hz cycling rate. The fatigue test was interrupted at intervals to permit static load and no-load NDT measurements. Fracture was characterized by crack initiation at the inner surface of 2.54 mm (0.1 inch) diameter notches, propagation along the 12.7 mm (1/2 inch) specimen thickness, and subsequent emergence on the specimen surface.

The NDT methods included in the evaluation were acoustic emission, dye penetrant, exoelectron emission, visual inspection including a 10X borescope, eddy current, air gaging, and compliance gaging. The latter four techniques could be applied only to the 12.7 mm (1/2 inch) diameter hole area and showed limited applicability. Acoustic emission and dye penetrant measurements were made on the majority of specimens and appeared to be closely related in terms of showing significant responses at approximately the same percentages of fatigue life, namely the range 5 to 15 percent which coincided with the initial macrocracking stage. The exoelectron data showed significant current changes earlier in the fatigue life than either of the acoustic emission or penetrant methods. These changes are plotted in Figure 43 and indicate an initial current increase and definite current changes prior to the macrocracking detected by the acoustic emission and penetrant methods. Electron microscopy of replicates taken in the notch surface, and subsequent verification by tensile fracturing of the specimen confirmed the presence of macrocracking

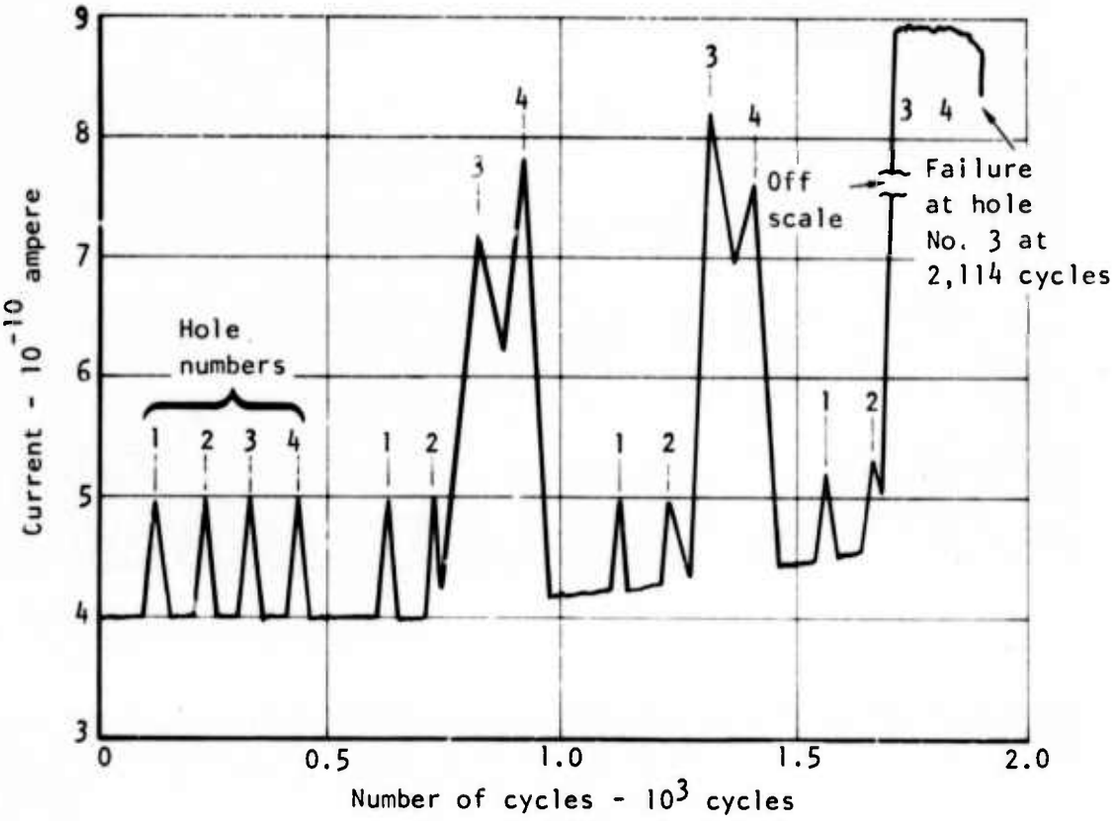

Figure 41. Change in exoelectron emission current at four holes in a 7075-T6 aluminum alloy specimen with fatigue.

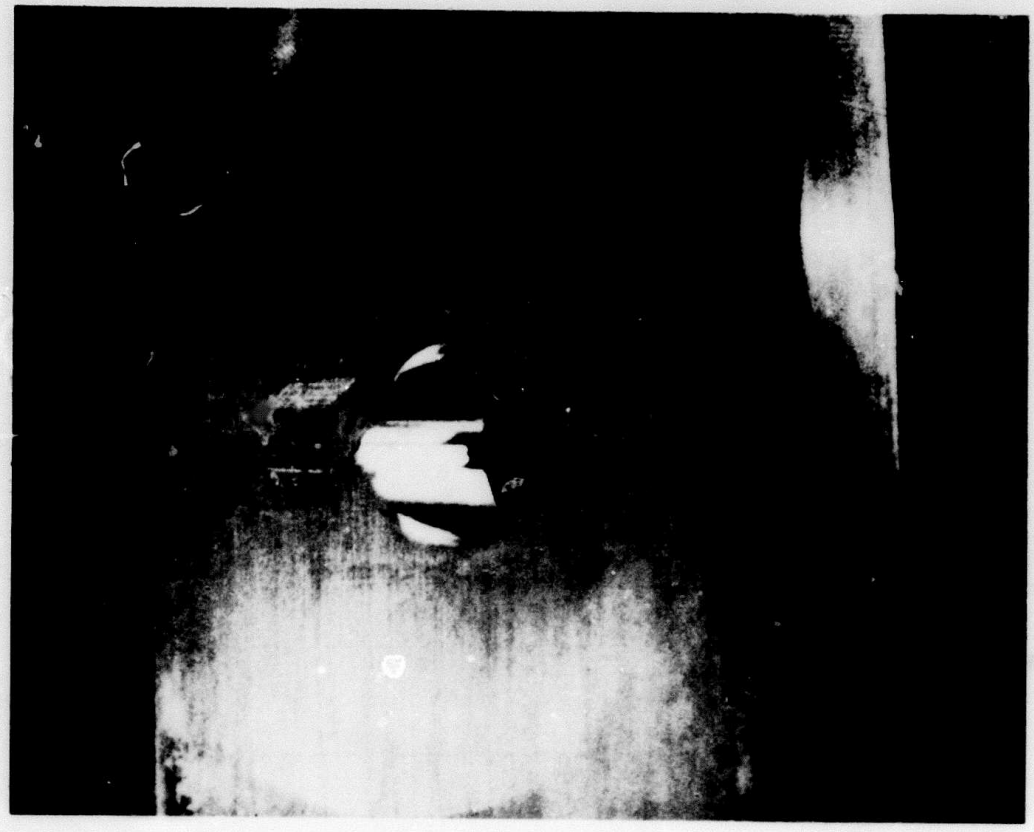

2.4 X

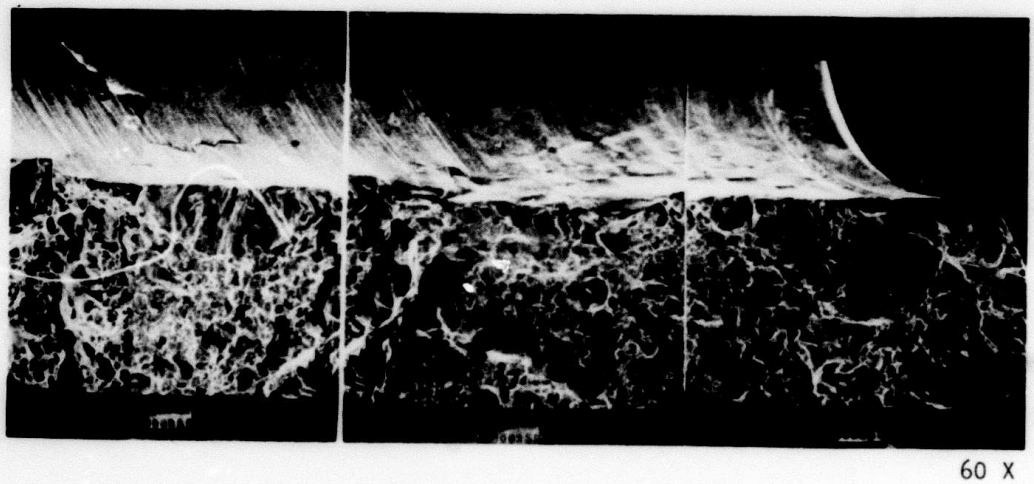

60 X

Figure 42. Open-hole notched specimen (K_t = 4.7) and fatigue fracture surface.

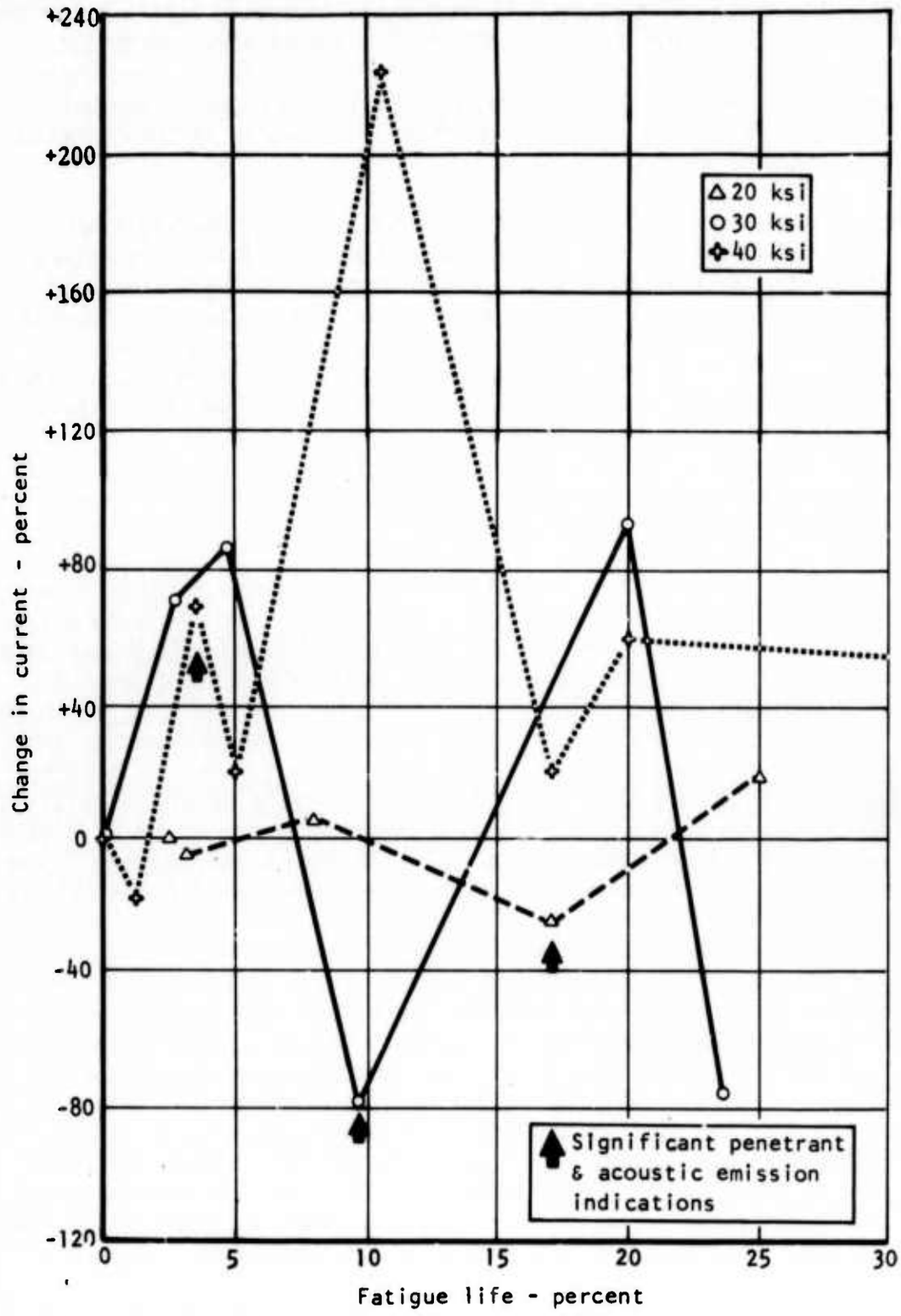

Figure 43. Early changes in exoelectron current with fatigue life of 2219-T851 aluminum alloy

(Figure 42). The exoelectron current in both tests increased as the macrocracks were detected. Further, the current level for the higher stressed specimen exhibits a proportionately earlier and higher excursion which is consistent with the present mechanism model. The initial current changes at approximately 5 and 7 percent of the fatigue life were attributable to the formation of slip bands and microcracks.

To further study the emission at fatigue damage sites, one steel machine screw was inserted in each of the four holes drilled in a 2024-T81 specimen. The screws were countersunk, held in place with nuts at the back side, and were not subject to loading during the test. The hole was virtually covered by the screw head. The specimen surface was scanned on the side containing the countersunk screws. The emission at three of the holes increased steadily during the duration of the test. The current at hole No. 4 was always larger than that from the other holes, and current surges were noted at 2,500 and 4,700 cycles (Figure 44). As in the test on open holes, failure occurred at hole No. 4 where the current surges were observed. The failure site could be predicted at about 30 percent of the life.

The exoelectron emission behavior at holes in high-cycle fatigue, however, appears different. Figure 45 shows that the exoelectron current curves for three holes 3.2 mm (1/8 inch) diameter and 12.7 mm (1/2 inch) center-to-center distance in a 2024-T81 specimen tested at a net stress of 10 ksi display a similar steady decrease for one-half of the total life. Thereafter, the current rises, but is still appreciably lower than the initial value even at the moment of specimen failure at No. 2 hole. It is impossible to predict the final failure site because the emission curves for No. 1 and 2 holes are quite similar and very close. This is in contrast with the observation in the low-cycle fatigue in which the failure site is located by the more rapid increase in current above the initial value during the test. The reason for this discrepancy is not understood. It is speculated, judging the close similarity of the three curves in Figure 45, that the holes suffer more or less the same fatigue damage in high-cycle fatigue at a relatively low stress. Final failure could occur at the hole where the damage became slightly higher than at the other holes. Because the stress is relatively high in low-cycle fatigue, the slightly varying stress concentrating condition of the holes could produce significantly different damage. The hole subjected to the most unfavorable deformation would fail first, and the exoelectron emission would be expected to differ appreciably from the other holes. It is also possible that cracks initiated and propagated at the other side of the specimen which was not scanned during fatigue test. A change in emission due to crack extension similar to the change shown in Figure 39 could thus not be detected by the transducer.

Specimens Containing No Discontinuities

The localized, marked change in exoelectron current at discontinuities was observed in the standard specimen which does not contain discontinuities.

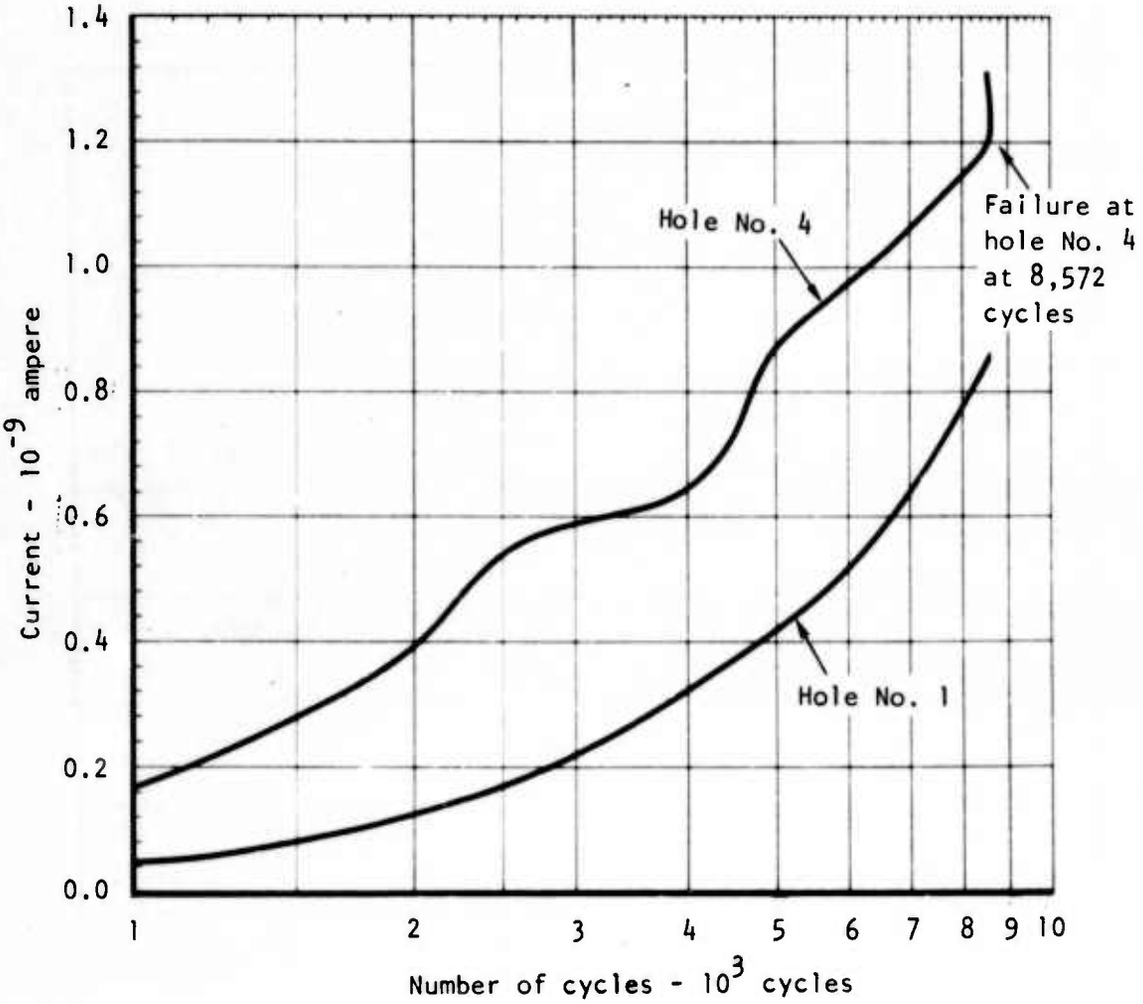

Figure 44. Change in exoelectron emission current at two holes filled with screws in a 2024-T81 aluminum alloy specimen with fatigue

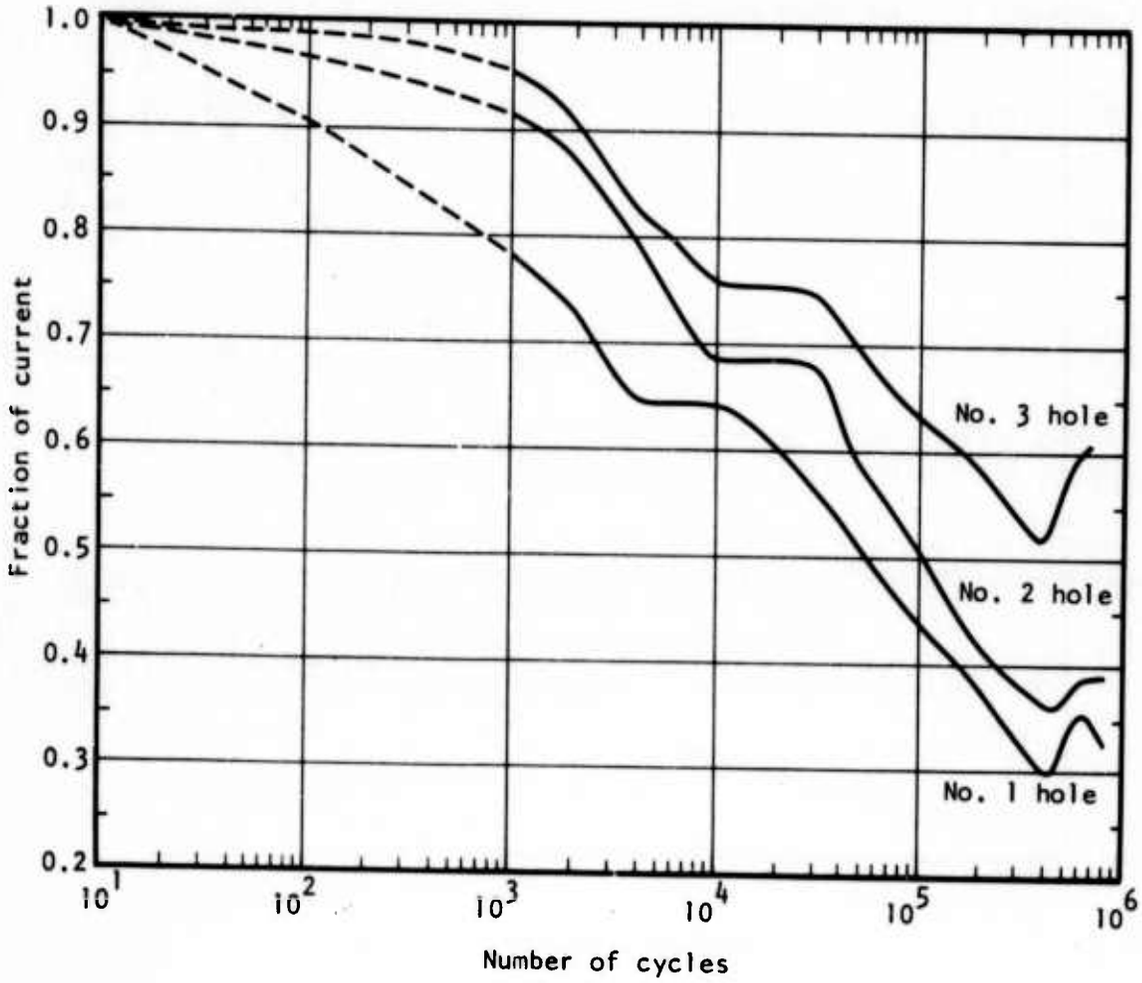

Figure 45. Exoelectron emission curves for three holes in a 2024-T81 aluminum alloy specimen under fatigue in air at 10 ksi.

The failure site of these specimens is located by means of the quantitative method. This method for analyzing both specimen surfaces was applied to fifteen 2024-T81 standard specimens containing no discontinuities. The representative curves for the change in exoelectron current at both sides of a specimen (H30) are shown in Figures 46 and 47. According to the specimen layout shown in Figure 47, the failure site was between locations 8 and 9. The curves for both locations obtained from the emission data for one side (side 1) indicate a very similar change in current and lie in the envelope (Figure 46). When the emission data for the other side (side 2) were analyzed, the results are quite different. In Figure 47, the curve for location 9 is significantly different from the other curves, while the current at location 8 lies in the envelope containing the other curves. However, the failure site is located between locations 8 and 9.

Examination of the fracture surface by scanning electron microscopy showed that the fatigue crack initiated at the edge of the specimen and emerged first on side 2 of the specimen. If the current had been measured only on the opposite side of the specimen, very little current change would be expected. The failure site of eight of the fifteen specimens tested would be predicted by the exoelectron emission measurements. Statistical analysis gives the probability of accurately locating the failure site of a specimen from 0.26 to 0.79 at a 95 percent confidence level.

An experiment was conducted to determine the effect of installing a specimen in the fatigue load machine and continuously operating the exoelectron emission scanning-measuring system over a several-day period without applying a load to the specimen. A 2024-T81 specimen was placed in the fatigue fixture and both sides were scanned for 3 days.

Five positions were selected for monitoring the variation in exoelectron current along the specimen length. Locations 1 and 5 were located each near the end of the straight test section and 56 mm (2.2 inches) apart. Locations 2, 3 and 4 were located near the center of the specimen and were 5 mm (0.19 inch) apart. Figures 48 and 49 show the current-time curves at these locations on both sides of the specimen. The current change at locations 2, 3 and 4 was expectedly very similar since the current from a small region (10 mm) should not change appreciably. However, there is a relatively large difference between the change in current at locations 1 and 5 in the first 24 hours. This difference was not attributed to a specimen geometry or transducer effects. Different initial localized surface conditions might account for this change. This change in exoelectron current without fatigue stressing is similar to the change in background current observed during a fatigue test. The change in exoelectron emission due to fatigue effects increases with cycling and long before the final specimen failure, it may reach a maximum level and decrease to a new minimum level. As shown in Figures 48 and 49, the background current decreases with time. Therefore, if the increase in exoelectron current due to

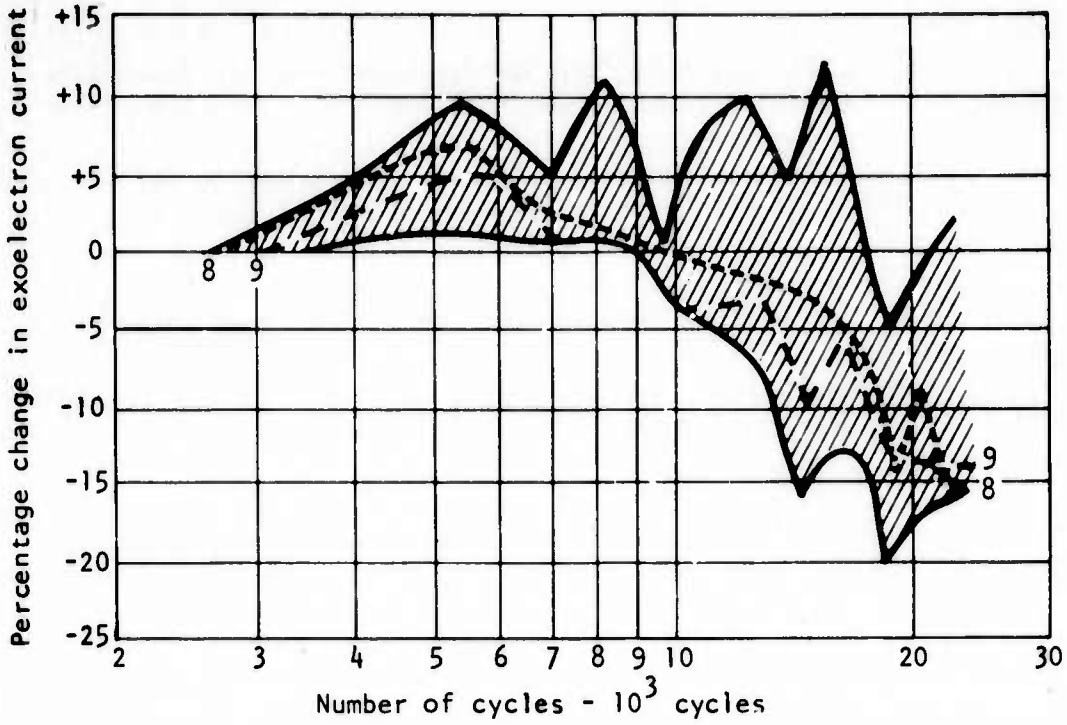

Figure 46. Change in exoelectron current with fatigue on side 1 of 2024-T81 aluminum alloy specimen H30.

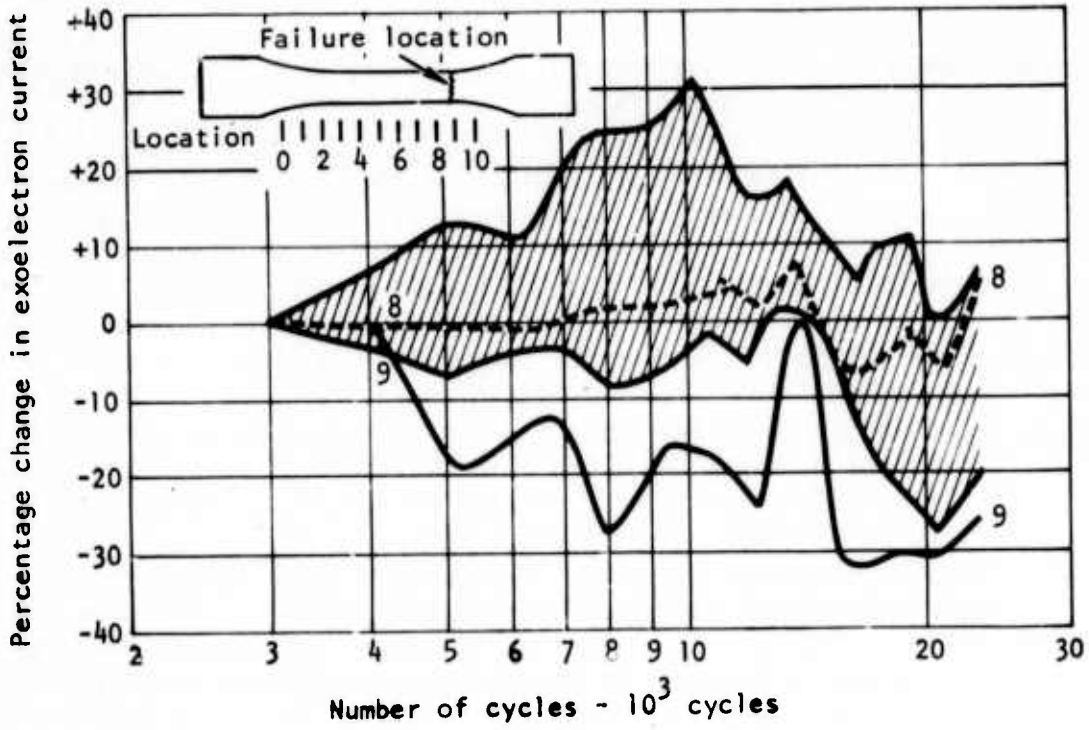

Figure 47. Change in exoelectron current with fatigue on side 2 of 2024-T81 aluminum alloy specimen H30.

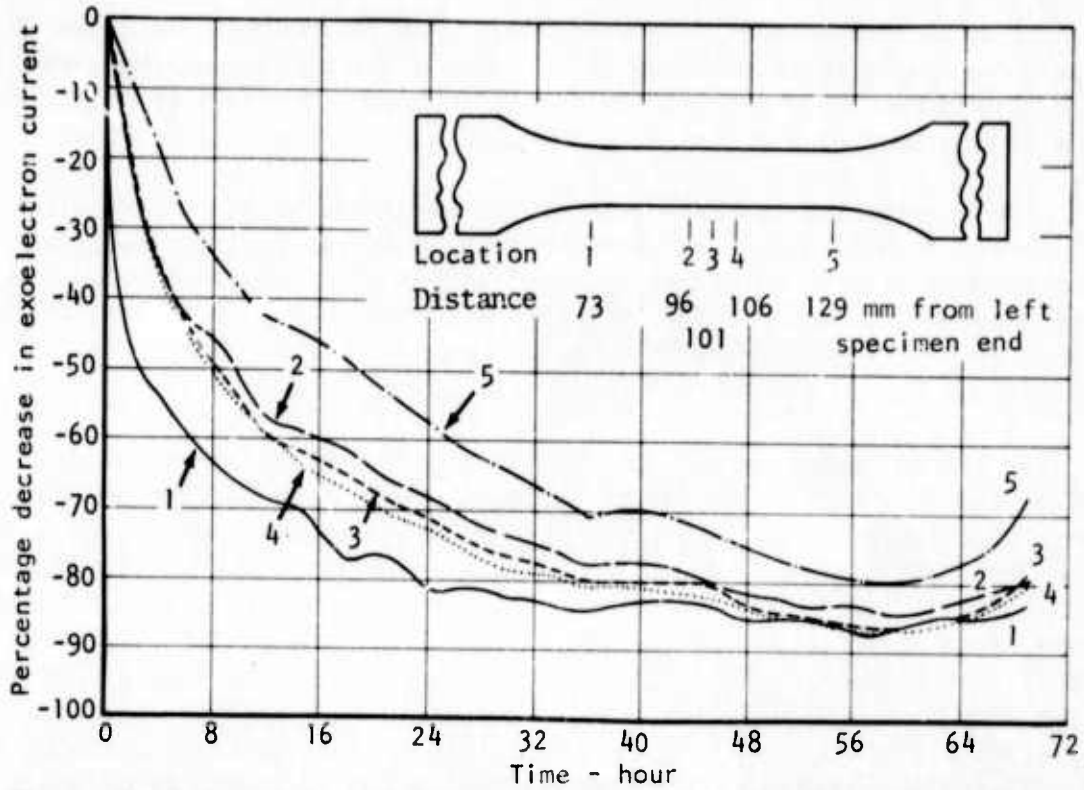

Figure 48. Change in exoelectron current with time on side 1 of a 2024-T81 aluminum alloy specimen without fatigue.

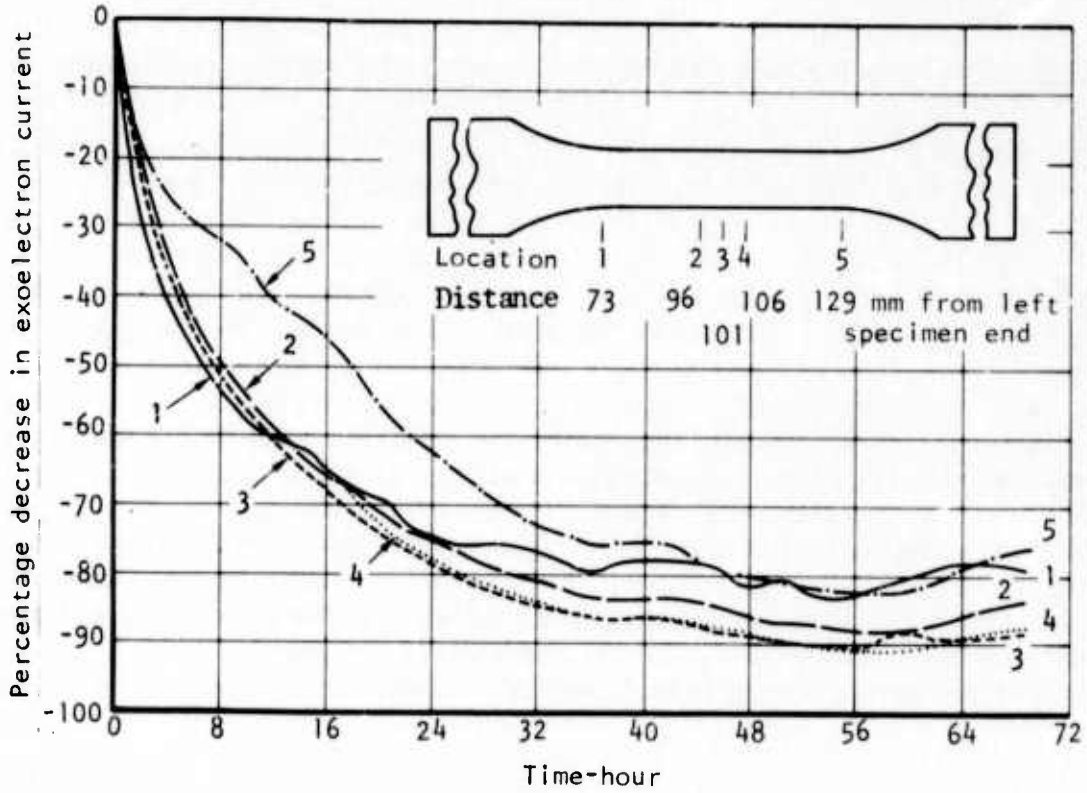

Figure 49. Change in exoelectron current with time on side 2 of a 2024-T81 aluminum alloy specimen without fatigue.

fatigue effects in a test is always lower than the decrease in background level, the whole emission curve will be below the initial current level. This phenomenon is an explanation for the apparent decrease or even lack of emission in some of the fatigue tests conducted during this program.

The current curves recorded from the specimens whose failure sites were not located by the quantitative method were examined again to ascertain whether a comparison of neighboring curves rather than all the curves at one specimen side could indicate the failure site. Most of the failure sites of the specimens whose current curves were thus reexamined, however, could not be identified.

It should be noted that, in addition to the accumulating damage in a fatigue test, the change in current at locations can also differ because of their relative positions in the test section. This can happen even if the specimen is not subject to fatigue test, as illustrated by locations 1 and 5 in Figures 49 and 50. If the change in current due to position of the locations alone is of about the same magnitude as the change due to varying severity of fatigue damage, no single current curve would show significant differences from the remaining curves. It is speculated that this might offer an explanation why the quantitative analysis is only partially successful in identifying the failure site. Additional experimental work is needed to develop methods to improve the applicability of this method for nondestructively locating the fatigue failure site.

Bolted Joints

The screws in the fatigue test of Figure 44 were not stress-loaded and merely acted as hole fillers. A simulated bolted joint (Figure 50) was made by bolting together two broken 2024-T81 specimens 12.7 mm (1/2 inch) wide and 2.3 mm (0.09 inch) thick with a large bolt and two 10-32 steel screws (brazier head type) to determine whether the failure site of the bolted joint could be located by exoelectron emission. This bolted joint was designed to cause failure to occur around the screw holes in a fatigue test at 650 pounds. The emission from the holes containing the two screws was very similar prior to the test. After the cycling began, the emission from both holes varied with time, but the emission from hole No. 2 always exceeded that of hole No. 1. The difference in current level became larger after 3,000 cycles, as indicated in Figure 51. The emission from both holes reached their peak values at approximately 5,000 cycles. Thereafter, it decreased steadily to approximately 6,000 cycles, when the test was interrupted. After a 20-hour delay in an unloaded condition over the weekend, the specimen was again scanned before the fatigue test was resumed. Though some decay had occurred, the emission level from

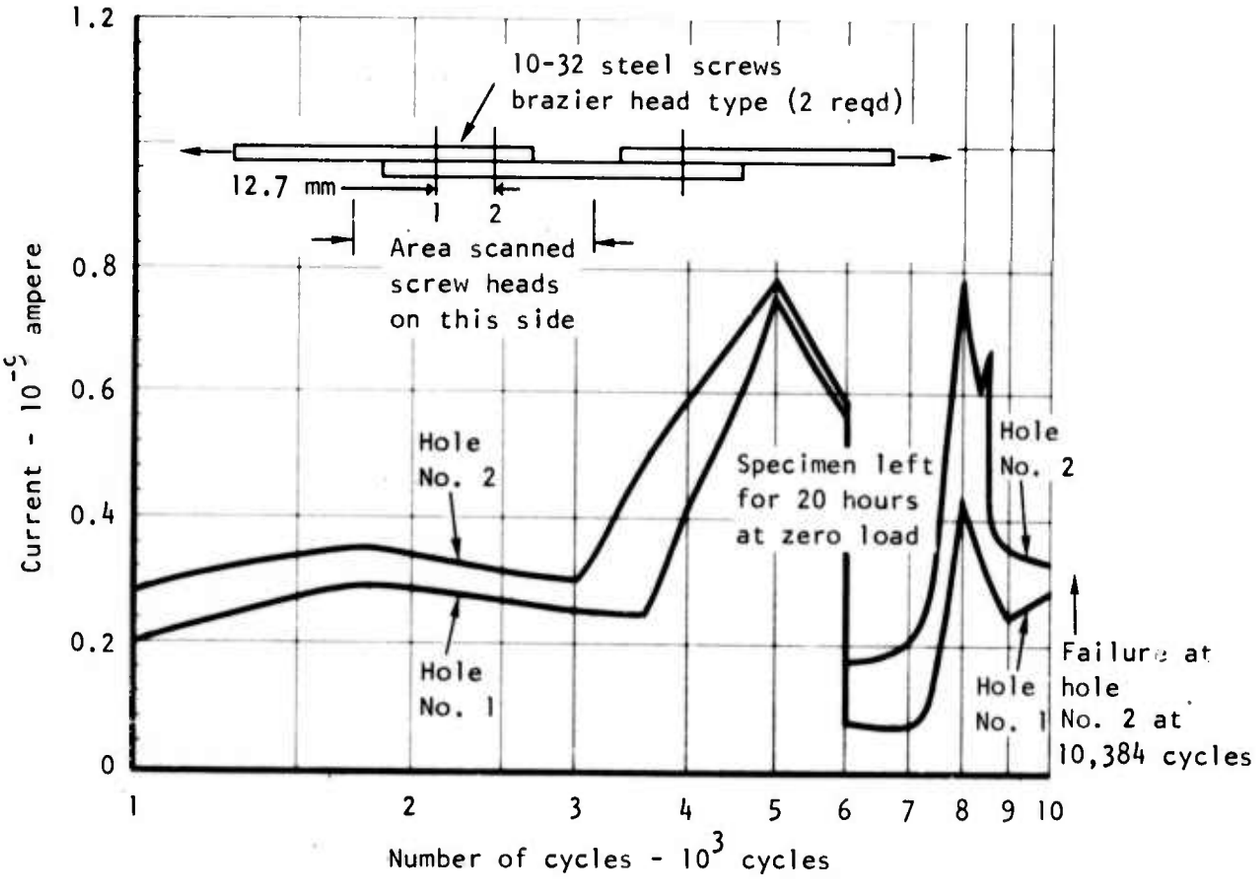

Figure 50. Change in exoelectron emission current at two holes in a 2024-T81 aluminum alloy bolted specimen with fatigue.

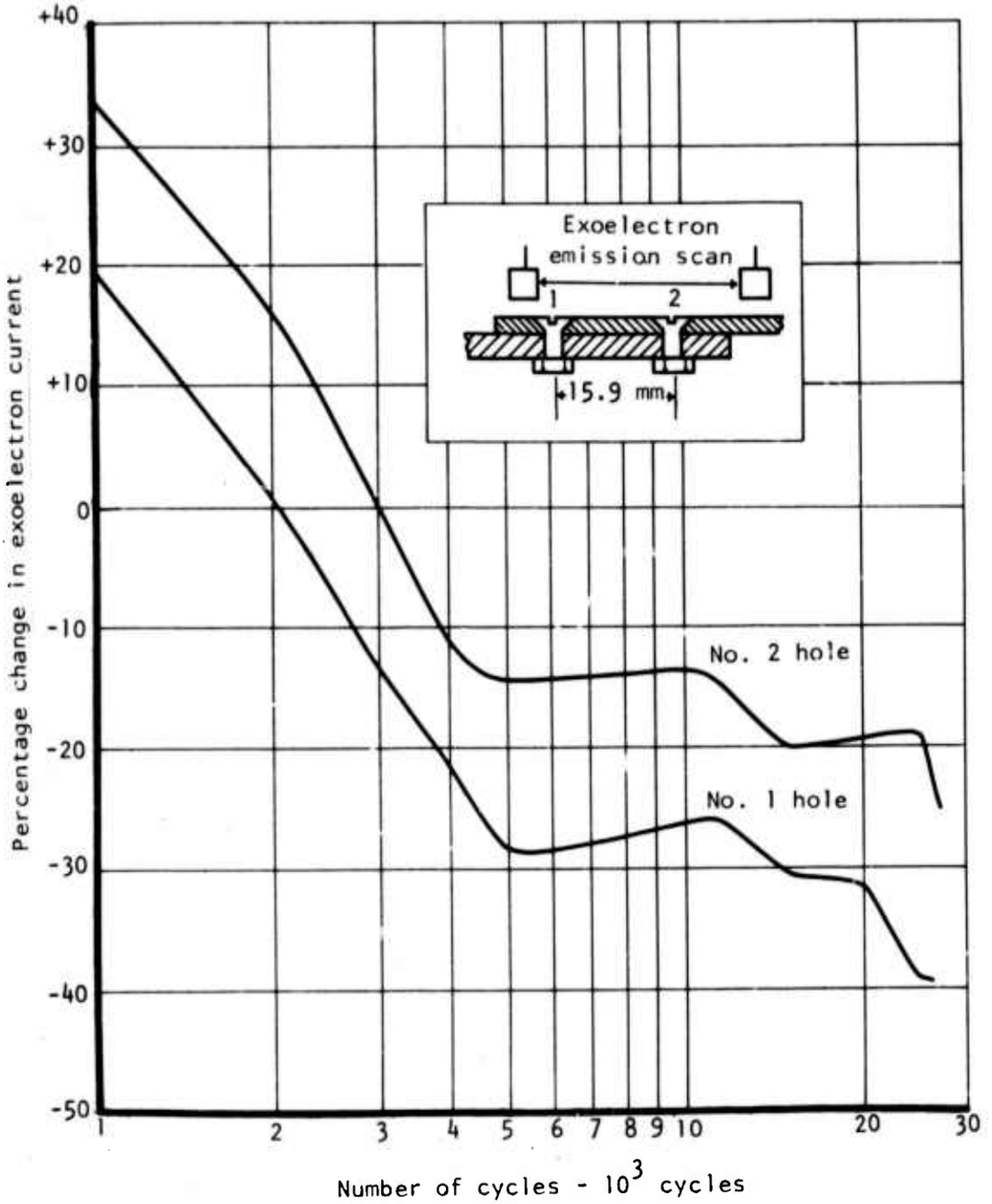

Figure 51. Exoelectron emission around holes of 2024-T81 aluminum alloy lap joint.

hole No. 2 was still significantly larger than that from hole No. 1. During the subsequent cycling, the emission from both holes increased with time. A surge of current was observed at 7,800 cycles from hole No. 2, followed by a similar, but smaller, surge from hole No. 1. The emission from both holes then decreased with a second surge at the No. 2 hole before failure occurring at 10,384 cycles adjacent to hole No. 2.

A lap joint was simulated by joining two 2024-T81 blanks, each 12.7 mm (0.5 inch) wide and 2.2 mm (0.088 inch) thick, with two 6-32 countersunk machine screws 15.9 mm (0.625 inch) apart. The fatigue test was conducted at a load of 250 pounds. Identification of failure site could not be ascertained by the method used in Figure 50. The emission pattern at both holes was similar and remained practically unchanged throughout the test. Moreover, the current after an initial increase began to drop below the initial value early in the test. When the change in current at each hole with respect to the initial value was computed, it was noted as shown in Figure 51 that the current at No. 1 hole underwent greater change than at No. 2 hole. Therefore, regardless of the sign of change in the exoelectron current, fracture was more likely to take place at No. 1 hole, which turned out to be the actual failure site.

Weld Joints

Weld specimens were prepared from 3.2-mm-thick (0.125 inch) 2219-T851 weldments, 12.7 mm (0.5 inch) wide and 6.4 mm (0.25 inch) long. The six of the eight specimens contained various levels of porosity. These levels were defined as high, medium or low, based on a measurement of the pore area (measured by radiography on the weldment before machining) of 19.4 to 20.6, 11.6 to 12.9 and 3.2 to 3.9 square millimeters (0.03 to 0.032, 0.018 to 0.02 and 0.005 to 0.006 square inch) in a 19.1-millimeter (0.75 inch) length of weld. The remaining two specimens were free of flaws and served as control specimens. The porosity level and fatigue test conditions for each specimen are given in Appendix C.

The exoelectron emission and surface potential difference measurements were made on each specimen before the first fatigue test and at the indicated intervals. The exoelectron emission and potential difference graphs of each specimen displayed a number of maxima and minima points which were considered as potential failure sites. It was observed that a minimum was usually located at the weld zone and correlated with the presence of pores. Therefore, it was possible to accurately locate the failure site by noting the minimum on the graph. The prediction accuracy of the nondestructive measurements was again determined by dividing the number of true and false indications. Since the weld is only 6 to 7 mm long and since fracture occurred within this zone, a true indication was assigned to an indicated potential failure site if it falls in the range of ±1 mm of the actual failure site. A potential failure site located outside this ±1 mm range was considered a false indication. Results of the evaluation of the nondestructive measurements are presented in Table 5.

TABLE 5. LOCATING FATIGUE FAILURE SITE IN 2219-T851 ALUMINUM ALLOY WELD BY NONDESTRUCTIVE EVALUATION

Specimen No. and Porosity Level	Potential Failure Site, mm from Specimen (203 mm Length) End				Actual Failure Site, mm from Specimen End	Prediction Accuracy (True or False)	
	Exoelectron Emission		Surface Potential Difference			EEE*	SPD*
	First Test	Second Test	First Test	Second Test			
CC1; control	105	99	**	**	101	0T 2F	**
CC2; control	106	100	101, 106	102, 105	101	1T 1F	1T 2F
PL1; low	106	***	101, 106	***	104	0T 1F	0T 2F
PL2; low	99	***	104, 106	***	100	1T 0F	0T 2F
PM2; medium	101	***	101	***	102	1T 0F	1T 0F
PM3; medium	101	***	101	***	101	1T 0F	1T 0F
PH1; high	105, 107	***	101, 106, 107	***	103	0T 2F	0T 3F
PH2; high	107	***	101	***	103	0T 1F	0T 1F

*EEE = Exoelectron emission
SPD = Surface potential difference
**There is no maximum or minimum located within the weld zone in the graph.
***No second test was conducted because the specimen failed in fatigue.

The potential failure site of a defective specimen was determined based on the surface where the pore emerged. When the pore penetrated both sides, such as in specimen PH1, the potential site located by exoelectron emission had two such values. Also, more than one potential site per side was determined by surface potential difference measurements since scans were made along the specimen center line and along both edges.

It is noted that the nondestructive measurement data made prior to the first fatigue test were not included in Table 5. This is because analysis of the data disclosed no indication of potential failure site of any one specimen. After the specimen underwent fatigue test, Table 5 shows that four of the eight failure sites can be predicted accurately within ±1 mm by exoelectron emission, surface potential difference or both.

Curved Shapes

A complex structure in the form of curved shape was scanned for exoelectron emission during fatigue test to identify the failure site. The initial 6.3 mm (1/4 inch) thickness of a 7075-T6 plate was reduced by milling with a 12.7 mm (1/2 inch) diameter cutter to produce a change in section thickness from 3.2 mm (0.125) to 1.8 mm (0.071 inch). It was expected that this curved specimen would break at a critical area where the changes in thickness took place. The specimen was tested at a load of 1,000 pounds. The current at and around both critical areas changed as cycling proceeded. However, there was a marked variation in emission pattern at one curved section and failure was considered more likely here. Two more similar-shaped specimens with thickness changes from 3.2 mm (0.125 inch) to 2.3 mm (0.09 inch) and 1.9 mm (0.075 inch) were tested; fracture occurred at the critical area where a larger change in emission was observed during the test.

ENVIRONMENTAL TESTS

A series of experiments were conducted to determine the ability of the NDT methods to detect fatigue damage under service conditions including general plastic deformation and evaporation in terms of relative humidity, and corrosion. Both exoelectron emission and surface potential difference were measured on the fatigued specimens which had been subjected to tensile loading to induce plastic deformation prior to the fatigue test. Because of the particular environmental conditions imposed by evaporation and corrosion upon the specimens, only exoelectron emission was measured on these specimens during the fatigue test.

General Plastic Deformation

Two specimens each of 2024-T81 and 2024-T3 (B7, E20, A4, and B12) were used to study the effect of general plastic deformation. The specimens were

fatigue tested, and the nondestructive measurements were performed during two interruptions of the fatigue cycling. The results for identifying the potential failure sites of the four specimens are given in Table 3. If the prediction system developed for evaluating fatigue damage of the specimens in the baseline group is used, the actual failure site of the four specimens can be detected by a true indication either by both exoelectron emission and surface potential difference or by surface potential difference alone. Such a high probability of detecting fatigue damage by approximately locating the failure site, therefore, indicates that both exoelectron emission and surface potential difference measurements are not adversely affected by the state of the specimen surface when altered by prior plastic deformation.

Evaporation

The effect of evaporation on the fatigue damage detection capability of the exoelectron emission method was evaluated on 2024-T81 aluminum alloy and heat treated (SRH-1050 condition) PH14-8 Mo steel specimens in fatigue. The ten-point quantitative method was applied to locate the failure site of the specimens. Figure 52 shows the change in exoelectron current with time at several locations in the test section of a 2024-T81 specimen during fatigue test in 30-percent relative humidity. It is noted that not all of the ten curves are shown because of superposition of many of the curves. Locations of the ten current measurements are also shown in this figure. The current at each location increased with cycling. Except for the curve at location 10, the data is very similar until about 35,000 cycles. The curve at location 9 then shows a distinct change and the failure site predicted by the largest change in exoelectron current should be at the vicinity of location 9. Final failure at 42,081 cycles did occur near this location. There is also a marked change on the curve at location 10 at 35,000 cycles. However, failure was not expected here since the local stress level was low due to larger cross-sectional area. The exoelectron current change with time of another 2024-T81 specimen during fatigue test in a higher relative humidity of 65 to 70 percent and at a lower stress level of 26.6 ksi is plotted in Figure 53. Early in the test the overall current levels show a similar decrease. Afterwards the current change varied without a specific trend. At 32,000 cycles, an increasing trend was indicated. This was particularly evident at location 8 where an almost 80 percent increase (from -90 to -11 percent) was measured from 32,000 to 49,000 cycles. The specimen failed close to location 8 at 51,020 cycles. The curves of locations 9 and 8 in Figures 52 and 53, respectively, were replotted (Figure 54) as a function of the percentage of fatigue life. Exoelectron current at a failure site varies during fatigue test in different levels of relative humidity. Note that neither of the two curves starts at zero percent of life either because the test was interrupted or because of erratic measurements made during the first few thousand cycles. No significance should be made of the observations in Figure 54 that there is a continuous increase in current in low (30 percent) relative humidity and that the current decreases as well

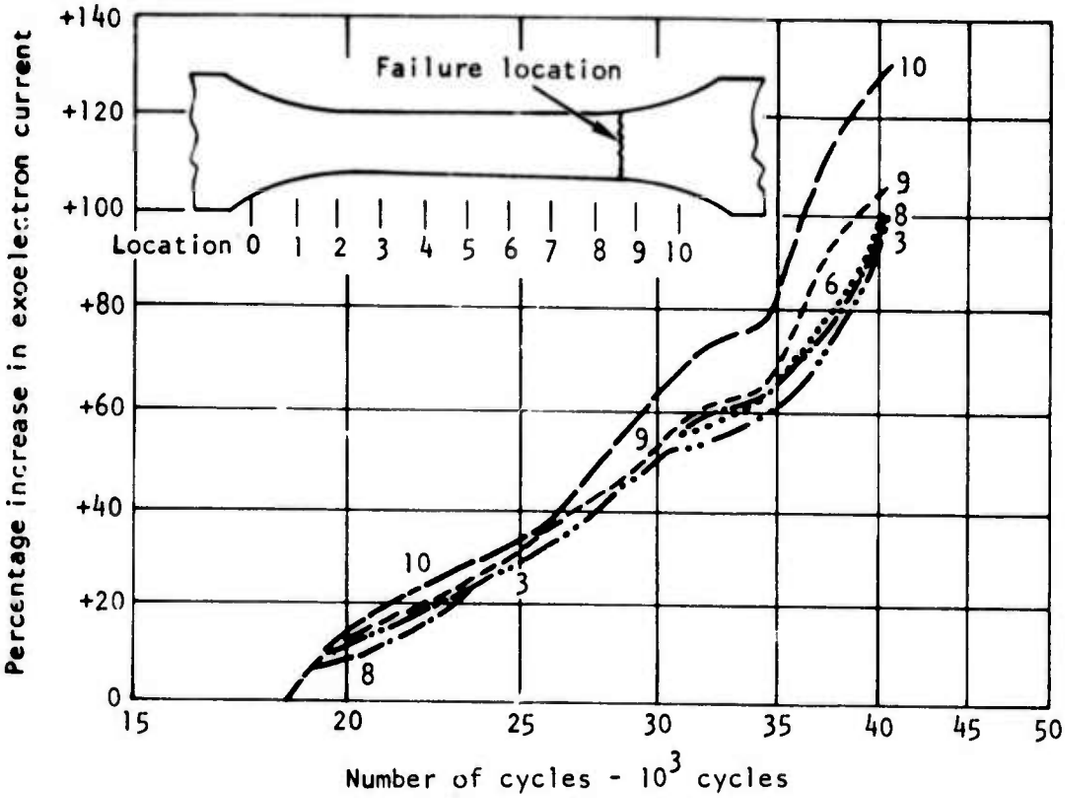

Figure 52. Change in exoelectron current during fatigue of 2024-T81 aluminum alloy at 32 ksi and 30 percent relative humidity.

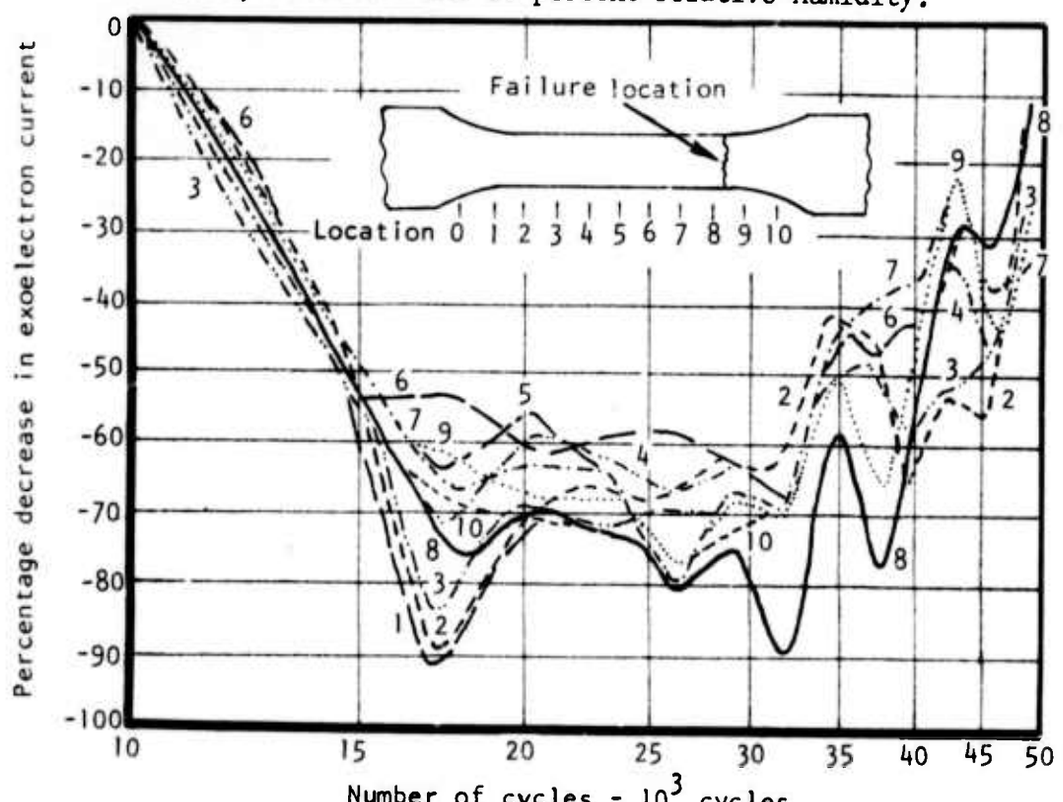

Figure 53. Change in exoelectron current during fatigue of 2024-T81 aluminum alloy at 26.6 ksi and 65 to 70 percent relative humidity.

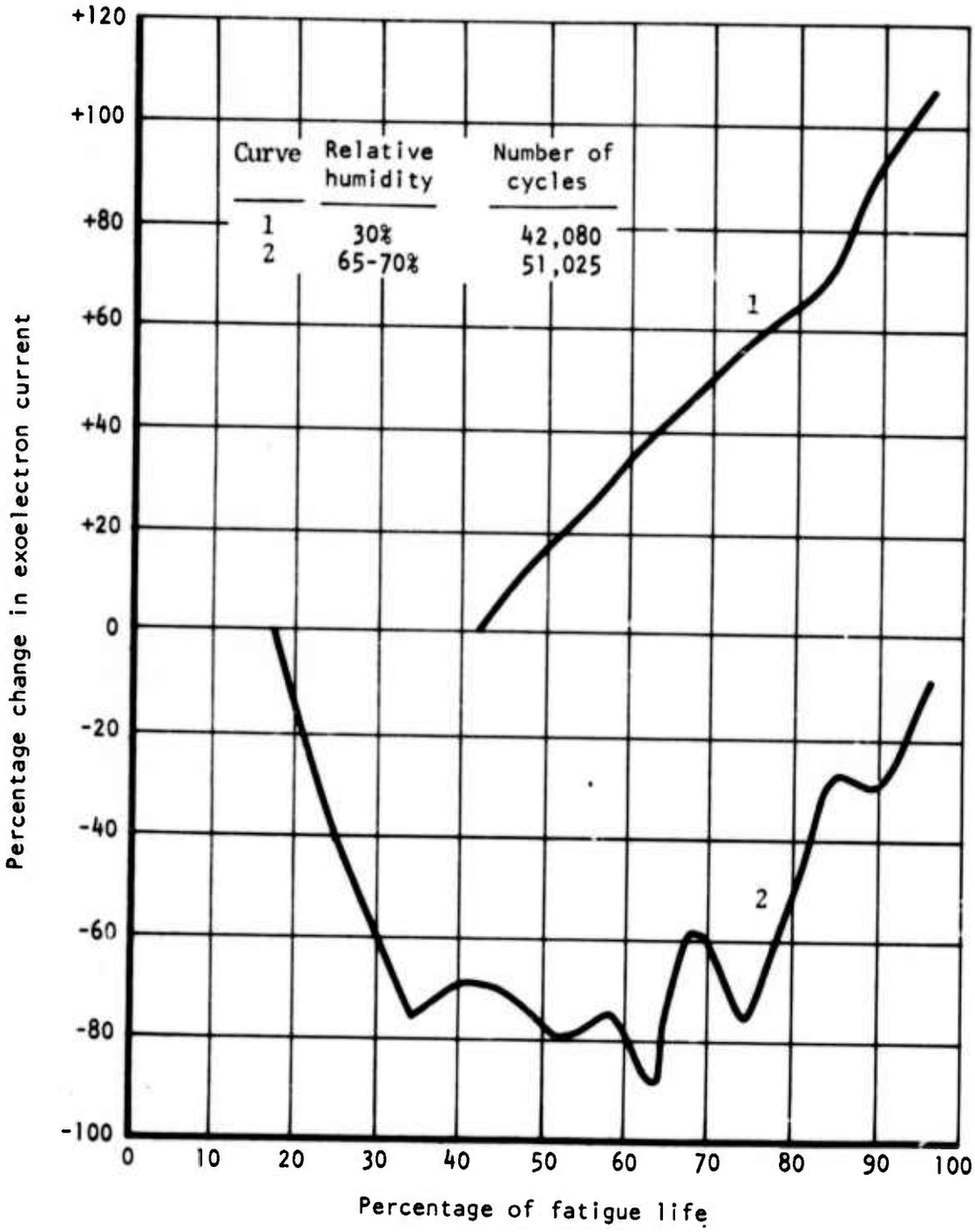

Figure 54. Change in exoelectron current at failure site of 2024-T81 aluminum alloy during fatigue test at two levels of relative humidity.

as increases in high (65 to 75 percent) relative humidity. This figure is intended to demonstrate that the ability of exoelectron emission to predict the fatigue failure site is not impaired by varying the relative humidity conditions. A number of test parameters, probably including relative humidity, can influence the exoelectron emission behavior of a metallic material in fatigue. Their individual as well as combined action are still not well understood. The apparent decrease in current depicted in Figure 54 is due to the method the current change was computed. This subject was previously discussed in connection with Figures 48 and 49.

Intermittent Tests

Generally, the fatigue loading on an aircraft structure is intermittent rather than continuous. To investigate whether the interruption of a fatigue test can influence the prediction of failure site by the exoelectron emission method, an SRH-1050 condition PH14-8 Mo steel specimen was tested in two sequences with an intermediate unloaded period of 18 hours. The specimen was fatigued for 53,900 cycles, unloaded for 18 hours, and fatigued to failure at 96,930 cycles. The emission data for each test were evaluated separately. Figure 55 shows the change in exoelectron current at 10 locations during the first test. A single curve for location 9 is given, the remaining nine curves being represented by an envelope. The emission data for the second test are similarly presented in Figure 56. Upon initiation of the test sequence the transducer malfunctioned and data was not obtained during the 54,000 to 55,600 cycle period. Therefore, after repairing the transducer, the test was continued using a new reference. In Figure 55, the curve for location 9 is not markedly different from the other curves until the end of the first test. The current change at all ten locations decreased after the start of the second test(Figure 56) and decreased more at location 9. At 60,000 cycles (about 6,000 cycles from the end of the first test), the current change increased and the change at location 9 increased more rapidly than at other locations denoted by the envelope. After 65,000 cycles (about 11,000 cycles from the end of the first test) the current curve of location 9 was consistently above the envelope till the end of the second test. According to the specimen layout in Figure 56, location 9 is the failure site.

Reexamination of Figure 55 shows that the current curve of location 9 had already started to separate from the envelope near the end of the first test. Had this test been carried out beyond 54,000 cycles without interruption, it is expected that this curve would have continued to proceed above the envelope in a manner illustrated in Figure 56. Therefore, the initiation of separation of the curve at location 9 near the end of the first test can be considered as an indication of detecting the failure site. Interruption of the test in this case does not adversely affect the capability of the exoelectron emission method to locate the failure site.

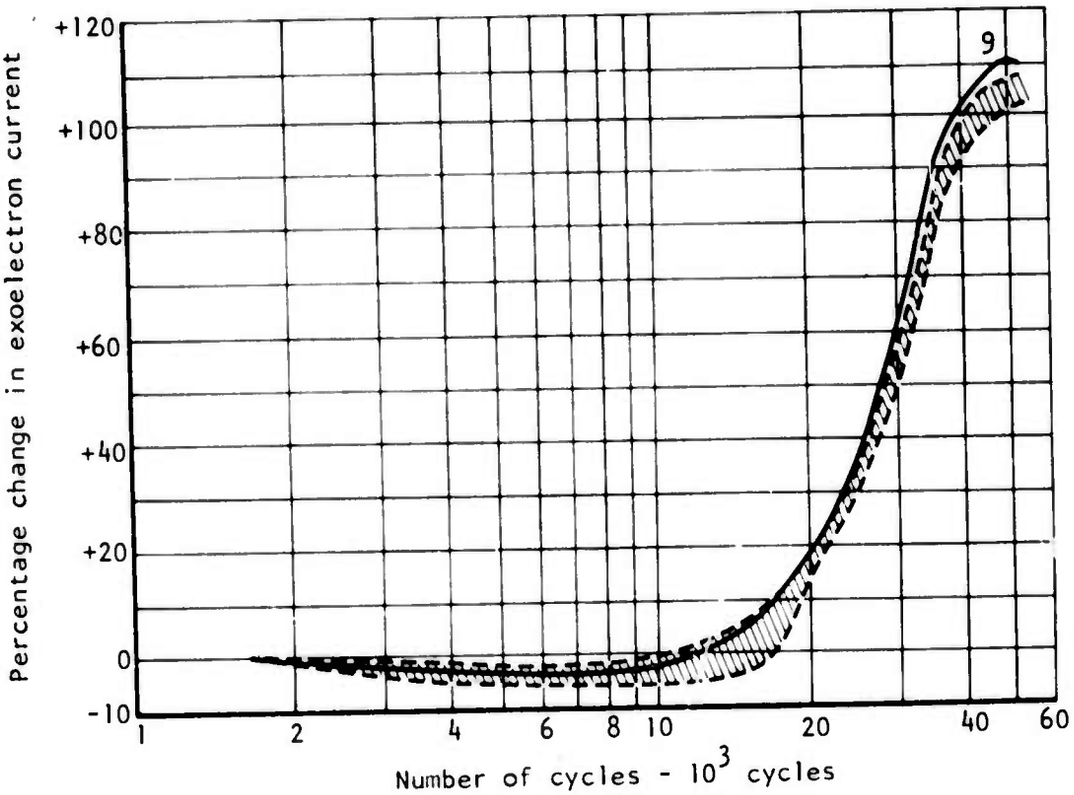

Figure 55. Change in exoelectron current during fatigue of SRH-1050 condition PH14-8 Mo steel at 44.6 ksi and 68 to 74 percent relative humidity.

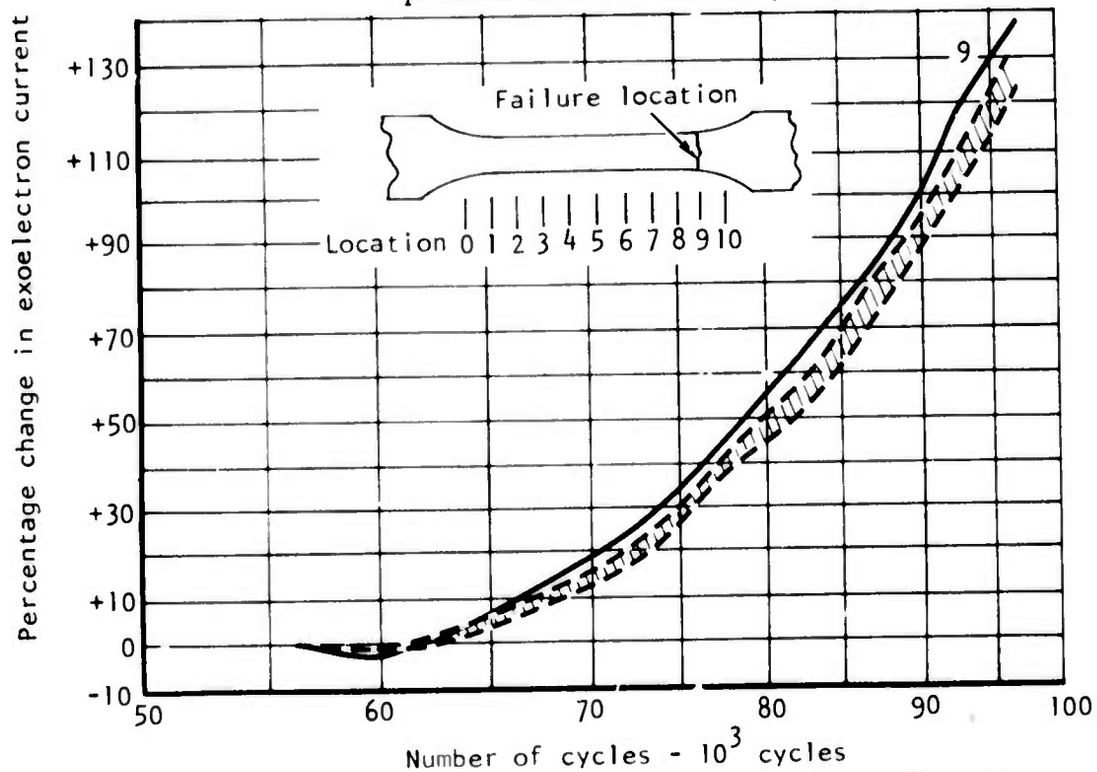

Figure 56. Change in exoelectron current during fatigue of SRH-1050 condition PH14-8 Mo steel at 44.6 ksi and 68 to 74 percent relative humidity.

Corrosion

The surface of the 2024-T81 specimen soaked in 0.05M salt solution for 24 hours was badly corroded; many pits were seen on the surface. Some of the pits became intense exoelectron emission sources in the subsequent fatigue test. Though the fatigue life was shortened, exoelectron emission of the specimen could still be measured despite heavy corrosion.

SCANNING ELECTRON MICROSCOPIC EVALUATION

An investigation was made using scanning electron microscopy to learn more about the characteristics of the cause and location of the final fracture sites. A detailed examination by scanning electron microscopy was conducted on the fracture surface of specimen H30 and four other 2024-T81 specimens. The surface was examined to locate the crack initiation site and to trace the propagation path. The crack was found, in all cases, to initiate at one of the chem-milled pits at the specimen edge rather than at the specimen surface. Propagation of the crack appears to take place in a somewhat preferential way so that the crack emerges at one specimen surface sooner than at the other surface. The scanning electron micrograph of specimen H30 in Figure 57 (a) shows the fracture site (indicated by an arrow). It is observed that cracking originated at the specimen edge, propagating initially toward side No. 2. The enlarged view of the external surface of the specimen edge in relation to the fracture site in Figure 57(b) indicates clearly that the fatigue crack originated at one of the chem-milled pits. Typical fatigue striations in the area adjacent to the fatigue origin are illustrated in Figure 57(c). Since side No. 2 was the side on which fatigue crack first emerged and on which a large change in exoelectron current at location 9 was observed in Figure 47, the marked changes in the current appear to directly correlate with that side. As revealed by the scanning electron microscopic photographs, this current change is related to an early stress concentration buildup and subsequent surface cracking.

EVALUATION OF ADDITIONAL NDT METHODS

ACOUSTIC EMISSION

Acoustic emission measurements are becoming generally accepted as a means of detecting and monitoring fatigue damage. The use of acoustic emission techniques in the present investigation was limited, primarily because of the lack of quantitative information relative to practical measurement conditions; i.e., sensitivity, threshold levels, frequency characteristics, effect of test machine noises, etc. However, since the capability to monitor

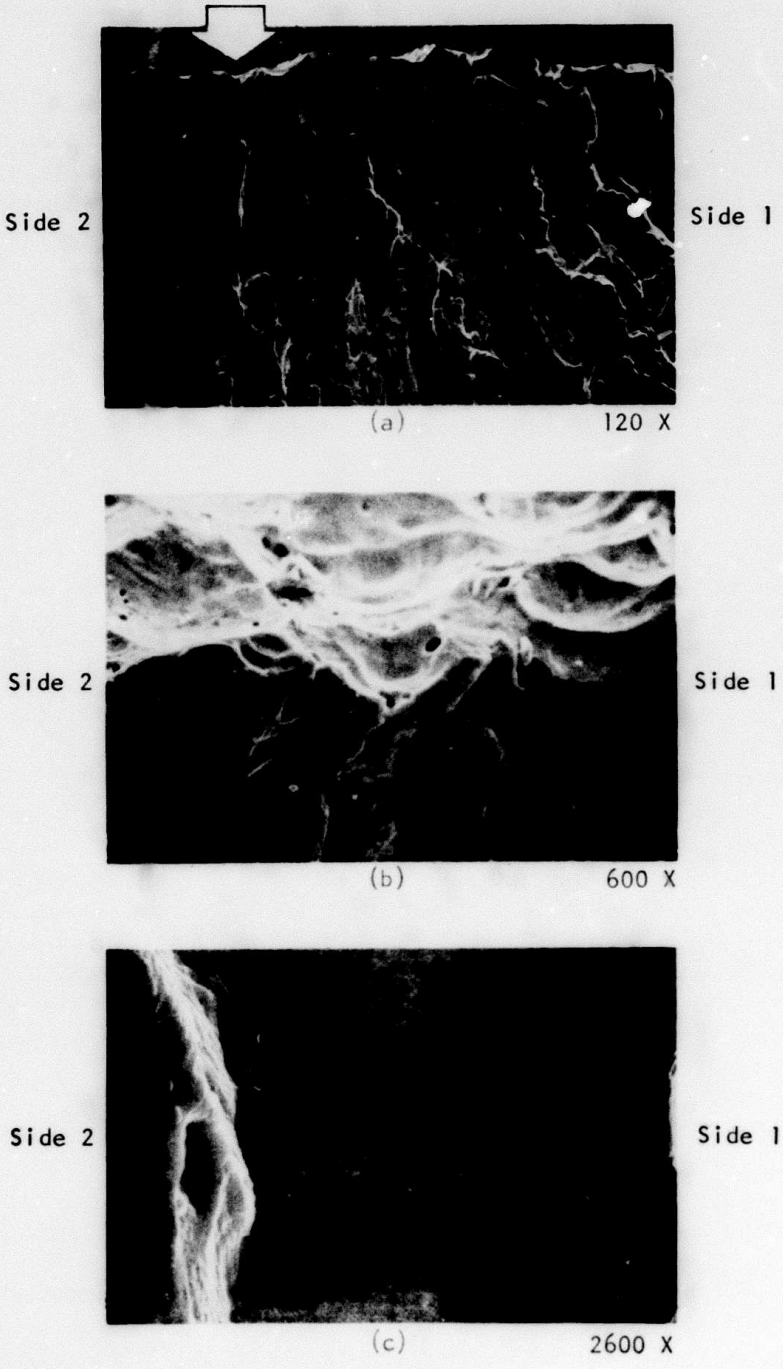

Figure 57. Scanning electron micrographs of 2024-T81 aluminum alloy specimen H30 showing fatigue failure site and fatigue striations.

acoustic emission events was available in the same area where the exoelectron emission fatigue cycling was performed, and since it was believed that the acoustic emission data could potentially be used to supplement the other NDT measurement data, a complete acoustic emission analysis was performed using techniques and equipment described by Graham and Alers.[48]

The parameters that are of interest in the characterization of acoustic emission phenomenon are the rate of event occurrence, the amplitude distribution and the frequency content. A determination of these parameters and their dependence on external variables such as stress and environment is necessary in order to identify and measure all of the sources of the acoustic emission at the test location. To meet this requirement, the acoustic emission evaluation system should be sensitive and braodbanded, and the analysis system must be capable of handling fast, short-duration, transient bursts. The components of the evaluation system used in the present investigation are described herein. The acoustic emission transducer used in the system calibration and for the fatigue experiments were calibrated using a "white acoustic noise" generator in which the transducer was exposed to the noise produced by the grinding of an abrasive powder between a glass rod and a metal cup. This calibration showed relatively comparable transducer performance between the calibration and test transducers. To evaluate the test system, it is necessary to analyze a single acoustic emission event which must first be recorded by some means and played back repetitively into a frequency analyzer so that the frequency sweep mechanism can sample the signal at consecutive frequencies. A modified video tape recorder system was used to perform this function and provide a broadband analysis of the transient signals as shown in Figure 58.

The unit is equipped with a "stop action" feature which allows a 17 msec record to be continuously repeated at a rate of 60 Hz. (17 msec is the time required to record one frame of a TV picture.) A single acoustic emission burst typically has a duration of 1 msec therefore, this unit allows the repetitive playback of a single burst for examination on an oscilloscope or for frequency spectrum analysis. Because some electronic noises associated with the 17 msec period could not be eliminated, an electronic gate was used so that the time interval containing the acoustic emission burst could be separated out. The presence of this gate made it possible to examine the background noise occurring just before a burst as well as at small intervals within the burst to determine if the frequency content had changed during the rise and fall of the burst signal. The frequency response of the tape recorder extended up to 3 MHz which is higher than most digital systems used for frequency analysis. The dynamic range was about 30 db.

---

[48] Graham and Alers, 1972

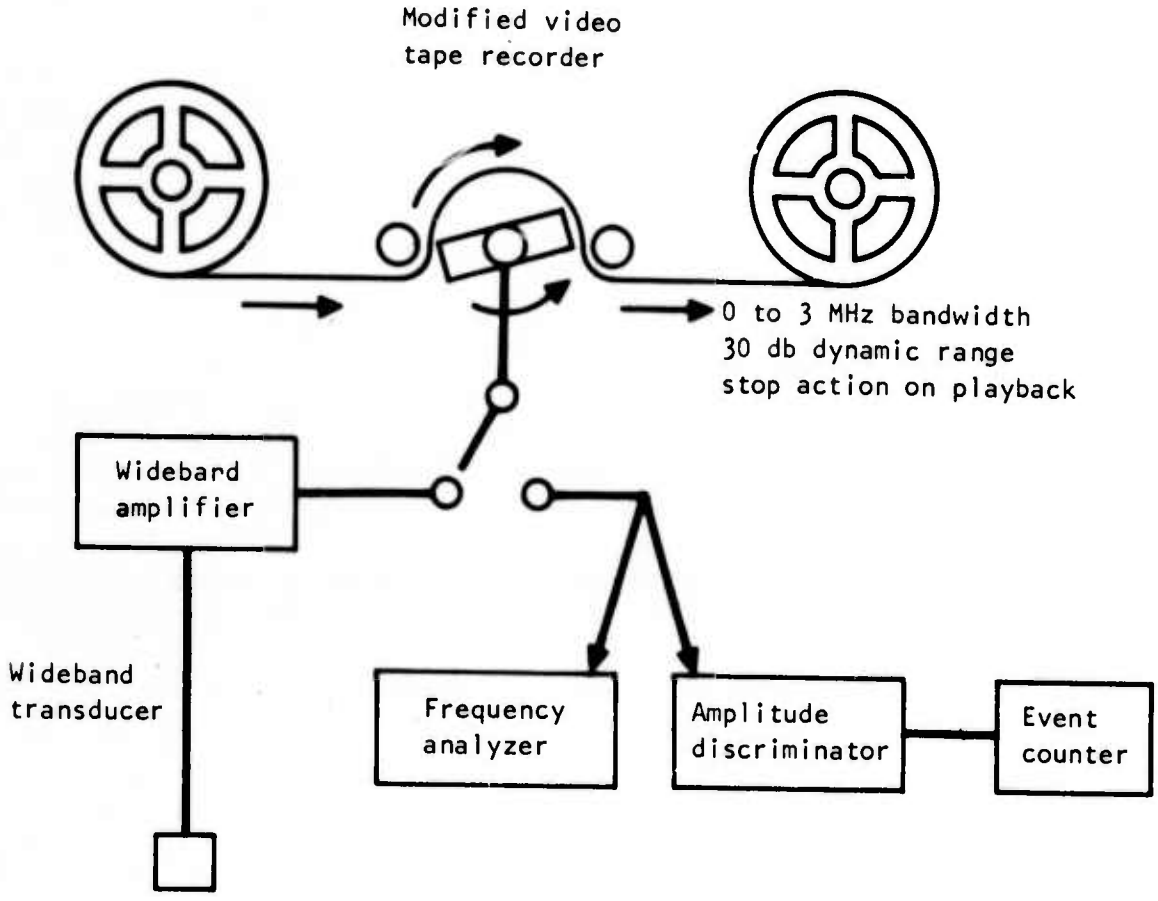

Figure 58. Block diagram of video tape recorder system for acoustic emission analysis.

The amplitude characteristics of the acoustic emission signals generated during the evaluation and recorded on a magnetic tape were obtained by replaying the magnetic tape into an event counter with a known, preset level and counted.

The acoustic emission recording system was employed to measure acoustic bursts occurring at the surface of an aluminum 2024-T81 alloy specimen (H1) during fatigue cycling. The calibration transducer was positioned at the exact location on the specimen surface as the normal test transducer. In this manner, the calibration data was expected to establish accurate in situ measurement requirements. The following test conditions were evaluated:

- Background noise level with and without cycling
- Cycling under no load, medium load, normal load, and high load conditions
- Variations in cycling rate
- Operation of the exoelectron emission scanner

The acoustic emission evaluation data are shown in Figure 59, 60, and 61. Figure 59 shows the calibration data. Photo A shows the frequency response of the calibration transducer using an acoustic white noise source. The response is fairly broadbanded and was used as a reference when comparing the influence of the test conditions. Photos B, D, and E display the response caused by electronic noise and the nature of the noise bursts. Photo D also shows the effect of filtering out responses below 100 KHz. Photos C and F show that negligible additional noise is attributed to operating the exoelectron scanner up (F) or down (C) along the specimen length. Figure 60 shows the acoustic response of the operating the fatigue cycling system. Photos A, B, and E show the acoustic emission spectrums for maximum, medium, and normal cyclic load conditions, respectively. These data indicate a relatively high level of energy in the 0 to 300 KHz frequency range, with some activity as high as 600 KHz. The data for normal load (photo E) would suggest that filtering to remove the energy below 300 KHz would provide a relatively constant energy level. Comparing the data in photos A and C shows that under maximum load conditions, a reduction in cyclic rate from 8 Hz (photo A) to 1 Hz (photo C) significantly reduces the overall energy spectrum, but high energy levels are still present in the 0 to 200 KHz range. Again, filtering out energy below 300 KHz would also provide a relatively constant energy level. The maximum load signal is further characterized in photo D. Photo F shows the spectrum for another load signal that appeared to occur at the cyclic rate.

Figure 61 shows the data obtained for acoustic emission bursts occurring at times other than the periodic machine bursts and produced by selecting extraordinarily high load conditions. These bursts are attributed to fatigue

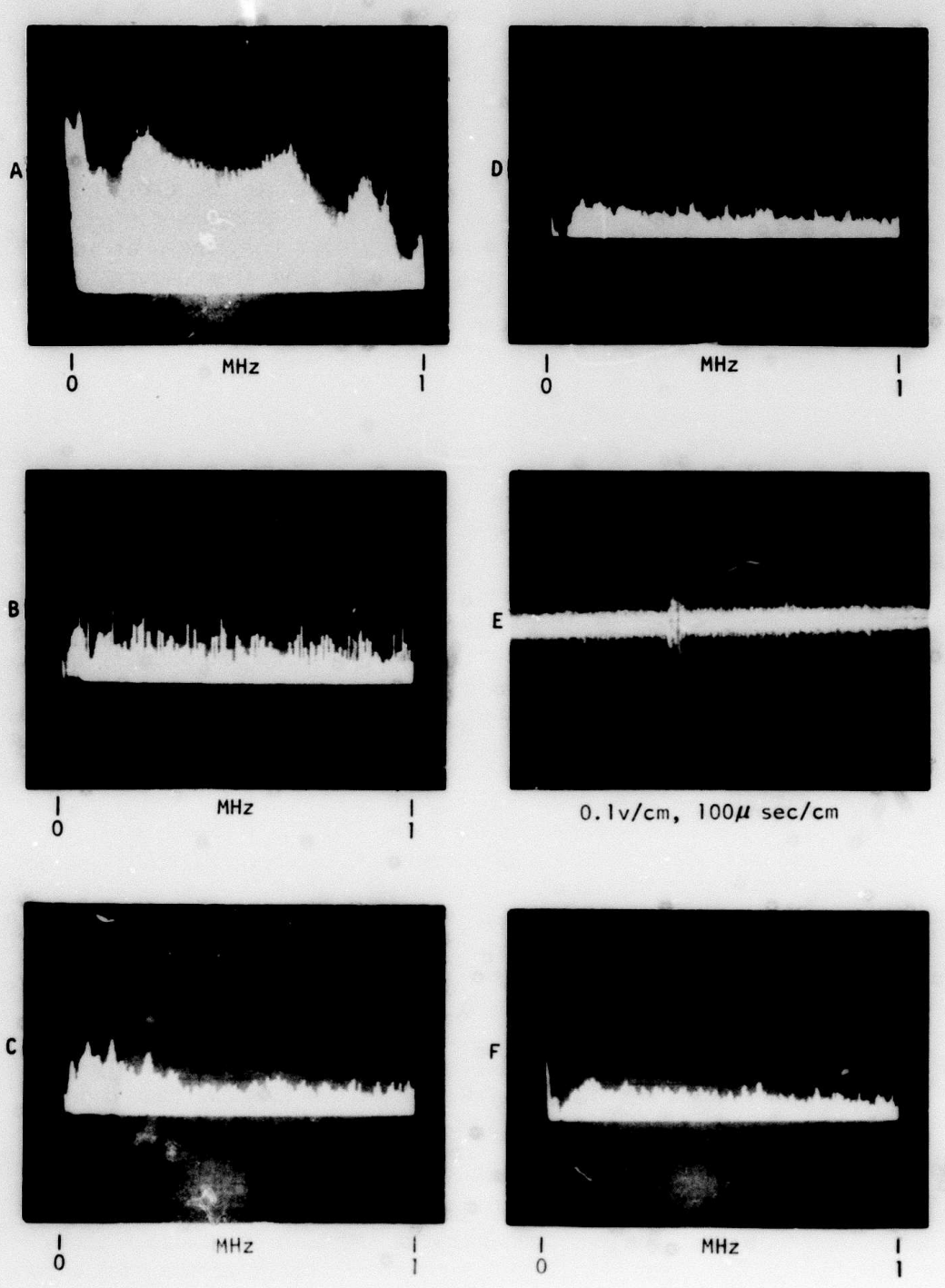

Figure 59. Acoustic emission data for calibration.

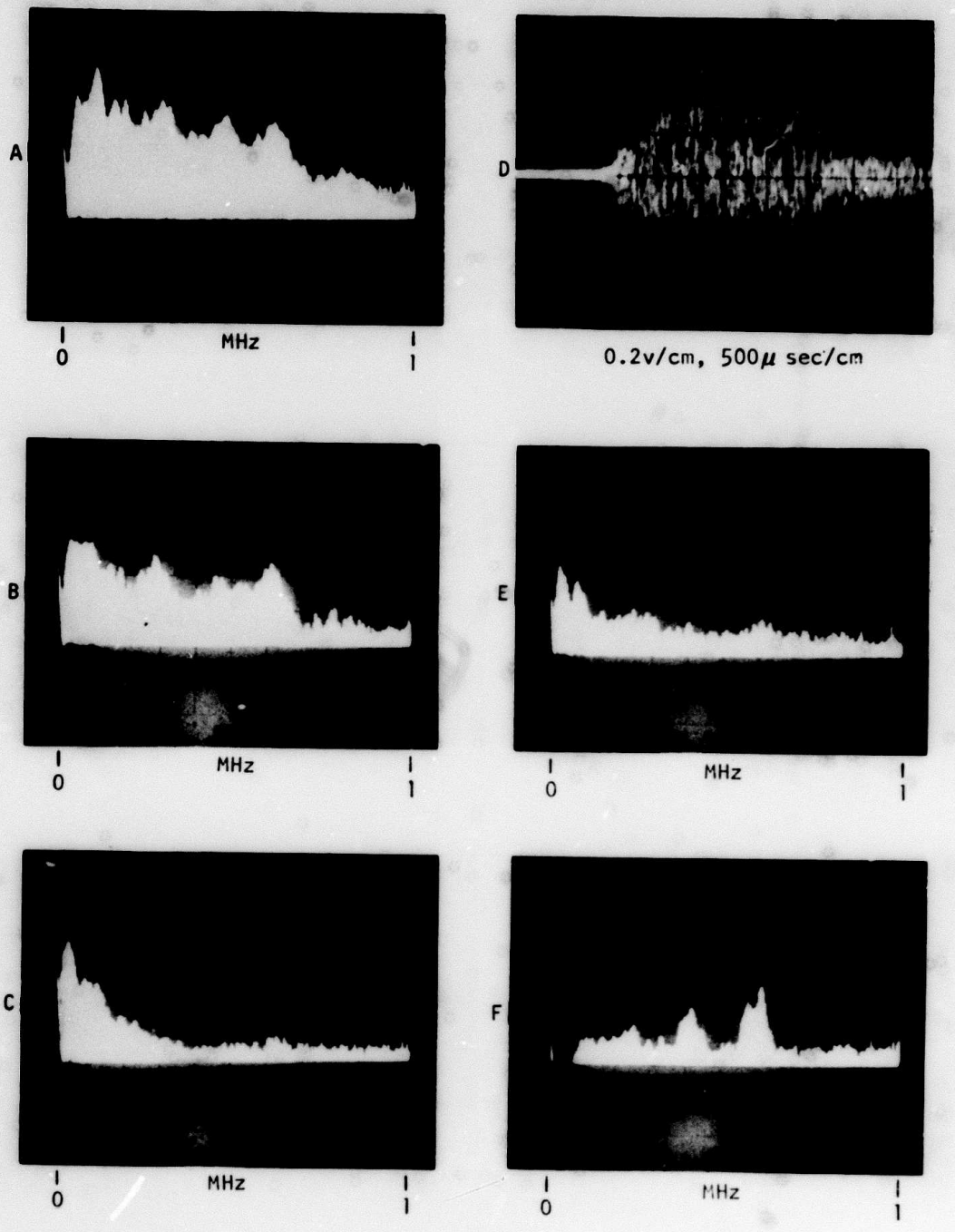

Figure 60. Acoustic emission data related to operation of fatigue loading equipment.

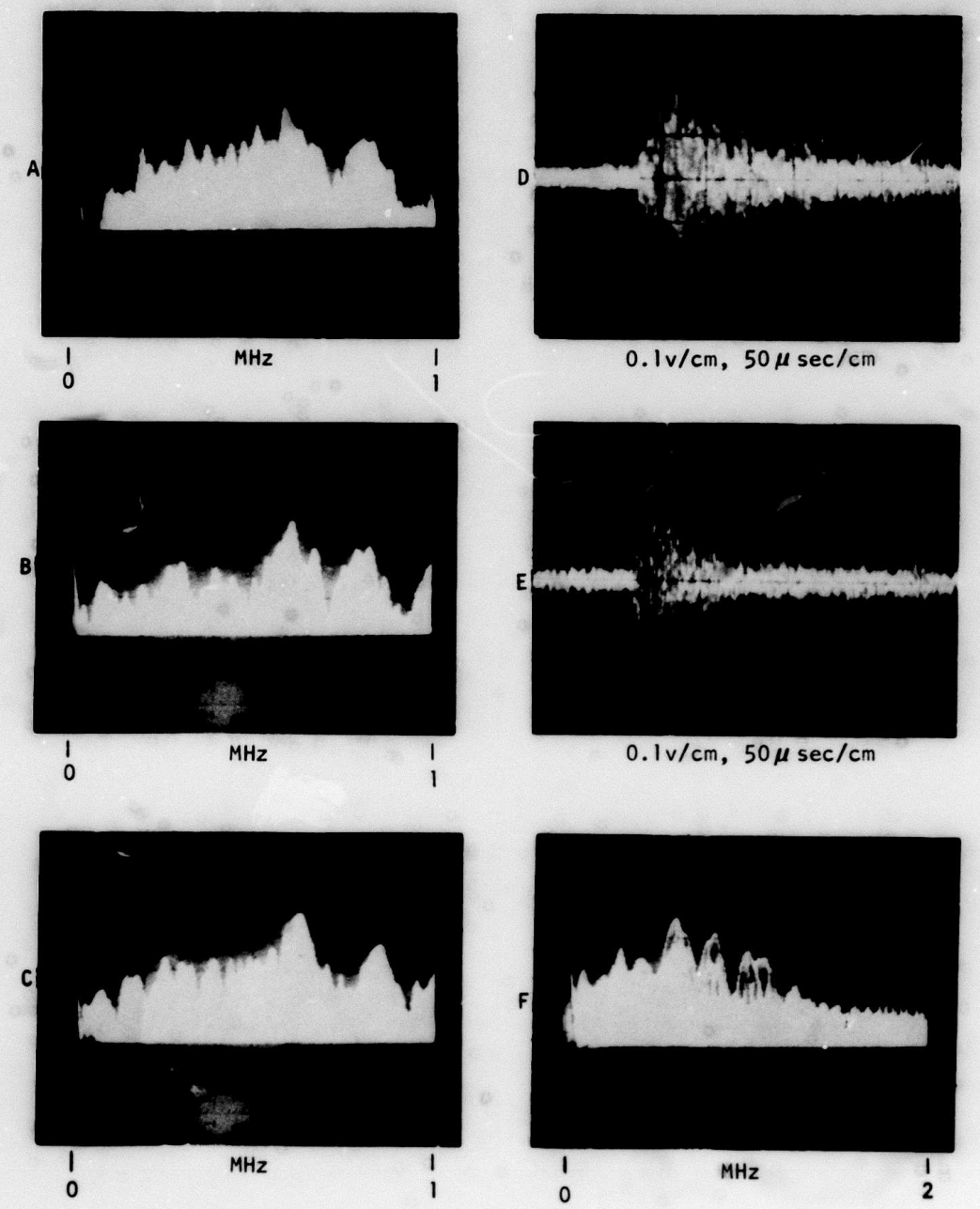

Figure 61. Typical acoustic emission data.

damage in the aluminum test specimen. The bursts frequency analyzed in photos A and B are shown as a function of time in photos D and E, respectively. Additional bursts are shown in photos C and F. It was generally observed that the frequency content of these bursts showed significant energy above 500 KHz, suggesting that a system capable of preferentially detecting bursts in the 0.5 to 1 MHz would provide data applicable to the aluminum test specimen. This approach is consistent with the earlier observation that the fatigue loading system bursts could be effectively reduced or eliminated by filtering out energy below 300 KHz.

An evaluation was also made of the cyclic nature of the load system bursts and the occurrence of fatigue related bursts as shown in Figure 62.

Three types of repetitive bursts are shown. Type 1 bursts are associated with the application of the fatigue load and typically occur at 8 Hz. Type 2 bursts were not identified. Type 3 bursts were relatively small and occurred approximately 180 degrees from the type 1 bursts. The acoustic emission bursts shown as random events not apparently related to the cyclic bursts were attributed to the aluminum fatigue damage. The exact nature and cause of the acoustic emission bursts occurring at the fatigue cyclic rate are unknown. It is believed that the bursts were characteristic of the particular hydraulic pump, servo valve, actuator and surge chamber. The fact that the bursts were repetitive allows one to assume that a certain number of acoustic events, if detected, can be attributed to the loading systems. Further, the frequency analysis of typical loading related bursts (Figure 60) showed that filtering should be effective in discriminating these from metal fatigue bursts. (Figure 61).

A series of 2024-T81 aluminum alloy specimens were monitored for acoustic emission characteristics during continuous fatigue cycling. The data from five of these specimens are plotted in Figure 63 to show the apparent relationship between the cumulative number of acoustic events and fatigue life. As noted, the applied loads of 26 and 28 ksi are very close and similar fatigue life data was expected; a large difference in acoustic characteristics was not expected. The specimen fatigue life data were very similar ranging from approximately 119,000 to 180,000 cycles. It is evident that this difference appears to be reflected in the acoustic emission activity with the specimens having the longer fatigue life exhibiting higher and earlier cumulative acoustic emission. Further, it is observed that the higher stress conditions tend to produce relatively lower initial acoustic emission activity. For example, comparing the increase in acoustic activity at the 10- and 50- percent levels of fatigue life, the lower stress condition shows a two to three times emission increase, while the higher stress level shows only a one to 1.75 times emission increase. The basis for these apparent relationships was not determined.

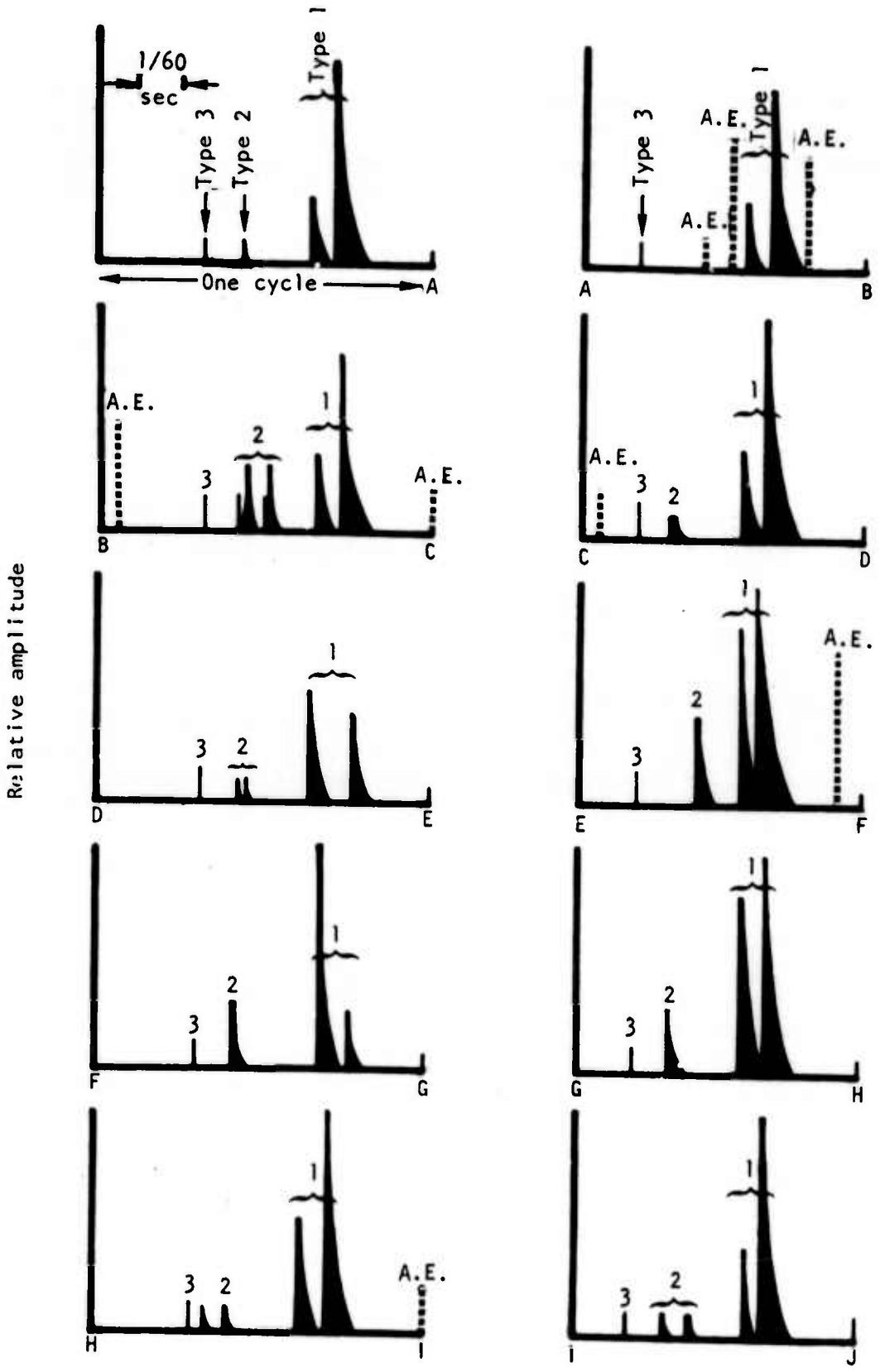

Figure 62. Relationship between acoustic events and fatigue cycling conditions.

•	H2	26 ksi	165,000 cycles
○	H3	26 ksi	180,000 cycles
◇	H4	28 ksi	165,000 cycles
△	H5	26 ksi	125,000 cycles
□	H8	28 ksi	119,000 cycles

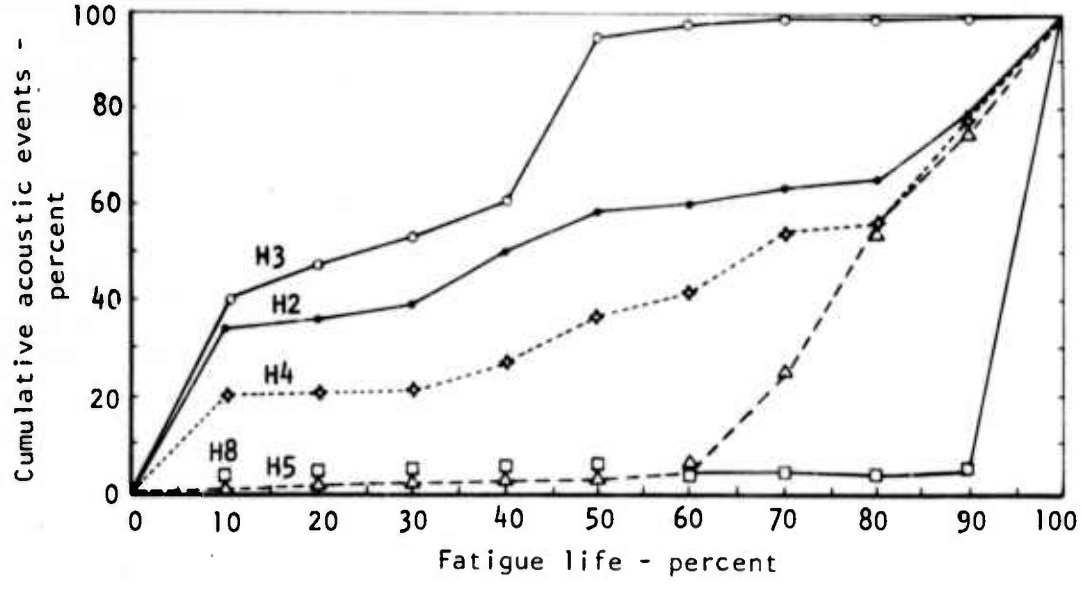

Figure 63. Relationship between acoustic emission events and fatigue life in 2024-T81 aluminum alloy specimens.

ULTRASONIC ATTENUATION

Earlier ultrasonic surface wave experiments to detect fatigue damage[1] showed that, although velocity measurements were not directly related to fatigue damage as evaluated, ultrasonic attenuation measurements appeared to show a possible correlation with fatigue damage.

The attenuation measurements were made with a newly developed ultrasonic measurement system capable of making comparative measurements along the length of a specimen. It was planned that such a system would have the potential for scanning a part and detecting/measuring attenuation changes relating to fatigue damage. The surface wave was generated by commercial wedge transducers driven by 10 μsec, 200-volt RF bursts from an Arenberg pulsed oscillator. The transducer was centered in one end of the specimen and so directed that energy would propagate through the test section (Figure 64). A laser probe and the associated electronic device were used to determine the amplitude of the surface vibration as well as its phase relative to that of the driving electrical signal. Attenuation was measured by noting the change of amplitude with distance from the source. The laser detection technique depends on reflecting light from the specimen surface and the surface reflectivity of the fatigued specimen was quite poor. The laser system measurements were adversely affected by the generation of several wave modes causing indefinite wave mode definition. It was concluded that an improved means of controlling the ultrasonic wave generation and propagation was required. An experiment was made to determine if improved coupling reproducibility could be obtained using commercial-type transducers applied with a constant force and a low viscosity coupling film.

A series of experiments were performed using Automation Industries type 57A3076 and 57A3063 surface wave transducers operating at 10 and 5 MHz, respectively. The transducers were yoked together at a 101.6-mm (4-inch) spacing to insure the same transmission distances for repeated measurements. A deadweight load of approximately 3 pounds was used to provide a constant coupling force. The acoustic coupling fluid was Dow Corning 200 silicone oil. An Immerscope model 725 was used for the ultrasonic pulser-receiver system and was operated in the through-transmission, two-transducer mode.

Preliminary tests were made on six prefatigued 2024-T81 aluminum specimens which were subsequently fatigued to failure. The attenuation data is shown in Figure 65 as a function of the percent of fatigue life. Both 5 and 10 MHz data are plotted. Each data point represents an average of the two attenuation measurements taken from the two sides of each specimen. The 5 MHz data shows an initial increase in ultrasonic energy with a leveling off between 40 and 75 percent of the fatigue life. The 10 MHz data also shows an initial energy increase, but appears to decrease as the fatigue process continues. The reason for the difference between these two plots is unknown.

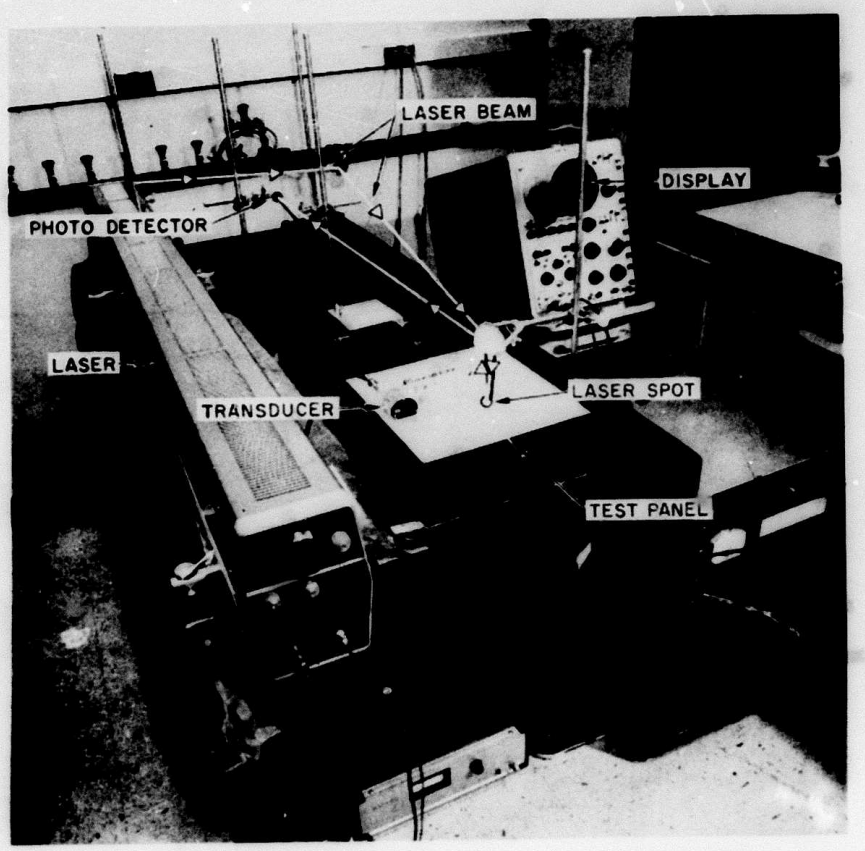

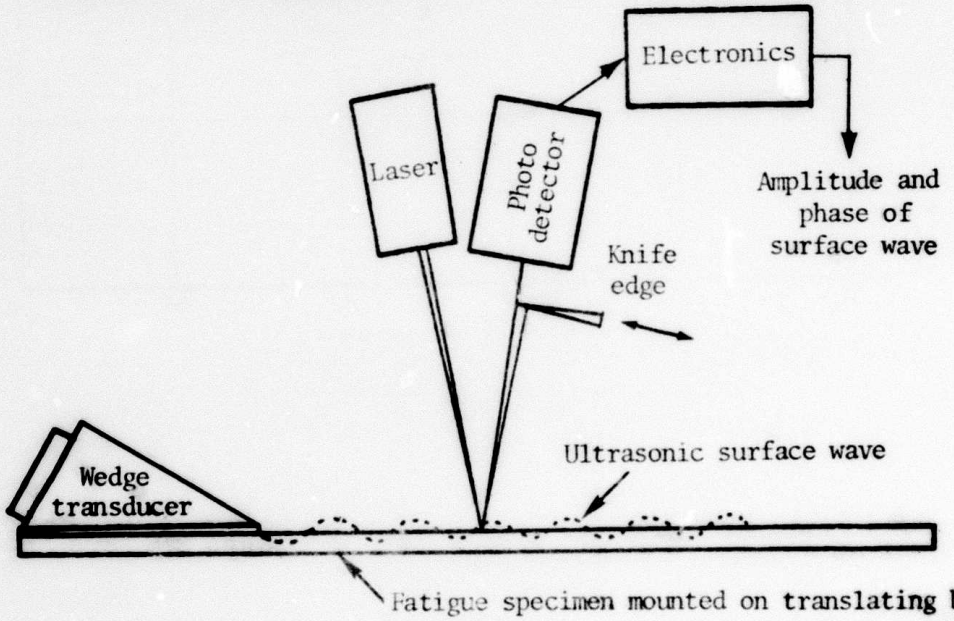

Figure 64. Photograph and schematic diagram of the ultrasonic surface wave measuring system.

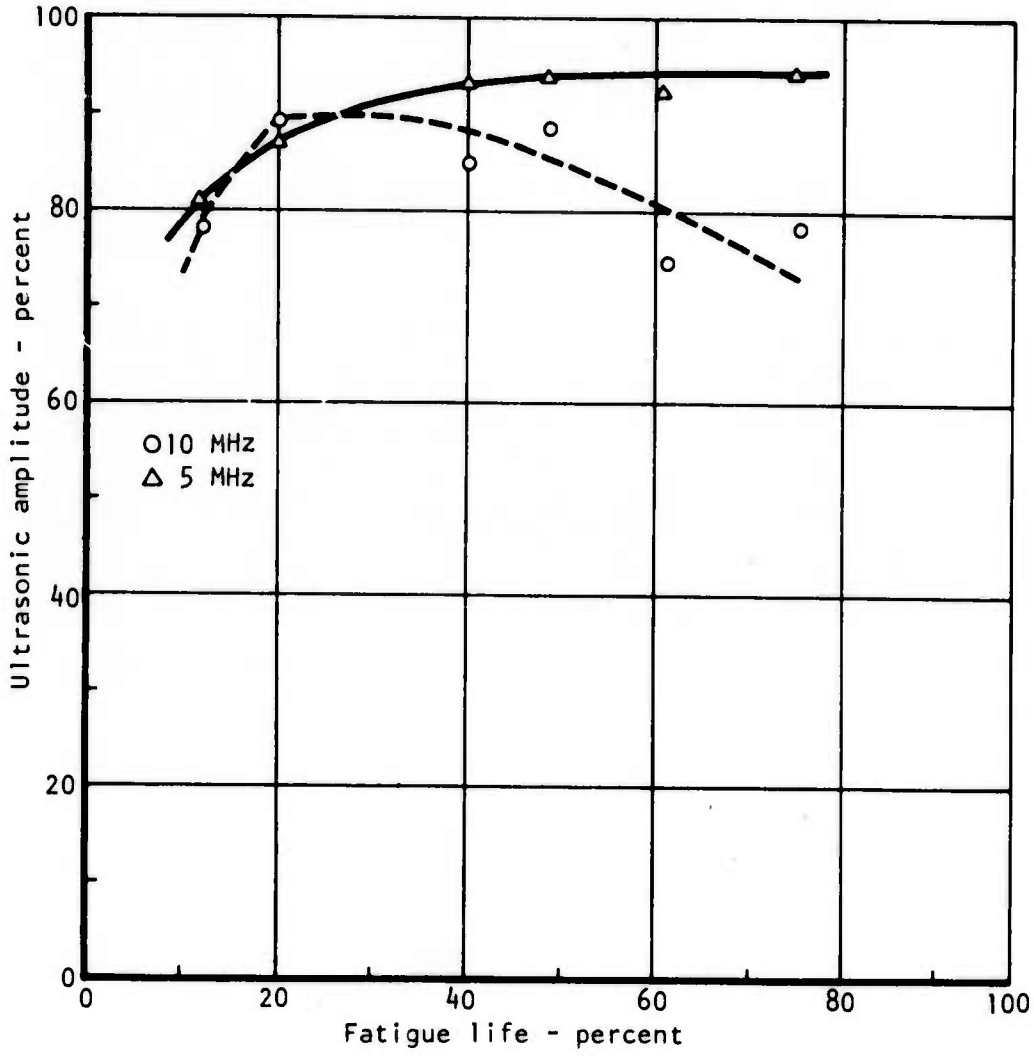

Figure 65. Relationship between ultrasonic attenuation and fatigue life in aluminum 2024-T81 specimen.

It is possible that, at the higher test frequency and decreased depth of penetration, the surface fatigue damage may affect a higher proportion of the surface wave energy.

Section VIII

PROTOTYPE EXOELECTRON EMISSION TEST SYSTEM

This section describes the development of the exoelectron emission test system used for the laboratory experiments, the development of transducers for inspecting variously shaped structures, the development of a mechanical scanner system, and the evaluation of methods used to improve the stimulation of the exoelectron emission and prepare the surface of a test material prior to inspection.

LABORATORY TEST SYSTEM

A brief description of the experimental system used for the majority of exoelectron emission tests is given to provide both a clearer understanding of the system and to provide a basis for the prototype system. A simplified block diagram of the complete NDT system, scanning system and fatigue loading system is shown in Figure 66. Details of the fatigue loading system are shown in Figure 67. Wiring interconnections for the exoelectron emission measuring system and scanner are shown in Figure 68. It should be evident that the experimental system is basically an assembly of general laboratory equipment and provides the flexibility necessary for laboratory type evaluations. During laboratory testing, it became necessary to transport the exoelectron emission measurement system and scanner to another building for fatigue tests on another fatigue machine. All of the necessary equipment was installed on an equipment cart to provide a portable test system.

The system operation was optimized in terms of the reliability of the exoelectron emission measurement. Scan rates of approximately 25 to 50 mm (1 to 2 inches) per minute were generally used. Although the scanner could have been operated continuously during the fatigue test, it was not considered likely that an error of several thousand cycles in fatigue life periods of 1 to 10 million cycles in detecting a change in exoelectron emission would be significant, nor would an instance occur where an emission would initiate and then cease in a similar period. Therefore, using a selector switch on the load cycling programmer, an exoelectron scan could be made at either 10^2, 10^3, or 10^4 load cycles. The sensing transducer was moved at a preset rate along the surface of the specimen. The length of the scan is determined by limit switches. The magnitude of the electron current was measured using a Kethley model 602 electrometer operated in the "fast" feedback mode. The output plug of the Keithley provides a signal to a Brush recorder. The recorder chart drive operated only during the periods in which the specimen was scanned. Automatic operation of the sensing, scanning, and recording functions permitted the unit to perform reliably while unattended at night or on weekends, as required for high cycle fatigue experiments.

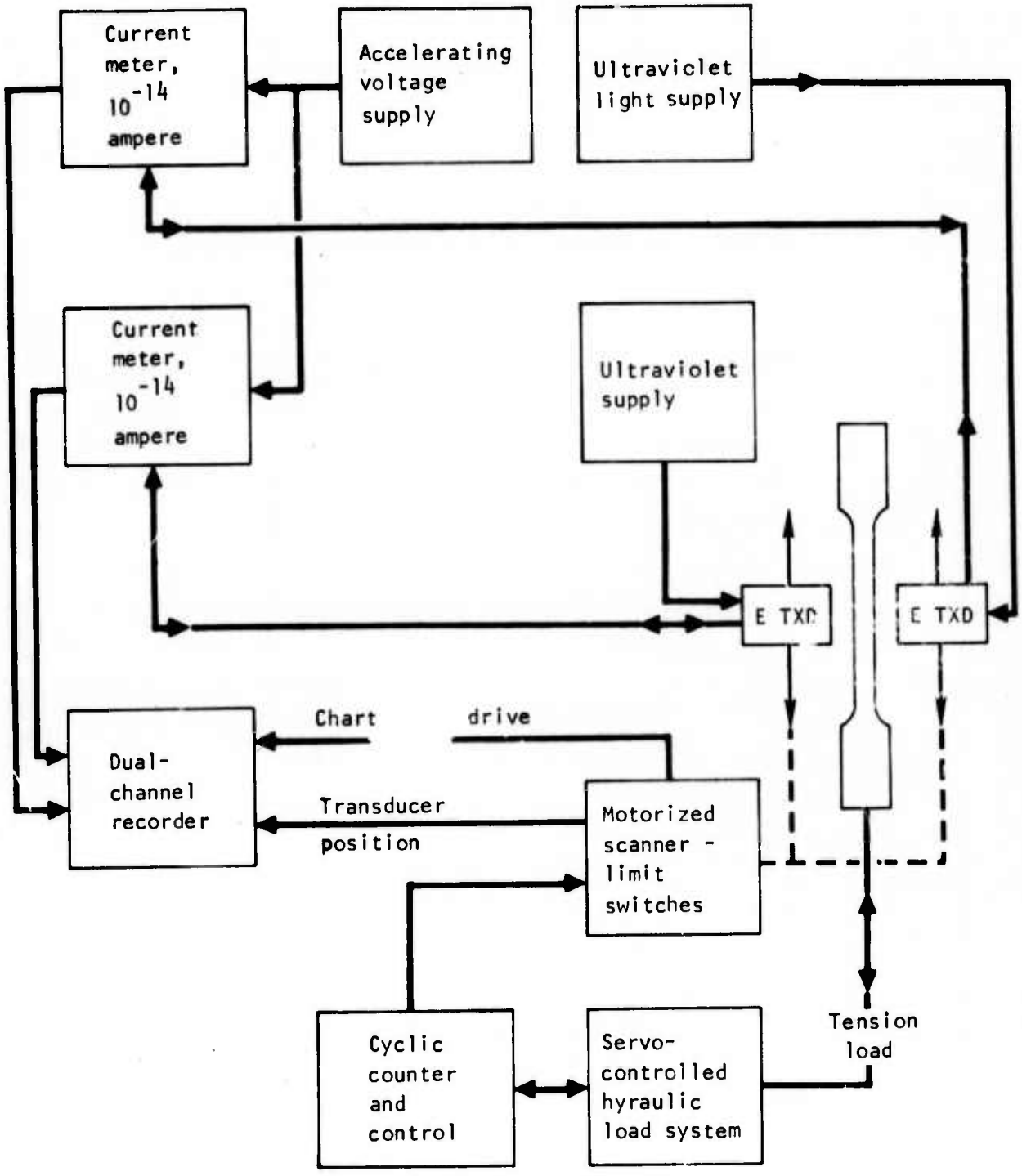

Figure 66. Simplified block diagram of exoelectron emission NDT system and scanner.

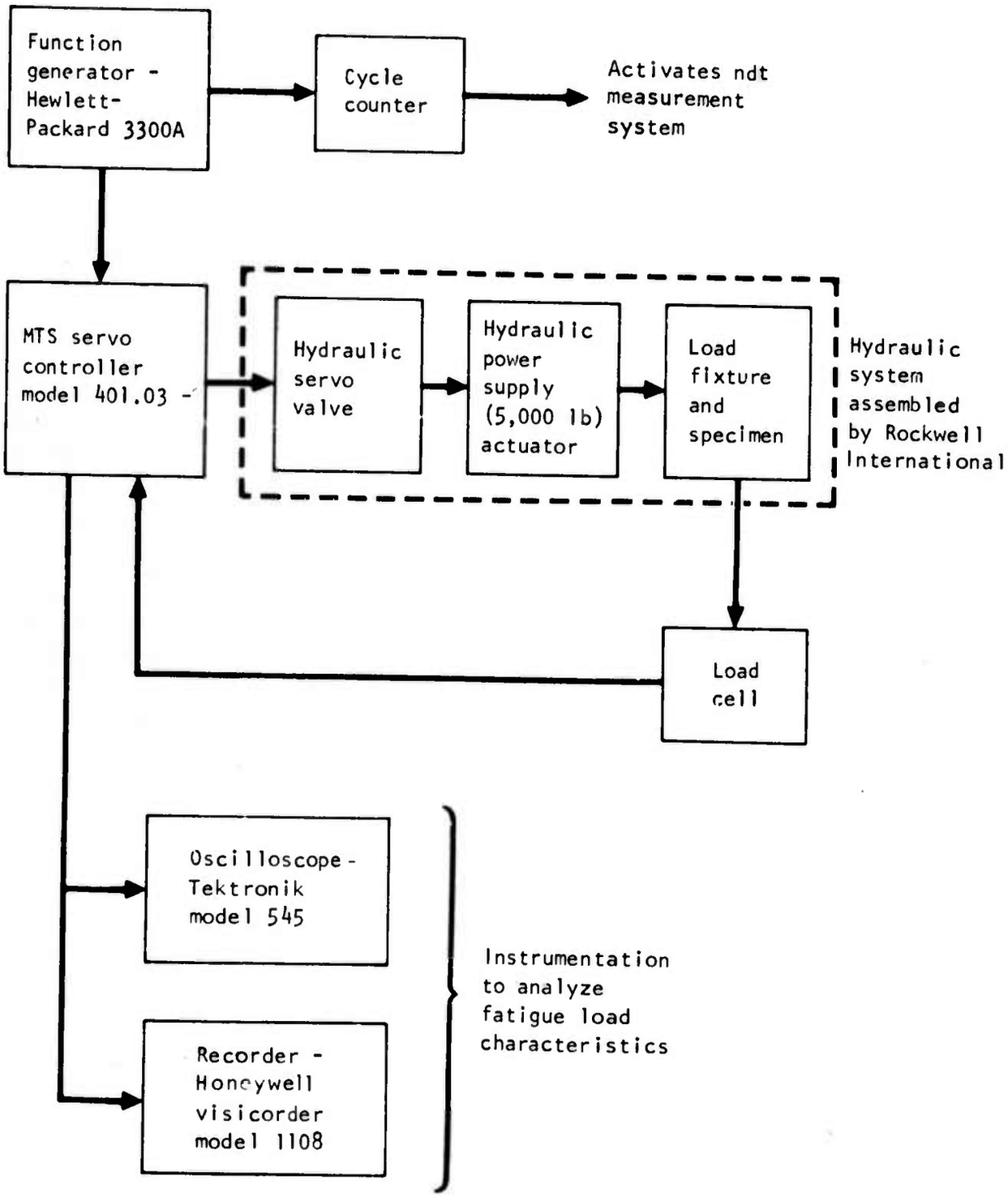

Figure 67. Block diagram of fatigue loading system.

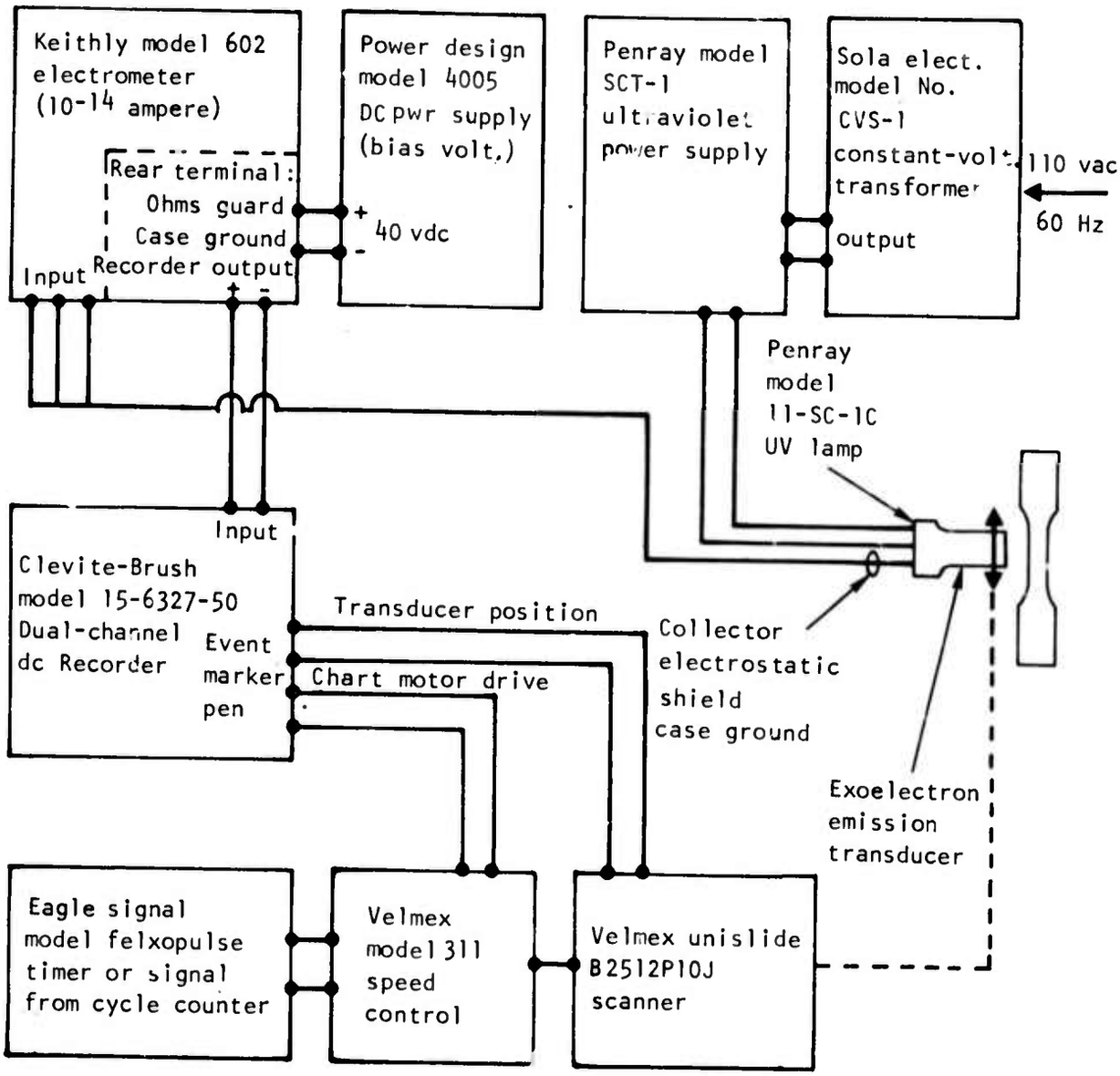

Figure 68. Wiring schematic for exoclectron emission test and measuring system.

EXOELECTRON CURRENT MEASURING SYSTEM AND TRANSDUCERS

A handheld exoelectron emission transducer was developed in which the current detector is located at the end of a cylindrical housing. The transducer dimensions are nominally 19 mm (0.75-inch) in diameter and 76 mm (3 inches) long. This design approach has the advantage of using the transducer in the manner of a flashlight, thereby facilitating handling and scanning requirements. The transducer uses an altraviolet source in which the light emerges from a flat window at the end of the tubular lamp. Figure 69 shows the individual components of the transducer. The ultraviolet light passes through an aperture mask to the test specimen. These masks are interchangeable and have apertures of different shapes and sizes depending on the desired inspection area. The mask material is copper clad on both sides. The front surface of the mask collects the exoelectrons for the current measurement and the rear surface acts as an electrostatic shield to reduce noise and interference.

A special exoelectron emission transducer was developed for measuring the effects of fatigue damage inside a hole 12.7 mm (0.5 inch) diameter with 2.5-mm-diameter (0.1 inch) side notches and located in a 12.7 mm (0.5 inch) thick 2219 T-851 aluminum specimen (Figure 42). The transducer was developed by fitting a commercial Penray ultraviolet lamp assembly with a slotted sheath to allow projection of a relatively long and narrow beam. The emission detector was prepared by painting a silver conducting stripe around the periphery of the ultraviolet aperture and installing an electrical shield. During test, the transducer in pencil form was positioned within the 12.7-mm-diameter (0.5-inch) hole and rotated to produce a scanning beam which impinged on the opposite and interior surfaces of the 2.5-mm-diameter notches. The transducer was rotated to obtain a maximum exoelectron emission current level. These experiments were successful in the early detection of fatigue damage and microcracking in this particular material configuration and stress concentration conditions (Figure 42).

Based on this evaluation, a transducer was developed for scanning holes without side notches. This transducer was fitted with locating pins so that it could be readily inserted for an exoelectron measurement along a line of holes as illustrated in Figure 70. The transducer was successfully used on additional 2219-T851 aluminum fatigue tests.

A dual exoelectron emission transducer assembly was developed to allow simultaneous current measurements on both sides of the fatigue specimen. Details of the flat surface transducer are shown in Figure 71. Figure 72 shows the complete assembly used for noncontact inspection of the specimen surfaces.

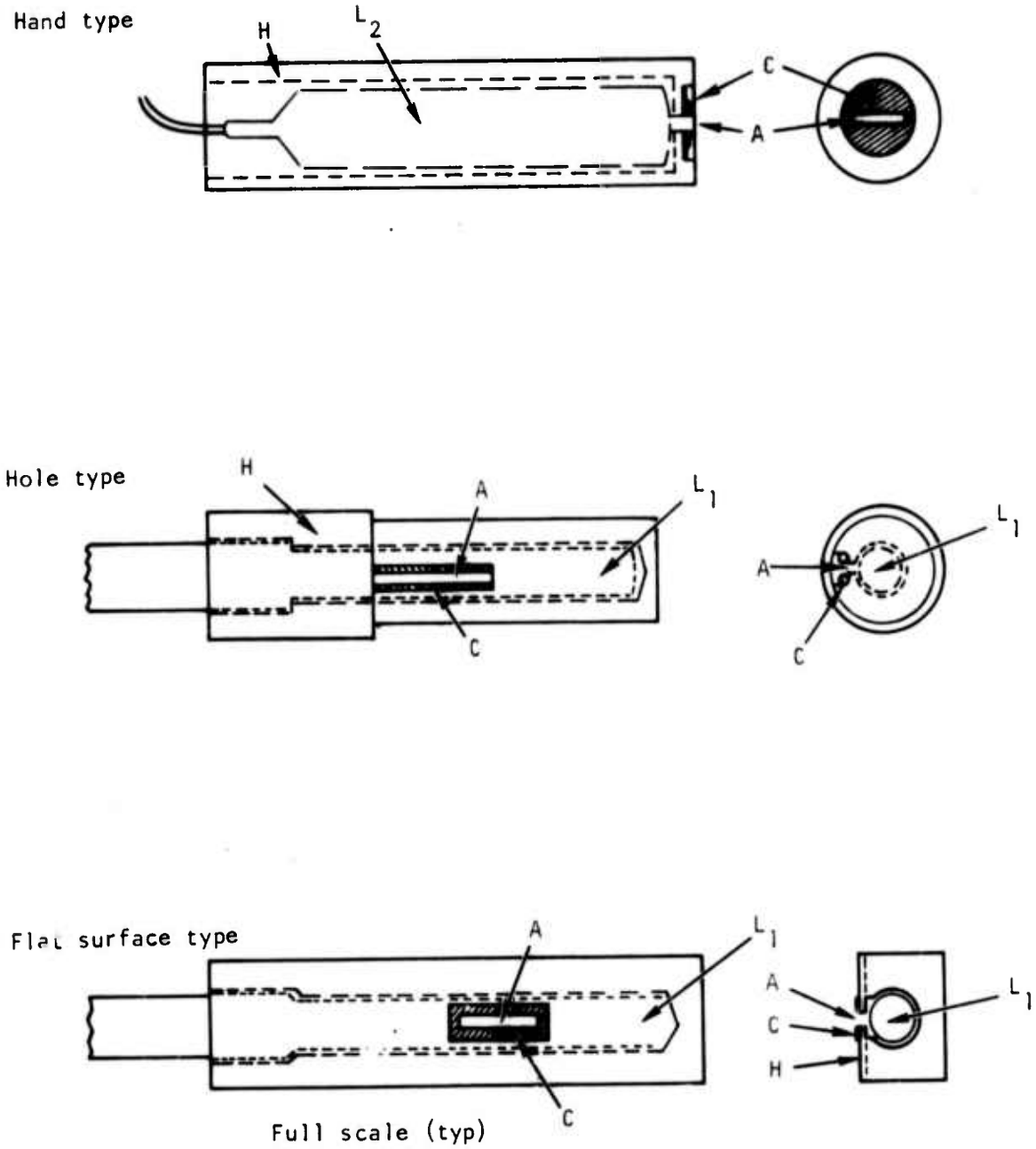

L_1 - Lamp (Penray 11-SC-1C)
L_2 - Lamp (Penray AD-004A)
A - Aperture (1.6 mm width)
C - Collector electrode
H - Housing (polycarbonate)

Figure 69. Prototype exoelectron emission transducers.

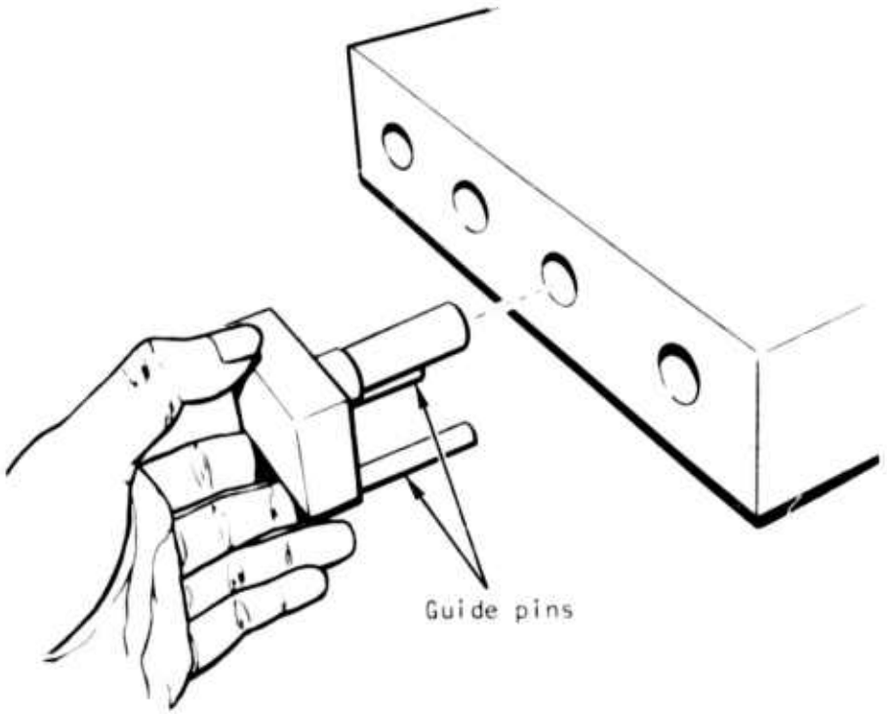

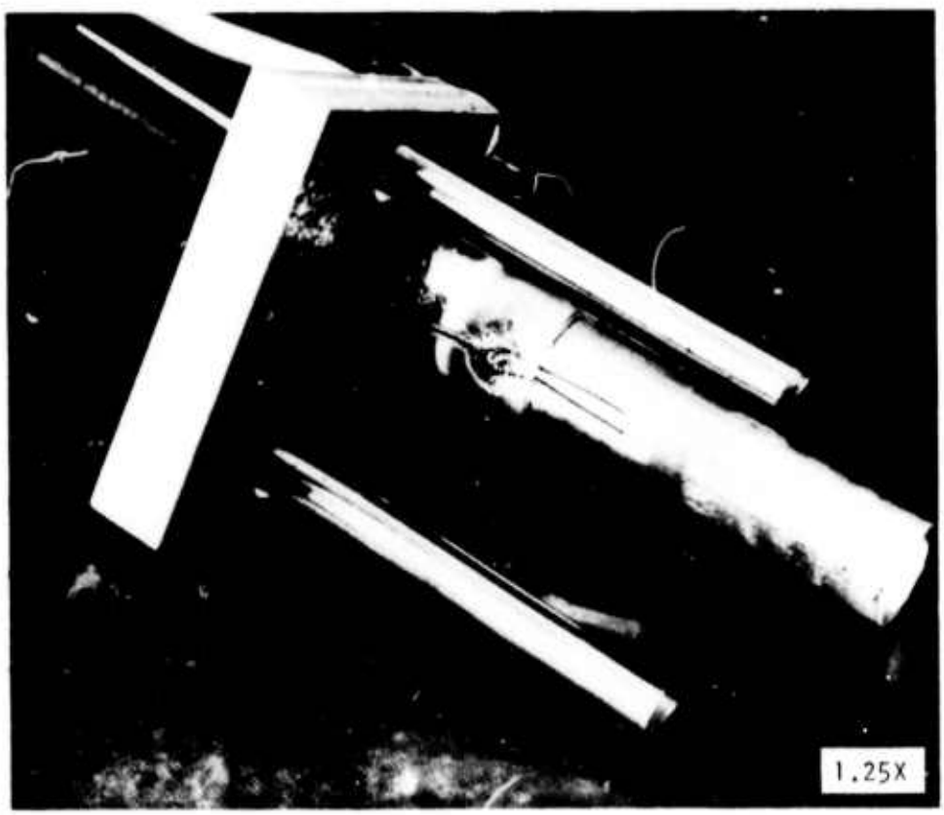

Figure 70. Exoelectron emission transducer assembly for testing inside holes.

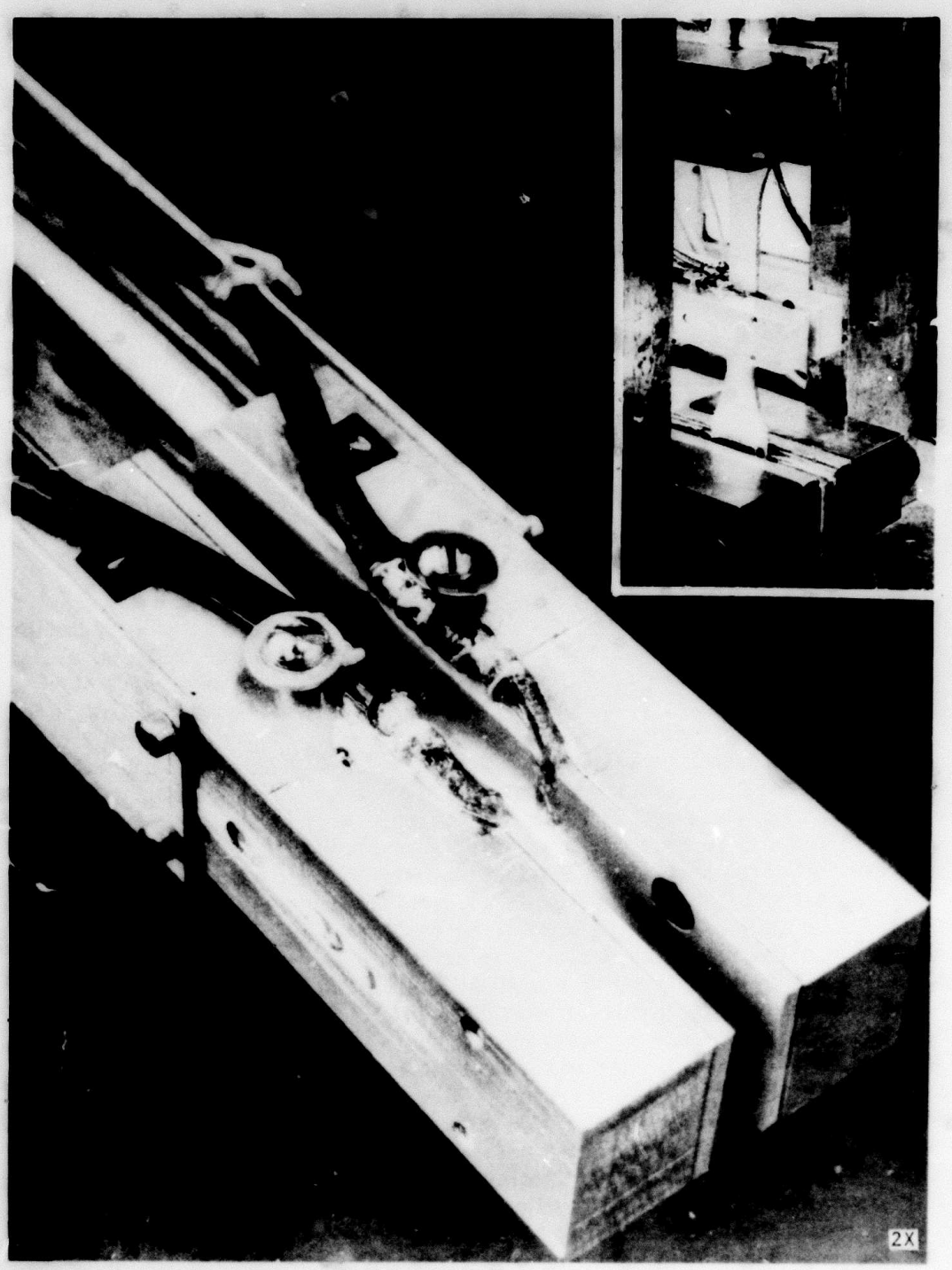

Figure 71. Dual exoelectron emission transducer assembly used for simultaneous measurements on both sides of specimen.

MECHANICAL SCANNER ASSEMBLY

The design requirements for the mechanical scanner are as follows:

1. Provide a stable reference plane for accurately positioning and scanning the exoelectron emission transducer.

2. Scan travel rate to be constant and adjustable from approximately 25 to 254 mm per minute (1 to 10 inches per minute).

3. Scan travel distance approximately 305 mm (12 inches).

4. Scan direction to be reversible with the potential for translating the transducer in a direction at right angles to the scan direction to provide a raster type x-y scan capability.

5. Potential scan capability for inspecting inside holes.

6. Scan mechanism life in the order of 100,000 cycles.

Based on these requirements, a number of mechanical scanner manufacturers were contacted to determine the availability and approximate costs of a commercial unit. The most promising motor-driven scanner was the Velmex UniSlide assembly ranging in cost from $100 to $500, depending on length and drive control requirements. These scanners consist of a UniSlide mechanical slide unit specifically designed for motor driven application, adjustable limit switch control, and speed control circuitry. These scanners may be compounded to produce xy, xz, or xyz coordinate axis motions. The mechanical slide which would support the transducer assembly consists of an aluminum 60-degree dovetail stock which has been precision machined and lapped and fitted with molydisulfide impregnated Teflon sliding elements. The slide is typically capable of supporting loads up to 30 pounds. A Velmex UniSlide assembly was evaluated for scanning specimens in the fatigue machine. The scanner assembly was fitted with a dual exoelectron emission transducer assembly to provide measurement data from both sides of the test specimens during fatigue. The lead screw projects beyond the opposite or open end of the UniSlide assembly and was fitted with a momentary switch circuit to provide a signal for each complete shaft rotation. This signal is recorded as a spike on the same record with the exoelectron emission current and provides a positive identification for the transducer position relative to the specimen. This spike is also used to identify discrete locations for the point by point data analysis method. A prototype design was prepared for adapting this type of scanner to various inspection applications. This design is shown in Figure 74. Here the transducer is positioned at a fixed distance from the specimen surface using a spring-loaded Teflon roller assembly fitted on the opposite side of

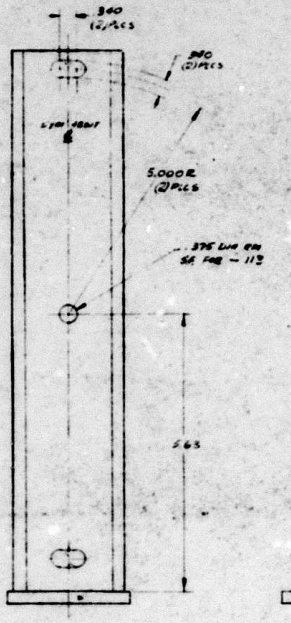

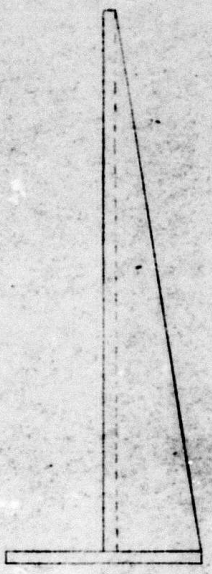

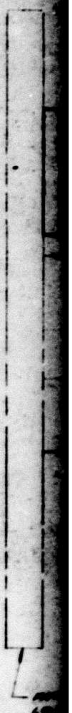

(101) COMMERCIAL ITEM: NEWARK # AS SHOWN SK 16307 SCALE: 1/1

(117) SK 16307 SCALE: 1/1

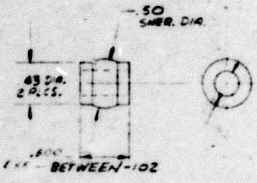

(121) SK 16307 SCALE 1/1

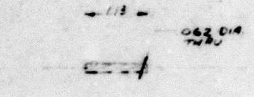

(111) SK 16307 SCALE 1/1

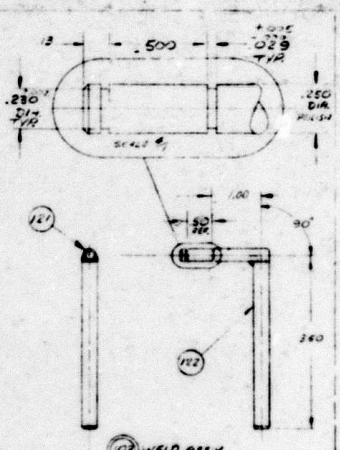

(103) WELD ASSY SK 16307 SCALE 1/1 NOTED

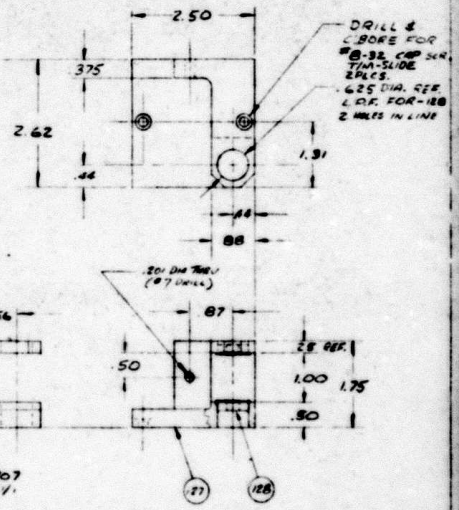

(109) SK 16307 SCALE 1/1

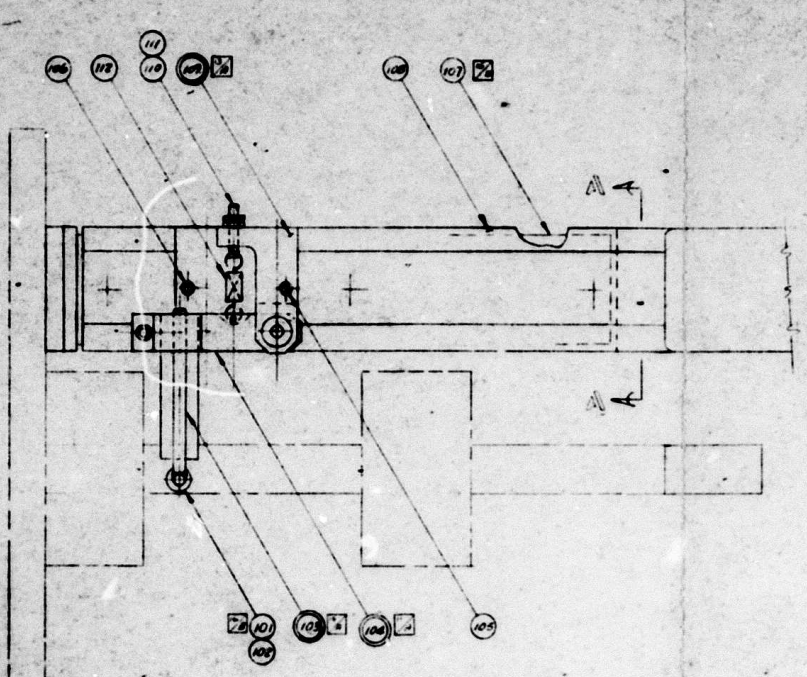

FATIGUE TEST MACHINE
LOCATED IN DEPT. (1) IS 1802

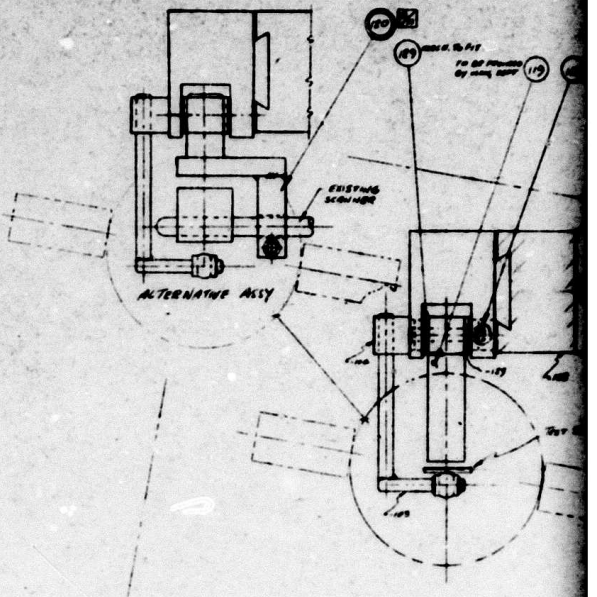

SECT. A-A

DRILL & C'BORE FOR
#8-32 CAP SCR.
TYP-SLIDE
SPACES.
.625 DIA. SEE
L.AT. FOR 1-18
2 HOLES IN LINE

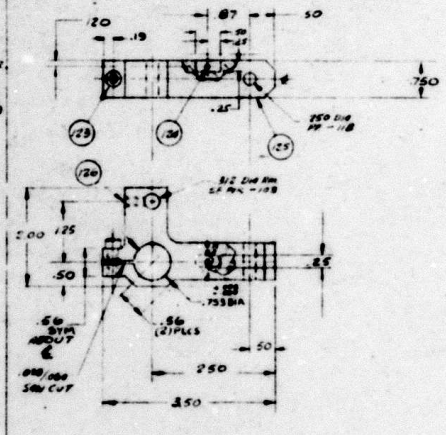

(104) SK 16307
SCALE 1/1

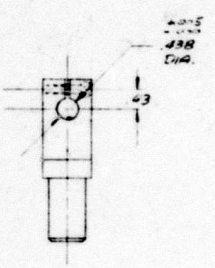

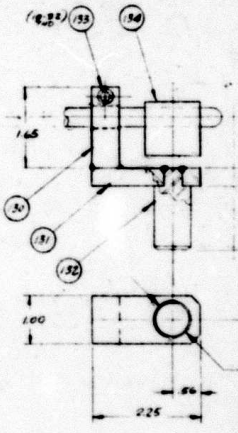

(120) WELD ASSY
SK 16307
SCALE 1/1

	FRAME 2		
	SK16307		1

B

REVISIONS			
	DESCRIPTION	DATE	APPROVED
	DESIGNED PER LETTER FROM TF MOORE D 115 DATED 10/31/78		

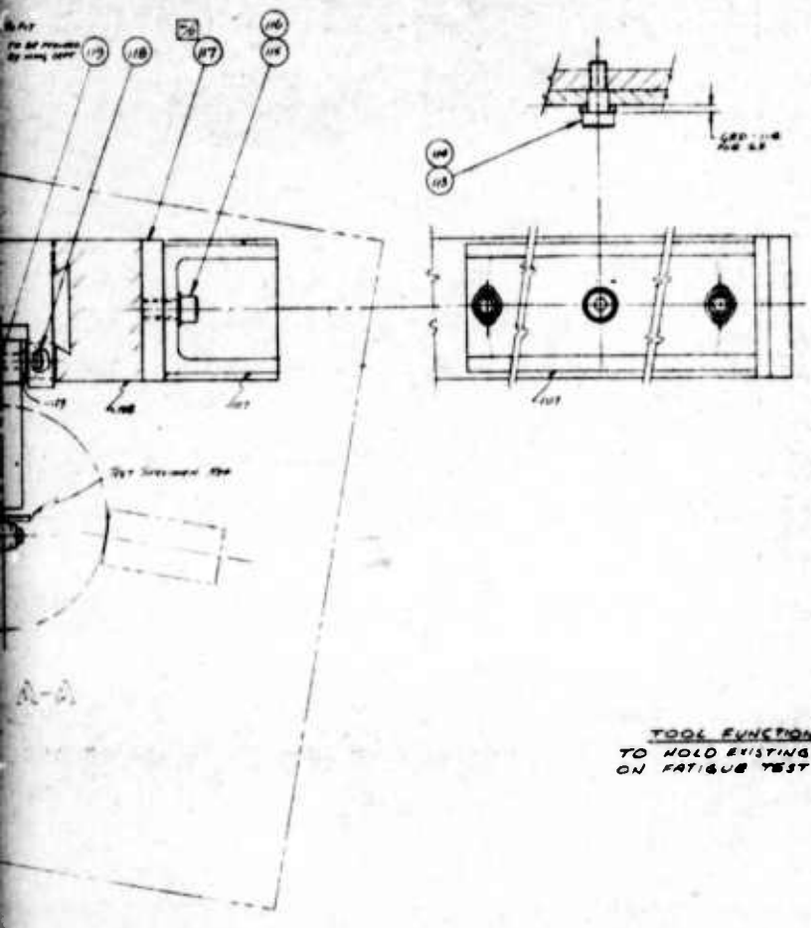

TOOL FUNCTION:
TO HOLD EXISTING TRANSDUCERS ON FATIGUE TEST MACHINES

NOTES:
1. SCALE DIM'S NOT SHOWN W/N.I.09
2. DEPT. (11) 115, 3802 S TO MOUNT HARDWARE ON FATIGUE TEST MACHINES
3. WELD PER TPS 40

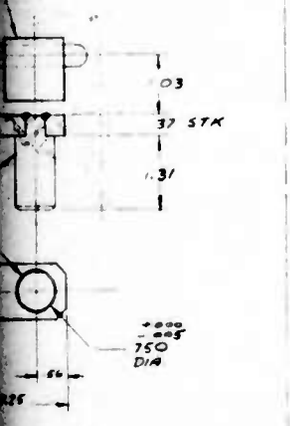

CONTRACT FED TPS 10	UNLESS OTHERWISE SPECIFIED DIMENSIONS ARE IN INCHES	CONTRACT	73657-70C-0
TOLERANCES FED TPS 14	TOLERANCES ON DECIMALS ANGLES .X ± .03 .XX ± .01 .XXX ± .005 ±1°	DESIGNED	D. Gandolfi 11/11/78
FINISH PER STANDARD SHOP PRACTICE		CHECKED	G. MILLER 11/9/78
			11/12/78
			11/27/78
THIS TOOL MUST BE COORDINATED WITH	THIS TOOL ACCOMMODATES	MFG RELEASE	

B-1 Division
North American Rockwell
INTERNATIONAL AIRPORT LOS ANGELES, CALIFORNIA 90009

TOOL DESIGN

SCANNER, CONSTANT RATE. FATIGUE SPECIMEN

SIZE	CODE IDENT. NO.	TOOL NO.
J	43999	SK16307

SCALE/FULL | DRAWING SHEET — | SHEET 1 OF 2

ITEM	QTY	PART NO.	DESCRIPTION	MATERIAL
120	1		SUB ASSY	
121	1		ALUM ROD (6061-T6)	
122	1		ALUM ROD (6061-T6)	
123	2		SOC HD CAP SCR	
124	2		SPACER (6061-T6)	
125	2		ALUM (6061-T6)	
126	2		SOC SET SCR	
127	2		ALUM (6061-T6)	
128	4		FLANGED BALL BEARING (SEE MAINT MAN)	
129	4		ALUM TUBING (SEE MAINT MAN)	
130	1		ALUM (6061-T6)	
131	1		ALUM (6061-T6)	
132	1		ALUM (6061-T6)	
133	1		SOC HD CAP SCR	
134	1		TEE HANDLE ASSY, PURCHASED BY USING DEPT	

ITEM	QTY	PART NO.	DESCRIPTION	MATERIAL
101	1		BASE ASSY	
102	4		STANDOFF (SEE MAINT MAN)	
103	2		HEX NUT	
104	2		SUB ASSY	
105	2		SOC HD CAP SCR	
106	2		SOC HD CAP SCR	
107	1		HANDLE ASSY (SEE MAINT MAN)	
			DEPARTMENT 01/115, 3802.	
108	1		PURCHASED SLIDE; PROVIDED BY USING DEPT 01, 115, 3802.	
109	2		SUB ASSY	
110	2		TOOL STEEL - STEEL OR EQUAL	
111	4		LOCK NUTS STEEL OR EQUAL	
112	2		SPRING (SEE MAINT MAN)	
113	1		SPACER SUB	
114	1		STEEL HOUSE	
115	2		SOC HD CAP SCR	
116	2		STD STK WASHER	
117	2		CRS	
118	2		TRANSDUCER SEE SHOP TOOL (SEE MAINT MAN)	
119	2		TRANSDUCER PURCHASED BY USING DEPT	

1

REVISIONS					
ZONE	LTR	DESCRIPTION	DATE	APPROVED
		DESIGNED PER LETTER FROM J.F. MOORE D/115 DATED 01/31/75		

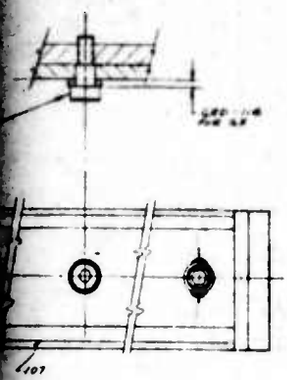

TOOL FUNCTION:
TO HOLD EXISTING TRANSDUCERS ON FATIGUE TEST MACHINES

NOTES:
1. SCALE DIM'S NOT SHOWN W/115.03
2. DEPT. (11) 115.5802 S TO MOUNT HARDWARE ON FATIGUE TEST MACHINES
3. WELD PER TPS 40

CONTRACT	73965-70C-0		
DESIGNED	D.GUMAN	11 11 72	
CHECKED	G.MILLER	11/14/73	
		11 12 73	
APPROVED		11/14/73	

B-1 Division
North American Rockwell
INTERNATIONAL AIRPORT LOS ANGELES, CALIFORNIA 90009

TOOL DESIGN

SCANNER, CONSTANT RATE. FATIGUE SPECIMEN

SIZE	COST CENTER NO.	TOOL NO.
J	43999	SK16307

SCALE FULL | OBSOLETE SHEETS — | SHEET 1 OF 2

Constant-rate mechanical scanner.

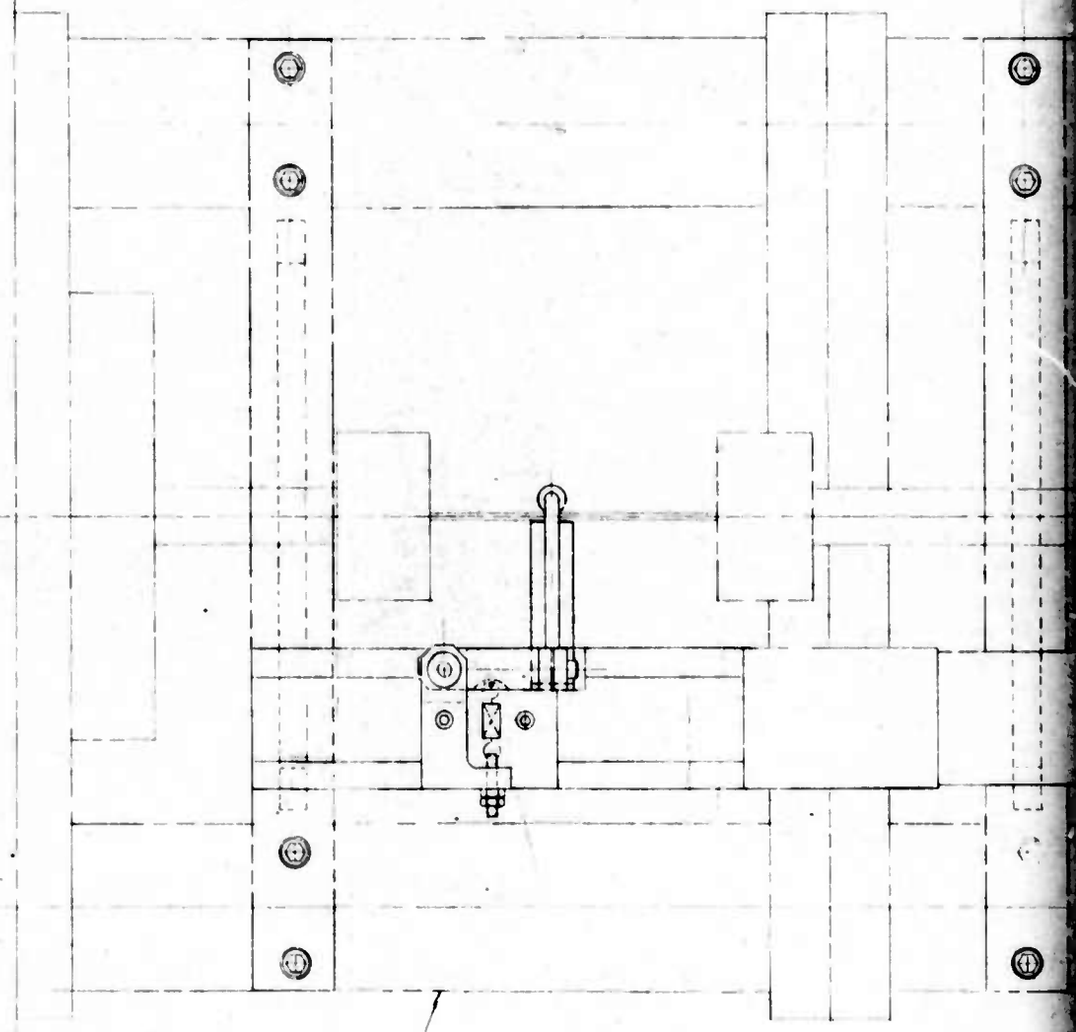

FATIGUE TEST MACHINE
LOCATED IN STRUCTURS LAB.

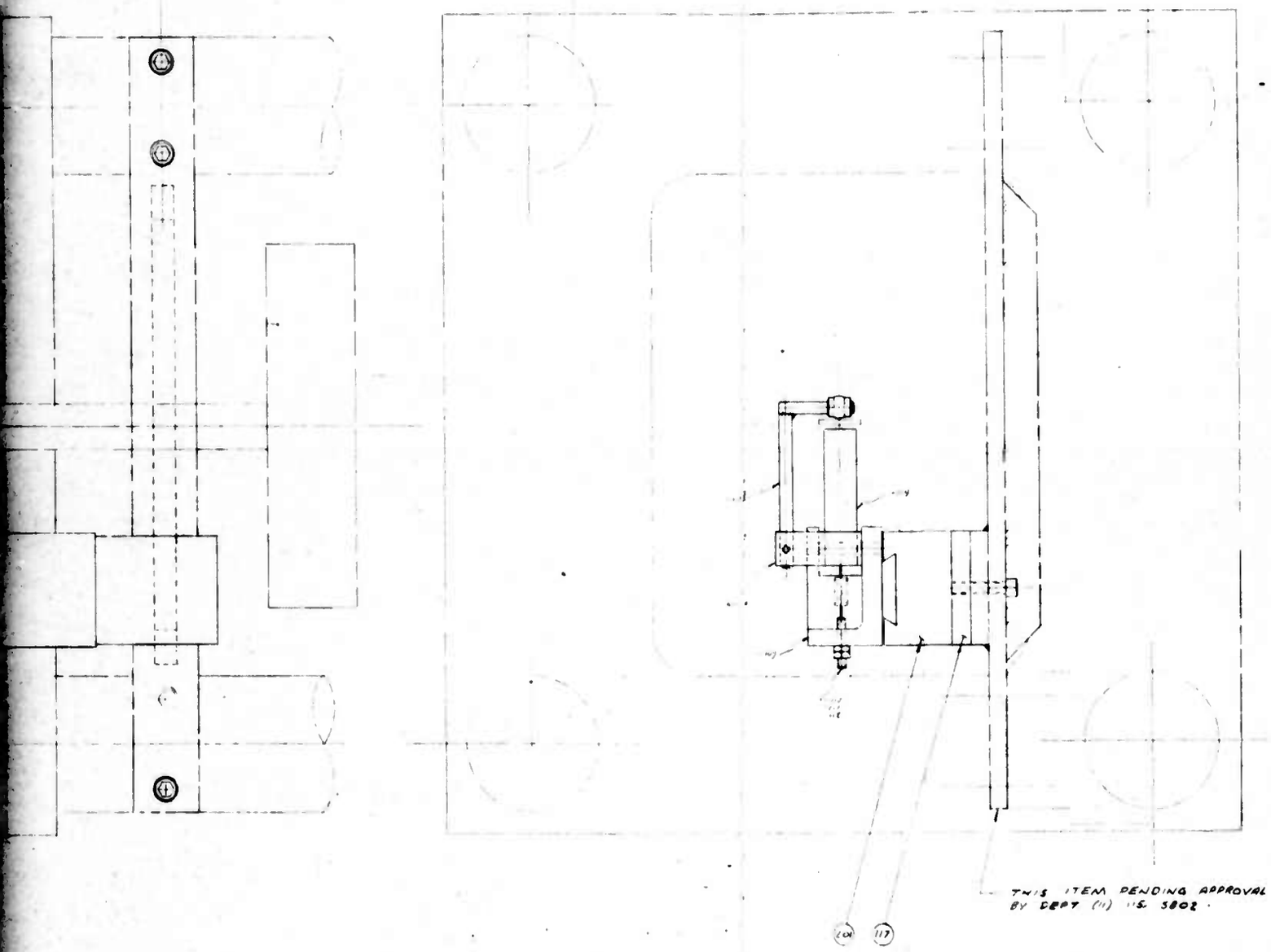

THIS ITEM PENDING APPROVAL
BY DEPT (11) W.S. 5802.

B

	FRAME 2		
TOOL NO	SK 16307	ECN 416	SHT 2

7	6	5	4	3

REVISIONS				
ZONE	LTR	DESCRIPTION	DATE	APPROVED

APPROVAL

C

MATERIAL PER SPS 10	UNLESS OTHERWISE SPECIFIED DIMENSIONS ARE IN INCHES TOLERANCES ON	CONTRACT	FIRST RELEASE	
TOLERANCES PER SPS 14	DECIMALS ANGLES	DESIGNED	D. CLEMENS 10-1-73	
Other than Manufacturer Shop Control	.X ± .1 .XX ± .03 .XXX ± .010 ± 1° 30'	CHECKED	G. MILLER 11/6/73	
			[illegible] 11/7/73	
		APPROVED		
THIS TOOL MUST BE COORDINATED WITH	THIS TOOL ACCOMMODATES	APPROVED FOR RELEASE		

North American Rockwell — 8-1 Division — TOOL DESIGN
INTERNATIONAL AIRPORT LOS ANGELES, CALIFORNIA 90009

SCANNER, CONSTANT RATE, FATIGUE SPECIMEN

MFR	TOOL DRWG NO	TOOL NO
J	43999	SK16307

SCALE FULL — OBSOLETE SHEETS — — SHEET 2 OF 2

7	6	5	4	3

ZONE	LTR	DESCRIPTION	DATE	APPROVED

ZONE	LTR	DESCRIPTION	DATE	APPROVED

ZONE	LTR	DESCRIPTION	DATE	APPROVED

ZONE	LTR	DESCRIPTION	DATE	APPROVED
201	1	MOTORIZED SLIDE MOVEMENT USING DEPT. [illegible] 5802		

[redacted]. Constant-rate mecha[redacted]

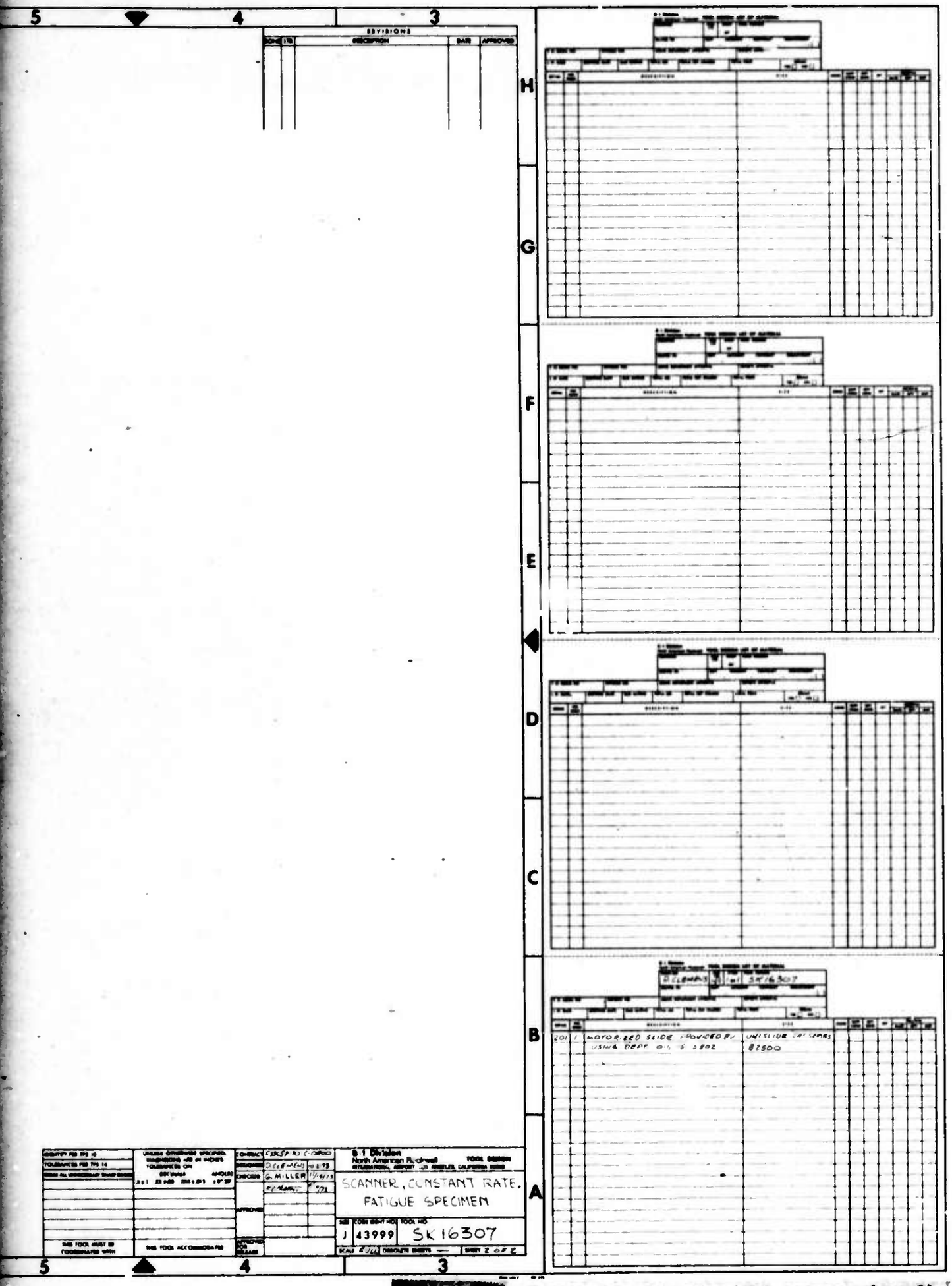

[redacted]. Constant-rate mechanical scanner (concl).

[redacted]

D

the specimen. The concept of scanning both sides of the specimen may obviate the need for a positioning roller. In this approach, the dual transducer is alined on a yoke that fits on both sides of the specimen. The scanner is alined with the specimen axis and operated without contacting the specimen. The positioning roller provides the additional capability of scanning variously shaped, concave and convex structures. Other scans may be required in a number of similar locations such as holes in a wing structure. It would be impractical to have a fixed exoelectron emission detector at every hole. In this case, the transducer can be scanned along a line of holes or rotated within specific critical holes. For other situations, it might be appropriate to fix the transducer(s) and use a single, focussed ultraviolet source which could periodically illuminate the critical areas and stimulate emission. The detected current could similarly be sampled by a synchronously coupled measurement system.

SYSTEM RECOMMENDATIONS

A relatively simple exoelectron emission measuring system was developed in this program using the instruments and transducers previously described. For example, the following instruments would form a complete measuring system for approximately $1,500:

Instrument	Cost
Keithley model 602 electrometer	$745.00
Penray model AD-004A ultraviolet lamp	80.00
Penray model SCT-1 transformer	34.00
Velmex UniSlide assembly P/N B2512P10J	252.00
Velmex speed control model 311	87.00
Power design model 4005 power supply	250.00
Sola electric constant voltage transformer No. CVS-1	50.00
Total	$1,498.00

The system preparation and operation includes the following tasks:

1. Provide the transducer accelerating voltage by interconnecting the dc voltage supply and the Keithley electrometer: negative supply connected to the Keithley rear terminal "CASE GROUND," positive supply connected to "OHMS GUARD" terminal. The Keithley shorting bar is not used. The accelerating voltage is now available at the Keithly input terminal.

2. Connect the exoelectron transducer to Keithley input terminal using the triaxial cable connecter. The connecter includes the transducer collector current referenced to specimen ground, the accelerating voltage, and an electrostatic shield.

3. Connect the transducer ultraviolet lamp(s) to the power supply using a polarized two-pin plug. The ultraviolet lamps require a 3- to 5-minute warmup period for steady continuous operation.

4. Connect the Keithley signal output terminal to an appropriate dc recorder. Caution should be exercised since the Keithley output signal leads are both above equipment ground. It may be necessary to isolate the recorder case from ground if there is significant leakage within the recorder.

5. Normal settings of the Keithley are as follows:

   a. Feedback switch (S105): FAST

   b. Meter switch (S107): MINUS

   c. Multiplier switch (S106): 1 or 3

   d. Range switch (S103): 10^{-9} to 10^{-10} ampere, selected to provide a midscale meter indication.

6. Exoelectron transducer can be scanned in or on the test article using a nominal transducer to part spacing of 0.8 to 1.6 mm (1/32 to 1/16 inch) and scan rate of approximately 8 mm/second (0.3 inch/second)

The operation of this system could be directly monitored on the electrometer or an auxiliary dc recorder could plot the emission current as a function of transducer position, time, etc. An on-line magnetic recording system could also be used to provide a high-speed data analysis capability to determine changes in exoelectron emission levels.

An alternate system approach is recommended where a large number of structural locations need to be continuously or periodically monitored. The use of a fixed NDT system is recommended consisting of an ultraviolet lamp, pick up wire and lamp power supply in each critical area. If a number of such systems were required, they could be sequentially connected into a picoammeter readout module, and it would be possible to periodically check a large number of critical areas in the aircraft structure. Multiplex techniques of this type are now in general use in the aircraft industry. The cost per module would be low because the expensive picoammeter readout module could be located

in a central location and used by many detection systems. With a system of this type installed in a structure, it would be possible to sense prefailure exoelectron emission and warn the pilot or test manager before failure occurs.

ELECTRON STIMULATION TECHNIQUE IMPROVEMENT

The present ultraviolet source operating at a wavelength of 2,537 angstroms has proved adequate to stimulate exoelectron current during fatigue from the aluminum, titanium, and steel specimen materials evaluated in this program. However, based on literature reviews and personal experience, it is known that other methods of stimulation are feasible. Therefore, several experimental and analytical evaluations were made to determine an optimum stimulation system in terms of signal-to-noise ratio and ease of application. The areas evaluated include alternate forms and frequencies of ultraviolet sources, and thermal and acoustic sources.

ULTRAVIOLET STIMULATION SOURCES

Specimen areas having high electron emission have been mapped using a current-sensing transducer containing an ultraviolet light source. The transducer is fitted with an aperture to restrict the beam diameter and provide a relatively small ultraviolet source to permit point-by-point scanning of test specimens. The Penray ultraviolet lamps presently used are about 50.8 mm (2 inches) long and 6.4 mm (0.25 inch) in diameter. The aperture transmits energy from a relatively small area of the lamp surface, and thus very little of the lamp energy is effectively utilized. The light energy spreads rapidly after passing through the aperture. This produces an illuminated area which is larger than the aperture, and rather poorly defined.

A laser-type ultraviolet system was evaluated for application as a concentrated, high-intensity scanning excitation source for the exoelectron emission measurement system. The laser ultraviolet system (Spectra-Physics model 185) is reported to be the only continuous wave system capable of operating at very short wavelengths - in this case 3,250 angstroms. It was estimated that the laser system could provide an energy level increase of three to four times with a significant reduction in beam diameter, as compared to the presently used Penray ultraviolet source. Additionally, the optical characteristics of the laser system offer a capability for automatically scanning a material surface as required for inspecting structures. The evaluation was based on the comparison of the stimulation effects of the laser and Penray systems on prepared aluminum, titanium, magnesium, and stainless steel test coupons. The results presented in the following table show that the laser system produced a greater current level increase than the Penray ultraviolet lamp for a scratched or distressed area, as compared to a normal

surface. Rather large changes in current level were observed for the aluminum and magnesium materials, but neither ultraviolet source produced significant current increases from the stainless steel or titanium materials.

Material	Stimulation Source					
	Laser			Penray		
	Current (10^{-12} amp)			Current (10^{-12} amp)		
	Normal Area	Scratched Area	Current Ratio	Normal Area	Scratched Area	Current Ratio
Aluminum	0.18	11	61.1	2.4	52	21.7
Magnesium	0.15	150	1,000	1.5	50	33.3
Stainless steel	0.12	0.15	1.25	4.7	6.2	11.3
Titanium	0.12	0.15	1.25	3.7	4.3	1.2

Two possible mechanisms have been suggested to account for the higher ratio of current increase with the laser system. First, the wavelength of laser energy is 3,250 angstroms, while the Penray energy is concentrated at 2,537 angstroms, and the emission characteristics may be frequency dependent. Secondly, the current differences may be attributable to the size and shape of the ultraviolet light beams. The electron source used for these tests was a fresh scratch on an otherwise undisturbed metal surface. Therefore, the source would affect a relatively small percentage of the stimulating and measuring areas of the comparatively large area of the Penray-type transducer, with respect to the highly concentrated laser beam area. The continued evaluation of the laser ultraviolet source was not possible due to the unavailability of the equipment. It should be noted that these systems were priced in the $15,000 range.

Another ultraviolet source operating at the 3,660-angstrom wavelength and at the same energy level as the 2,537-anstrom Penray source was evaluated without significantly improving the stimulated current level.

ACOUSTIC STIMULATION SOURCE

Acoustic stimulation of exoelectron emission has been reported and discussed in the screening experiments, it was expected that acoustic waves would produce surface modulations, on a periodic basis, which would be expected

to couple incident light stimulation to surface plasmons, and initiate and enhance emission. Therefore, several acoustic sources were considered. Experiments using a commercial ultrasonic surface wave transducer operating at 2.25 MHz, continuous wave mode, did not show an appreciable change in the measured exoelectron emission current.

OTHER STIMULATION SOURCES

The radioactive 0.01-millicurie Americium 241 source used for the surface potential difference measurements was evaluated as a possible exoelectron stimulation source. The radioactive source was positioned immediately adjacent to the ultraviolet lamp so that both sources were directed at the same location on the specimen. No improvement in stimulation was evidenced.

Low-level thermal stimulation techniques were evaluated using a forced air heat gun. The specimen was subjected to the heated air stream (estimated at 70° C) for periods up to 10 minutes without changing the measured exoelectron emission current.

The accelerating voltage was evaluated as a means of improving the stimulation. Normally, this voltage was set between 40 and 90 volts. By increasing the voltage from 60 to 300 volts dc, the exoelectron emission current level increased from approximately 650 to 1,125 picoamperes. Although some improvement is available by this technique, it is preferred to operate at the lower voltage levels since the signal-to-noise ratio is not affected and the transducer components are not required to operate at a high breakdown potential.

MATERIAL SURFACE PREPARATION

A series of experiments were conducted to determine the effect of various material surface treatments on the exoelectron emission measurements. The following solutions were evaluated to determine their efficiency for cleaning aluminum surfaces of contaminants as encountered in air vehicle service (oil, grease, glycerine) without using deoxidizers that would adversely affect an aluminum anodized condition:

- Methylethylketone (MEK) scrub followed with a heated alkaline cleaner and water rinse
- Acetone rinse
- Distilled water rinse

- Alcohol rinse
- Stoddard solvent
- Rockwell P5F-1.0 Penetrant with water rinse

It is concluded that, in most instances, a cleaning procedure using a Stoddard solvent cleaning, followed by an MEK rinse and water rinse would adequately prepare most surfaces for an exoelectron emission measurement within a several-minute time period.

Section IX

CONCLUSIONS AND RECOMMENDATIONS

CONCLUSIONS

The screening experiments demonstrated that the exoelectron emission produced in aerospace materials due to the processes of fatigue may be characterized in terms of changes in the surface state of the material. The emission is enhanced by the surface roughening of the material surface generated by the fatigue cycling. The surface oxide acts as an attenuator, not as a source, of emission. The final failure site can be approximately located by comparing the exoelectron emission and surface potential difference measurements made on material during a sequence of interruptions in the fatigue process. A method of analyzing the exoelectron emission data during a fatigue test using a data sampling procedure along the length of a test specimen has shown that the exoelectron measurement method has a good potential for developing into a new NDT technique for assessing fatigue damage and locating the failure site. A prototype exoelectron emission measurement system was demonstrated including a variety of transducers suitable for detecting fatigue damage in a number of structural shapes and materials. The accuracy of the exoelectron emission method for predicting areas of fatigue damage is considered to be very high; the accuracy of predicting the location of the final fatigue failure site where several areas are experiencing fatigue damage was over 50 percent. The reason for this relatively low accuracy value may be attributed to the fact that the failure sources were not always accessible to the exoelectron measurement method or that multiple areas evidence the effects of fatigue damage and the area experiencing the greatest damage may change several times during the fatigue life. The generally successful detection of fatigue failure sites in materials fatigued in high, low, and spectrum loaded conditions, under a variety of environmental conditions and material configurations, demonstrates a high potential for the application of the exoelectron emission method in the aerospace industry. Further, the method is well suited for high-speed noncontact inspection of the commonly used aluminum, steel, and titanium alloys. The major limitations of the exoelectron emission method are the present inability to accurately locate the final fatigue failure site with a high reliability and the inability to predict the magnitude of fatigue damage and predict remaining safe life. The first limitation can probably be overcome through improved data analysis/interpretation techniques. The second limitation may be overcome through a more complete understanding of the mechanism of exoelectron emission presently under study by the Rockwell International Science Center, or possibly through further development of the apparently complementary measurement method surface potential difference which showed promise in this program.

RECOMMENDATIONS

1. Continued research to define the mechanism of exoelectron emission as related to fatigue.

2. Determination of a supplementary test method or material characteristic indicative of the accumulative fatigue damage of a material that can be correlated with the exoelectron emission data to uniquely define the actual fatigue state.

3. Development of an on-line data analysis system to predict the location of the final failure site as soon as reliable data is obtained.

4. Continued use of the exoelectron emission measurement capability for detecting early fatigue damage, detecting microcracking and macrocracking, and measuring crack propagation characteristics.

5. Review of potential applications for the exoelectron emission method in the production and flight testing of aerospace structures and adaption/improvement of the prototype system for potential application.

Section X

REFERENCES

1. Moore, J. F., Tsang, S., and Martin, G., "The Early Detection of Fatigue Damage," AFML-TR-71-185, 1971

2. Hoenig, S. A., "New Techniques in Nondestructive Testing (Exoelectron Emission Phase)," AFML-TR-71-140, Part I, 1971

3. Wielke, B., Birkhan, F., and Weiss, B., "Dissipated Energy During Cyclic Deformation, "Physica Status Solidi (A), Vol 17, 1973, p 149

4. Mason, W. P., and Wood, W. A., "Fatigue Mechanism in FCC Metals at Ultrasonic Frequencies," J. Appl. Phys, Vol 39, 1968, p 5581

5. Hockenhull, B. S., "Fatigue at Ultrasonic Frequency in Some Age-Hardening Aluminum Alloys," Physics and Nondestructive Testing, Edited by W. J. McGonnagle, Gordon and Breach, Science Publishers, Inc, New York, 1967, p 145

6. Wood, W. A., and Mason, W. P., "Fatigue Mechanism in Iron at Ultrasonic Frequency," J. Appl. Phys., Vol 40, 1969, p 4514

7. MacDonald, D. E., and Wood, W. A., "Fatigue Mechanism in Titanium at Ultrasonic Frequency," J. Appl. Phys, Vol 42, 1971, p 5531

8. Wood, W. A. "Elastic Fatigue in Titanium Studies by Scanning Electron Microscopy," AD 705512, 1970

9. MacDonald, D. E., and Wood, W. A., "Application of the Scanning Electron Microscopy to Study of Mechanisms of Metal Fatigue," AD 719927, 1971

10. MacDonald, D. E., and Wood, W. A., "Slipless Fatigue in Titanium," Technical Report No. 7, Contract No. N-00014-67-A-0214-0011, The George Washington University, 1971

11. Schijve, J., "Crack Propagation Studies of Aircraft Structure Materials," Closed Loop, Summer, 1972, p 8; also to be published in Engineering Fracture Mechanics

12. McMillan, J. C., and Hertzberg, R. W., "The Application of Electron Fractorgraphy to Fatigue Studies," Electron Fractography, ASTM STP436, 1968, p 89

13. Gilmore, C. M., MacDonald, D. E., and Wood, W. A., "Some Fracture Modes in Metal Fatigue," Technical Report No. 12, Contract N-00014-67-A-0214-0011, The George Washington University, July 1972

14. Walton, D., and Ellison, E. G., "Fatigue Crack Initiation and Propagation," International Metallurgical Reviews, Vol 17, 1972, p 100

15. Freudenthal, A. M., "Fatigue and Fracture Mechanics," Technical Report No. 11, Contract No. N-00014-67-A-0214-0011, The George Washington University, May 1972

16. Grosskreutz, J. C., and Shaw, G. G., "Mechanics of Fatigue in 1100-0 and 2024-T4 Aluminum," AFML-TR-65-127, 1965

17. Grosskreutz, J. C., and Shaw, G. G., "Critical Mechanisms in the Development of Fatigue Cracks in 2024-T4 Aluminum," AFML-TR-68-137, 1968

18. Grosskreutz, J. C., and Shaw, G. G., "Mechanics of Fatigue in 7075-T6 Aluminum," AFML-TR-66-96, 1966

19. Dunsby, J. A., and Wiebe, W., "Effect of Atmospheric Humidity on Aircraft Structural Alloy Fatigue Life," Materials Research and Standards, Feb 1969, p 15

20. The Boeing Company, "Third B-52C Through F Destructive Structural Teardown Inspection," Report No. D3-8641, 1971

21. Scot, I. G., "The Early Detection of Fatigue Damage," Australian Defence Scientific Service, ARL/Met 62, 1969

22. Marom, E., and Mueller, R. K., "Optical Correlation for Impending Fatigue Failure Detection," Int. J NDT, Vol 3, 1971, p 171

23. Bond, R. L, Beissner, R. E., and Lankford, J., Jr., "Optical Correlation Evaluation of Surface Deformation Due to Fatigue," NASA SP-299, 1971, p 177

24. Jenkins, R. W., and McIlwain, M. C., "Solder Joint Fatigue Measurement by Optical Cross-Correlation," NASA SP-299, 1971, p 183

25. Moross, G., "Inductive Sensing Technique Advancement," USAAMRDL-TR-71-51, 1971

26. Padilla, V. E., and Parks, J. W., "Definition of Fatigue Crack Geometry by Eddy Current Techniques," Proceedings of the Seventh Symposium on Nondestructive Evaluation of Components and Materials in Aerospace, Weapons Systems and Nuclear Applications, 1969, p 79

27. Kusenberger, F. N., and Barton, J. R., "Development of a Prototype Equipment for the Automatic Detection of Fatigue Damage in Helicopter Transmission Gears," Proceedings of the Seventh Symposium on Nondestructive Evaluation of Components and Materials in Aerospace, Weapons Systems and Nuclear Applications, 1969, p 98

28. Hruby, R. J., and Feinstein, L., "A Novel Nondestructive, Noncontracting Method of Measuring the Depth of Thin Slits and Cracks in Metals," The Review of Scientific Instruments, Vol 41, 1970, p 679

29. Norris, E. B., Viaclovsky, S. A., and Whiting, A. R., "An Ultrasonic Detection System for Determining Crack Initiation and Rate of Propagation," Proceedings of the Seventh Symposium on Nondestructive Evaluation of Components and Materials in Aerospace, Weapons Systems and Nuclear Applications, 1969, p 32

30. Green, R. E., and Pond, R. B., "An Ultrasonic Technique for Detection of Onset of Fatigue Damage," Annual Report, Contract No. F44620-71-C-0062, Johns Hopkins University, 1973

31. Harbert, J. D., and Stephens, R. I., "S/N Fatigue Gage Response to Cumulative Damage," Proceedings of the Seventh Symposium on Nondestructive Evaluation of Components and Materials in Aerospace, Weapons Systems and Nucleas Applications, 1969, p 85

32. Andreev, L. A., and Palige, Y. A., "The Effect of Deformation on the Work Function of Monocrystalline Molybedenum Filaments," Soviet Physics - Solid State, Vol 3, 1962, p 2238

33. Andreev, L. A., and Palige, Y. A., "Change of the Electron Work Function of Molybdenum and Tantalum Upon Cold Deformation Under Ultrahigh Vacuum Conditions," Soviet Physics - Doklady, Vol 8, 1964, p 1003

34. Mintz, R. I., Melekhin, V. P., Partenskii, M. B., and Ievlev, I. YU., "Exoemission Under Recrystallization Conditions During Plastic Deformation," Soviet Physics - Doklady, Vol 18, No. 2, 1973, p 143

35. Huber, E. E., Jr., and Kirk, C. T., Jr., "Work Function Changes Due to the Chemisorption of Water and Oxygen on Aluminum," Surface Sciences, Vol 5, 1966, p 447

36. Gel'man, A. G., and Fainshtein, A. I., "Possible Mechanism for the Two Stages of Exoelectron Emission During Oxidation of a Metal," Soviet Physics - Solid State, Vol 14, 1973, p 1752

37. Langenecker, J. A. M., and Ray, D. B., "Exoelectron Emission Due to Ultrasonic Irradiation," J. Appl. Phys., Vol 35, 1964, p 2586

38. Williams, R. A., "An Investigation of Exoelectron Emission From Various Materials Using Abrasion and Ultrasonic Techniques," RM 630.328-04, Naval Ordnance Systems, Navy Department, 1966

39. Seeger, K., "Die verzögerte Elektronenemission von Metallen," Z. für Physik, Vol 141, 1955, p 221

40. Seeger, K., "Verzögerte Elektronenemission und äusserer Photoeffekt von Germanium nach Elektronenbeschuss," Z. für Physik, Vol 149, 1957, p 453

41. Vogel, A., "Beitrage zur Exoelektronenemission von Kristallen und Metallen," Z. für Physik, Vol 158, 1960, p 77

42. Hieslmair, H., and Müller, H., "Zur Temperaturabhängigkeit der röntgenstimulierter Exoelektronenemission," Z. für Physik, Vol 152, 1958, p 642

43. Seidl, R., "Die Exoelektronenemission von Germanium," Z. für Physik, Vol 157, 1959, p 568

44. Kortov, V. S., Mints, R. I., and Petukhova, T. M., "Effect of Laser Action on the Exoelectron Emission From the Surface of Metals," FTD-HT-23-93-71, 1971

45. Endriz, J. G., and Spicer, W. E., "Study of Aluminum Films. I. Optical Studies of Reflectance Drops and Surface Oscillations on Controlled-Roughness Films," Physical Review B, Vol 4, 1972, p 4144

46. Endriz, J. G., and Spicer, W. E., "Study of Aluminum Films. II. Photoemission Studies of Surface-Plasmon Oscillations on Controlled-Roughness Film," Physical Review B, Vol 4, 1972, p 4159

47. Baxter, W. J.," A Study of Plastic Deformation by Exoelectron Emission," Vacuum, Vol 22, No. 11, 1972, p 571

48. Graham, L. J., and Alers, G. A., "Investigation of Acoustic Emission from Ceramic Materials," Final Report, Contract N00019-71-C-0344, Rockwell International Corporation, 1972

Appendix A

BIBLIOGRAPHY OF RECENT LITERATURE RELATING TO EXOELECTRON EMISSION

(SUPPLEMENT TO BIBLIOGRAPHY IN AFML-TR-71-185)

ELECTRON EMISSION FROM ANODICALLY OXIDIZED
ALUMINUM DUE TO TENSILE DEFORMATION

D.R. Arnott and J.A. Ramsey

Surface Sciences, Vol 28, 1971, pp 1-18

MATERIAL

Polycrystalline commercial high purity Al

SPECIMEN PREPARATION

Gage length = 6.3 mm, width = 5 mm, and thickness = 0.25 mm
Annealing at 500° C for 1 hour
Washing in ethanol, demineralized water, a solution containing 36g Cr_2O_3 and 100 ml H_2SO_4 per liter at 70-80° C for 20 minutes, and again in demineralized water
Anodizing at 10^{-7} amp/sq m

EXCITING CONDITION

Tensile loading
Illumination with wavelength longer than 3450 Å

DETECTION EQUIPMENT

Be-Cu particle multiplier and electrometer

RESULT

Specimen coated with thin anodic oxide film (less than 0.45 μm):
Start of photostimulated emission at strains less than the fracture strain at pressures of the order of 10^{-5} torr; increase in this strain with increase in film thickness; continuation of emission after specimen breakage; emission markedly pressure dependent - a reduction in emission current maximum with decreasing pressure
Photostimulated emission associated with absorption of freshly exposed metal surface resulting from slip breaking through oxide film
Specimen coated with thick anodic oxide film (greater than 0.45 μm):
Two categories of emission - 1. pressure dependent photostimulated emission upon or after breakage by tensile loading 2. start of emission at 2 or 3 percent strain with or without photostimulation; no emission with termination of straining; increase in emission without photostimulation with increasing oxide thickness to 1.13 μm
Emission without photostimulation generated by propagating cracks in oxide film
Specimens coated with oxides of intermediate thickness (0.4 to 0.5 μm):
Start of small emission without photostimulation at about 3-percent strain
Emission without photostimulation at low strains, and emission with photostimulation at high strains at 4×10^{-6} torr
Transverse cracking independent of grain boundaries responsible for emission without photostimulation; slip penetration of oxide at large strains responsible for emission with photostimulation

ON THE TEMPERATURE DEPENDENCE OF
PHOTOSTIMULATED EXOELECTRON EMISSION
D.R. Arnott and J.A. Ramsey
Physica Status Solidi (A), Vol 13, 1972, pp K167-K168

MATERIAL
Aluminum

SPECIMEN PREPARATION

EXCITING CONDITION
Abrading

DETECTION EQUIPMENT

RESULT
The decay in photosimulated exoelectron emission current is described as a sum of two, or perhaps three, exponential terms:

$$i = \sum_{j=1}^{2,3} M_j \exp(-N_j t),$$

where M_j and N_j are, respectively, the preexponential coefficients and the decay constants.
A predicted activation energy for oxide growth on the abraded aluminum surface is of the right order for the decay constants.
This evidence supports the view that oxide growth on aluminum is responsible for the decay in photoelectron emission.

VISUAL DISPLAY OF FATIGUE DAMAGE
BY MEANS OF EXOELECTRON EMISSION

W.J. Baxter

Applied Physics Letters, Vol 21, 1972, pp 590-592

MATERIAL

1100 aluminum

SPECIMEN PREPARATION

Electropolish

Minimum width in test section = 1/4 inch

EXCITING CONDITION

Cantilever bending (zero to maximum tension) with 6×10^{-3} and 12×10^{-3} strain amplitude

Illumination with mercury arc lamp from which a beam of ultraviolet light is scanned along the gage length of the specimen

DETECTION EQUIPMENT

Channeltron electron multiplier array and phosphor screen

RESULT

Photographs of the emission pattern observed on the phosphor screen disclose a quite uniform emission of very low intensity after 200 fatigue cycles. Much stronger emission develops after 6,000 cycles in the lower portion of the photograph, revealing the onset of localized damage. Three main horizontal bands of emission, oriented perpendicular to the specimen length, are observed after 1.265×10^{6} cycles. After doubling the strain amplitude to 12×10^{-3} and a further 85,000 cycles at this strain level, the emission increases mainly in one region. This region of most intense emission corresponds to the final location of failure.

The earlier strong emission at 6,000 cycles can be associated with the accumulation of plastic deformation in regions which ultimately develop into cracks.

EXOELECTRON EMISSION FROM DEFORMED METAL SURFACES

W.J. Baxter

General Motors Research Publication, GMR-1205, 1972

MATERIAL

1100 Al

SPECIMEN PREPARATION

Gage section: 0.1 x 0.1 x 0.060 in.

Aging at room temperature for a week to suppress any exoelectron emission associated with deformation by machining

No special preparation other than degreasing

EXCITING CONDITION

Fatigue in bending mode

Illumination with a 1 kw mercury arc lamp, spot of light on specimen (formed by two quartz lenses) = 15 or 70 μm diameter

DETECTION EQUIPMENT

Electron multiplier operating at 10^{-8} torr

RESULT

At high strain amplitude 9.2×10^{-3} - One large photostimulated emission peak located in the region of maximum strain after 10 and 20 cycles; increase in height of this peak after 1,000 cycles plus new smaller peaks at other locations

At low strain amplitude 4.6×10^{-3} - Emergence of photostimulated emission peaks above the noise level after 2,000 cycles; emission peaks clearly defined after 3,500 cycles; growth of these peaks and appearance of fresh peaks with increasing number of cycles

Very early emission from aluminum in the fatigue life (0.07- and 0.6-percent life at strains 9.2×10^{-3} and 4.6×10^{-3}, respectively); localized emission regions (less than 100 μm wide); growth of large emission peaks associated with development of fatigue cracks

A STUDY OF PLASTIC DEFORMATION BY EXOELECTRON EMISSION

W.J. Baxter

Vacuum, Vol 22, 1972, pp 571-575

MATERIAL

1100 aluminum and 1080 steel

SPECIMEN PREPARATION

Dimensions of test section: length = 0.1 inch, width = 0.1 inch
Degreasing prior to insertion in the vacuum (10^{-8} torr) chamber

EXCITING CONDITION

Bending
Illumination with ultraviolet light with beam spot diameter 15 or 70 μm

DETECTION EQUIPMENT

Electron multiplier

RESULT

The onset of exoelectron emission of aluminum by unidirectional tension is detected at 1 percent strain and increases rapidly thereafter. No change in the emission by compressive deformation, even at 5 percent strain. The onset of emission of steel occurs at 2.5 percent tensile strain, but a compressive strain of 8 percent produces no emission.

Exoelectron emission peaks are observed in fatigue-cycling aluminum after 10 cycles at a maximum strain of 9×10^{-3}. Additional cycling causes these initial emission peaks to grow, and fresh peaks also emerge. The specimen fails after 14,000 cycles in the vicinity of a dominated peak first detected at 10 cycles.

The emission peaks in fatigue-cycling steel are observed after 1,000 cycles. The growth of some peaks saturates approximately halfway through life; simultaneously, a smaller peak grows very rapidly and becomes dominant. Failure occurs in the location of this ultimately largest peak.

The exoelectron emission detected in tensile deformation and early fatigue cycling is presumably associated with the microcracks in the oxide.

THE DETECTION OF FATIGUE DAMAGE BY EXOELECTRON EMISSION

W.J. Baxter

Journal of Applied Physics, Vol 44, 1973, pp 608-614

MATERIAL

1100 aluminum and 1080 steel

SPECIMEN PREPARATION

Flat specimen with 0.1- by 0.1-inch test section, and dog-bone specimen with a radius of 0.2- and 1/4-inch minimum width

Degreasing

EXCITING CONDITION

Bending fatigue

Illumination with a 1 kw mercury arc lamp with light spot diameter of 15 or 70 μm

Photon energy in the light spot limited to about 5.6 eV by inserting a Corning 9-54 color filter

DETECTION EQUIPMENT

Electron multiplier

RESULT

Photostimulated exoelectrons are emitted from aluminum and steel very early in fatigue life. The regions of emission are very localized (usually less than 100 μm wide).

The growth of the large emission peaks is associated with the development of fatigue cracks.

The emission is extremely stable, except for a slight transient during the first few minutes after cessation of fatigue cycling. The stability of localized emission indicates that neither the diffusion of lattice vacancies nor surface absorption are playing an important role in the electron emission process.

The increase in exoelectron emission results from two factors. First, the work function of the fresh metal revealed by the cracks in the brittle oxide is considerably lower than the work function of the oxide-coated surface. Second, the area of this metal surface increases as the deformation becomes more severe.

IMAGING OF SURFACES WITH THE
EXOELECTRON MICROSCOPE

P. Braünlich, B. Rosenblum, J. P. Carrico,
L. Himmel and P. K. Rol

Applied Physics Letters, Vol 22, 1973, pp 61-63

MATERIAL
BeO

SPECIMEN PREPARATION

EXCITING CONDITION
50-kV x-rays at room temperature
Heating at 0.5°C/sec to about 250°C

DETECTION EQUIPMENT
Exoelectron microscope consisting of electrostatic immersion lens, microchannel bundle and phosphor screen

RESULT
Exoelectron image of BeO was photographed at temperatures below and above the emission peak temperature at 230°C. The granular pattern on the photograph is evidence for pronounced local variations of the exoelectron emission current. There seems no obvicus correlation between the emission pattern and the grain structure.

Exoelectron image of BeO covered with 100-μm-wide aluminum strip of about 1000-Å thickness was also photographed below and above the emission peak temperature at 230°C. At temperatures below 230°C only the edges of the aluminum sections emitted electrons. Emission from the center part of the aluminum strip was observable at much higher temperatures (230-250°C).

THERMALLY STIMULATED EXOELECTRON EMISSION
CAUSED BY LOADS ON BeO CERAMIC

J. Brunsmann, M. Euler, W. Kriegseis, and A. Scharmann

Physica Status Solidi (A), Vol 17, 1971, pp K91-K93

MATERIAL

Sintered BeO

SPECIMEN PREPARATION

Annealed (30 minutes at 900° C) specimen 19 mm diameter by 1.5 mm thickness

EXCITING CONDITION

Compression at hydraulic pressures of 2,000, 4,000, 6,000, and 8,000 kp/cm^2
Heat

DETECTION EQUIPMENT

Secondary electron multiplier operating at 10^{-5} torr

RESULT

The peak of each grow curve appears at the same temperature of 250° C, and the shape of the curve is independent of the hydraulic pressure from 0 to 5 x 10^3 kp/cm^2; there is a nearly linear relation between pressure and the peak emission intensity at 250° C.

The exoelectron emission on heating after mechanical treatment is possibly caused by the pyroelectric properties of BeO.

CONTRIBUTION TO THE SPONTANEOUS REGENERATION OF THE CENTERS OF EXOEMISSION ON ELECTRONS IN MG AND AL

P. Craciun

Physica Status Solidi (A), Vol 10, 1972, pp 175-181

MATERIAL

Al and Mg

SPECIMEN PREPARATION

EXCITING CONDITION

Scratching with a wire brush for 3 to 5 seconds in the presence of counting gas
Illumination with monochrometic light 4360Å

DETECTION EQUIPMENT

Geiger-Mueller counter containing argon-butane 9:1 at 60 torr and operating at 900 v
Accelerating external field between specimen and counter = 30 v/cm

RESULT

When the working parameters (illumination, accelerating external field, and operating voltage of the counter) are removed for a short time interval (16 to 20 minutes) sometime after beginning of the scratching, the exoelectron emission rate versus time curves afterward rapidly exhibit a shape similar to that of the initial curve
Crystal lattice defects on the metal - Oxide interface may act as traps for the metal electrons which have passed via the tunneling effect the metal-oxide junction; exoemission centers are spontaneously created in this region.

UNTERSUCHUNG VON REIBUNGSVORGÄNGEN MIT HILFE DER EXOELEKTRONENEMISSION

D.Fischer

Doctoral Dissertation, Berlin Technical University, Berlin
(NASA Technical Translation NASA-TT-F-14044, 1971)

MATERIAL

Al, Cu, and Fe all with purity better than 99.99 percent

SPECIMEN PREPARATION

Pin specimen: 5 mm diameter x 19 mm height with a radius of curvature 10 mm at the front convex surface; rectangular specimen: 5 mm x 13 mm x 43 mm
Polishing with diamond paste immediately before test

EXCITING CONDITION

Rubbing of pin specimen against rectangular specimen under different air (or oxygen) pressures (10^{-6} to 760 torr)
Electron bombardment at 45 kv for 6 minutes
Heat up to 450° C
Illumination with a 25-watt incandescent lamp placed 15 cm from specimen

DETECTION EQUIPMENT

17-stage secondary electron multiplier with Cu-Be dynodes
Distance between entrance opening of multiplier and specimen = 37 mm

RESULT

Cu-Cu:

A maximum of exoelectron emission intensity at about 90° C, independent of oxygen pressure; increase in number of emission peaks with increase in temperature; a small peak at 60° C only under oxygen pressure 760 torr
Presence of Cu_2O and CuO (detected by electron diffraction) on Cu surface; emission peak at 60° C and 90° C due to, respectively, the presence of CuO and Cu_2O
Decrease in height of emission peak at 90° C with decrease in oxygen pressure
Emission count rate under electron bombardment (encountered in determining electron diffraction patterns of Cu oxides) higher by two orders of magnitude than with excitation by friction

Fe-Fe:

No emission with excitation by friction and electron bombardment; no emission by stimulation by heat or light
Evidence of emission only in tensile breaking

Al-Al:

Emission strongly dependent on stimulation by light; no emission without light illumination

Al-Cu and Al-Cu:

Transfer of Al to Cu or Fe specimen in friction process demonstrated by evidence and lack of exoelectron through alternate illumination and darkening of Cu of Fe specimen and by electron microprobe analysis

RELATION OF EXOELECTRON EMISSION OF MAGNESIUM
WITH OXIDATION AND DEFORMATION EXCITATION

A. G. Gel'man and I. L. Roikh

Soviet Physics - Solid State, Vol 12, 1971, pp 2763-2765

MATERIAL

Magnesium

SPECIMEN PREPARATION

Cast sample and vacuum condensate, 1 cm^2 square cross section, thermally deposited on glass substrate at 10^{-4} torr, followed by annealing

EXCITING CONDITION

Abrading with steel brush

Compression at a stress of 15×10^{-6} N/m^2

Illumination with an incandescent lamp (8 v, 20 w) through an absorption filter to cut off infrared and red parts of the spectrum

DETECTION EQUIPMENT

Air-filled counter with a hemispherical cathode and a teardrop-shaped anode operating in the proportional section of the current-voltage characteristic

RESULT

Measurement at 25° C and 60- to 65-percent relative air humidity starts 30 seconds after abrading with steel brush; rapid decay in exoelectron emission of the vacuum condensate specimen, followed by a stabilization of the emission as surface oxide thickens with time; the oxide growth and the change in surface potential on vacuum condensate specimen occur more intensely than on the cast sample.

The surface potential and oxide growth kinetics of compressed and undeformed cast specimens have the same nature after etching with 3-percent solution of acetic acid before measuring, but the surface potential is higher and the oxide thicker on the deformed specimens

Structural defects which arise during deformation are not direct sources of exoelectrons; the emission kinetics are governed by the oxidation processes, whose nature may change the metal deformation.

POSSIBLE MECHANISM FOR THE TWO STAGES
OF EXOELECTRON EMISSION DURING OXIDATION
OF A METAL

A.G. Gel'man and A.I. Fainshtein

Soviet Physics - Solid State, Vol 14, 1973, pp 1752-1755

MATERIAL
Magnesium

SPECIMEN PREPARATION

EXCITING CONDITION
Abrading with steel brush
Illumination with a DKSSh-500 lamp with photon energies 3.55, 3.78, and 4.27 eV

DETECTION EQUIPMENT
Air-filled proportional counter

RESULT
A working hypothesis is offered to explain the existence of two stages of photostimulated exoelectron emission in the oxidation of a metal.
During the first stage, the thickness of the growing surface film is smaller than the wavelength of the electrons escaping from the metal, and exoemission is an oxidation-stimulated photoelectric effect from the metal, with a red boundary shifted toward longer wavelengths.
Emission enters the second stage when the oxide film thickness is greater than the wavelength of the electrons emitted. Scattering and capture of electrons by the film defects become important. Electrons liberated from local levels associated with oxide defects and absorbed molecules participate in the emission.
As the stimulated photon energies increase, the correspondence between the time dependence of the emission from magnesium and the surface potential is disrupted at a lower oxide thickness; i.e., the transition from the first to the second stages of the process occurs earlier. This observation yields evidence in support of the hypothesis.

NEW TECHNIQUES IN NONDESTRUCTIVE TESTING
(EXOELECTRON EMISSION PHASE)
S.A. Hoenig
AFML-TR-71-140 Part I, 1971

MATERIAL
1100-0 and 7075-T6 Al alloy, Ni, and Pt

SPECIMEN PREPARATION
Al alloy:
dogbone type specimen with 3 x 1/2 inch test section chemical milling or surface grinding to 60-microinch finish
Ni:
0.032-inch-diameter wire with etched test section
Pt:
0.010-inch-diameter wire in annealed condition

EXCITING CONDITION
Fatigue
Heat
Illumination with short-wave ultraviolet light

DETECTION EQUIPMENT
Picoammeter
Field-effect transistor operational amplifier coupled to transistor amplifier

RESULT
Al alloy:
Emission current measured in air under illumination with ultraviolet light from 1100-0 when heated to 90° C after fatigue; larger current from specimens having been subjected to longer fatigue; emission current also measured in air under illumination from 7075-T6 alloy when heated either to 90° C for specimens having spent 25 to 50 percent life or to 160° F for specimens having spent 75 percent life
Ni:
Increase in emission current in vacuum at 10^{-8} torr with increasing number of cycles; emission current measured in vacuum from specimen when heated to 800° C after fatigue; larger current from the specimen having been subject to longer fatigue
Pt:
Quenching from 1275° C to room temperature followed by step heating at 50° C increment to 450° C with 6 minutes at each temperature; a sudden drop in emission current followed by a slow increase at each temperature

EFFECT OF LASER ACTION ON THE EXOELECTRON EMISSION FROM THE SURFACE OF METALS

V.S. Kortov, R.I. Mints and T.M. Petukhova

FTD-HT-23-93-71, 1971

MATERIAL

Au, Ni, Pd, Pt (all with 99.99 percent purity) and austenitic alloys 1kh18N9T and 40N25

SPECIMEN PREPARATION

Polishing and annealing in vacuum at 1,000° C for unspecified time

EXCITING CONDITION

Type K-3M laser in the free-generation mode with a pulse duration 3×10^{-3} sec and a power 1.5j, creating on specimen surface 10 craters occupying 2 x 6 mm segments

Heating to 300° C

Illumination with an incandescent lamp

DETECTION EQUIPMENT

15-stage secondary electron multiplier with Cu-Be dynodes operating at 2×10^{-5} torr

RESULT

No exoelectron emission from laser-irradiated pure metals at room temperature; rise in emission with temperature exhibiting one peak in the case of Au or Ni and two peaks for Pd or Pt

First emission peak due to the intensified oxidation process in the crater zone; second emission peak corresponding to beginning of recrystallization of disturbed surface layer

Two emission peaks in emission - temperature curve for unstable 40N25 alloy; appearance of a new phase in $\gamma \rightarrow \alpha$ transformation responsible for second peak; only one emission peak for stable 1kh18N9T alloy

Significant changes in physical state of surface caused by appearance of pulse fields of thermal stresses, cracks, structural defects, and new phases and by etching of segments adjacent to craters by gas or ion jets

Detection of changes in relief and in state of stress of specimen in zone of metal/laser beam interaction

EFFECT OF LASER ACTION ON THE EXOELECTRON EMISSION FROM THE SURFACE OF METALS

V.S. Kortov, R.I. Mints and T.M. Petukhova

FTD-HT-23-93-71, 1971

MATERIAL

Au, Ni, Pd, Pt (all with 99.99 percent purity) and austenitic alloys 1kh18N9T and 40N25

SPECIMEN PREPARATION

Polishing and annealing in vacuum at 1,000° C for unspecified time

EXCITING CONDITION

Type K-3M laser in the free-generation mode with a pulse duration 3×10^{-3} sec and a power 1.5j, creating on specimen surface 10 craters occupying 2 x 6 mm segments

Heating to 300° C

Illumination with an incandescent lamp

DETECTION EQUIPMENT

15-stage secondary electron multiplier with Cu-Be dynodes operating at 2×10^{-5} torr

RESULT

No exoelectron emission from laser-irradiated pure metals at room temperature; rise in emission with temperature exhibiting one peak in the case of Au or Ni and two peaks for Pd or Pt

First emission peak due to the intensified oxidation process in the crater zone; second emission peak corresponding to beginning of recrystallization of disturbed surface layer

Two emission peaks in emission - temperature curve for unstable 40N25 alloy; appearance of a new phase in $\gamma \rightarrow \alpha$ transformation responsible for second peak; only one emission peak for stable 1kh18N9T alloy

Significant changes in physical state of surface caused by appearance of pulse fields of thermal stresses, cracks, structural defects, and new phases and by etching of segments adjacent to craters by gas or ion jets

Detection of changes in relief and in state of stress of specimen in zone of metal/laser beam interaction

ÜBER EXOEMISSION BEI DER DEHNUNG VON ALUMINIUM IM ULTRAHOCHVAKUUM

V. S. Kortov, R. I. Mints, and V. G. Teplov

Physica Status Solidi (A), Vol 7, 1971, pp K89-K90

MATERIAL

Al

SPECIMEN PREPARATION

EXCITING CONDITION

Tension

Illumination with filtered mercury arc lamp having a maximum energy of 4.1 ev

DETECTION EQUIPMENT

Secondary electron multiplier operating at 2×10^{-9} torr

RESULT

Exoelectron emission of the aluminum specimen starts at a tensile stress of 3 kp/mm^2, and the emission rate increases with increase of the tensile stress; the emission rate increases further when the stress is maintained at 4 kp/mm^2, reaching 300 counts/sec in 45 minutes and then falls off to zero; there is a rapid increase in the emission rate, when the stress is raised from 4 kp/mm^2.

Cause of the exoelectron emission in ultrahigh vacuum is probably the lowering of work function due to the formation of structural defects by tensile deformation; the action of the defects and the local electrical field, produced by the cracking of the oxide film, should also be considered to influence the emission.

EFFECT OF DEFORMATION CONDITIONS ON THE ENERGY SPECTRUM OF THE EXOELECTRON EMISSION OF METALS

V.S. Kortov, R.I. Mints and I.Ye. Myasnikov

FTD-HS-23-1261-72, 1972

MATERIAL

Al, Ti, and W

SPECIMEN PREPARATION

EXCITING CONDITION

Abrading with steel brush in air and in vacuum at 5×10^{-6} torr

Illumination with a mercury lamp through filters selected to avoid exoelectron emission from undeformed surface of specimen

DETECTION EQUIPMENT

Open-type secondary electron multiplier operating at 5×10^{-6} torr

RESULT

Exoelectron emission from Al during deformation in total darkness as well as under illumination; increase in exoelectron energy with decrease in temperature; at the same temperature, exoelectron energy under illumination greater than the energy in darkness; maximum energy in darkness at 113K and 293K = 6 and 1.8 electron volts, respectively

Exoelectron energy from specimens deformed in air significantly lower than the energy from specimens deformed in vacuum; reduction in the energy dependent upon the elapse of time between deformation and measurement

Condition for exoelectron emission in darkness: deformation-stimulated energy of the surface $\geq$ work of electron yield of the deformed surface

MESSUNG DER ENERGIE UND INTESITÄT VON EXOELEKTRONEN
NACH DER VERFORMUNG VON ALUMINIUM BEI NIEDRIGER TEMPERATUR

V. S. Kortov and I. E. Myasnikov

Physica Status Solidi (A), Vol 9, 1972, pp K119-K122

MATERIAL

Al (99.99%)

SPECIMEN PREPARATION

EXCITING CONDITION

Abrading in vacuum with a steel wire brush

Illumination with a mercury arc lamp equipped with an optical filter BC-5 (wavelength ≥ 310 mm)

DETECTION EQUIPMENT

Secondary electron multiplier operating at 5×10^{-6} torr

RESULT

The electron energy rises to 8 ev, while the specimen is abraded at 77° K, but falls off to 0.85 ev after abrading ceases; there is no monotonic dependence of the electron energy on temperature in the range 77° to 723° K investigated; high emission rate usually accompanies low electron energy, or vice versa.

Variation of emission and electron energy could be explained by the action of patches of local electrical field on the specimen surface on the active centers emitting electrons because of lower work function.

RELATION BETWEEN VACANCY CONCENCENTRATION AND
INTENSITY OF EXOELECTRON EMISSION

I. Ye. Kurov and A. I. Sidorova

Physics of Metals and Metallography, Vol 28, No. 4, 1969, pp 118-122

MATERIAL

Pure Al (99.6%)

SPECIMEN PREPARATION

Dumbbell-shaped specimen 20 by 8 by 12.5 mm or 20 by 8 by 0.2 mm, with mean grain size of 6.5 and 0.12 mm.

EXCITING CONDITION

Tensile deformation in 4-percent intervals

Quenching in water from 200°, 300°, 400°, and 500° C

DETECTION EQUIPMENT

Closed end-window counter T-25-BFL, with a mica window 1.3 mg/cm^2 thick operating at 2 x 10^{-5} torr

Accelerating electric field between specimen and counter = 1,000 v/cm

RESULT

On completion of the first stage of deformation, there is a tendency for a slow rise in exoelectron emission up to a certain level, after which it falls; the emission behavior in the second and third stages of deformation remains as before, but both the rate and height of the rise increase; there is an increase in the maximum value of the emission, and the maximum occurs after a short time at a higher stage of deformation.

Thin (0.2 mm thick) specimens quenched from lower temperatures have stronger emission at the same periods after quenching; a sort of saturation occurs on going from low to high quenching temperatures.

Dislocations form by plastic flow which develops during quenching because of the the presence of thermal stresses; the higher quenching temperature generates more dislocations, which act as traps for vacancies, resulting in weaker emission.

The variation in the nature of exoelectron emission during plastic deformation and quenching is of the same character as the variation in vacancy concentration during this kind of deformation.

EXOEMISSION UNDER RECRYSTALLIZATION CONDITION DURING PLASTIC DEFORMATION

R.I. Mints, V.P. Melekhin, M.P. Partenskii, and I.Yu. Ievlev

Soviet Physics - Doklady, Vol 18, No. 2, 1973, pp 143-144

MATERIAL

Lead

SPECIMEN PREPARATION

Annealing at 373° K for 2 hours

EXCITING CONDITION

Stretching at a rate of 0.36 mm per minute

DETECTION EQUIPMENT

Secondary electron multiplier in 5×10^{-6} torr

RESULT

The initial stage of the deformation (0 to 5 percent elongation) is characterized by intensive hardening and sharp reduction in the work function. Exoelectron emission also rises rapidly in this stage.

The elongation interval from 10 to 25 percent is characterized by dynamic equilibrium between the numbers of defects being formed and vanishing. Intense heat liberation, associated with the progress of recrystallization process, occurs. Both the stress and work functions remain practically constant, but the emission current continues to rise.

Because of the inhomogeneous stress distribution in the specimen subject to plastic straining, heat liberation occurs nonuniformly and there exists domains whose local temperature can fluctuate strongly relative to the mean value. The heated regions rapidly go over into thermal equilibrium with the surrounding crystal because of heat conduction. The growth in emission current where there is negligible change in work function is probably due primarily to an increase in the total area of the heated sections, and not to the rise in their temperatures.

The influence of exothermal effects due to recrystallization during plastic deformation appears mainly for metals with low values of the recrystallization and Debye temperatures.

THE EARLY DETECTION OF FATIGUE DAMAGE
J.F. Moore, S. Tsang and G. Martin
AFML-TR-71-185, 1971

MATERIAL
1100-0 and 7075-T6 Al alloy, annealed Ti-6Al-4V, and heat treated D6AC steel

SPECIMEN PREPARATION
6-inch radius at each side of test specimen test section, minimum width = 1/2 inch
Chemical milling
Electrolytic polishing

EXCITING CONDITION
Tension
Fatigue
Illumination with ultraviolet light

DETECTION EQUIPMENT
Channeltron electron multiplier operating at 10^{-5} torr
Field-effect transistor operational amplifier

RESULT
1100-0 Al:
Exoelectron emission during tensile and fatigue deformation in vacuum; increase in emission intensity with increase in fatigue stress; no emission during fatigue in complete darkenss; increase in emission by illumination with long-wave ultraviolet light
Exoelectron emission during fatigue in air when illuminated with short-wave ultra-violet light; emission intensity independent of fatigue stress
7075-T6, Ti-6Al-4V, and D6AC steel: No detectable emission current from specimens during fatigue in air when illuminated with short-wave ultra-violet light.

ELECTRON EMISSION IN THE TRANSITION TO THE SUPERPLASTICITY STATE

V.G. Reznikov, G.I. Rozenman, V.P. Melekhin, and R.I. Mints

JETP Letters, Vol 17, 1973, pp 428-429

MATERIAL

Lead +43.5% bismuth alloy

SPECIMEN PREPARATION

Predeformed by compression on specimen 3 x 3 x 20 mm

EXCITING CONDITION

Tensile loading at a rate of 1.85×10^{-3} sec^{-1} at room temperature in 10^{-5} torr

DETECTION EQUIPMENT

VEU-1A secondary electron multiplier

RESULT

During the initial stage of deformation up to 15 percent elongation, when the material work hardens and the tensile load increases, no electron emission is observed.

With further deformation, the load decreases (without formation of a neck in the specimen, corresponding to the superplasticity state) and reaches a steady-state value at an elongation 85 to 90 percent. An emission is registered at the instant when the superplasticity state sets in. Simultaneously with the decrease of the tensile load, the emission intensity increases appreciably. Stabilization of the load corresponds to the maximum value of the emission current.

In plastic deformation, there exist regions whose local temperatures differ from the mean value. The fluctuations of the local temperatures stimulate electron emission in the superplasticity process. The growth of the emission current is due to the increase of the summary area of the heated metal during the first stage of deformation, which remains constant on going over into true superplasticity.

DEPENDENCE OF THE EXOEMISSION CURRENT
ON THE ELECTRON WORK FUNCTION

A.M. Shkil'ko, V.D. Rogozhin, and A.A. Kvesnin

Soviet Physics - Solid State, Vol 15, 1973, pp 180-181

MATERIAL
Silver

SPECIMEN PREPARATION

EXCITING CONDITION
Stretching

DETECTION EQUIPMENT

RESULT
The Fermi distribution of the electron energies in a metal gives rise to an exponential dependence of the exoemission current on the electron work function.
This theoretical dependence is in agreement with the experimental data.

SUR L'EXOEMISSION EXOELECTRIQUE DE L'ALUMINIUM
W. M. van der Varst and M. D. Demuer
Comptes Rendus Series B, Vol 271, 1970, pp 1066-1069

MATERIAL
Al

SPECIMEN PREPARATION

EXCITING CONDITION
Rubbing
Heat

DETECTION EQUIPMENT
Secondary electron multiplier operating at 10^{-5} torr

RESULT
After rubbing at -180° C, the grow curve between -180° and 0° C exhibits four emission peaks at -130°, -95°, -20°, and -5° C; after rubbing at 20° C, three emission peaks at 80°, 125°, and 200° C appear on the emission curve between 20° and 300° C; at any given temperature, the emission decay does not take place until after reaching a slight maximum.
The emission intensity at the peak in the grow curve is inversely proportional to the average electron energy measured at that temperature.

INFLUENCE OF NORMAL LOAD ON THE EXOELECTRONIC EMISSION OF STEEL DURING FRICTION

V. D. Yevdokimov

Physics of Metals and Metallography, Vol 27, No. 5, 1969, pp 198-199

MATERIAL

Steel 25

SPECIMEN PREPARATION

Annular specimen with 16 mm outer diameter and 15 mm thickness

EXCITING CONDITION

Sliding friction at various normal loads
Illumination with ultraviolet light with filter

DETECTION EQUIPMENT

Open end-window plus window with heat regulation

RESULT

Exoelectron emission in air during sliding friction at a normal load of 13.2 kg increases with friction time and then levels off; there is a greater increase in emission in the first minute at a higher normal load of 52.8 Kg, followed by a decrease and then leveling off.

Increase and then stabilization in microhardness occurs in the same time with the emission change at 13.2 kg.

When the normal load changes from 13.2 kg to 26.4 kg, there is a short, rapid rise in emission, followed by emission decay; the same emission pattern is also observed when the normal load is further raised to 52.8 kg.

Drop in emission corresponds to a similar drop in microhardness.

THE CORRELATION BETWEEN EXOELECTRON EMISSION AND SUSCEPTIBILITY TO CORROSION UNDER STRESS IN IRON ALLOYS

L.E. Zamiryakin, L.T. Shepelina and E.H. Gutman

FSTC-HT-23-841-71, 1971

MATERIAL

Austenitic Fe-Ni alloys containing 14.3 to 48.0 percent Ni

SPECIMEN PREPARATION

Y-shaped specimen with unspecified dimensions

Homogenizing for three hours at 1,250° C, quenching in water and electrolytic polishing in a sulphur-chromium-phosphate bath

EXCITING CONDITION

Local plastic deformation: pyramid - shaped identation by diamond under 200 grams load; area of identation = 0.005 sq mm

Tensile stress of 0.9X yield strength at 320° C to simulate condition of stress corrosion in alkali solution of NaOH (500 gram/liter on conversion to Na_2O)

DETECTION EQUIPMENT

T-25-BFL end window counter operating at 2×10^{-5} torr

RESULT

Intensive exoelectron emission due to local plastic deformation or tensile stressing at 320° C from surface of specimen susceptible to stress corrosion cracking (alloys containing less than 30 percent Ni); only weak emission due to same sources from surface of specimen not susceptible to stress corrosion cracking (alloys containing more than 30 percent Ni)

The tendency to stress corrosion cracking accompanied by a sharp increase in emission after local deformation or during heating in a stressed state

The lower the Ni content in the alloy, the shorter the time to failure by stress corrosion and the stronger the exoelectron emission

Appendix B

SPECIMEN DESIGN FOR THE SCREEN EXPERIMENTS

In order for all of the measurement systems planned in the screening experiments to see equal degrees of fatigue damage, the specimen must be shaped so that the surface strain is constant over the measurement area. If a simple bending beam with a uniform cross section were used, the strain would all be concentrated at the top of the specimen near the clamp. A uniform strain can be developed over the entire length of a loaded beam if the beam has a width that decreases linearly from the clamped to the free end. Thus, a triangular shaped specimen is optimum for the planned experiments. However, a relatively large mass (armature of the driver) is attached to the end of the specimen and its inertia must be considered in the case of a dynamic test.

The following analysis is generalized for the dynamic case and determines the limits for the simple static results for a triangular beam shape. It is assumed that the flexural behavior of a thin beam can be described by classical beam theory. For beams of constant thickness H and varying width W(x), the equation of motion is of the form

$$\frac{\partial F}{x} = HW\rho \frac{\partial^2 y}{\partial t^2} \tag{1}$$

where F is the shearing force acting on a cross section of the beam, y is the transverse displacement of the beam, and ρ is the density. Within the classical approximations, the shearing force is related to the bending moments M and the curvature of the beam by the expressions

$$F = \frac{\partial M}{\partial x} \tag{2}$$

and

$$M = - EK^2 HW(x) \frac{\partial^2 y}{\partial x^2} \tag{3}$$

where E is Young's modulus and K^2 is the radius of gyration of a cross section. (K^2 equals $H^2/12$ for the case of interest here.) The peak strain within the beam is maximum at the upper and lower surfaces and is given by

$$(\epsilon_{xx})_{max} = \pm H/2 \frac{\partial^2 y}{\partial x^2} \tag{4}$$

For the present fatigue experiments, it is desirable to shape the specimens in such a manner that the strain, and hence the fatigue, is uniform at the surface over the entire length of the beam. The necessary shape may be derived by first noting, from equation 4 and the constancy of strain, that the deflection must be of the form $y = a+bx+cx^2/2$. For beams clamped at $x = 0$, the boundary conditions simplify this to the form

$$y = cx^2/2 \tag{5}$$

Only those beam shapes producing this form of deflection can have constancy of strain.

To find the required W(x), equations 1, 2, 3, and 5 may be combined to obtain

$$\frac{d^2W}{d\xi^2} = \xi^2 W \tag{6}$$

where

$$\xi = X/D$$

and

$$D^{-1} = \left(\frac{\omega^2 \rho}{2EK^2}\right)^{1/4}$$

This is a homogeneous second-order linear differential equation and must have two linearly independent solutions, $W_{1(\zeta)}$ and $W_{2(\zeta)}$. The desired beam shape is found by taking the particular linear combination of these, which satisfies the boundary conditions at x - L, the end of the beam.

The solutions for the static case are $W_1 = \alpha$ and $W_2 = \beta x$, where α and β are constants to be determined by the boundary conditions. If a force F_o is applied to the end of the beam at x = L (but exerts no torque about the midplane), then the boundary condition dictates $\beta = -\alpha/L$. The beam must have a triangular shape, tapering uniformly to a point at x = L. This may in fact be impractical because of the physical difficulty of applying a force at a point. Often it is more convenient to taper the beam to a small, but finite, width and apply the force to a rigid extension of the end of the beam. Such a rigid extension may be experimentally obtained by simply increasing the thickness H of the beam beyond the region in which flexure is desired. The boundary conditions for such a situation are

$$F(L) = F_o \tag{7}$$

$$M(L) = -F_o X_o \tag{8}$$

where F_o is the applied force and X_o is the distance of its point of application beyond the end of the beam. Substitution of equations 2 and 3 into 7 and 8 along with the previously described results

$$y = cx^2/2 \tag{9}$$

$$W(x) = \alpha + \beta x \tag{10}$$

yields the solution

$$\alpha = \frac{F_o(L + X_o)}{EHK^2c} \tag{11}$$

$$\beta = \frac{F_o}{EHK^2c} \tag{12}$$

In this case, the beam must be uniformly tapered so that its extension would come to a point at the application of the force, $x = L + X_o$.

These results are all familiar and are only repeated here to establish a basis for the discussion of the dynamic case. For the vibration frequency $\omega \neq 0$, equation 10 does not satisfy equation 6. Transformations of variables could be used to change equation 6 into a form of the Hermite differential equation or the confluent hypergeometric equation, and the solutions could then be expressed in terms of tabulated functions. However, it has been more convenient to numerically generate the solutions of equation 6 from its recursion relation. The results for two linearly independent solutions are shown in the figure. It is seen that for $\xi < 0.5$, the two solutions are essentially (to better than 1 percent) those of the static case. For greater values of ξ, large deviations between the static and dynamic cases appear. Thus, in designing the specimens for the present experiments, it is most convenient to choose conditions such that

$$\xi(L) = \frac{L}{D} < 0.5 \tag{13}$$

so that a simple triangular shape may be used. For greater values of L/D, more complex geometric shapes would have to be used. In the present case, $\omega = 6 \times 10^3$, $\rho = 2.7$ gm/cc, $E = 7.1 \times 10^{11}$ d/cm^2, and $H = 0.5$ mm; therefore, $D = 1.3$ cm, and L should not exceed 0.65 cm (0.26 inch).

If the beam is loaded with a mass M having a moment of inertia I about a center of mass located at $x = L + X_{cm}$ and $y = Y_{cm}$, then the boundary conditions take the form

$$M(L) + F(L)\, X_{cm} = I_{cm} \frac{\partial^3 y}{\partial x\, \partial t^2}\,(L) \tag{14}$$

$$-F(L) = \bar{M} \frac{\partial^2}{\partial t^2} \left[y(L) + X_{cm} \frac{\partial y}{\partial x}\,(L) \right] \tag{15}$$

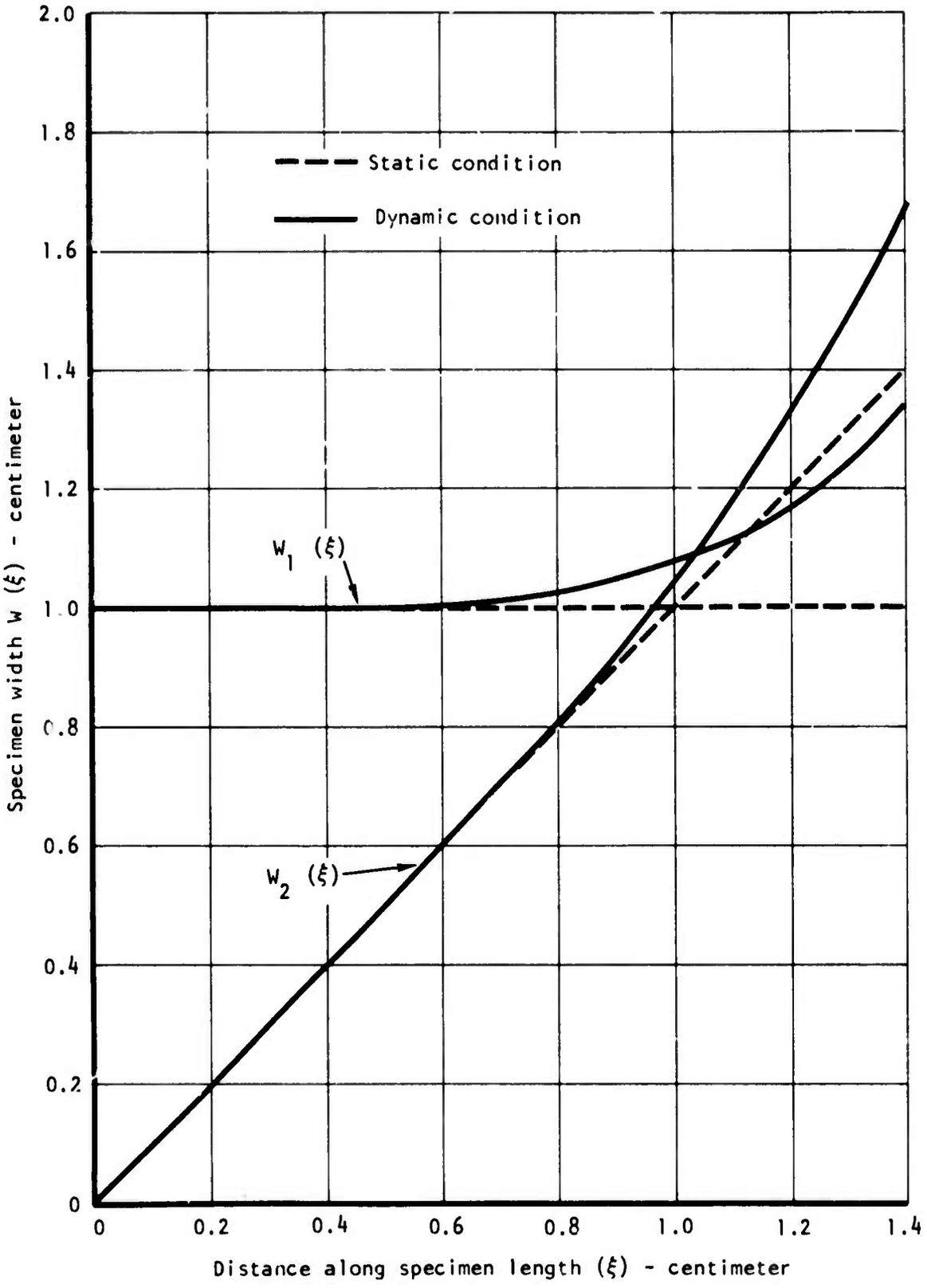

Figure B-1. Graphical solutions to differential equation 6.

which is just the angular and linear rigid body equations of motion of the load referred to its center of mass. Under the conditions of equation 13, W(x) can be approximated by equation 10, with the result

$$\alpha = \left(\frac{\omega^2 L}{2EK^2H}\right)\left[2I + M(L^2 + 3LX_{cm} + 2X_{cm}^2)\right] \tag{16}$$

$$\beta = \left(\frac{\omega^2 L}{2EK^2H}\right)\left[\bar{M}(L + 2X_{cm})\right] \tag{17}$$

The beam is again triangularly shaped, and the extension of its sides should come to a point at

$$x = L + X_{cm} + \frac{2I}{\bar{M}(L + 2X_{cm})} \tag{18}$$

The importance of the moment of inertia is to shift the apex of the extended triangular sides beyond the location of the center of mass.

As a final conclusion, it should be noted that the surface strains can be easily monitored for a beam vibrating in uniform strain. If the peak-to-peak change of slope at the end of the beam during a vibration period is θ, then according to equations 4 and 9, the peak strains are

$$(\epsilon_{xx})_{max} = \pm \frac{\theta H}{2L} \tag{19}$$

The angle θ was easily monitored by reflecting a light beam from a small reflector at the end of the beam.

Appendix C

LIST OF FATIGUE TEST SPECIMENS AND TEST CONDITIONS

TABLE C-1. LIST OF FATIGUE TEST SPECIMENS AND TEST CONDITIONS

Material and Test Condition	Specimen Ident	Fatigue Load Condition	NDT: EEE = Exoelectron SPD = Surface Potential	Note
Aluminum 2024-T81				
High Cycle - 25% Life	A27	22 ksi, 1.25×10^6 cycles then to 5×10^6 cycles; 38 ksi, failure at 7×10^4 cycles	EEE and SPD at 1.25×10^6 cycles and 5×10^6 cycles	Complete
	D1	22 ksi, 1.25×10^6 cycles then to 4.27×10^7 cycles 38 ksi, failure at 7.2×10^4 cycles	EEE and SPD at 1.25×10^6 and 4.27×10^7 cycles	Complete
	C14	22 ksi, 1.25×10^6 cycles then to failure at 1.58×10^6 cycles	EEE at 1.25×10^6 cycles	Complete
High Cycle - 50% Life	B6	22 ksi, 2.5×10^6 cycles then to 5×10^6 cycles; 38 ksi, failure at 7.3×10^4 cycles	EEE and SPD at 1.25×10^6 and 5×10^6 cycles	Complete
	A10	22 ksi, 2.5×10^6 cycles then to failure at 3.96×10^6 cycles	EEE at 2.5×10^6 cycles	Complete
	C6	22 ksi, 2.5×10^6 cycles then to 4.4×10^7 cycles; 38 ksi, failure at 6.8×10^4 cycles	EEE and SPD at 2.5×10^6 and 4.4×10^7 cycles	Complete
High Cycle - 75% Life	D11	22 ksi, 3.75×10^6 cycles then to 5×10^6 cycles; 38 ksi, failure at 6.3×10^4 cycles	EEE and SPD at 1.25×10^6 and 5×10^6 cycles	Complete
	D3	22 ksi, 3.75×10^6 cycles then to failure at 4.45×10^6 cycles	EEE at 3.75×10^6 cycles	Complete
	C10	22 ksi, 3.75×10^6 cycles then to 4.37×10^7 cycles; 38 ksi, failure at 8.6×10^4 cycles	EEE and SPD at 3.75×10^6 and 4.37×10^7 cycles	Complete
Low Cycle - 25% Life	A22	38 ksi, 1.5×10^4 cycles then to 5.5×10^4 cycles; 38 ksi, failure at 2.3×10^4 cycles	EEE and SPD at 1.5×10^4 and 5.5×10^4 cycles	Complete
	A7	38 ksi, 1.5×10^4 cycles then failure at 1.24×10^5 cycles	EEE and SPD at 1.5×10^4 cycles	Complete
	A5	38 ksi, 1.5×10^4 cycles then to failure at 7.1×10^4 cycles	EEE and SPD at 1.5×10^4 cycles	Complete

TABLE C-1. LIST OF FATIGUE TEST SPECIMENS AND TEST CONDITIONS (CONT)

Material and Test Condition	Specimen Ident	Fatigue Load Condition	NDT: EEE = Excelectron SPD = Surface Potential	Note
Low Cycle - 50% Life	E3	38 ksi, 3 x 10^4 cycles then to 5.5 x 10^4 cycles; 38 ksi, failure at 3.4 x 10^4 cycles	EEE and SPD at 3 x 10^4 and 5.5 x 10^4 cycles	Complete
	A29	38 ksi, 3 x 10^4 cycles then to failure at 6.2 x 10^4 cycles	EEE and SPD at 3 x 10^4 cycles	Complete
	B10	38 ksi, 3 x 10^4 cycles then to failure at 7.4 x 10^4 cycles	EEE and SPD at 3 x 10^4 cycles	Complete
Low Cycle - 75% Life	C18	38 ksi, 4.5 x 10^4 cycles then to 5.5 x 10^4 cycles; 38 ksi, failure at 3 x 10^4 cycles	EEE and SPD at 4.5 x 10^4 and 5.5 x 10^4 cycles	Complete
	D11	38 ksi, 4.5 x 10^4 cycles then to failure at 6 x 10^4 cycles	EEE and SPD at 4.5 x 10^4 cycles	Complete
	D17	38 ksi, 4.5 x 10^4 cycles then to failure at 7.4 x 10^4 cycles	EEE and SPD at 4.5 x 10^4 cycles	Complete
	S-73-1	1,000 lb, failure at 55,000 cycles	EEE during fatigue test	Complete
	S-73-2	1,500 lb, failure at 69,772 cycles		
Elastic Loading	E17	11 and 38 ksi, 1 x 10^7 and 3 x 10^4 cycles, respectively	EEE at 1 x 10^7 and 3 x 10^4 cycles, SPD at 1 x 10^7 cycles	No failure, test completed
	E3	11 and 38 ksi, 2.5 x 10^6 and 3 x 10^4 cycles, respectively; 38 ksi failure at additional 3.8 x 10^4 cycles	EEE and SPD at 1 x 10^7 and 3 x 10^4 cycles	Complete
	E4	11 and 38 ksi, 2.5 x 10^6 and 3 x 10^4 cycles, respectively; 38 ksi, failure at additional 4.8 x 10^4 cycles	EEE and SPD at 1 x 10^7 and 3 x 10^4 cycles	Complete
General Plastic Deformation - Pretensile Loading by 2.7% Strain	B7	2 tests at 38 ksi, each at 1.5 x 10^4 cycles; 38 ksi, failure at additional 2.7 x 10^4 cycles	EEE and SPD twice each at 1.5 x 10^4 cycles	Complete
	E20	38 ksi, 3 x 10^4 cycles; 38 ksi, failure at additional 4.7 x 10^4 cycles	EEE and SPD at 3 x 10^4 cycles	Complete

TABLE C-1. LIST OF FATIGUE TEST SPECIMENS AND TEST CONDITIONS (CONT)

Material and Test Condition	Specimen Ident	Fatigue Load Condition	NDT: EEE = Exoelectron SPD = Surface Potential	Note
Spectrum Loading: Low - High	B24 A3 A26	22, 26, 30, 34, and 38 ksi for 36×10^4, 10×10^4, 3×10^4, 8×10^3, and 2×10^3 cycles, respectively; repeat same loading; 22 ksi on B24, failure at 1.8×10^4 cycles; 38 ksi on A3 and A26, failure at 7.2×10^4 and 6.1×10^4 cycles, respectively	EEE and SPD after each spectrum loading, except the second loading on B24	Complete
Spectrum Loading: High - Low	B28	38, 34, 30, 26, and 22 ksi for 2×10^3, 8×10^3, 3×10^4, 10×10^4, and 36×10^4 cycles, respectively; repeat same spectrum loading; 38 ksi, failure at 9.5×10^4 cycles	EEE and SPD after each spectrum loading	Complete
	C4 C12 F5	38, 34, 30, and 26 ksi for 2×10^3, 8×10^3, 3×10^4, and 10×10^4 cycles, respectively; 22 ksi, failure of C4, C12, and F5 at 18×10^4, 12×10^4, and 10×10^4 cycles, respectively	None; see note	Failure to complete first loading
	E18	38, 34, and 30 ksi for 2×10^3, 8×10^3, and 3×10^4 cycles, respectively; 26 ksi, failure at 9×10^4 cycles.		
Spectrum Loading: Low - High - Low	D7	22, 26, 30, 34, 38, 34, 30, 26, and 22 ksi for 18×10^4, 5×10^4, 1.5×10^4 4×10^3, 2×10^3, 4×10^3, 1.5×10^4, 5×10^4, and 18×10^4 cycles, respectively; repeat spectrum loading, failure at first 22 ksi at 7.6×10^4 cycles	EEE and SPD after first spectrum loading	Complete
	A16 D12	22, 26, 30, 34, 38, 34, 30, and 26 ksi for 18×10^4, 5×10^4, 1.5×10^4, 4×10^3, 2×10^3, 4×10^3, 1.5×10^4, and 5×10^4 cycles, respectively; 22 ksi, failure of A16 and D12 at 1.79×10^4 and 1.33×10^4 cycles, respectively	None; see note	Failure to complete first loading
	F3	22, 26, 30, 34, 38, 34 and 30 ksi for 18×10^4, 5×10^4, 1.5×10^4, 4×10^3, 2×10^3, 4×10^3, and 1.5×10^4 cycles, respectively; 26 ksi, failure at 4.1×10^4 cycles		

TABLE C-1. LIST OF FATIGUE TEST SPECIMENS AND TEST CONDITIONS (CONT)

Material and Test Condition	Specimen Ident	Fatigue Load Condition	NDT: EEE = Exoelectron SPD = Surface Potential	Note
Fatigue Location - No Hole or Slot	H1	24 ksi, 2.1 x 10^4 cycles; 25 ksi, 8 x 10^5 cycles; 30 ksi, 5.2 x 10^5 cycles; 32 ksi, 13.8 x 10^4 cycles; 34 ksi, failure at 1.41 x 10^6 cycles		
	H2	26 ksi, failure at 1.65 x 10^6 cycles		
	H3	26 ksi, failure at 1.8 x 10^5 cycles		
	H4	28 ksi, failure at 16.55 x 10^4 cycles		
	H5	26 ksi, failure at 12.3 x 10^4 cycles	EEE during fatigue test	Complete
	H7	25 ksi, 6.1 x 10^6 cycles; 28 ksi, 1.15 x 10^6 cycles; 32 ksi, failure at 10.7 x 10^4 cycles		
	H8	28 ksi, failure at 11.88 x 10^4 cycles		
	H9	25 ksi, 2 x 10^6 cycles; 28 ksi, 5.14 x 10^5 cycles; 30 ksi, failure at 5.39 x 10^4 cycles		
	H10	28 ksi, failure at 82,760 cycles		
	H11	26 ksi, failure at 2.9 x 10^5 cycles		
	H12	26 ksi, 6.38 x 10^6 cycles; 30 ksi, failure at 3.6 x 10^5 cycles		
	H13	28 ksi, failure at 3.2 x 10^5 cycles		
	H14	28 ksi, failure at 2 x 10^5 cycles		Failure near specimen end outside test zone
	H15	26 ksi, failure at 4.1 x 10^5 cycles		
	H16	28 ksi, failure at 3.8 x 10^5 cycles		Complete
	H17	26 ksi, failure at 5.7 x 10^5 cycles		
	H72	30 ksi, failure at 2.8 x 10^5 cycles		

TABLE C-1. LIST OF FATIGUE TEST SPECIMENS AND TEST CONDITIONS (CONT)

Material and Test Condition	Specimen Ident	Fatigue Load Condition	NDT: EEE = Exoelectron SPD = Surface Potential	Note
Fatigue Location - No Hole or Slot (Cont)	H18	24 ksi, 1.6×10^6 cycles; 28 ksi, failure at 8.9×10^5 cycles		
	H19	26 ksi, failure at 1.7×10^5 cycles		
	H20	26 ksi, 1.5×10^6 cycles; 28 ksi, failure at 1.7×10^5 cycles	EEE during fatigue test	Complete
	H21	27 ksi, failure at 2.8×10^5 cycles		
	H22	27 ksi, failure at 1.6×10^5 cycles		
	H23	27 ksi, failure at 2×10^5 cycles		
	H24	26 ksi, 9.1×10^6 cycles; 28 ksi, failure at 7.6×10^5 cycles		
	H25	28 ksi, 2.8×10^6 cycles; 30 ksi, 1.6×10^6 cycles; 32 ksi, 1.7×10^6 cycles; 34 ksi, 1.7×10^6 cycles; 38 ksi, failure at 1.6×10^5 cycles		
	H47	28 ksi, failure at 2.4×10^5 cycles		
	H50	26 ksi, 1.2×10^6 cycles; 28 ksi, failure at 2.4×10^5 cycles		
	H59	28 ksi, 1.7×10^6 cycles; 30 ksi failure at 4.2×10^5 cycles		
	H62	28 ksi, 1.6×10^6 cycles; 30 ksi, 1.4×10^6 cycles; 34 ksi, failure at 11.64×10^4 cycles		
	H65	32 ksi, failure at 1×10^5 cycles		
	H68	30 ksi, failure at 2.1×10^5 cycles		
	H71	28 ksi, failure at 6.1×10^5 cycles		
	H93	1,000 lb, failure at 90,822 cycles		

TABLE C-1. LIST OF FATIGUE TEST SPECIMENS AND TEST CONDITIONS (CONT)

Material and Test Condition	Specimen Ident	Fatigue Load Condition	NDT: EEE = Exoelectron SPD = Surface Potential	Note
Fatigue Location - No Hole or Slot (Cont)	H97	26 ksi, 8.94 x 10^4 cycles; 28 ksi, 8.92 x 10^4 cycles; 30 ksi, failure at 6.89 x 10^4 cycles	EEE during fatigue test	Failure near specimen end outside test zone
	H98	1,000 lb, failure at 79,155 cycles		
	H26	1,500 lb, failure at 49,627 cycles		
	H27	1,000 lb, failure at 98,653 cycles		
	H28	1,500 lb, failure at 50,005 cycles		
	H38	750 lb, failure at 134,996 cycles		Complete
	H41	1,500 lb, failure at 49,060 cycles		
	H29	1,500 lb, failure at 81,340 cycles		
	H30	1,500 lb, failure at 24,192 cycles		
	H40	1,000 lb, failure at 120,661 cycles		
	H48	1,250 lb, failure at 81,098 cycles		
	H52	2,000 lb, failure at 12,163 cycles		
	H57	1,250 lb, failure at 57,192 cycles		
	H61	1,500 lb, failure at 29,168 cycles		
	H64	1,250 lb, failure at 44,267 cycles		
	10-73-1	22.25 ksi failure at 68,819 cycles		
Fatigue Location - 3 holes	D19	18 ksi, failure at 1.03 x 10^5 cycles	EEE during fatigue test	Complete
	C23	15 ksi, failure at 2.1 x 10^5 cycles		
	D24	14 ksi, failure at 2.11 x 10^5 cycles		
	E12	13 ksi, failure at 2.04 x 10^5 cycles		

TABLE C-1. LIST OF FATIGUE TEST SPECIMENS AND TEST CONDITIONS (CONT)

Material and Test Condition	Specimen Ident	Fatigue Load Condition	NDT: EEE = Exoelectron SPD = Surface Potential	Note
Fatigue Location - 3 holes (Cont)	E11	13 ksi, failure at 2.22×10^5 cycles		
	E7	12 ksi, failure at 2.48×10^5 cycles		
	A23	10 ksi, failure at 8×10^5 cycles		
	X3	500 lb, failure at 53,890 cycles	EEE during fatigue test	Complete
	H43	800 lb, failure at 6,277 cycles		
	H93	800 lb, failure at 10,307 cycles		
	11-72-4	650 lb, failure at 39,480 cycles		
Fatigue Location - 4 holes	C26	1,000 lb, failure at 9,988 cycles	EEE during fatigue test	Complete
	11-72-1	650 lb, failure at 7,581 cycles		
Fatigue Location - 4 Holes (with screws)	11-72-2	650 lb, failure at 8,572 cycles	EEE during fatigue test	Complete
	11-72-3	1,000 lb, failure at 5,136 cycles		
Fatigue Location - 7 Holes	H45	600 lb, failure at 38,783 cycles	EEE during fatigue test	Complete
	H70	800 lb, failure at 15,935 cycles		
Fatigue Location - Bolts	11-72-5	650 lb, failure at 10,384 cycles	EEE during fatigue test	Complete
	7-73-1	250 lb, failure at 27,236 cycles		
Fatigue Location - 3 Slots	X13	8 ksi, 1.25×10^6 cycles; 13 ksi, failure at 2.04×10^5 cycles	EEE and SPD at 1.25×10^6 cycles	Complete
	X12	8 ksi, 1.25×10^6 cycles; 13 ksi, failure at 2.1×10^5 cycles		
	X14	8 ksi, 1.25×10^6 cycles; 13 ksi, failure at 2.59×10^5 cycles		

TABLE C-1. LIST OF FATIGUE TEST SPECIMENS AND TEST CONDITIONS (CONT)

Material and Test Condition	Specimen Ident	Fatigue Load Condition	NDT: EEE = Exoelectron SPD = Surface Potential	Note
Fatigue Location - 3 Slots (Cont)	E2	8 ksi, 2.5×10^6 cycles; 13 ksi, failure at		
	B23	8 ksi, 2.5×10^6 cycles; 13 ksi, 11.2×10^6 cycles; 22 ksi, failure at 1.38×10^5 cycles	EEE and SPD at 2.5×10^6 cycles	Complete
	X11	8 ksi, 2.5×10^6 cycles; 13 ksi, 3.97×10^6 cycles; 18 ksi, failure at 1.52×10^5 cycles		
	D28	8 ksi, 1.25×10^6 cycles then to 2.7×10^6 cycles; 10 ksi, 8.5×10^6 cycles; 13 ksi, failure at 2.4×10^5 cycles	EEE and SPD at 1.25×10^6 cycles; EEE during fatigue test at 10 and 13 ksi	Complete
	E 10	13 ksi, failure at 4.1×10^5 cycles	EEE during fatigue test	Complete
Evaporation (Relative Humidity)	7-73-2	33.8 ksi, failure at 51,025 cycles		Test in 60-65% relative humidity, test completed
	7-73-3	26.6 ksi, failure at 51,020 cycles		Test in 65-70% relative humidity, test completed
	7-73-4	21 ksi, failure at 89,888 cycles		
	7-73-5	27 ksi, failure at 153,635 cycles		Test in 45% relative humidity, test completed
	7-73-6	32 ksi, failure at 42,081 cycles	EEE during fatigue test	Test in 30% relative humidity, test completed
	8-73-1	21 ksi, failure at 73,568 cycles		Interrupted test in 65% relative humidity (specimen stored in 100% relative humidity for 2-5 days before resumption of test), test completed
	8-73-2	26.3 ksi, failure at 44,115 cycles		
	8-73-3	31.8 ksi, failure at 25,594 cycles		
Corrosion	6-73-1	1000 lb, failure at 43,575 cycles		Corrosion study (24-hour soak in 0.05 M salt solution before test), test completed

TABLE C-1. LIST OF FATIGUE TEST SPECIMENS AND TEST CONDITIONS (CONT)

Material and Test Condition	Specimen Ident	Fatigue Load Condition	NDT: EEE = Exoelectron SPD = Surface Potential	Note
Aluminum 2024-T3				
General Plastic Deformation Pretensile Loading by 2.7% Strain	B12	2 tests at 30 ksi, each at 2×10^4 cycles; 38 ksi, failure at additional 19.87×10^5 cycles	EEE and SPD after first two fatigue tests	Complete
	A4	30 ksi, 4.1×10^4 cycles; 30 ksi, 1.9×10^4 cycles; 30 ksi, failure at additional 6.32×10^5 cycles		
Aluminum 7075-T6				
Fatigue Location - Slots	9-72-1	12.5 ksi, failure at 4,015 cycles	EEE during fatigue test	Complete
	9-72-2	6.25 ksi, failure at 8,628 cycles		
	9-72-3	6.25 ksi, failure at 7,703 cycles		
Fatigue location - 1 Hole	9-72-4	1,000 lb, failure at 4,680 cycles		
Fatigue Location - 4 Holes	9-72-5	3.75 ksi, failure at 2,944 cycles		
	9-72-6	5 ksi, failure at 2,114 cycles		
Fatigue Location - Curved Shapes	6-73-1	500 lb, failure at 35,858 cycles	EEE during fatigue test	Complete
	6-73-2	1,000 lb, failure at 20,380 cycles		
	7-73-1	21.2 ksi, failure at 82,927 cycles		
Aluminum 2219-T851 Weld				
Fatigue Location - No Flaws	CC1	15 ksi, 10^5 cycles; 20 ksi, 14.46×10^6 cycles; 32 ksi, failure at 1.76×10^5 cycles	EEE and SPD after the first two fatigue tests	Control specimen; test completed
	CC2	15 ksi, 10^5 cycles; 20 ksi, 10.303×10^6 cycles; 32 ksi, failure at 1.39×10^5 cycles		

TABLE C-1. LIST OF FATIGUE TEST SPECIMENS AND TEST CONDITIONS (CONT)

Material and Test Condition	Specimen Ident	Fatigue Load Condition	NDT: EEE = Exoelectron SPD = Surface Potential	Note
Fatigue Location - With Pores	PL1	13 ksi, 10^5 cycles; 16 ksi, failure at 9.81×10^5 cycles	EEE and SPD after the first fatigue test	Low porosity, test completed
	PL2	13 ksi, 10^5 cycles; 16 ksi, failure at 20.85×10^5 cycles		
	PM2	13 ksi, 10^5 cycles; 16 ksi, failure at 3×10^5 cycles		Medium porosity, test completed
	PM3	13 ksi, 10^5 cycles; 16 ksi, failure at 11×10^5 cycles		
	PH1	10 ksi, 10^5 cycles; 15 ksi, failure at 14×10^3 cycles		High porosity, test completed
	PH2	10 ksi, 10^5 cycles; 15 ksi, failure at 3×10^3 cycles		
Titanium, Annealed Ti-6Al-4V				
High Cycle - 25% Life	F19	40 ksi, 1.25×10^6 cycles	None	Reserve
	F14	2 tests at 40 ksi, each at 1.25×10^6 cycles; 110 ksi, failure at 9.3×10^4 cycles	EEE and SPD after first two fatigue tests	Complete
	F15	3 tests at 40 ksi, 1.25×10^6, 1.25×10^6 and 1×10^7 cycles; 110 ksi, failure at 16.2×10^4 cycles	EEE after first two fatigue tests; SPD after first three fatigue tests	
High Cycle - 50% Life	F54	40 ksi, 1.25×10^6 cycles	None	Reserve
	F20	3 tests at 40 ksi, 2.5×10^6, 1.25×10^6 and 1×10^7 cycles; 110 ksi, failure at 21.3×10^4 cycles	EEE after first two fatigue tests; SPD after first three fatigue tests	Complete
	F45	3 tests at 40 ksi, 2.5×10^6, 1.25×10^6 and 1×10^7 cycles; 110 ksi, failure at 6×10^4 cycles		

TABLE C-1. LIST OF FATIGUE TEST SPECIMENS AND TEST CONDITIONS (CONT)

Material and Test Condition	Specimen Ident	Fatigue Load Condition	NDT: EEE = Exoelectron SPD = Surface Potential	Note
High Cycle - 75% Life	F56	40 ksi, 3.75×10^6 cycles	None; see note	Reserve
	F61	3 tests at 40 ksi, 3.75×10^6, 1.25×10^6 and 10.12×10^6 cycles; 110 ksi, failure at 5.4×10^4 cycles	EEE after first two fatigue tests; SPD after first three fatigue tests	Complete
	F62	3 tests at 40 ksi, 3.75×10^6, 1.25×10^6 and 1×10^7 cycles; 110 ksi, failure at 6.8×10^4 cycles		
Low Cycle - 25% Life	F17	88 ksi, 1.5×10^4 cycles	None; see note	Reserve
	F3	3 tests at 88 ksi, 1.5×10^4, 1.5×10^4 and 11.83×10^6 cycles; 110 ksi, failure at 8×10^4 cycles	EEE after first two fatigue tests; SPD after first three fatigue tests	Complete
	F12	3 tests at 88 ksi, 1.5×10^4, 1.5×10^4 and 12.21×10^6 cycles; 110 ksi, failure at 17.9×10^4 cycles		
Low Cycle - 50% Life	F39	88 ksi, 3×10^4 cycles	None, see note	Reserve
	F22	2 tests at 88 ksi, 3×10^4 and 1.5×10^4 cycles; 110 ksi, failure at 1.03×10^6 cycles	EEE and SPD after first two fatigue tests	Complete
	F23	2 tests at 88 ksi, 3×10^4 and 1.5×10^4 cycles; 110 ksi, failure at 6.5×10^4 cycles		

TABLE C-1. LIST OF FATIGUE TEST SPECIMENS AND TEST CONDITIONS (CONT)

Material and Test Condition	Specimen Ident	Fatigue Load Condition	NDT: EEE = Exoelectron SPD = Surface Potential	Note
Low Cycle - 75% Life	F51	88 ksi, 4.5×10^4 cycles	None	Reserve
	F40	2 tests at 88 ksi, 4.5×10^4 and 1.5×10^4 cycles; 110 ksi, failure at 1.31×10^6 cycles	EEE and SPD at first two fatigue tests	Complete
	F47	2 tests at 88 ksi, 4.5×10^4 and 1.5×10^4 cycles; 110 ksi, failure at 7.7×10^4 cycles		
Spectrum Loading: Low-High	F11	40, 52, 64, 76, and 88 ksi for 36×10^4, 10×10^4, 3×10^4, 8×10^3, and 2×10^3 cycles, respectively	None; see note	Reserve
	F2 F6	40, 52, 64, 76, and 88 ksi for 36×10^4, 10×10^4, 3×10^4, 8×10^3, and 2×10^3 cycles, respectively; repeat same spectrum loading; 110 ksi, failure of F2 and F6 at 7.6×10^4 and 7.2×10^4 cycles, respectively	EEE and SPD after each spectrum loading	Complete
Spectrum Loading: High-Low	F46	88, 76, 64, 52, and 40 ksi for 2×10^3, 8×10^3, 3×10^4, 10×10^4, and 36×10^4 cycles, respectively	None; see note	Reserve
	F13 F21	88, 76, 64, 52, and 40 ksi for 2×10^3, 8×10^3, 3×10^4, 10×10^4, and 36×10^4 cycles, respectively; repeat same spectrum loading; 110 ksi, failure of F13 and F21 at 36.9×10^4 and 4.8×10^4 cycles, respectively	EEE and SPD after each spectrum loading	Complete
Spectrum Loading: Low-High-Low	F60	40, 52, 64, 76, 88, 76, 64, 52, and 40 ksi for 18×10^4, 5×10^4, 1.5×10^4, 4×10^3, 2×10^3, 4×10^3, 1.5×10^4, 5×10^4, and 18×10^4 cycles, respectively	None; see note	Reserve

TABLE C-1. LIST OF FATIGUE TEST SPECIMENS AND TEST CONDITIONS (CONCL)

Material and Test Condition	Specimen Ident	Fatigue Load Condition	NDT: EEE = Exoelectron SPD = Surface Potential	Note
Spectrum Loading: Low-High-Low (Cont)	F49 F55	40, 52, 64, 76, 88, 76, 64, 52, and 40 ksi for 18×10^4, 5×10^4, 1.5×10^4, 4×10^3, 2×10^3, 4×10^3, 1.5×10^4, 5×10^4, and 18×10^4 cycles, respectively; repeat same spectrum loading; 110 ksi, failure of F49 and F55 at 5.2×10^4 and 71.6×10^4, cycles, respectively	EEE and SPD after each spectrum loading	Complete
Fatigue Location - 3 Slots	2-73-1	350 lb, failure at 53,027 cycles	EEE during fatigue test	Complete
	2-73-2	400 lb, failure at 40,839 cycles		
	2-73-3	500 lb, failure at 20,200 cycles		
Fatigue Location - No Hole or Slot	F29	3,400 lb, failure at 120,661 cycles	EEE during fatigue test	Complete
Steel, Annealed PH14-8Mo				
Fatigue Location - No Hole or Slot	B1	1,000 lb, failure at 111,741 cycles	EEE during fatigue test	Complete
Fatigue Location - 3 Slots	F8	300 lb, failure at 69,643 cycles	EEE during fatigue test	Complete
Steel, Heattreated PH14-8Mo				
Fatigue Location - No Hole or Slot	3-73-1	3,000 lb, failure at 38,507 cycles	EEE during fatigue test	Complete
	3-73-2	2,500 lb, failure at 106,215 cycles		
Evaporation (64 - 74% Relative Humidity)	8-73-1	44.6 ksi, failure at 96,930 cycles	EEE during fatigue test	Complete
	8-73-2	45.9 ksi, failure at 118,188 cycles		
	8-73-3	55.6 ksi, failure at 54,154 cycles		
	8-73-4	69 ksi, failure at 23,428 cycles		
	8-73-5	69 ksi, failure at 31,036 cycles		
	9-73-1	44 ksi, failure at 217,922 cycles		